**Doctoral Dissertation**
**博士論文**

# Spin-orbit entanglement induced phenomena in pyrochlore materials (パイロクロア物質における スピン軌道もつれ誘起の現象)

A Dissertation Submitted for
the Degree of Doctor of Philosophy
December 2021
令和３年１２月博士（理学）申請

Department of Physics, Graduate School of Science,
The University of Tokyo
東京大学大学院理学系研究科
物理学専攻

Masashi Hosoi
細井　將史

# *Abstract*

The concept of spontaneous symmetry breaking has developed our understanding of various phenomena in strongly correlated electron systems. However, this historically successful paradigm has been challenged by the discovery of the quantum spin liquid phase and multipolar ordered phases. Quantum spin liquids are considered long-range entangled paramagnets and possess deconfined fractionalised excitations that can couple to emergent gauge fields. Because they do not exhibit any anomalies associated with spontaneous symmetry breaking down to the lowest temperatures, there are still many aspects of their nature that remain a mystery. Multipolar ordered phases are quantum phases that are elusive from a different perspective. They present spontaneous symmetry breaking at the transition temperature; however, their properties are not easily revealed because of the complexity of the order parameters that govern the symmetry breaking.

Rare-earth pyrochlore systems offer an ideal platform for investigating these prominent quantum phases because they have the potential to display both phases. The combination of the $D_{3d}$ symmetric crystal electric field and the strong spin-orbit interaction of $f$-electrons yields a non-trivial ground state doublet described by multipolar moments. In addition, the pyrochlore lattice hosts a three-dimensional geometrically frustrated structure, which is used to form the quantum spin liquid phase. Therefore, we expect that rare-earth pyrochlore systems are useful for independently investigating the properties of quantum spin liquids and multipolar ordered phases as well as investigating their combination.

Motivated by this expectation, two themes are discussed in this thesis, with lattice degrees of freedom as the common denominator: (i): Multipolar quantum spin ice and novel experimental probes; (ii): Relationship between the spin ice, magnetic field, and lattice.

In (i), we study a new class of quantum spin liquid, namely multipolar quantum spin ice, in a dipolar-octupolar pyrochlore system. The quantum spin liquid phase induced by the frustration of multipoles can be realised in a certain type of rare-earth pyrochlore system. Additionally, we clarify that the ground state of $Ce_2Zr_2O_7$ belongs to multipolar quantum spin ice by comparing neutron scattering measurements and our theoretical calculations. Furthermore, a novel experimental method known as magnetostriction measurement, is proposed to experimentally classify quantum spin liquids.

In (ii), we discuss the spin ice phase of non-Kramers pyrochlore systems under an external magnetic field along the [110] crystal direction. Within the strong field limit, the system is decoupled into a series of one-dimensional chains, which can then be considered a one-dimensional Ising chain. Moreover, by introducing the phonon degree of freedom to this chain, an emergent transverse field Ising model is realised in the non-Kramers py-

rochlore system. We demonstrate that the quantum phase transition associated with the emergent one-dimensional model is captured as a unique behaviour of nuclear magnetic resonance (NMR) relaxation time measurement.

# Contents

# Chapter 1

# Introduction

To develop a robust understanding of emergent phenomena in strongly correlated electron systems, deep insight is required into the many-body ground state and the excitations it can support [1, 2]. In the study of magnetism, many studies on the many-body ground states have focused on long-range ordered phases such as ferromagnetic, antiferromagnetic, and spin nematic phases, and the excitations are described by the spin wave theory. Therefore, the discovery of novel magnetic orders and their unique properties had been a main objective for several decades. However, this historically successful paradigm has been challenged in recent times by two prominent examples: quantum spin liquids (QSLs) and multipolar ordered states (MPOs).

In this chapter, two key concepts of this thesis are reviewed, namely QSLs and MPOs. In Section 1.1, we describe the basic concepts and developments in QSL research, and provide a detailed explanation for $U(1)$ QSLs, which is the main topic in the following chapters. In Section 1.2, we introduce the theoretical basis of multipoles and their properties, focussing on the MPOs emerging in $f$ electron systems. Finally, in Section 1.3, the overall structure of this thesis is provided.

## 1.1 Quantum spin liquids

Quantum spin liquids (QSLs) are considered to be long-range entangled correlated paramagnets and host deconfined fractionalised excitations (spinons) that couple to an emergent gauge field [3, 4, 5]. Here, the term "fractionalised excitation" means that the quasiparticle excitations cannot be constructed from the elementary degree of freedom, spin, but instead they are described by the fraction of a spin. The zero-point fluctuations are so strong that QSLs prevent conventional magnetic long-range orders. This lack of magnetic ordering presents an obvious challenge in its detection with conventional probes, such as in neutron scattering experiments. In fact, despite numerous efforts, a smoking-gun signature for QSLs has proven to be elusive, which has made QSL research extremely challenging.

QSLs originate from a variety of mechanisms, such as geometrical frustration [6, 7, 8, 9] and anisotropic bond-dependent spin interactions [10, 11, 12, 13]. The search for QSLs from the two mechanisms has contributed to a deep understanding of $U(1)$ spin liquids and $\mathbb{Z}_2$ spin liquids, respectively. In this section, we review both types of QSLs.

Most of the intriguing features of $\mathbb{Z}_2$ spin liquids are derived from the celebrated Kitaev honeycomb model, whereas $U(1)$ spin liquids are studied in a variety of contexts, not only those originating from classical spin ice which will be discussed below. Several are obtained from the extension of the Kitaev model; therefore, after briefly discussing the properties of the Kitaev model and the $\mathbb{Z}_2$ spin liquids based on Kitaev's original paper in Section 1.1.2, we discuss the origin and interesting properties of $U(1)$ spin liquids in Section 1.1.3. Finally, we will explain why $U(1)$ spin liquids in pyrochlore materials are the most attractive object to study from the viewpoint of multipoles.

### 1.1.1 Brief history

Before moving on to the main topic, we briefly review the history of QSL research. The QSL phase was firstly introduced by P. Anderson as the ground state of a triangular antiferromagnet system [14]. He proposed that the ground state of the spin 1/2 Heisenberg model on a triangular lattice is described as a quantum superposition of the possible spin-singlet pairs, which he referred to as the resonating valence bond (RVB) state (Fig. 1.1). Although this prediction proved to be incorrect, it paved a new way for the identification of QSLs in geometrically frustrated spin systems.

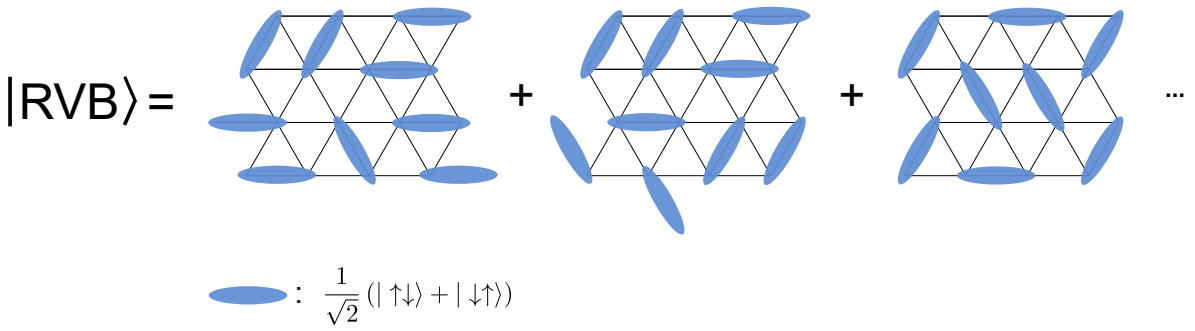


Figure 1.1. A resonating valence bond state. The blue ellipses indicate spin-singlet dimers.

The first paradigm shift occurred in 1987 when a theoretical model was proposed describing the realisation of high-temperature superconductivity in a doped RVB state [15, 16]. A series of studies suggested that superconductivity can emerge in doped QSLs and revealed the existence of quasiparticle excitations, now known as spinons. These proposals were based on the hypothesis that the ground state of the Hubbard or $t$–$J$ Hamiltonian is a non-degenerated disordered RVB state. Although valid proof for the existence of such a phase has not yet been obtained and the stability of the RVB ground state is still under discussion, the discovery of spinon excitation was the turning point in QSL research; shortly thereafter, QSLs with gapless fermionic spinons and gapped bosonic spinons were found one after another [17, 18].

Despite the development of many theories for QSLs during this period, material synthesis was unsuccessful. However, a proposal for a precisely solvable quantum spin model for QSLs by A. Kitaev and the discovery of its potential realisation with real materials by G. Jackeli and G. Khaliullin incited optimism [10, 11]. This was the second paradigm

shift. The Kitaev model is an ideal example for QSLs because it hosts a variety of interesting QSL phases with gapped and gapless excitations, one of which being a chiral QSL phase that possesses nonabelian Ising anyons. Quasiparticle excitation with nonabelian statistics is also important in the field of quantum computation because of its usefulness in fault-tolerant quantum computers [19]. As we will show in the following section, this model is rewritten as a free Majorana fermion model in a static $\mathbb{Z}_2$ gauge field. In this sense, QSLs of the Kitaev model belong to a class of $\mathbb{Z}_2$ spin liquids. In the experimental side, G. Jackeli and G. Khaliullin pioneered the feasibility of material synthesis for the Kitaev model by conducting extensive research on $5d$ transition metal oxides [11, 20]. Since then, a plethora of Kitaev materials have been proposed, including $\alpha$-$RuCl_3$ [21, 22], $A_2IrO_3$ (A=Na, Li) [23, 24, 25], and $A_3LiIr_2O_6$ (A=H, D, Ag, etc.) [26, 27, 28, 29]. Furthermore, a three-dimensional extension of the Kitaev model hosting a hyperhoneycomb or a stripyhoneycomb lattice was suggested and their corresponding materials are actively being studied [30, 31, 32, 33, 34, 35]. However, almost all the materials exhibit magnetic orders rather than QSL phases at the lowest temperature owing to the existence of non-Kitaev interactions, such as the Heisenberg exchange interaction $J$ and the off-diagonal interaction $\Gamma$. Motivated by these experimental results, a variety of spin models, in which extra terms are appended in addition to the Kitaev interaction, have been extensively theoretically studied [36, 37, 38, 39, 40, 41, 42, 43, 44]. In this way, research on QSLs in Kitaev model has progressed while theory and experiments have had a complementary and positive influence.

Simultaneously, the search for QSLs supported by traditional mechanisms, for example, geometrical frustration, has yielded significant progress in the last two decades. Examples include QSLs in a geometrically frustrated triangular lattice [45, 46, 47, 48, 49, 50] and kagome lattice [7, 51, 52, 53, 54, 55, 56]. Interestingly, the concept of geometrical frustration has been extended to three-dimensions, which led to a new class of QSL, namely the $U(1)$ spin liquid. The origin of $U(1)$ spin liquids dates back to the 1997 discovery of the classical spin ice state in $Dy_2Ti_2O_7$ and $Ho_2Ti_2O_7$ [57]. In classical spin ices, only rare-earth ions carry the magnetic moment, which reside on a network of corner-sharing tetrahedra, that is, a pyrochlore lattice. Their local spins are large and regarded as classical vectors, and interact ferromagnetically with each other under the constraint that they point along the local $z$ [111] Ising direction. This situation is equivalent to the frustrated antiferromagnetic Ising model on the pyrochlore lattice: $H = J\sum_{\langle i,j\rangle} S_i^z S_j^z$ with $J > 0$. It is known that this model possesses a macroscopic number of ground states given by a simple ice rule that two spins point inwards and the remaining two spins point outwards from the centre of each tetrahedron; this is called the two-in two-out configuration. A schematic illustration of the spin ice ground state is depicted in Fig. 1.2. The existence of classical spin ice in real materials is promising for general research on QSLs in magnetic materials. Although many theoretical models with QSL ground states are artificial, as explained later, applying quantum fluctuations on the classical spin ice states can be realistic and be expected to support a QSL phase with photon-like excitations. Consequently, the name '$U(1)$ spin liquids' is derived from these emerging lattice electrodynamics with $U(1)$ global gauge symmetry in the QSL phase.

Thus far, we have reviewed the history of QSL research, focussing on two classes of QSLs, $\mathbb{Z}_2$ spin liquids and $U(1)$ spin liquids. Table. 1.1 contains a detailed classification

of QSLs, including ones not mentioned in this section. We only provide a theoretical explanation for $\mathbb{Z}_2$ and $U(1)$ spin liquids in the following sections.

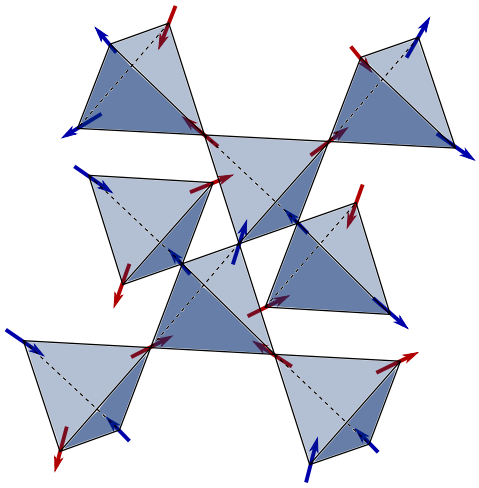

Figure 1.2. Classical spin ice ground state (two-in two-out spin configuration) on a pyrochlore lattice.

Table 1.1: Classification of QSLs reconstructed from Ref. [5]. Note that the acronyms in the table are as follows: ASL: algebraic spin liquid, FQH: fractional quantum Hall effect, CSL: chiral spin liquid. The quantity $\gamma$ is the topological entanglement entropy.

| Class | Subclass | Stability | Excitations | Models | Properties |
|---|---|---|---|---|---|
| $\mathbb{Z}_2$ | | | | | |
| | gapped | $d \geq 2$ | $e$,$m$,$\epsilon$ (= anyons) | Toric code model<br>Gapped phase of<br>the Kitaev model | $\gamma = \ln 2$ |
| | gapless | $d \geq 2$ | Gapless fermions | Kitaev model and<br>its generalizations | Potential to exhibit<br>a nonabelian phase<br>under perturbation |
| $U(1)$ | | | | | |
| | Pure | $d \geq 3$ | Gapless photon,<br>Gapped gauge charges | Compact QED,<br>Quantum spin ice | Sharp photon pole<br>in $S(q,\omega)$,<br>$T^3$ specific heat |
| | ASL = $U(1)$ Dirac | $d = 2$ | Gapless fermions with<br>electric charge and<br>strongly coupled gauge field | $QED_3$ | Conformal field theory,<br>emergent $SU(N)$ symmetry.<br>$S(q,+0) > 0$ at isolated $q$ |
| | Spinon Fermi surface | $d \geq 2$ | Gapless fermions with<br>electric charge and<br>strongly coupled gauge field | Triangular Heisenberg<br>+ Ring exchange | Nontrivial power laws,<br>emergent $SU(N)$ symmetry,<br>Broken area law,<br>$S(q,+0) > 0$ at all $q$ |
| FQH/CSL | | $d = 2$ | Laughlin $1/m$ anyons | Semiconductor electron<br>gases, $J_{1,2,3}$ kagome<br>Heisenberg | Broken time-reversal,<br>gapless edge states,<br>$\gamma = -\frac{1}{2}\ln m$ |

### 1.1.2 $\mathbb{Z}_2$ spin liquid

**Theoretical review of the Kitaev model and $\mathbb{Z}_2$ spin liquids**

The Kitaev model is a spin-1/2 model with nearest-neighbour anisotropic interactions on a honeycomb lattice. Bonds in the honeycomb lattice are divided into three types depending on their direction: the $x$, $y$, and $z$ bonds (Fig. 1.3(a)). The Hamiltonian is given as

$$H = J_x \sum_{x\text{-bond}} \sigma_i^x \sigma_j^x + J_y \sum_{y\text{-bond}} \sigma_i^y \sigma_j^y + J_z \sum_{z\text{-bond}} \sigma_i^z \sigma_j^z, \tag{1.1}$$

where $\sigma_i^\mu$ is the $\mu$ component of the Pauli matrix on site $i$. Then, we define the operator associated with the plaquette (see Fig. 1.3(a))

$$\hat{W}_p = \sigma_1^x \sigma_2^y \sigma_3^z \sigma_4^x \sigma_5^y \sigma_6^z. \tag{1.2}$$

This operator satisfies the relation $[\hat{W}_p, \hat{W}_{p'}] = 0$ and $[\hat{W}_p, H] = 0$, and thus the eigenvalue $W_p = \pm 1$ is a constant of motion. To solve the eigenstate problem of Eq. (1.1), we first divide the total Hilbert space into sectors according to the set of $W_p$ for each plaquette. The dimension of each *physical* subspace is $2^N$, where $N$ is the number of unit cells. We can clarify this by introducing Majorana fermions.

Spins are represented by Majorana operators $b^\mu$ ($\mu = x, y, z$) and $c$ as $\sigma^\mu = \mathrm{i} b^\mu c$. The Hamiltonian in Eq. (1.1) is rewritten as

$$H = \frac{\mathrm{i}}{4} \sum_{\langle i,j \rangle} \hat{A}_{ij} c_i c_j, \quad \hat{A}_{ij} = 2 J_{\mu_{ij}} \hat{u}_{ij}, \tag{1.3}$$

where $\mu_{ij}$ is the type of bond to which the $ij$–link belongs, and the bond operators $\hat{u}_{ij} = \mathrm{i} b_i^{\mu_{ij}} b_j^{\mu_{ij}}$. Remarkably, they commute with the Hamiltonian similar to the plaquette operator introduced above. Therefore, the total Hilbert space can be partitioned into subspaces according to the sets of eigenvalues of $\hat{u}_{ij}$. Within a certain subspace, we can replace $\hat{u}_{ij}$ with $c$-numbers, which enable us to exactly solve the Hamiltonian $H_{\{u\}}$ because it corresponds to a free fermion system. Here the index $\{u\}$ denotes the set of eigenvalues of $\hat{u}_{ij}$. However, owing to the dimension redundancy of Majorana fermions, the eigenstate of $H_{\{u\}}$, $|\Psi_{\{u\}}\rangle$ does not belong to the physical subspace. In order for the state to be physical, the following gauge invariance must hold for all $i$:

$$D_i |\phi\rangle = |\phi\rangle, \qquad D_i = b_i^x b_i^y b_i^z c_i. \tag{1.4}$$

We can enforce this gauge invariance by operating the projection $P = \prod_i \frac{1+D_i}{2}$ on an arbitrary state. Note that $D_i$ is considered the generator of $\mathbb{Z}_2$ gauge symmetry. The physical state is constructed as

$$|\Phi_{\mathcal{W}}\rangle = \prod_i \left( \frac{1 + D_i}{2} \right) |\Psi_{\{u\}}\rangle. \tag{1.5}$$

In the physical subspace, the ground state is characterised by the plaquette operator $\mathcal{W}_p = \pm 1$, defined as the product of $\hat{u}_{ij}$ along the boundary of the plaquette, instead of the set of $u$. Here,

$$\mathcal{W}_p = \prod_{\langle i,j \rangle \in \partial p} \hat{u}_{ij}. \tag{1.6}$$

This coincides with the aforementioned constant of motion $W_p$. Moreover, we can regard $\hat{u}_{ij}$ as a gauge potential and $\mathcal{W}_p$ as the associated $\mathbb{Z}_2$ flux combined with free Majorana fermions $c$.

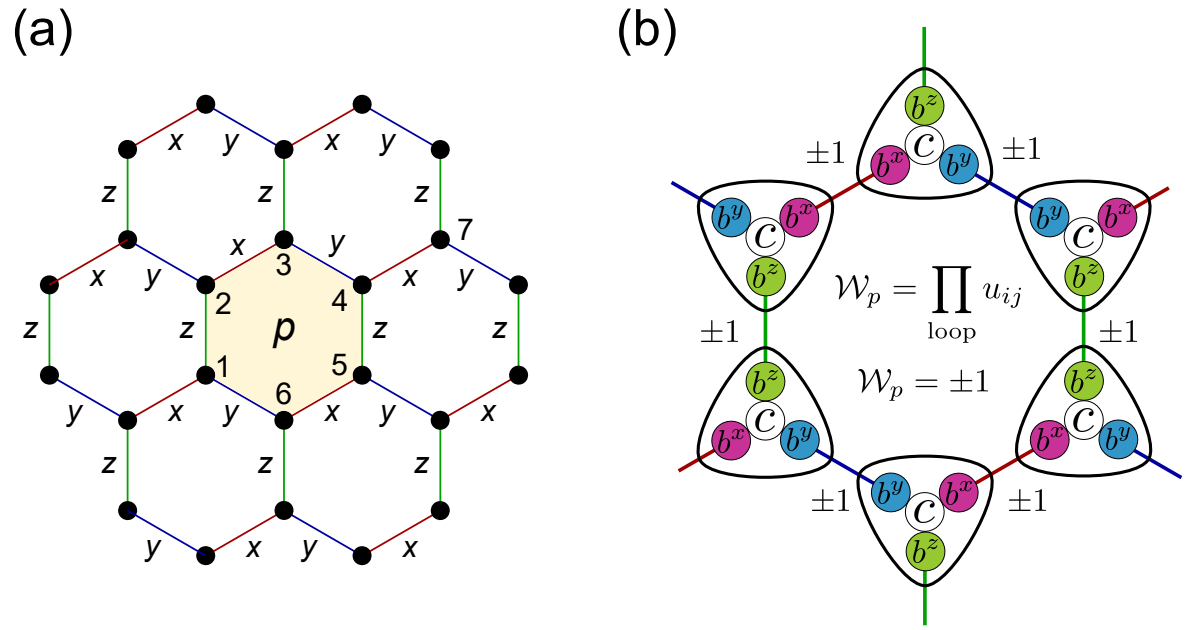


Figure 1.3. (a): Bond configuration of the Kitaev model and the plaquette in which the $W_p$ is defined. (b): Schematic illustration of the Majorana decomposition of each spin.

Thus far, we have rewritten Eq. (1.1) as a free Majorana fermion system under the emergent $\mathbb{Z}_2$ gauge flux. The next question to consider is "What is the flux configuration that minimises the ground state energy?". Notably, the celebrated Lieb's theory provides a rigorous answer to this question, and the flux-free state, that is, $\forall p\ \mathcal{W}_p = 1$, is found to be the ground state [58]. This indicates that the bond operator $u_{ij} = 1$ for all bonds and a translational symmetry recovers, which enables us to analytically calculate the energy spectrum of Majorana fermions. An intriguing property is that the spectrum can be both gapped and gapless depending on the coupling constant. We present in Fig. 1.4 the phase diagram of the Kitaev model, where the triangle represents the $J_x + J_y + J_z = 1$ plane of the positive octant. $A_x$, $A_y$, and $A_z$ phases represent the gapped phase and relate to each other by rotation symmetry. $B$ phase is gapless and the spectrum has two gapless Dirac points at $\boldsymbol{q} = \pm\boldsymbol{q}_0$ along the $q_y = 0$ line. These phases are called the gapless and gapped $\mathbb{Z}_2$ spin liquids, respectively. To explicitly verify that these phases have the properties of QSLs, we calculate the long-range correlation. For example, the $x$ component of the correlation between sites 6 and 7 in Fig. 1.3(a) is

$$\begin{aligned}
\langle \mathrm{GS}|\sigma_6^x\sigma_7^x|\mathrm{GS}\rangle &= \langle \mathrm{GS}|\hat{W}_p\sigma_6^x\sigma_7^x\hat{W}_p|\mathrm{GS}\rangle \\
&= \langle \mathrm{GS}|\sigma_1^x\sigma_2^y\sigma_3^z\sigma_4^x\sigma_5^y\sigma_6^z\sigma_6^x\sigma_7^x\sigma_1^x\sigma_2^y\sigma_3^z\sigma_4^x\sigma_5^y\sigma_6^z|\mathrm{GS}\rangle \\
&= \langle \mathrm{GS}|\mathrm{i}\sigma_6^y\sigma_7^x\sigma_6^z|\mathrm{GS}\rangle \\
&= \langle \mathrm{GS}|-\sigma_6^x\sigma_7^x|\mathrm{GS}\rangle = 0,
\end{aligned} \tag{1.7}$$

where we use the relation $W_p = 1$ in the first line for the ground state. Similarly, we can show that the correlation is strictly zero except between nearest neighbours, which indicates the lack of long-range order and the realisation of the QSL phase.

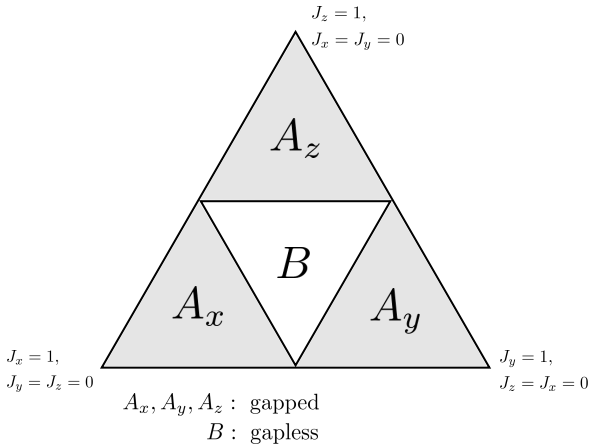


Figure 1.4. Phase diagram of the Kitaev model. The triangle represents the $J_x + J_y + J_z = 1$ plane of the positive octant.

As mentioned at the beginning of this chapter, the second key component of QSLs is fractionalised excitations. We now briefly describe them in gapped and gapless $\mathbb{Z}_2$ spin liquids. In gapped phases, flux excitation, that is, $\exists p W_p = -1$, can be regarded as the excitation of $e$- or $m$-particles. Here, the $e$- and $m$-particles are bosons with nontrivial mutual statistics: if an $e$-particle turns around a $m$-particle, the overall quantum state acquires an additional phase factor $e^{\mathrm{i}\pi} = -1$ (Note that the particles with this nontrivial mutual statistics in two-dimensional system are called *anyons*). In order to understand the relationship between the flux excitation and the $e$- and $m$-particles, let us consider a loop operator that shifts a flux along a certain loop. This operator coincides with $\hat{W}_p$, where $p$ is a plaquette index in the loop. Therefore, if $W_p = -1$, moving a flux around the defect flux leads to an additional $\pi$ phase shift. This mutual statistic is exactly the same as the one between the $e$ and $m$ anyons. In addition, the system contains itinerant Majorana fermions identified with the $\epsilon$ particle. In summary, there are three types of quasiparticle excitations, namely the $e$, $m$, and $\epsilon$ particles, inherent in gapped $\mathbb{Z}_2$ spin liquids.

Conversely, in the gapless phase, $e$- and $m$-particles do not exist because the mutual statistics is ill-defined. This is because the process of moving fluxes aforementioned above involves the dynamics of zero-energy Majorana fermions (the adiabatic transport of fluxes is impossible). Thus, fractionalised excitations in gapless $\mathbb{Z}_2$ spin liquids are simply referred to as Majorana fermion excitation and electric charge excitation, which correspond to the itinerant Majorana fermions and the flux excitation, respectively. However, in the presence of a magnetic field, the system acquires a gap and the $e$ and $m$ particles become well-defined. Remarkably, these excitations obey nonabelian statistics, and its nonzero Chern number guarantees chiral edge modes. This field-induced gapped phase is called a chiral quantum spin liquid, and it has attracted extensive attention in the field of quantum computing owing to its use in fault-tolerance.

### Experimental progress

Much effort has been devoted to capturing intriguing properties in the Kitaev model from an experimental perspective. A main approach is adopting the so-called Jackeli–Khaliullin mechanism, which uses a pseudospin degree of freedom induced by a strong spin-orbit coupling in $4d/5d$ transition metal oxides. Iridium and ruthenium ions ($Ir^{4+}$ and $Ru^{3+}$) have $5d^5$ and $4d^5$ electron configurations, respectively. The five-fold $d$ orbital is split into the lower-energy triplet $t_{2g}$ orbital and the higher-energy doublet $e_g$ orbital under an octahedral crystal field as shown in Fig. 1.5(a). Then, owing to the strong spin-orbit coupling of $4d/5d$ materials, the $t_{2g}$ orbital is separated into the lower $\Gamma_8$ quartet ($j_{\text{eff}} = 3/2$) and upper $\Gamma_7$ doublet ($j_{\text{eff}} = 1/2$). For $4d^5$ and $5d^5$ configurations, the $\Gamma_8$ orbital is fully occupied and the $\Gamma_7$ is hall-filled. This situation is regarded as a one-hole system with $j_{\text{eff}} = 1/2$, that is, a pseudospin-1/2 system (Fig. 1.5(a)). In $4d/5d$ transition-metal-based Kitaev materials, magnetic ions build a honeycomb lattice supported by edge shared octahedrons. Considering super-exchange interactions via oxygen, we obtain the effective Kitaev Hamiltonian Eq. (1.1) with $J_x = J_y = J_z = K$ (Fig. 1.5(b)).

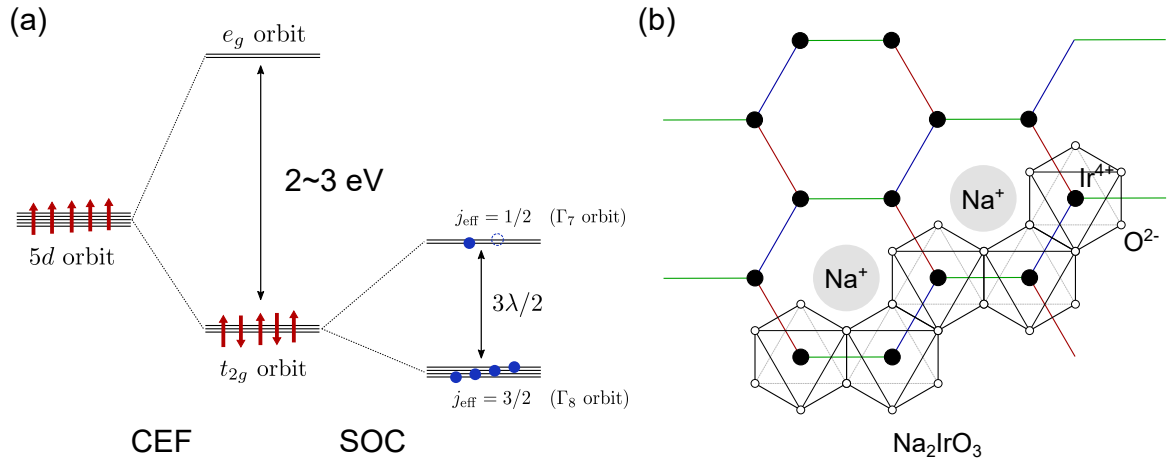


Figure 1.5. (a): Electron state of the $Ir^{4+}$ ion. The pseudospin-1/2 system is realised owing to a strong spin-orbit interaction. (b): Schematic diagram of the crystal structure of $Na_2IrO_3$, which is the first Kitaev candidate. The red, blue, and green bonds represent the $x$, $y$, and $z$ bonds in the Kitaev model, respectively. The octahedral configuration of oxygen ions acts as an octahedral crystal electric field.

However, in reality, Kitaev materials exhibit magnetic orders at low temperatures because of interactions other than the Kitaev term arising from the lattice distortion; hence, it is difficult to find the QSL ground state. Furthermore, the difficulty in capturing the QSL state arises partly from the fact that there is no singularity in conventional physical quantity such as specific heat and magnetic susceptibility. Thus, instead, research to capture the characteristic properties caused by fractionalised excitations has attracted extensive attention to prove the existence of $\mathbb{Z}_2$ or chiral spin liquid phases. In Table 1.2, we summarise the Kitaev candidates and their magnetic orders at low temperatures.

Table 1.2: Material candidates for the Kitaev spin liquid. Recently, Kitaev materials from mechanisms other than Jackeli–Khaliullin have been proposed. Note that the $\Gamma$ term mentioned in $\alpha$-$RuCl_3$ is defined as $\Gamma \sum_{\langle ij \rangle \in \gamma\text{-bond}} (\sigma_i^\alpha \sigma_j^\beta + \sigma_i^\beta \sigma_j^\alpha)$, where $\alpha$ and $\beta$ are the two remaining directions.

| Material | Dimension | Magnetic order | Other properties |
|---|---|---|---|
| $Na_2IrO_3$ | 2D | zigzag (13.3 K) [59] | The first candidate<br>Heisenberg-Kitaev model |
| $Li_2IrO_3$ | 2D | incommensurate spiral (15 K) [60] | extended Heisenberg-Kitaev model |
| $\alpha$-$RuCl_3$ | 2D | zigzag (7 K) [61, 62] | Suppressed magnetic order<br>by in-plane fields<br>K$\Gamma$ model<br>Half-integer thermal Hall effect<br>$\rightarrow$ CSL? |
| $Na_3Co_2SbO_6$ | 2D | zigzag (5 K) [63] | $d^7$ ions based material |
| $YbCl_3$ | 2D | Néel (0.6 K) [64] | $f$ ions based material |
| $H_3LiIr_2O_6$ | 2D | no magnetic order (0.05 K) [26] | Quenched disorders |
| $\beta$-$Li_2IrO_3$ | 3D | noncollinear order<br>(incommensurate spiral) [35] | Hyperhoneycomb lattice |
| $\gamma$-$Li_2IrO_3$ | 3D | noncoplanar order<br>(incommensurate spiral) [32] | Stripyhoneycomb lattice |

Now, we focus on $\alpha$-$RuCl_3$ which has received the most experimental attention as a candidate for gapless $\mathbb{Z}_2$ spin liquids. This material exhibits a zigzag magnetic order below 7 K; therefore, much effort has been devoted to indirectly proving the existence of the gapless $\mathbb{Z}_2$ spin liquid phase by investigating novel phenomena caused by fractionalised excitations above the transition temperature. Figures 1.6(a), (b), and (c) show the thermodynamic properties of $\alpha$-$RuCl_3$ [65]. The singularity of the magnetic susceptibility $\chi$ at approximately $T_N = 7$ K corresponds to a development of the zigzag magnetic order. The magnetic specific heat $C_M$ shows a characteristic broad peak at approximately $T_H = 100$ K as well as a sharp peak at $T_N$. As theoretically predicted, this broad peak is associated with the free Majorana excitations (see Fig. 1.6(d)), and a linear $T$ dependent $C_M$ below $T_H$ is also in accordance with the nature of free Majorana fermions [66]. Another piece of evidence can be found in the nature of entropy release, as shown in Fig. 1.6(c). The latter half of the two-step entropy release predicted by the theory is observed (Fig. 1.6(e)). Although the electric-charge-induced peak in the specific heat is masked due to the magnetic order, the above experimental results strongly support the existence of Majorana excitations.

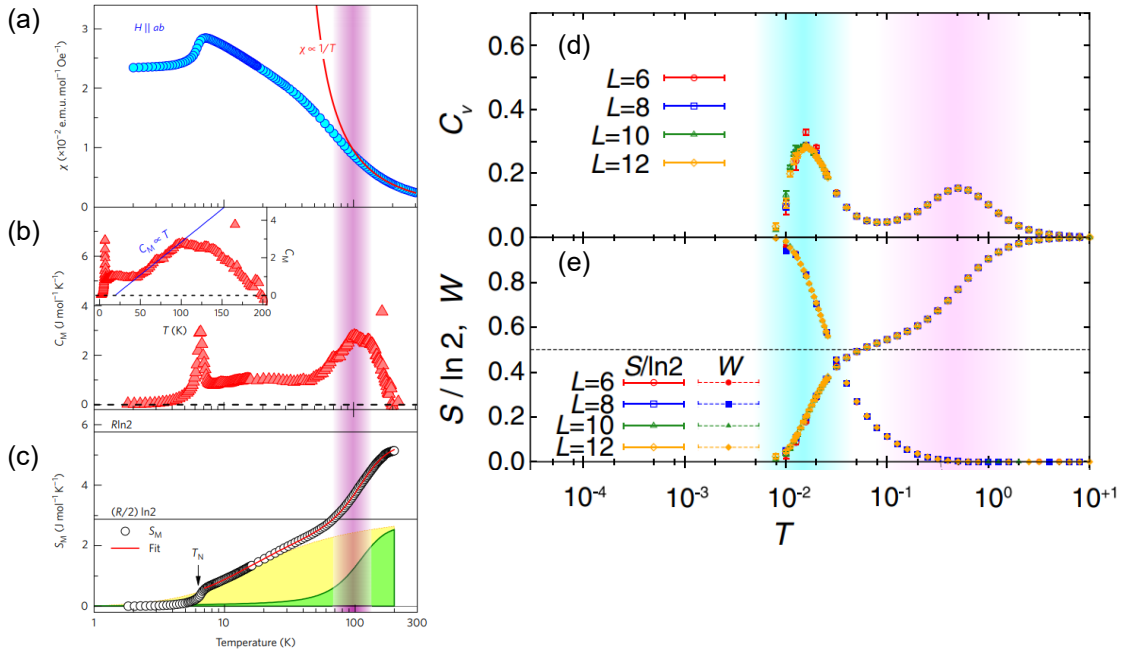


Figure 1.6. (a): Temperature dependence of the magnetic structure factor of $\alpha$-$RuCl_3$. The broad peak at approximately $T_N = 7$ K indicates the onset of the zigzag magnetic order. A magnetic field is applied within the $ab$ plane (honeycomb plane). (b): Temperature dependence of the magnetic specific heat $C_M$, where the contribution from the lattice is subtracted from the total specific heat. In addition to the sharp peak at $T_N$, a broad peak at approximately $T_H = 100$ K is observed. This is associated with the free Majorana fermions, and the linear-in-$T$ dependence for 50 K $\leq T \leq$ 100 K supports this prediction (see inset). The flat region below 50 K is attributed to the contribution of electric charge excitations. (c): Entropy release of $\alpha$-$RuCl_3$. The fitted red line is a sum of contributions from the localised and free Majorana excitations based on theoretical calculations. The yellow (green) shaded region corresponds to the contribution from the localised (free) Majorana fermions. (d): A quantum Monte Carlo calculation in the cluster with $2 \times L^2$ spins for the specific heat. The peak structures at low and high temperatures are associated with the electric charge excitation and free Majorana excitation, respectively. (e): Entropy per site and the thermal average of the density of the flux $W = \frac{2}{N}\sum_p \langle W_p \rangle$. The two-step entropy release is observed at low and high temperatures. The drastic decrease in $W$ at low temperatures indicates that the first entropy release is related to electric charge excitations. Fig. (a), (b), and (c) are reprinted by permission from Springer Nature: [65], Copyright (2021), and (d) and (e) are reprinted with permission from Copyright (2021) by the American Physical Society [66].

Furthermore, the researches on dynamical responses have succeeded in capturing the nature of the Kitaev spin liquid [22]. Figure 1.7(a) shows the results of the inelastic neutron scattering experiment on the $[HH0]$–$[K\bar{K}0]$ plane. The incident energy was 40 meV and the temperature was 5.0 K (below transition temperature), and data was

integrated over the range 4.5 meV $\leq E \leq$ 7.0 meV and $L = [-2.5, 2.5]$. The high intensity at the $\Gamma$ point and other peak structures are consistent with the theoretical expectation of the gapless Kitaev spin liquid shown in Fig. 1.7(b). The peak at the $\Gamma$ point is not only observed up to 120 K, but it is also observed over a wide range of energies. This behaviour is not explained by the spin-wave theory and indicates the existence of other continuum spectra, namely Majorana excitations.

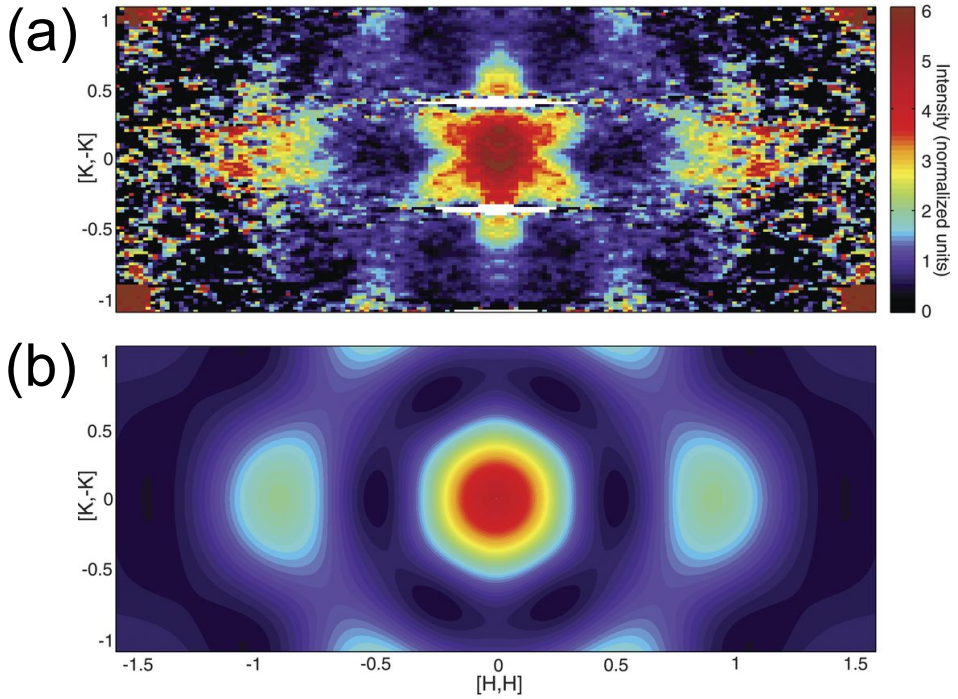


Figure 1.7. (a): Neutron scattering measurement with an incident energy of 40 meV at 5 K. The result is projected on the $[HH0]$–$[K\bar{K}0]$ plane, where the integration is taken over the range 4.5 meV $\leq E \leq$ 7.0 meV and $L = [-2.5, 2.5]$. (b): Theoretical calculation of the neutron signal under the same conditions as (a) on the isotropic Kitaev model. Reprinted with permission from AAAS [22].

Recently, a notable experiment to measure the half-integer thermal quantum Hall effect on $\alpha$-$RuCl_3$ was conducted [67]. It was proposed that the zigzag order in $\alpha$-$RuCl_3$ below 7 K is suppressed by an in-plane field, recovering the quantum disordered phase [61]. Reference [67] shows that this phase belongs to the aforementioned chiral spin liquid phase of the Kitaev model by detecting half-integer quantised thermal Hall conductivity. In the chiral spin liquid phase, the system acquires a nonzero Chern number of sgn$\Delta$, where $\Delta \sim \frac{h_x h_y h_z}{K^2}$, $h_\mu$ is the $\mu$ component of the applied magnetic field, and $K$ is the amplitude of the isotropic Kitaev interaction. Thus, the existence of the quantum Hall state is expected from the analogy of two-dimensional electron gas. The thermal Hall conductivity of the integer quantum Hall state is given as

$$\kappa_{xy} = \frac{\pi^2 k_B^2}{3h} T\nu \qquad \nu = 1, 2, 3, \ldots. \tag{1.8}$$

Meanwhile, noting that Majorana particles have half the degrees of freedom of complex fermions, we obtain the thermal Hall conductivity of the chiral spin liquid phase as

$$\kappa_{xy}^{\mathrm{CSL}} = \frac{\pi^2 k_B^2}{6h} T. \tag{1.9}$$

This is exactly the half value of the $\nu = 1$ case for two-dimensional electron gas. Figure 1.8 contains schematic diagrams comparing the above two situations, a phase diagram, and graphs on thermal Hall conductivity, which are all adopted from Ref. [67]. In Figs. 1.8(a) and (b), the red (blue) region is a high (low) temperature area. Electrons (green spheres) or itinerant Majorana fermions (yellow rods) at the edge, which contribute to the one-dimensional edge mode, carry the heat current. Note that, in a Kitaev quantum spin liquid, localised spins are separated into Majorana fermions and $Z_2$ flux, and thus the carrier degree of freedom is half that of the electrons. A phase diagram for $\alpha$-$RuCl_3$ in a magnetic field with a 60°tilting angle from the $c$ axis is shown in Fig. 1.8(c). The zigzag magnetic order observed below 7 K in the zero magnetic field disappears when the in-plane component of the magnetic field increases. The blue diamonds represent the transition temperature to the zigzag order, and open (closed) points are determined with respect to the $T$ ($H$) dependence of the longitudinal thermal conductivity. The red shaded region is the area in which half-integer quantised thermal Hall conductivity is observed, and thus the chiral spin liquid phase is expected. At points indicated by open squares, the half-integer quantised thermal Hall conductivity disappears, that is, transition to the trivial phase occurs. Figures 1.8(d), (e) and (f) show the observed half-integer quantised thermal Hall conductivity at 3.7, 4.3, and 4.9 K, respectively. The dashed line represents the $\kappa_{xy}^{\mathrm{CSL}} = \pi^2 k_B^2/6h$ line. These results support the realisation of the chiral spin liquid phase.

The field-induced spin liquid in the Kitaev model is not limited to the chiral spin liquid. Recent theoretical study suggests the emergence of a field-driven $U(1)$ QSL in the Kitaev honeycomb model [68]. In the following subsections, we present theoretical review of $U(1)$ spin liquids and the candidate system including the one in the Kitaev model.

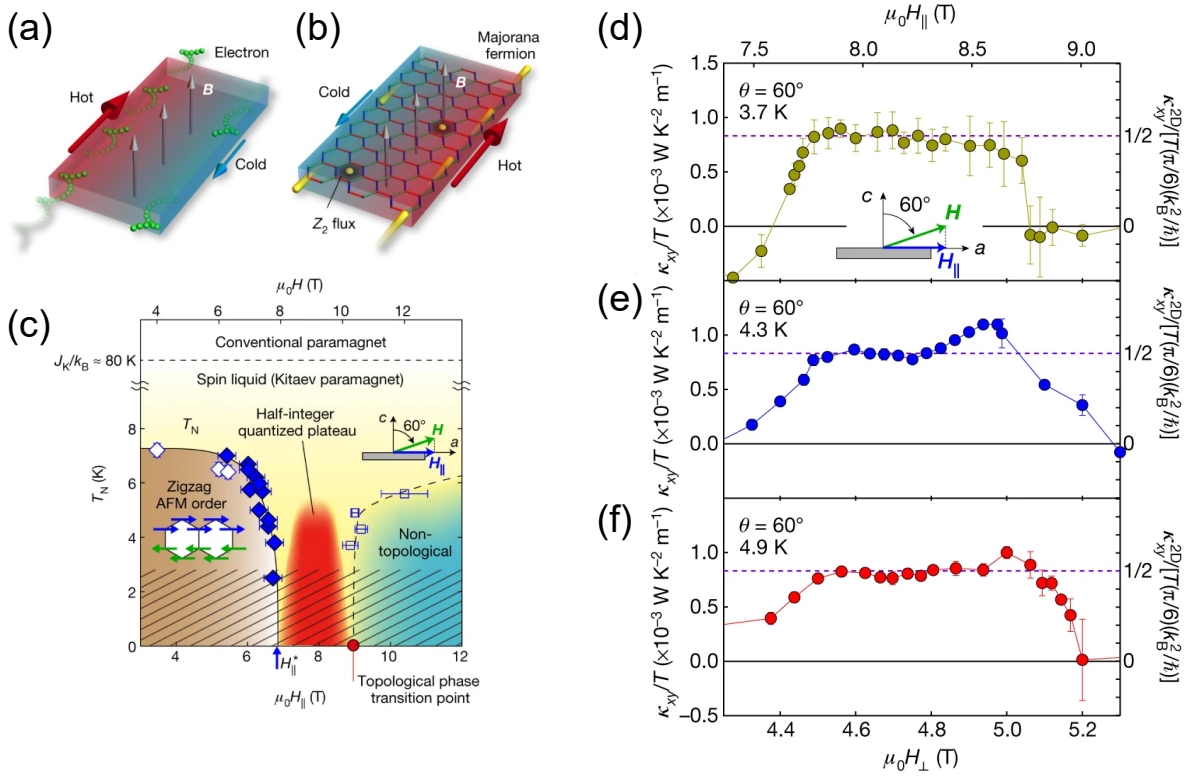


Figure 1.8. (a, b): Schematic diagram of heat transport in the integer quantum Hall state of a two-dimensional electron gas and in the Kitaev model in a magnetic field perpendicular to the two-dimensional plane. (c): Phase diagram of $\alpha$-$RuCl_3$ in a magnetic field $H$. The direction of the field is tilted away from the $c$ axis by 60°(see inset). The horizontal axis shows the in-plane component of the magnetic field. Diamond-shaped plots represent the transition points to the zigzag order, where the open and closed points are transition temperatures determined by the $T$ and $H$ dependences of the longitudinal thermal conductivity. The red shaded field is expected to be the chiral spin liquid phase, which exhibits the half-integer quantised thermal Hall effect. Blue open squares describe the points at which the half-integer quantised thermal Hall conductivity are not observed. Below 80 K, the Kitaev spin liquid phase is assumed to be realised. (d–f): Half-integer quantised thermal Hall conductivity plateau at 3.7, 4.3, and 4.9 K, respectively. Dashed lines represent the $\kappa_{xy}^{\mathrm{CSL}} = \pi^2 k_B^2/6h$ line. Reprinted by permission from Springer Nature: [67], Copyright (2021).

### 1.1.3 $U(1)$ spin liquid

Because there are a wide variety of systems that exhibit $U(1)$ quantum spin liquids, it is a good idea to first explain a common property of $U(1)$ gauge theory. Quantum electrodynamics (QED) is based on $U(1)$ gauge theory. In a spin system on a lattice, compact $U(1)$ gauge theory is naturally defined as discussed below.

#### Compact $U(1)$ gauge theory

In this section, we review the explanation in Ref. [5]. Assume there are field operators that satisfy the canonical commutation relation on each bond of a square lattice.

$$[A_{ij}, E_{ij}] = \mathrm{i}, \tag{1.10}$$

where $i$ and $j$ are the site indices, and we define $A_{ij} = -A_{ji}$, $E_{ij} = -E_{ji}$. We can associate $A$ and $E$ with the vector potential and the electric field in the usual electrodynamics, respectively. In this thesis, we discuss the QSL phases in the pyrochlore lattice where effective spin models possess the compact $U(1)$ gauge symmetric structure, and thus we start from the compact QED Hamiltonian

$$H = V \sum_i (\nabla \cdot E)_i^2 - K \sum_p \cos(\nabla \times A) + \frac{U}{2} \sum_{\text{link}} E_{ij}^2. \tag{1.11}$$

The first term corresponds to the energy of charge density as in the Maxwell equation, and the last two terms are the energy of the electromagnetic fields on a lattice. The cosine term is introduced to obtain the compact formulation of lattice QED from vacuum electrodynamics. In the discrete lattice, the divergence is defined as

$$(\nabla \cdot E)_i = \sum_{j \in \mathrm{NN-site}} E_{ij}, \tag{1.12}$$

and the magnetic field on a plaquette is

$$B_p = (\nabla \times A)_p = \sum_{\partial p} A_{ij}. \tag{1.13}$$

Figure 1.9 shows a schematic diagram of the above definition.

The difference between Eq. (1.11) and vacuum electrodynamics is that the magnetic field is included as the cosine term in the former. Owing to this difference, the wave function has to be periodic: $\psi(\tilde{A}_{ij}, \dots), \tilde{A}_{ij} = A_{ij} \pmod{2\pi}$. This structure defines compact $U(1)$ gauge theory. From the commutation relation in Eq. (1.10), we find that $e^{\mathrm{i}\theta E_{ij}}$ is a unitary operator which shifts the phase of the vector potential $A_{ij}$ by $\theta$. Therefore, the eigenvalues of $E_{ij}$ must be integers to satisfy the periodic condition of $A_{ij}$. Similar to the usual electrodynamics, there is a gauge uncertainty on the vector potential $A_{ij}$. Its lattice version is given as

$$A_{ij} \to A_{ij} + \chi_j - \chi_i, \tag{1.14}$$

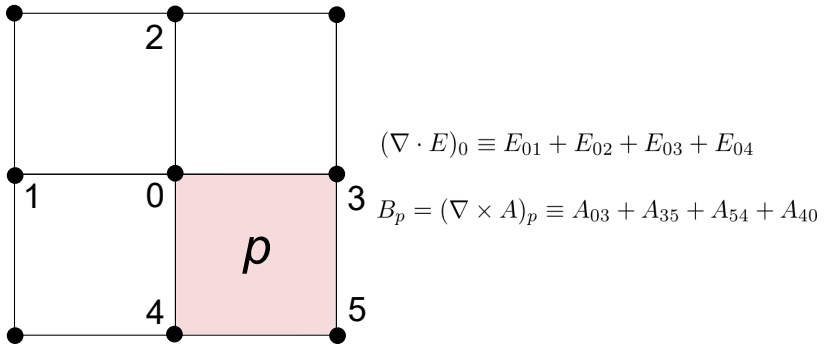


Figure 1.9. Definition of the divergence and rotation on the square lattice. Note that the edge of the plaquette is viewed in a clockwise direction.

where $\chi_j - \chi_i$ is the lattice gradient of an arbitrary function. Using the relation $E_{ij} = -E_{ji}$, we can derive that such a gauge transformation is obtained by a unitary operator

$$U = \exp\left[\mathrm{i}\sum_i \chi_i (\nabla \cdot E)_i\right]. \tag{1.15}$$

Since this is a symmetry operator, the charge operator $(\nabla \cdot E)_i$ commutates with the full Hamiltonian for all $i$, and its eigenvalue $Q_i$ is conserved, which corresponds to hyper charge conservation in usual non-compact $U(1)$ gauge theory. Normally, we are interested in the ground state and focus on the $Q_i = 0$ sector and $B_p = 0$ for all $p$. As we will later see, excitation to a nonzero $Q_i$ sector requires an energy gap of the order $V$ and is regarded as one of the fractionalised excitations in QSLs.

### Coulomb phase

The most intriguing feature of the compact $U(1)$ gauge theory is its potential to exhibit a deconfined Coulomb phase. Assuming the gauge fluctuation is sufficiently small and thus the fluctuation of a gauge field $B_p$ is also small, the low-energy description of the compact $U(1)$ gauge theory is given as non-compact QED without gauge charge, that is,

$$H \sim \frac{U}{2}\sum_{\text{link}} E_{ij}^2 - \frac{K}{2}\sum_p B_p^2. \tag{1.16}$$

When this assumption is valid, it is said that the system is in the Coulomb phase or deconfined phase. As we will later see, in the spin model on the pyrochlore lattice, this phase is stable in three-dimensional systems, and the $U(1)$ QSL phase belongs to this class. Because the Hamiltonian corresponds to usual non-compact QED, we expect (gauge) photon excitation modes with two transverse polarisations. As the second type of excitations, in a high energy region of the order $V$, there are gapped magnetic gauge charge excitations. In the spin model, this gauge charge stems from a fractionalised spin; hence, it characterises $U(1)$ QSLs. Note that these gauge charges experience the Coulomb potential $q_i q_j / r_{ij}$ like real charges, where $r_{ij}$ is the distance between site $i$ and

$j$. In the intermediate energy scale between the photon excitation and the magnetic charge excitation, there exists the third type of excitation named electric gauge charge excitation, which arises due to the compactness of the theory. It is considered as point defects, where the fluctuation is locally strong and the compactness recovers. Because this situation forms a magnetic flux excitation, it is analogous to the gapped $Z_2$ flux excitation of $\mathbb{Z}_2$ QSLs. Remarkably, it is known that electric charges also experience the Coulomb interaction between each other. A schematic figure of the spectrum of these excitations is shown in Fig. 1.10

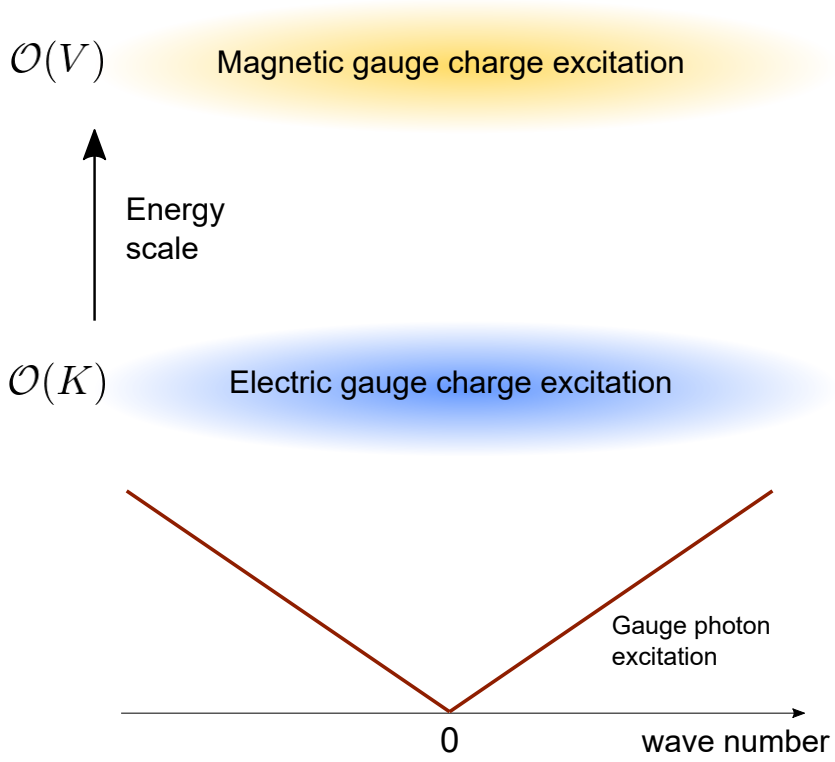


Figure 1.10. Schematic illustration of the energy scale of the three excitations, the gapless gauge photon, electric gauge charges, and magnetic gauge charges.

### Spin models with the $U(1)$ gauge structure

Now that we have briefly reviewed the compact $U(1)$ gauge theory, we can consider whether this can be realised in real spin models. Here, we provide examples to which the compact $U(1)$ gauge theory can be applied.

#### (i) Pyrochlore lattice

Spin models on the pyrochlore lattice are the most famous example of an emergent $U(1)$ gauge structure [69]. Consider the Hamiltonian

$$H = J_z \sum_{\langle i,j \rangle} S_i^z S_j^z + J_\perp \sum_{\langle i,j \rangle} (S_i^+ S_j^- + S_i^- S_j^+). \tag{1.17}$$

The first term is the Hamiltonian for the classical spin ice, which was introduced in Section 1.1.1, and the second term describes the quantum fluctuation. The first term is rewritten up to constant as $(J_z/2)\sum_t(\sum_{i\in t} S_i^z)^2$; therefore, we can easily understand that there is a macroscopic degeneracy with the two-in two-out manifold. Here, the index $t$ represents the tetrahedron. When the quantum fluctuation is small, that is, $J_\perp \ll J_z$, it is known that a degenerate perturbation theory yields the following effective ring exchange Hamiltonian:

$$H_{\text{eff}} = J_{\text{ring}} \sum_{\hexagon} (S_1^+ S_2^- S_3^+ S_4^- S_5^+ S_6^- + \text{h.c.}). \tag{1.18}$$

Here, $J_{\text{ring}} \sim \mathcal{O}(J_\perp^3/J_z^2)$, and the summation is taken over all the hexagons on the kagome layers of the pyrochlore lattice. It is convenient to change the sign of the ring exchange amplitude by applying a unitary transformation, which acts as a $\pi$ rotation about the local $z$ axis. Then, we obtain

$$H_{\text{eff}} = -J_{\text{ring}} \sum_{\hexagon} (S_1^+ S_2^- S_3^+ S_4^- S_5^+ S_6^- + \text{h.c.}). \tag{1.19}$$

We define the gauge field as

$$S_i^z = \eta_{\boldsymbol{r}} E_{\boldsymbol{r}\boldsymbol{r}'}, \quad S_i^+ = e^{\mathrm{i}\eta_{\boldsymbol{r}} A_{\boldsymbol{r}\boldsymbol{r}'}}, \tag{1.20}$$

where $\boldsymbol{r}$ indicates the site of the dual diamond lattice, and $\eta_{\boldsymbol{r}} = 1(-1)$ when $\boldsymbol{r}$ specifies the $A(B)$ sublattice. Note that site $i$ resides at the midpoint of the vector that connects $\boldsymbol{r}$ and $\boldsymbol{r}'$. We can easily verify that the relations $E_{\boldsymbol{r}\boldsymbol{r}'} = -E_{\boldsymbol{r}'\boldsymbol{r}}$ and $A_{\boldsymbol{r}\boldsymbol{r}'} = -A_{\boldsymbol{r}'\boldsymbol{r}}$ are satisfied. Enforcing the constraint $S_i^z = \pm 1/2$ with a Lagrange multiplier $U$, Eq. (1.19) is rewritten in the compact $U(1)$ gauge form up to constant:

$$H_{\text{QED}} = \frac{U}{2} \sum_{\langle \boldsymbol{r}\boldsymbol{r}' \rangle} E_{\boldsymbol{r}\boldsymbol{r}'}^2 - 2J_{\text{ring}} \sum_{\hexagon} \cos(\nabla \times A)_{\partial\hexagon}. \tag{1.21}$$

This is the same as the compact $U(1)$ gauge theory without gauge charge. Note that $U \to \infty$ must be taken to recover the original spin Hamiltonian.

We can rewrite Eq. (1.19) using the quantum rotor variables $Q_{\boldsymbol{r}\boldsymbol{r}'} \in \mathbb{Z}$ and $\phi_{\boldsymbol{r}\boldsymbol{r}'} \in [-\pi, \pi)$, which satisfy the commutation relations $[Q_{\boldsymbol{r}i}, \phi_{\boldsymbol{r}'j}] = \mathrm{i}\delta_{ij}\delta_{\boldsymbol{r}\boldsymbol{r}'}$. In the context of the quantum rotor model, the model should enter a Coulomb phase for small $U/K$. However, Monte Carlo simulations for Eq. (1.21) reveal that the Coulomb phase extends to the infinite $U$ limit. This result indicates that, as long as $J_\perp \ll J_z$ is fulfilled, the ground states are in the Coulomb phase and $U(1)$ QSL state because no long-range order is observed. A complete analysis of the spin model on the pyrochlore lattice is provided in the next chapter since the concept of multipoles is crucial.

**(ii) Hubbard model on a triangular lattice**

Beyond spin models with short-range pairwise interactions, the Hubbard model has been studied as a candidate model that exhibits $U(1)$ QSL ground states [70]. The Hubbard model is expressed as

$$H = -\sum_{\langle i.j \rangle, \sigma} (t_{ij} c_{i\sigma}^\dagger c_{j\sigma} + \text{h.c.}) + \frac{U}{2} \sum_i n_i(n_i - 1). \tag{1.22}$$

Here, $c^\dagger_{i\sigma}(c_{i\sigma})$ is the creation (annihilation) operator at the $i$-th site with spin $\sigma$ and $n_i = \sum_\sigma c^\dagger_{i\sigma} c_{i\sigma}$. The transfer integral can take the complex value with $t_{ij} = |t_{ij}|e^{-\mathrm{i}A_{ij}}$, where the vector potential $A_{ij}$ arises from an external electromagnetic field. Introducing the aforementioned quantum rotor variables, the electron operator is rewritten as $c_{i\sigma} = f_{i\sigma}e^{-\mathrm{i}\phi_i}$ with the spinon annihilation operator $f_{i\sigma}$. The extended Hilbert space has a constraint $Q_i = f^\dagger_{i\uparrow}f_{i\uparrow} + f^\dagger_{i\downarrow}f_{i\downarrow} - 1$, and the operator $e^{-\mathrm{i}\phi_i}$ acts as a lowering operator of the gauge charge $Q_i$. This representation leads to a $U(1)$ gauge redundancy, which appears as the invariance of electron operators under $\phi_i = \phi_i + \chi_i, f_{i\sigma} = e^{\mathrm{i}\chi_i}f_{i\sigma}$. Now, the $U(1)$ gauge invariant Hamiltonian is

$$H = -\sum_{\langle i.j\rangle,\sigma}(|t_{ij}|e^{\mathrm{i}(\phi_i-\phi_j-A_{ij})}f^\dagger_{i\sigma}f_{i\sigma} + \mathrm{h.c.}) + \frac{U}{2}\sum_i Q_i^2. \tag{1.23}$$

The spinons are free, except for the coupling to the slave rotor variant $\phi$ in the first term. This term can be separated by mean-field treatment into

$$-\sum_{\langle i.j\rangle,\sigma}(t^{\mathrm{eff}}_{ij}f^\dagger_{i\sigma}f_{i\sigma} + J_{ij}e^{\mathrm{i}(\phi_i-\phi_j-A_{ij})} + \mathrm{h.c.}). \tag{1.24}$$

Here, $t^{\mathrm{eff}}_{ij} = |t_{ij}|\langle e^{\mathrm{i}(\phi_i-\phi_j-A_{ij})}\rangle$ and $J_{ij} = |t_{ij}|\langle f^\dagger_{i\sigma}f_{j\sigma}\rangle$ [71]. The mean-field approximation reveals two possible phases. The first is a QSL with a spinon Fermi surface when the rotor fields are disordered, and the second is called the Higgs phase, which explains a Fermi liquid when the rotor fields are condensed, that is, $\langle e^{\mathrm{i}\phi_i}\rangle \neq 0$.

Recently, a piece of experimental evidence for a QSL with a spinon Fermi surface in a triangular lattice was reported [49]. $YbMgGaO_4$ demonstrates no magnetic ordering below 30 mK. In this material, $Yb^{3+}$ ions, which carry magnetic moments, form a Kramers doublet owing to the $D_{3d}$ crystal field, and its magnetic properties are well described by the effective spin half local moment. $Yb^{3+}$ ions form almost perfect triangular layers that are well-separated by non-magnetic $Mg^{2+}/Ga^{3+}$ ions. Hence, this system is considered a two-dimensional spin-half antiferromagnet on the triangular lattice. In Fig. 1.11, we show results from inelastic neutron scattering measurements at 70 mK. Figures 1.11(a–e) present experimental results on a certain energy plane, indicating the existence of diffusive excitations for every energy scale. Figure 1.11(f) is derived from a theoretical calculation based on the simplified mean-field model of spinons, $H_{\mathrm{mf}} = -t\sum_{\langle i,j\rangle}(f^\dagger_{i\sigma}f_{j\sigma} + \mathrm{h.c.}) - \mu\sum_i f^\dagger_{i\sigma}f_{i\sigma}$. A schematic diagram of the spinon Fermi surface derived from the same theoretical model is provided in Fig. 1.11(g). These experimental results strongly support the theoretical prediction of spinon Fermi surface $U(1)$ spin liquids.

**(iii) Field-induced $U(1)$ spin liquid in the Kitaev model**

In the previous section, we introduced the Kitaev model as an example of $\mathbb{Z}_2$ spin liquids. A recent theoretical study suggests the emergence of a field-driven $U(1)$ spin liquid in the Kitaev model [68]. The isotropic Kitaev model in a magnetic field is defined as

$$H = K\sum_{\langle i,j\rangle\in\gamma\text{–bond}} S^\gamma_i S^\gamma_j - \sum_i \boldsymbol{h}\cdot\boldsymbol{S}_i. \tag{1.25}$$

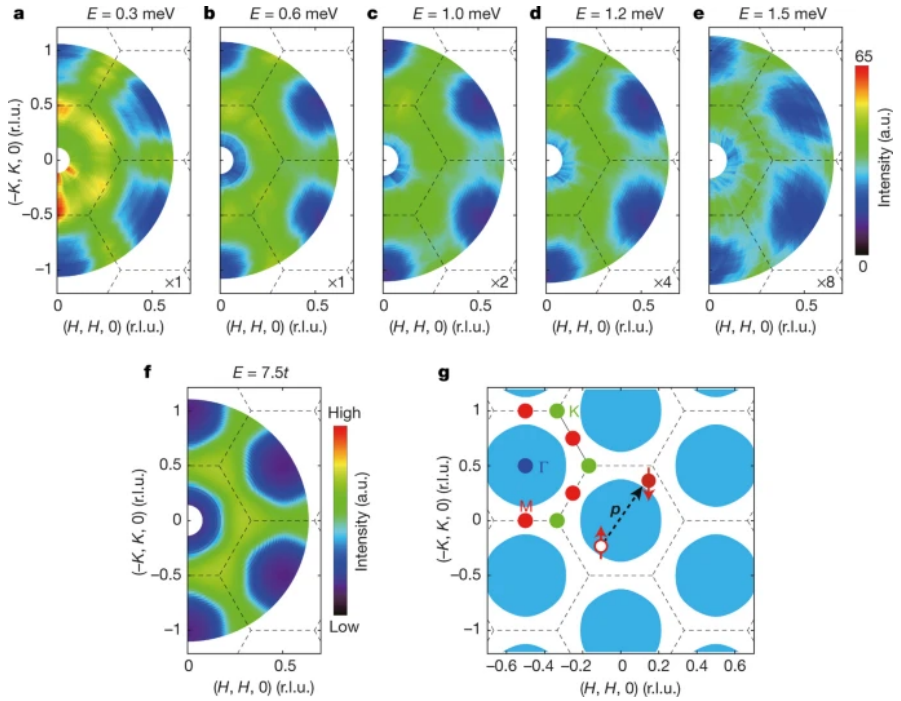


Figure 1.11. Signals from an inelastic neutron scattering (INS) measurement at 70 mK. (a–e): Several constant-energy planes exhibiting broad diffusive excitations in a wide range of Brillouin zones. (f): Theoretical calculation for the INS signals at $E = 7.5t$, where $t$ is the amplitude of universal transfers in the mean-field Hamiltonian introduced in the main text. (g): Schematic illustration of the spinon Fermi surface. Blue, red, and green circles describe the high symmetry points of the Brillouin zone ($\Gamma$, $M$, and $K$ points, respectively). Same colours indicate the equivalent points. The black dashed arrow depicts a pairwise excitation with momentum transfer $\boldsymbol{p}$ owing to an incident neutron. This enable us to observe the spinon Fermi surface in the INS measurement. Reprinted by permission from Springer Nature: [49], Copyright (2021).

In $\alpha$-$RuCl_3$, the $[11\bar{2}]$, $[\bar{1}10]$, and $[111]$ directions correspond to the $a$, $b$, and $c$-axis, respectively. The orientation is parameterised by angle $\theta$ from the $[111]$ direction. An exact diagonalisation for the antiferromagnetic Kitaev model ($K > 0$) suggests that the gapped chiral spin liquid phase extends beyond the perturbative limit and a novel gapless spin liquid phase emerges in the intermediate magnetic field region (Fig. 1.12(a)). A remarkable feature of the intermediate phase is that its density of states at low-energy regions is drastically enhanced (Fig. 1.12(b)). Taking the finite size effect into account, these excitation spectra are expected to be gapless, which indicates that gapless photon excitation exists in this intermediate phase. Moreover, it is confirmed that this phase is robust against non-Kitaev interactions, such as Heisenberg or $\Gamma$ terms.

However, the mere existence of gapless excitations is not sufficient to confirm that a $U(1)$ spin liquid has been realised. Reference [68] attempts to reveal the nature of this intermediate phase from various perspectives. First, we mention an intriguing feature

observed in the dynamic spin structure factor. In the intermediate state, they carry physical spin spectral weight over all momenta. Because only electric charge excitation carries the spin spectral weight in the Kitaev model without a magnetic field, the gap of electric charge excitations is expected to be closed in the intermediate state. Although one may expect that no electric charge gap will result in electric charge condensation and transition to the trivial magnetic ordered phase, this is not possible because they couple to the Majorana zero modes; thus, they cannot condensate by themselves. If this scenario is correct, the emergence of a $U(1)$ spin liquid seems to be reasonable in terms of the subsequent fermionic parton analysis. The spins of Abrikosov fermions are represented by $\boldsymbol{S}_i = \frac{1}{2} f^\dagger_{i\sigma} \boldsymbol{\sigma} f_{i\sigma}$ with the constraint $\forall i, f^\dagger_{i\sigma} f_{i\sigma} = 1$. Because the Kitaev model is invariant under the $U(1)$ gauge transformation $f_{i\sigma} \to e^{i\chi} f_{i\sigma}$, the Kitaev model can be regarded as possessing a $U(1)$ gauge structure. If we begin from this parton representation, the original Kitaev spin liquid state is viewed as the state with the instability of fermion pairing, which is a superconducting state in terms of fermionic partons. This superconducting condensation reduces the symmetry of the gapless $U(1)$ gauge field to the gapped $\mathrm{Z}_2$ field. It is also known that the topological properties of the Kitaev spin liquid require the superconductor to be of a chiral $p$-wave [72]. Therefore, the transition from the Kitaev spin liquid to the intermediate spin liquid phase is understood as the phase transition from a chiral $p$-wave parton superconductor with a gapped $Z_2$ field to an ordinary metal coupled to an emergent $U(1)$ gauge field, and the recovery of $U(1)$ gauge symmetry is accompanied by the gap closing of electric charge excitations [72, 73]. Although no rigorous proof for this scenario has been provided, nor has it been experimentally observed, it is expected to attract attention as a new system of $U(1)$ spin liquids.

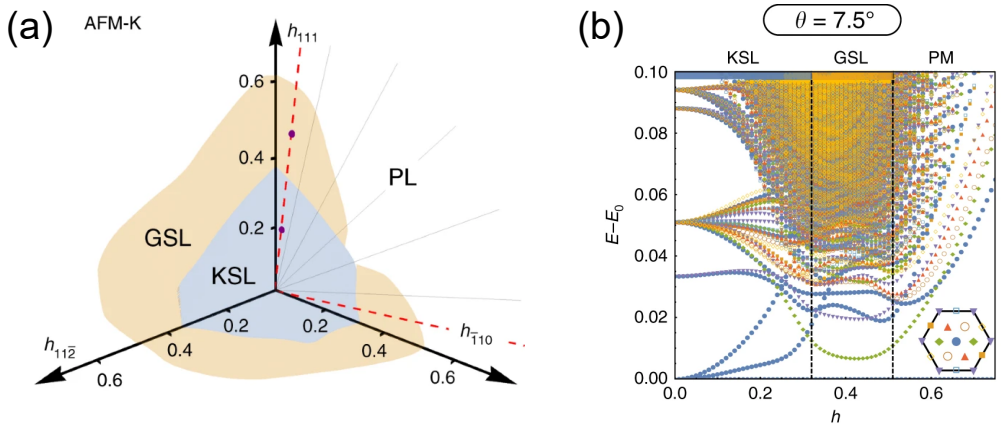


Figure 1.12. (a): Phase diagram obtained by an exact diagonalisation for the antiferromagnetic Kitaev model on a 24-site honeycomb cluster. KSL, GSL, and PL denote the chiral spin liquid phase in Kitaev's original paper, the intermediate spin liquid phase, which is assumed to be a $U(1)$ QSL, and a fully polarised phase, respectively. The red dotted lines indicate the $\theta$ =7.5° and 82.5° lines. The KSL extends beyond the perturbative region. (b): Energy spectrum in a magnetic field with $\theta$ =7.5°. The density of state of the GSL phase in this energy scale is approximately ten times larger than that of the KSL phase. Adopted from [68].

So far, we have introduced three examples that are expected to manifest the $U(1)$ QSL phase. Among them, only the spin-ice-induced $U(1)$ spin liquid may have pseudospins, that is, not real spins, which constitute the spin liquid state. In particular, the pseudospin sometimes yields higher-rank multipoles in rare-earth pyrochlore materials. In the subsequent section, we provide the concept of multipoles, their theoretical platform, and experimental progresses.

## 1.2 Multipolar ordered phases

In strongly correlated electron systems, crystal structures, spins, and orbitals are inextricably linked, which leads to exotic degrees of freedom, known as multipolar moments. Throughout this thesis, we will focus on the multipolar nature in rare-earth pyrochlore materials and review the basic concepts of them in this section. To understand multipolar degrees of freedom, it is better to focus on electronic states split by the electric field of the crystal and the spin-orbit interaction. Although this is an undergraduate-level topic, it is vital for the correct understanding of the properties of multipolar moments; therefore, we will begin with the basics. At the end of this section, we will apply the theoretical results to rare-earth compounds.

### 1.2.1 Two schemes for ground state multiplets

In the context of strongly correlated electron systems, transition metal oxides have long been a central research target. The complex interplay between the localised properties of $d$ electrons, crystal structures, spins, and orbitals, has continued to attract attention as a platform for the emergence of rich physical phenomena, ranging from Mott insulators to cuprate high-temperature superconductors. These traditional studies have mainly focussed on $3d$ electron systems, including iron, manganese, and copper. In contrast, compounds with strong spin-orbit interactions, including rare-earth materials that possess $4f$ electrons, tend to attract attention owing to their exotic phenomena. An example of these, the realisation of the Kitaev model supported by an emergent pseudospin-1/2 degree in iridium compounds, has already been provided in the previous section.

The spin-orbit interaction is naturally derived from the Dirac equation, a relativistic Hamiltonian. In general, it is represented as

$$H_{\mathrm{SO}} = \frac{\hbar^2}{2m^2c^2}\left(\frac{1}{r}\frac{dV}{dr}\right)\boldsymbol{l}\cdot\boldsymbol{s}, \tag{1.26}$$

where $\boldsymbol{l}$ and $\boldsymbol{s}$ are the orbital and spin angular momenta of electrons, respectively. $V(\boldsymbol{r})$ describes the potential experienced by electrons. If we use the Coulomb interaction from a nucleus as the potential, $V(r) = -Ze^2/r$, the amplitude of the spin-orbit interaction can be evaluated as

$$\lambda = \left\langle \frac{\hbar^2 Ze^2}{2m^2c^2r^3} \right\rangle. \tag{1.27}$$

Here, $\langle \dots \rangle$ is the average with regard to the wave function of electronic orbitals. From this formula, we expect that $4f$ or $5d$ electron systems with large atomic numbers host

a strong spin-orbit interaction[1]. For strong spin-orbit interactions, $\boldsymbol{l}$ and $\boldsymbol{s}$ are no longer suitable quantum numbers; instead, the total angular momentum, $\boldsymbol{j} = \boldsymbol{l} + \boldsymbol{s}$, becomes a suitable quantum number. Next, we will demonstrate that the total angular momentum scheme effectively describes the basis multiplet, using the $f^2$ electron configuration as an example.

The one-electron state of $f$ electron systems with an orbital angular momentum $l = 3$ in a spherically symmetric potential is determined by the combination of the magnetic quantum number ($l_z = -3, -2, \ldots, 3$) and spin ($s_z = \pm 1/2$); therefore, there are 14 degenerate states in total. For the $f^2$ electron configuration, such as in $Pr^{3+}$ ions, ${}_{14}C_2 = 91$ possible degenerate states are lifted by considering the Coulomb interaction between electrons. First, we consider the situation in which the Coulomb interaction is much greater than the spin-orbit interaction. In this regime, the lowest energy state is settled using Hund's rules: (i) The lowest energy state is the term with maximum $\boldsymbol{S}$; (ii) Under this constraint, the term with the largest $\boldsymbol{L}$ has the lowest energy; (iii) If the number of $f$ electrons is half-filled or less, the $J = |L - S|$ state gives the ground state multiplet. Otherwise, the $J = |L + S|$ state is the ground state. Here, $\boldsymbol{S}, \boldsymbol{L}$, and $\boldsymbol{J}$ are the total spin angular momentum, total orbital angular momentum, and total angular momentum, respectively. From Hund's rules, we find a $J = 4$ nine-fold state with $L = 5, S = 1$ constituting the ground state multiplet. This procedure to obtain the ground state multiplet is called the $LS$ coupling regime. In $f$ electron systems, this method provides a good approximation for the ground state multiplet because the amplitude of the Coulomb interaction is several tens of times larger than that of the spin-orbit interaction. Throughout the remainder of this thesis, we adopt this $LS$ coupling regime.

For completeness we next consider the inverse limit, where the spin-orbit interaction is much greater than the Coulomb interaction. In this scheme, we first take into account the effect of the spin-orbit interaction for the one-electron state and focus on the $j = 3 - 1/2 = 5/2$ state with six-fold degeneracy. Rules similar to Hund's rules can be applied to this case; the ground state is given by maximising the total angular momentum, which we call the extended Hund's rule. Applying the extended Hund's rule to our case, we find that the $\tilde{J} = 5/2 + 3/2 = 4$ state constructs the ground state multiplet. This method is called the $j$-$j$ coupling regime and is useful when hybridisation with conduction electrons is being considered. Figure 1.13 schematically illustrates the difference between these two schemes. Note that, although $J = 4$ and $\tilde{J} = 4$ have the same magnitude of angular momentum and degeneracy number, their wave functions are different because their configuration methods differ.

Starting from these ground state multiplets, the local ground state doublet can be realised by considering the crystal electric field. Notably, this emergent pseudospin 1/2 is not the same as the usual spin but can sometimes be regarded as a multipole. This fact is illustrated in subsequent sections.

[1]Strictly speaking, we should consider the quantum mechanical expectation value; however, this statement is also true if it is taken into account.

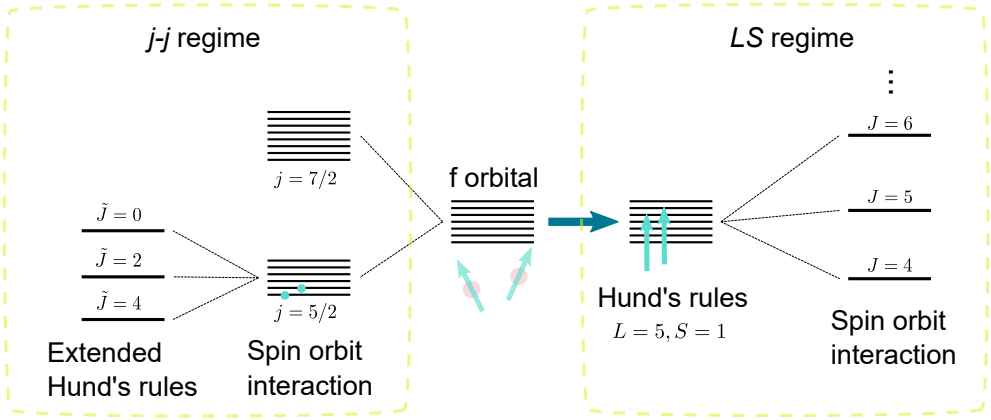


Figure 1.13. Schematic illustration of two schemes to identify the ground state multiplet of the $f^2$ configuration. In the $j$-$j$ coupling regime (left panel), we first consider the splitting of a one-electron state owing to the spin-orbit interaction. Then, the extended Hund's rule is applied to find the ground state multiplet. Conversely, in the $LS$ regime (right panel), we first apply Hund's rules, and then construct the ground state by considering the spin-orbit interaction. Note that the ground state wave functions of each regime are different, although they host a common total angular momentum, and the total angular momenta of the excited states are also different.

### 1.2.2 Multipolar moment

In this section, we provide basic concepts of multipoles based on Refs. [74, 75]. The orbital degree of freedom has been implicitly recognised because of the frequent occurrence of phenomena involving electron orbitals in $f$, $4d$, and $5d$ electron systems with strong spin-orbit interactions. With the rapid development of research in the last few decades, this degree of freedom has been developed into a more general concept for a multipolar degree of freedom that includes spin and orbital. In the following section, we will discuss the basic concept of a multipolar degree of freedom and how it is used.

#### Definition

A multipole is a quantity that characterises the anisotropy of the electric/magnetic charge distribution of a wave function and is naturally defined using the multipole expansion of the following scalar and vector potentials in classical electromagnetism:

$$\phi(\boldsymbol{r}) = \sum_{lm} a_l Q_{lm} \frac{Y_{lm}(\hat{\boldsymbol{r}})}{r^{l+1}}, \quad \boldsymbol{A}(\boldsymbol{r}) = \sum_{lm} b_l M_{lm} \frac{\boldsymbol{Y}^l_{lm}(\hat{\boldsymbol{r}})}{r^{l+1}} + c_l T_{lm} \frac{\boldsymbol{Y}^{l+1}_{lm}(\hat{\boldsymbol{r}})}{r^{l+2}}, \tag{1.28}$$

where $\hat{\boldsymbol{r}} = \boldsymbol{r}/r$. The normalisation factors are given by $a_l = \sqrt{4\pi/(2l+1)}$, $b_l = \mathrm{i}\sqrt{4\pi(l+1)/(2l+1)l}$, and $c_l = -\sqrt{4\pi/(l+1)}$. $Y_{lm}(\hat{\boldsymbol{r}})$ and $\boldsymbol{Y}^j_{lm}(\hat{\boldsymbol{r}})$ $(j = l, l \pm 1)$ are

Table 1.3: The parity of the physical quantities of inversion and time-reversal operators.

| physical quantities | inversion $\mathcal{P}$ | time-reversal $\mathcal{T}$ |
|---|---|---|
| Electrical charge $\rho_e$ | $+$ | $+$ |
| Magnetic charge $\rho_m$ | $-$ | $-$ |
| Toroidal charge $\rho_t$ | $+$ | $-$ |
| Electric multipole $Q_{lm}$ | $(-)^l$ | $+$ |
| Magnetic multipole $M_{lm}$ | $(-)^{l+1}$ | $-$ |
| Magnetic toroidal multipole $T_{lm}$ | $(-)^l$ | $-$ |
| Scalar potential $\phi(\boldsymbol{r})$ | $+$ | $+$ |
| Vector potential $\boldsymbol{A}(\boldsymbol{r})$ | $-$ | $-$ |
| Electric field $\boldsymbol{E}(\boldsymbol{r})$ | $-$ | $+$ |
| Magnetic field $\boldsymbol{B}(\boldsymbol{r})$ | $+$ | $-$ |

the usual spherical harmonics and the vector spherical harmonics. They are defined as

$$Y_{lm}(\hat{\boldsymbol{r}}) = (-1)^{\frac{m+|m|}{2}} \sqrt{\frac{4l+1}{4\pi}} \sqrt{\frac{(l-|m|)!}{(l+|m|)!}} P_l^m(\cos\theta) e^{\mathrm{i}m\phi}, \tag{1.29}$$

$$Y_{lm}^l(\hat{\boldsymbol{r}}) = \frac{1}{\sqrt{l(l+1)}} \boldsymbol{\ell} Y_{lm}(\hat{\boldsymbol{r}}), \tag{1.30}$$

$$Y_{lm}^{l-1}(\hat{\boldsymbol{r}}) = -\frac{1}{\sqrt{l(2l+1)}} (\mathrm{i}\hat{\boldsymbol{r}} \times \boldsymbol{\ell} - l\hat{\boldsymbol{r}}) Y_{lm}(\hat{\boldsymbol{r}}), \tag{1.31}$$

$$Y_{lm}^{l+1}(\hat{\boldsymbol{r}}) = -\frac{1}{\sqrt{(l+1)(2l+1)}} (\mathrm{i}\hat{\boldsymbol{r}} \times \boldsymbol{\ell} + (l+1)\hat{\boldsymbol{r}}) Y_{lm}(\hat{\boldsymbol{r}}), \tag{1.32}$$

where $P_l^m(x)$ are Legendre polynomials and $\boldsymbol{\ell} = -\mathrm{i}\hat{\boldsymbol{r}} \times \nabla$ [76, 77][2]. $Q_{lm}$, $M_{lm}$, and $T_{lm}$ in Eq. (1.28) are multipolar moments known as the electric, magnetic, and magnetic toroidal multipolar moments, respectively[3]. These multipolar moments are classified based on the nature of their response to inversion and time-reversal operators; arranging different types of "charges" constitutes the multipole. Parities against inversion- and time-reversal operators and related physical quantities are provided in Table 1.3.

[2]When a general vector field is expanded by vector spherical harmonic functions, it is expanded by these three independent components. Now, when we expand the vector potential, we are taking the Coulomb gauge $\nabla \cdot \boldsymbol{A} = 0$, in which case the $Y_{lm}^{l-1}(\hat{\boldsymbol{r}})$ component does not appear. Also, the second term in the expansion of the vector potential is often ignored because it disappears after rotation and does not affect the magnetic field. However, this degree of freedom often affects solid state properties and is actively being studied.

[3]Although it is possible to define the electric toroidal moment, such a term does not appear in multipole expansion.

From the multipole expansion, each multipolar moment is represented as

$$Q_{lm} = \int d\boldsymbol{r} r^l Z^*_{lm}(\hat{\boldsymbol{r}})\rho_e(\boldsymbol{r}), \quad M_{lm} = \int d\boldsymbol{r} r^l Z^*_{lm}(\hat{\boldsymbol{r}})\rho_m(\boldsymbol{r}), \quad T_{lm} = \int d\boldsymbol{r} r^l Z^*_{lm}(\hat{\boldsymbol{r}})\rho_t(\boldsymbol{r}), \tag{1.33}$$

where $Z_{lm}(\hat{\boldsymbol{r}}) = \sqrt{4\pi/2l+1}Y_{lm}(\hat{\boldsymbol{r}})$ is the Racah-normalised spherical harmonics. From the spatial and time-reversal symmetric nature of each "charge" and spherical harmonic functions, the parity of multipolar moments is as shown in Table 1.3. In addition, $l$ is the rank of the multipoles, where monopoles are known as ($l = 0$), dipoles ($l = 1$), quadrupoles ($l = 2$), octupoles ($l = 3$), and so on. For example, electric charges correspond to electric monopoles, magnetic spins correspond to magnetic dipoles, and a vector potential corresponds to the degree of freedom of magnetic toroidal dipoles.

In the presence of inversion symmetry, only multipoles with even parity can be active. That is, only even-ranked electric multipoles, magnetic toroidal multipoles, and odd-ranked magnetic multipoles are finite. Previous microscopic theories on multipoles have mainly focussed on even-parity multipoles localised at these atomic sites. Furthermore, magnetic toroidal multipoles become active only when the different angular momenta (*s*-*d* or *d*-*f* orbitals) are hybridised; however, this hybridisation is generally small and has not been specifically considered. Recently, there have been many attempts to discover odd-parity multipoles in such systems. The search for odd-parity multipoles in systems with locally-broken inversion symmetry has attracted much attention, where the multipoles are not localised at atomic sites but are defined in a whole unit cell (extended multipoles). The ordered phases of magnetic quadrupoles and electric octupoles have been theoretically proposed.

### Wigner–Eckart theorem and Stevens equivalent operators

In the following sections, we will restrict our discussion to the localised electric and magnetic multipoles, which are being actively studied. Because the observed quantities related to multipoles are thermal averages of the electric or magnetic charge distribution operators, we first need to construct the multipolar operators.

In the following chapters, we will frequently use polynomials in terms of total angular momentum $\boldsymbol{J}$ and call them "multipoles". Towards the end of this section, we will clarify the relationship between the multipolar operators defined by the total angular momentum and the multipolar operators defined by the anisotropy of the charge distribution described so far. Specifically, we mathematically show that polynomials in terms of total angular momentum $\boldsymbol{J}$ capture the geometrical property of multipoles. Readers who are familiar with this treatment are requested to skip this section and go to Section 1.2.3.

Let us assume that the electric charges distribute in points. The charge distribution operator is expressed as

$$\hat{\rho}_e(\boldsymbol{r}) = e\sum_i \delta(\boldsymbol{r} - \hat{\boldsymbol{r}}_i). \tag{1.34}$$

Note that $\hat{\boldsymbol{r}}_i$ is the position operator. Therefore, the electric multipole operator is

$$\hat{Q}_{lm} = e\sum_i r_i^l Z^*_{lm}(\hat{\boldsymbol{r}}_i). \tag{1.35}$$

The situation is similar for the magnetic multipole operator; however, the formula is more complex, reflecting the fact that the magnetic dipolar moment $\boldsymbol{M}$ must be distributed in a point-like manner due to the absence of magnetic charge. The result is

$$\hat{M}_{lm} = \mu_B \sum_i \left( \frac{2\boldsymbol{l}_i}{l+1} + 2\boldsymbol{s}_i \right) \cdot \nabla_i \left( r_i^l Z_{lm}^*(\hat{\boldsymbol{r}}_i) \right), \tag{1.36}$$

where $\mu_B$ is the Bohr magneton [77]. When the active multipolar moment is derived, we must calculate the matrix elements by taking the expectation values of the above operators in terms of the ground state multiplet, which is specified by the total angular momentum $J$ and its $z$ component $M$, $\langle J'M'|\hat{X}_{lm}|JM\rangle$ $(X = Q, M)$. As explained in the previous section, the ground state multiplet is represented by a *many-body* wave function; thus it is difficult to calculate the expectation value of *one-body* operators included in multipolar operators. Fortunately, this problem is resolved using the Wigner–Eckart theorem and the Stevens equivalent operator method, as described below.

**Wigner–Eckart theorem**

Let us consider a spherical tensor operator with rank $k$: $\boldsymbol{T}^{(k)} = \{T_q^{(k)}\}$ $(q = -k, -k+1, \ldots, k)$. This operator satisfies the following commutation relations with the total angular momentum operator:

$$\begin{aligned} [J_z, T_q^{(k)}] &= qT_q^{(k)}, \\ [J_\pm, T_q^{(k)}] &= \sqrt{(k \mp q)(k \pm q + 1)}T_{q\pm1}^{(k)}. \end{aligned}$$

The Wigner–Eckart theorem states that the expectation value of this operator is given as follows:

$$\begin{aligned} \langle JM|T_q^{(k)}|J'M'\rangle &= \langle J||T^{(k)}||J'\rangle \frac{\langle J'M'kq|JM\rangle}{\sqrt{2J+1}} \\ &= \langle J||T^{(k)}||J'\rangle (-1)^{J'-k+M} \begin{pmatrix} J & J' & k \\ -M & M' & q \end{pmatrix}, \end{aligned}$$

where $\langle J||T^{(k)}||J'\rangle$ is referred to as the reduced matrix element, which includes the physical properties of the spherical tensor operator, the initial state, and the final state. Moreover, it is independent of $M, M'$, and $q$. $\langle J'M'kq|JM\rangle$ is the Clebsch–Gordan coefficient for the coupling $\boldsymbol{J} = \boldsymbol{J}' + \boldsymbol{k}$, and geometrical information on the matrix element is included. The $2 \times 3$ array in the second line denotes the $3j$ symbol, which represents the Clebsch–Gordan coefficients in a symmetric form. The key result is that the matrix elements of the spherical tensor operator are separated into the physical term and geometrical term.
More generally, the Wigner–Eckart theorem holds for any tensor operator with the same transformation as that of the basis of the irreducible representation.

**Outline of the proof**

Here, we prove that the matrix elements of the spherical tensor operator $\langle JM|T_q^{(k)}|J'M'\rangle$

are proportional to the Clebsch–Gordan coefficient $\langle J'M'kq|JM\rangle$. From the first commutation relation $[J_z, T^{(k)}_q] = qT^{(k)}_q$, we find

$$\begin{aligned}
&\langle JM|[J_z, T^{(k)}_q]|J'M'\rangle = \langle JM|qT^{(k)}_q|J'M'\rangle, \\
&\Rightarrow M\langle JM|T^{(k)}_q|J'M'\rangle - M'\langle JM|T^{(k)}_q|J'M'\rangle = q\langle JM|T^{(k)}_q|J'M'\rangle, \\
&\Rightarrow (M - M' - q)\langle JM|T^{(k)}_q|J'M'\rangle = 0.
\end{aligned}$$

Thus, $\langle JM|T^{(k)}_q|J'M'\rangle = 0$ unless $M = M' + q$. From the second commutation relation $[J_\pm, T^{(k)}_q] = \sqrt{(k \mp q)(k \pm q + 1)}T^{(k)}_{q\pm1}$, we can derive

$$\begin{aligned}
&\langle JM|[J_\pm, T^{(k)}_q]|J'M'\rangle = \langle JM|\sqrt{(k \mp q)(k \pm q + 1)}T^{(k)}_{q\pm1}|J'M'\rangle \\
&\Rightarrow \sqrt{(J \mp M + 1)(J \pm M)}\langle J, M \mp 1|T^{(k)}_q|J'M'\rangle \\
&\qquad\qquad - \sqrt{(J' \pm M' + 1)(J' \mp M')}\langle JM|T^{(k)}_q|J', M' \pm 1\rangle \\
&= \sqrt{(k \mp q)(k \pm q + 1)}\langle JM|T^{(k)}_{q\pm1}|J'M'\rangle.
\end{aligned}$$

In the above, each term is zero unless $M = q + M' \pm 1$. To demonstrate that this recursion relation resembles that of the Clebsch–Gordan coefficient, we consider the coupling $\boldsymbol{J} = \boldsymbol{J}' + \boldsymbol{k}$. Using the Clebsch–Gordan coefficient, the state $|JM\rangle$ is represented as

$$|JM\rangle = \sum_{M',q}\langle J'M'kq|JM\rangle|J'M'kq\rangle.$$

Applying the operator $J_\mp$, we obtain

$$\begin{aligned}
&\sqrt{(J \mp M + 1)(J \pm M)}|J, M \mp 1\rangle \\
&= \sum_{M',q}\sqrt{(J' \mp M' + 1)(J' \pm M')}\langle J'M'kq|JM\rangle|J', M' \mp 1, kq\rangle \\
&\qquad\qquad + \sum_{M',q}\sqrt{(k \mp q + 1)(k \pm q)}\langle J'M'kq|JM\rangle|J'M'k, q \mp 1\rangle \\
&\Rightarrow \sum_{M',q}\sqrt{(J \mp M + 1)(J \pm M)}\langle J'M'kq|J, M \mp 1\rangle|J'M'kq\rangle \\
&= \sum_{M',q}\sqrt{(J' \pm M' + 1)(J' \mp M')}\langle J', M' \pm 1, kq|JM\rangle|J'M'kq\rangle \\
&\qquad\qquad + \sum_{M',q}\sqrt{(k \pm q + 1)(k \mp q)}\langle J'M'k, q \pm 1|JM\rangle|J'M'kq\rangle.
\end{aligned}$$

Comparing the coefficients of the above equation, we find the recursion relation of the Clebsch–Gordan coefficient as

$$\begin{aligned}
&\sqrt{(J \mp M + 1)(J \pm M)}\langle J'M'kq|J, M \mp 1\rangle - \sqrt{(J' \pm M' + 1)(J' \mp M')}\langle J', M' \pm 1, kq|JM\rangle \\
&= \sqrt{(k \pm q + 1)(k \mp q)}\langle J'M'k, q \pm 1|JM\rangle.
\end{aligned}$$

This is the same as the recursion relation of $\langle JM|T_q^{(k)}|J'M'\rangle$, and each term is zero unless $M = q + M' \pm 1$ owing to a property of the Clebsch–Gordan coefficient. In other words, $\langle JM|T_q^{(k)}|J'M'\rangle$ and $\langle J'M'k, q|JM\rangle$ follow the same relation in terms of $J, M, J', M', k$, and $q$. Thus, we can derive

$$\langle JM|T_q^{(k)}|J'M'\rangle \propto \langle J'M'k, q|JM\rangle.$$

■

From the Wigner–Eckart theorem, we can derive the Stevens equivalent operator method. In reality, the spherical tensor operator can be constructed using total angular momentum operators [76]. In this case, the spherical tensor operator is described as

$$\tilde{T}_k^{(k)} = (-1)^k \sqrt{\frac{(2k-1)!!}{(2k)!!}} (J_+)^k, \quad [J_-, \tilde{T}_q^{(k)}] = \sqrt{(k+q)(k-q+1)} T_{q-1}^{(k)}, \tag{1.37}$$

and the reduced matrix element within a $J$ multiplet is[4]

$$\langle J||\tilde{T}^{(k)}||J\rangle = \frac{1}{2^k} \sqrt{\frac{(2J+k+1)!}{(2J-k)!}} \neq 0. \tag{1.38}$$

Therefore, the following formula is satisfied for the arbitrary spherical tensor operator $T_q^{(k)}$:

$$\langle JM|T_q^{(k)}|JM'\rangle = \frac{\langle J||T^{(k)}||J\rangle}{\langle J||\tilde{T}^{(k)}||J\rangle} \langle JM|T_q^{(k)}|JM'\rangle \propto \langle JM|T_q^{(k)}|JM'\rangle. \tag{1.39}$$

Remembering that the multipolar operators are defined in spherical symmetric space, we recognise that they also satisfy the properties of the spherical tensor operator. Thus, we can express the expectation values of the multipolar operators for the $f^n$ configuration as

$$\begin{aligned} \langle JM|Q_{lm}|JM'\rangle &= e\langle r^l\rangle g_n^{(l)} \langle JM|\tilde{T}_m^{(l)}|JM'\rangle, \\ \langle JM|M_{lm}|JM'\rangle &= \mu_B \langle r^{l-1}\rangle g_n^{(l)} \langle JM|\tilde{T}_m^{(l)}|JM'\rangle, \end{aligned} \tag{1.40}$$

where the radial average is $\langle r^l\rangle = \int dr r^2 r^l R^2(r)$. Here, $R(r)$ is the radial distribution function. The non-angle dependent part of the many-body wave function, that is, the physical factor, is absorbed by the coefficients $g_n^{(l)}$ and is called the generalised Stevens factor. Note that the values of $g_n^{(l)}$ are different for the $LS$ and $j$-$j$ coupling regimes because their wave functions differ. The formulae to calculate the matrix element of the multipolar operators via a spherical tensor operator constructed by the total angular momentum operators are called the Stevens equivalent operator method. The merit of this method is that we can easily obtain the matrix element of $\tilde{T}_m^{(l)}$. From Eq. (1.38) and the Wigner–Eckart theorem, we obtain

$$\langle JM|\tilde{T}_m^{(l)}|JM'\rangle = \frac{1}{2^l} \sqrt{\frac{(2J+l+1)!}{(2J-l)!}} (-1)^{J'-l+M} \begin{pmatrix} J & J' & k \\ -M & M' & q \end{pmatrix}. \tag{1.41}$$

[4]The reduced matrix element for different $J$ is zero, namely $\langle J'||\tilde{T}^{(k)}||J\rangle = 0$; hence, we cannot use this equivalent operator method in this case.

Moreover, using the fact that multipolar operators with rank $l$ are proportional to the $l$-th polynomial and the rank-1 spherical tensor operator $\tilde{\boldsymbol{T}}^{(1)}$ satisfies the relation

$$\begin{aligned}
&\langle JM|\tilde{T}_0^{(1)}|JM'\rangle = \langle JM|J_z|JM'\rangle = M'\delta_{M'M}, \\
&\langle JM|J_{\pm 1}^{(1)}|JM'\rangle = \left\langle JM \left| \mp\frac{1}{\sqrt{2}}(J_x \pm iJ_y) \right| JM' \right\rangle = \pm\frac{1}{\sqrt{2}}\sqrt{(J \mp M')(J+1 \pm M')}\delta_{M,M'\pm 1},
\end{aligned} \tag{1.42}$$

we can automatically calculate the matrix element of the multipolar operators in the following way. First, we convert the $l$-th order polynomial in the multipolar operators into the symmetrised product, that is,

$$x^a y^b z^c \to \frac{a!b!c!}{(a+b+c)!}\sum_{\mathcal{P}} \mathcal{P}(J_x^a J_y^b J_z^c), \tag{1.43}$$

where the summation is taken over all possible permutations. Then, we can evaluate the matrix element based on Eq. (1.42).

### 1.2.3 Reduction of representations

Thus far, we have introduced multipolar moments and a method of calculating their expectation values in terms of the $J$ multiplet. Now, we ask "Must we always consider the $(2J+1)\times(2J+1)$ matrix when evaluating multipolar moments in the system?". In real materials, $f$ electrons are surrounded by several crystal electric fields (CEFs) that arise from other ions, which results in a further splitting of the ground state multiplet. In this subsection, we will discuss the reduction of representations, which is a group-theoretic method for understanding how the original $J$ multiplet is split by a CEF, and finally, we derive what multipoles are active in rare-earth pyrochlore systems.

Any symmetric operators $R$ can be represented in a matrix form using an appropriate basis. A group of matrices that represents each symmetry operator in a certain group is known as the representation of the group. In general, the representation $D(R)$ is separated into the direct sum of irreducible representations by a unitary transformation, that is [78],

$$D(R) = \Gamma^{\alpha}(R) \oplus \Gamma^{\beta}(R) \oplus \Gamma^{\gamma}(R) \ldots. \tag{1.44}$$

In this case, the character of the representation $\chi(R)$ satisfies

$$\chi(R) = \chi^{\alpha}(R) + \chi^{\beta}(R) + \chi^{\gamma}(R) \cdots = \sum_{\mu} c_{\mu}\chi^{\mu}(R), \tag{1.45}$$

where $c_\mu$ indicates the number of times the irreducible representation $\Gamma^\mu$ appears in $D(R)$. The coefficient $c_\mu$ is given by

$$c_{\mu} = \frac{1}{h}\sum_{R} \chi^{\mu *}(R)\chi(R). \tag{1.46}$$

Here, $h$ is the order of the group. Since a $J$ multiplet is the ground state in a spherically symmetric potential, it is invariant under the rotation of any angle about any axis. This

means that the $(2J+1)$-dimensional matrix $D^{(J)}(R_\alpha)$ constructs an irreducible representation (irreps) of the rotational group, where the basis is the $J$ multiplet and $R_\alpha$ is the rotation operator by angle $\alpha$ about a certain axis. Generally, it is known that the character for the rotation by angle $\alpha$ about any axis in the rotation group is obtained from

$$\chi^{(J)}(R_\alpha) = \frac{\sin\left(J+\frac{1}{2}\right)\alpha}{\sin\frac{\alpha}{2}}. \tag{1.47}$$

As an example, we consider the splitting of the $f^2$ $(J=4)$ configuration in a CEF with $D_3$ point group symmetry, which is realised in rare-earth pyrochlore materials. We provide the calculated characters of the rotation group $D^{(J)}$ and the character table of the point group $D_3$ in Table 1.4, which is obtained from Eq. (1.47). When $J=4$, from Eq. (1.46) and Table 1.4, $c_\Gamma$ is

$$\begin{aligned}
c_{\Gamma_1} &= \frac{1}{12}(1\cdot 9 + 1\cdot 9 + 2\cdot 0 + 2\cdot 0 + 3\cdot 1 + 3\cdot 1) = 2,\\
c_{\Gamma_2} &= \frac{1}{12}(1\cdot 9 + 1\cdot 9 + 2\cdot 0 + 2\cdot 0 - 3\cdot 1 - 3\cdot 1) = 1,\\
c_{\Gamma_3} &= \frac{1}{12}(2\cdot 9 + 2\cdot 9 - 2\cdot 0 - 2\cdot 0 + 0\cdot 1 + 0\cdot 1) = 3,\\
c_{\Gamma_{4,5,6}} &= 0.
\end{aligned}$$

Therefore, the rotation group $D^{(4)}$ is reduced as

$$D^{(4)} = 2\Gamma_1 \oplus \Gamma_2 \oplus 3\Gamma_3. \tag{1.48}$$

Other possible reductions in rare-earth pyrochlore materials are summarised in Table 1.4. Although the CEF parameters determine which irreps become the ground state, the $\Gamma_3$ and $\Gamma_6$ irreps possess the potential to carry a pseudospin 1/2 owing to their two-dimensionality. In addition, one-dimensional $\Gamma_4$ and $\Gamma_5$ irreps are accidentally degenerate and can host a pseudospin-1/2 degree. In real materials, the $\Gamma_3$ ground state doublet can be realised in Pr-, Ho-, and Tb-based pyrochlores, the $\Gamma_6$ ground state doublet is realised in Er- and Yb-based pyrochlores, and the $\Gamma_4 \oplus \Gamma_5$ ground state doublet is realised in Ce-, Dy-, and Nd-based pyrochlores.

Now, another question is considered: can these pseudospin-1/2 states be regarded as usual spins, that is, magnetic dipoles? To answer this question, we will explain how to derive the active multipole degrees of freedom in a given Hilbert space. In general, for the matrix element of the operator $\mathcal{A}$, which belongs to the irreps $\tilde{\Gamma}$, to be non-zero within the state space of irreps $\Gamma$, the representation $\tilde{\Gamma}$ must appear when the product representation $\Gamma \otimes \Gamma$ is reduced. In other words, we can identify the active multipoles within a given Hilbert space by reducing the product representation and examining the basis functions of the irreps that arise via the reduction. We will follow this procedure by taking the $\Gamma_3$ ground state doublet in Pr-based pyrochlores as an example.

Because the characters of an arbitrary product representation $\Gamma_\alpha \otimes \Gamma_\beta$ for a symmetry operator $X$ are given by $\chi_{\Gamma_\alpha\otimes\Gamma_\beta}(X) = \chi_{\Gamma_\alpha}(X) \times \chi_{\Gamma_\beta}(X)$, the characters of $\Gamma_3 \otimes \Gamma_3$ for the symmetry operators of the $D_3$ group are as follows:

Table 1.4: Character table of the $D_3$ point group and the characters of the rotation group $D^{(J)}$. In the right two columns, we provide the representation reduction results of the rotation group and material examples.

| $D_3$ | $E$ | $R$ | $C_3$ $C_3^2R$ | $C_3^2$ $C_3R$ | $3C_2'$ | $3C_2'R$ | Reduction | Material Example |
|---|---|---|---|---|---|---|---|---|
| $\Gamma_1$ | 1 | 1 | 1 | 1 | 1 | 1 | | |
| $\Gamma_2$ | 1 | 1 | 1 | 1 | $-1$ | $-1$ | | |
| $\Gamma_3$ | 2 | 2 | $-1$ | $-1$ | 0 | 0 | | |
| $\Gamma_4$ | 1 | $-1$ | $-1$ | 1 | i | $-$i | | |
| $\Gamma_5$ | 1 | $-1$ | $-1$ | 1 | $-$i | i | | |
| $\Gamma_6$ | 2 | $-2$ | 1 | $-1$ | 0 | 0 | | |
| $D^{(5/2)}$ | 6 | $-6$ | 0 | 0 | 0 | 0 | $\Gamma_4 \oplus \Gamma_5 \oplus 2\Gamma_6$ | $Ce_2Zr_2O_7$ |
| $D^{(7/2)}$ | 8 | $-8$ | 1 | $-1$ | 0 | 0 | $\Gamma_4 \oplus \Gamma_5 \oplus 3\Gamma_6$ | $Yb_2Ti_2O_7$ |
| $D^{(4)}$ | 9 | 9 | 0 | 0 | 1 | 1 | $2\Gamma_1 \oplus \Gamma_2 \oplus 3\Gamma_3$ | $Pr_2Zr_2O_7$ |
| $D^{(9/2)}$ | 10 | $-10$ | $-1$ | 1 | 0 | 0 | $2\Gamma_4 \oplus 2\Gamma_5 \oplus 3\Gamma_6$ | $Nd_2Zr_2O_7$ |
| $D^{(6)}$ | 13 | 13 | 1 | 1 | 1 | 1 | $3\Gamma_1 \oplus 2\Gamma_2 \oplus 4\Gamma_3$ | $Tm_2Ti_2O_7$ |
| $D^{(15/2)}$ | 16 | $-16$ | $-1$ | 1 | 0 | 0 | $3\Gamma_4 \oplus 3\Gamma_5 \oplus 5\Gamma_6$ | $Er_2Ti_2O_7$ |
| $D^{(8)}$ | 17 | 17 | $-1$ | $-1$ | 1 | 1 | $3\Gamma_1 \oplus 2\Gamma_2 \oplus 6\Gamma_3$ | $Ho_2Ti_2O_7$ |

| $D_3$ | $E$ | $R$ | $C_3$ $C_3^2R$ | $C_3^2$ $C_3R$ | $3C_2'$ | $3C_2'R$ |
|---|---|---|---|---|---|---|
| $\Gamma_3 \otimes \Gamma_3$ | 4 | 4 | 1 | 1 | 0 | 0 |

Thus, we obtain

$$\Gamma_3 \otimes \Gamma_3 = \Gamma_1 \oplus \Gamma_2 \oplus \Gamma_3. \tag{1.49}$$

However, this reduction is not sufficient to identify the active multipoles because we cannot distinguish between electric and magnetic multipoles. To solve this problem, we first divide the product state $\Gamma_3 \otimes \Gamma_3$ into the symmetric representation $(\Gamma_3 \otimes \Gamma_3)_{\text{sym.}}$ and asymmetric representation $(\Gamma_3 \otimes \Gamma_3)_{\text{asy.}}$. It is known that the electric multipoles arise from symmetric (asymmetric) representation and the magnetic multipoles arise from asymmetric (symmetric) representation when $J$ is an integer (half integer). The characters of each representation are given by

$$\chi_{(\Gamma\otimes\Gamma)_{\text{sym.}}}(X) = \frac{1}{2}(\chi_\Gamma^2(X) + \chi_\Gamma(X^2)) \qquad \chi_{(\Gamma\otimes\Gamma)_{\text{asy.}}}(X) = \frac{1}{2}(\chi_\Gamma^2(X) - \chi_\Gamma(X^2)). \tag{1.50}$$

Thus, in this case, we obtain

| $D_3$ | $E$ | $R$ | $C_3$ $C_3^2R$ | $C_3^2$ $C_3R$ | $3C_2'$ | $3C_2'R$ |
|---|---|---|---|---|---|---|
| $(\Gamma_3 \otimes \Gamma_3)_{\text{sym.}}$ | 3 | 3 | 0 | 0 | 1 | 1 |
| $(\Gamma_3 \otimes \Gamma_3)_{\text{asy.}}$ | 1 | 1 | 1 | 1 | $-1$ | $-1$ |

Noting that $J = 4$ (integer) in the $f^2$ configuration, we find

$$(\Gamma_3 \otimes \Gamma_3)_{\text{sym.}} = \Gamma_{1g} + \Gamma_{3g}, \qquad (\Gamma_3 \otimes \Gamma_3)_{\text{asy.}} = \Gamma_{2u}, \tag{1.51}$$

where the index $g(u)$ indicates the electric (magnetic) multipoles. Examining the basis functions of each irreps in the character table of point group $D_{3d}$, we can determine that two $\Gamma_{3g}$ electric quadrupoles with the form $J_xJ_z+J_zJ_x$ and $J_yJ_z+J_zJ_y$ and a $\Gamma_{2u}$ magnetic dipole $J_z$ are active in the $\Gamma_3$ doublet. Note that the $\Gamma_{1g}$ electric monopole corresponds to the identity operator. Further calculations reveal that the Pauli matrices in this state can be represented as

$$\tau_x = J_xJ_z + J_zJ_x, \qquad \tau_y = J_yJ_z + J_zJ_y, \qquad \tau_z = J_z. \tag{1.52}$$

From this discussion, we can understand that the properties of an emergent pseudospin-1/2 degree of freedom in rare-earth pyrochlore materials are completely different from real spins. Similar calculations are applicable for other emergent doublets in rare-earth pyrochlore materials, the results of which are summarised in Table 1.5 [79, 80].

Table 1.5: Active multipoles for three types of emergent pseudospin-1/2 states in rare-earth pyrochlore materials. Here, $\overline{[\dots]}$ denotes the symmetrised product, for example, $\overline{J_xJ_yJ_y} = J_xJ_yJ_y + J_yJ_xJ_y + J_yJ_yJ_x$.

| Irreps. | $\tau_x$ | $\tau_y$ | $\tau_z$ |
|---|---|---|---|
| $\Gamma_6$ (Kramers) | $J_x$ ($\Gamma_{3u}$ dipole) | $J_y$ ($\Gamma_{3u}$ dipole) | $J_z$ ($\Gamma_{2u}$ dipole) |
| $\Gamma_4 \oplus \Gamma_5$ (Kramers) | $J_x^3 - \overline{J_xJ_yJ_y}$ ($\Gamma_{2u}$ octupole) | $J_y^3 - \overline{J_xJ_yJ_y}$ ($\Gamma_{1u}$ octupole) | $J_z$ ($\Gamma_{2u}$ dipole) |
| $\Gamma_3$ (non-Kramers) | $J_xJ_z + J_zJ_x$ ($\Gamma_{3g}$ quadrupole) | $J_yJ_z + J_zJ_y$ ($\Gamma_{3g}$ quadrupole) | $J_z$ ($\Gamma_{2u}$ dipole) |

### 1.2.4 Experimental limitation on identifying multipolar ordered states

Let us return to the general topic. Considering the effective spin model within the ground state, which hosts high-rank multipoles, we naturally expect the realisation of multipolar ordered states (MPOs). However, the extraction of features that indicate MPOs is not easy.

There is a wide range of experimental techniques for detecting magnetically ordered states. Because (real) spins carry a magnetic dipolar moment and can linearly couple to an external field or the magnetic moments of neutrons or nuclei, characteristic behaviours are captured using methods such as susceptibility measurements, neutron scattering, and nuclear magnetic resonance (NMR). While there are numerous tools for identifying magnetically ordered phases, there is a limited number of techniques for higher-rank MPOs. If MPOs are only constructed by electric quadrupoles, they can be measured using ultrasound because the electric quadrupoles can couple to the lattice distortion degree of freedom. By analysing the elastic constants obtained from the acoustic wave measurements, the uniform quadrupole susceptibility can be determined. The observed elastic constants and uniform quadrupole susceptibility $\chi^{\alpha\beta}$ follow the relation:

$$c_{\alpha\beta}(T) = \bar{c}_{\alpha\beta}(T) - \gamma_\alpha\gamma_\beta\chi^{\alpha\beta}, \tag{1.53}$$

where $\bar{c}_{\alpha\beta}(T)$ is the contribution from electrons other than those that are localised, $\alpha$ and $\beta$ are the indices for the quadrupolar moments, and $\gamma$ is the coupling between the lattice distortion and quadrupoles. From this formula, we expect a softening of the elastic constants to be observed as the uniform quadrupole susceptibility increases in a Curie-Weiss-like formation. In principle, much higher-ranked multipolar ordered states can be observed using resonant X-ray scattering. Theoretically, the analysis of electric quadrupole transitions (E2 transition) enables us to identify MPOs up to rank 4; however, the scattering intensity is extremely weak. Therefore, this is a difficult experiment to conduct [81].

Recently, effort has been made to understand the nature of multipoles by examining the cross-correlation response they induce [82]. For example, it is proposed that the magnetic piezoelectric effect can detect magnetic hexadecapoles, which are represented as

$$c_{\mu\nu} = a_{\mu\nu\gamma} j_\gamma, \tag{1.54}$$

where $c_{\mu\nu}$ is elastic distortion, $j_\gamma$ is current density, and $a_{\mu\nu\gamma}$ represents the piezoelectric tensor. This indicates that lattice distortion is induced by an electric current via a coefficient $a_{\mu\nu\gamma}$. In metallic $Ba_{1-x}K_xM_2As_2$, which exhibits a magnetic hexadecapole order, the lattice distortion $c_{xy}$ in the [110] direction is expected under an electric current along the $z$ axis. Thus, we can confirm the existence of higher-rank multipolar orders through a cross-correlation response [83].

These theoretical results indicate the importance of employing the lattice degree of freedom to capture MPOs with high-rank multipoles.

### 1.2.5 Recent progress in multipolar physics

One of the most exotic materials in the context of multipolar physics is a family of Pr-based 1-2-20 compounds such as $Pr(Ti,V,Ir)_2(Al,Zn)_{20}$, whose ground state doublet is described purely by higher-rank multipoles: two quadrupoles and an octupole. Owing to its uniqueness, extensive effort has been devoted to clarifying the multipolar nature of these materials [84, 85, 86, 87, 88, 89, 90]. Thus far, an antiferro-quadrupolar order at the low temperature has been reported in $Pr(Ir,Rh)_2Zn_{20}$ ($T_Q \sim 0.11$ K for the Ir system and $T_Q \sim 0.06$ K for the Rh system) [86, 88], and a ferro-quadrupolar order has been observed in $PrTi_2Al_{20}$ ($T_Q \sim 2$ K) [91]. Furthermore, successive phase transition has been reported in the high-quality single crystal $PrV_2Al_{20}$. The first transition is considered to be an antiferro-quadrupolar transition ($T_Q \sim 0.75$ K), and the second transition at $T^* \sim 0.65$ K might be associated with the octupolar degree of freedom; however, no distinct signature has been found because of limits in the experimental technique mentioned above [92]. A recent theoretical study based on the celebrated Landau theory revealed that a system with an antiferro-quadrupolar order possesses an accompanied ferro-octupolar order; thus, this hidden order can be considered a ferro-octupolar order [93].

Here, we briefly review the properties of each material. $PrIr_2Zn_{20}$ is confirmed to display an antiferro-quadrupolar order at $T_Q = 0.11$ K using an ultrasonic measurement [88]. Furthermore, transition to a superconducting phase is observed at $T_c = 0.05$ K, where the quadrupolar fluctuations play an important role to form Cooper pairs [86]. In the ultrasonic measurement, softening of the $(C_{11} - C_{12})/2$ elastic moduli suddenly

disappears at $T_Q$, which indicates growth of the quadrupolar order with an $O_2^2 = \sqrt{3}(J_x^2 - J_y^2)/2$ moment. The fitting parameters of the obtained data strongly suggest a negative quadrupole-quadrupole coupling constant; hence, the ordering will be antiferromagnetic. The entropy release at $T_Q$ is estimated as merely 20% of $R \ln 2$, which indicates that the fluctuation of the quadrupole moment remains to some extent, contributing to the formation of superconducting pairs at the lowest temperatures. Figure 1.14(a) shows a $B$–$T$ phase diagram obtained from Ref. [86].

$PrV_2Al_{20}$, which exhibits a two-step phase transition, has attracted extensive attention, from a theoretical point of view, as an observational example of the auxiliary ferro-octupolar order. This material was first investigated as a rare example of heavy-fermion superconductivity with an effective mass as high as $m^*/m_0 \sim 140$ and a transition temperature $T_c = 0.05$ K in a high-quality sample. In an attempt to capture the characteristics of heavy fermions from specific heat measurements, two anomalies were found to occur in the normal state (Fig. 1.14(b)). One was ascribed to the antiferro-quadrupolar phase transition, whereas the other remains elusive. A theoretical study based on the classical Landau theory proposed that an auxiliary ferro-octupolar order emerges with the antiferro-quadrupolar order and the experimentally observed anomaly in the specific heat arises from the contribution of a local octupolar degree [93]. The wave functions of the $\Gamma_3$ local doublet in these families are represented as [84]

$$\begin{aligned} |\phi_\alpha\rangle &= \frac{1}{2}\sqrt{\frac{7}{6}}|4\rangle - \frac{1}{2}\sqrt{\frac{5}{3}}|0\rangle + \frac{1}{2}\sqrt{\frac{7}{6}}|-4\rangle, \\ |\phi_\beta\rangle &= \frac{1}{\sqrt{2}}|2\rangle + \frac{1}{\sqrt{2}}|-2\rangle. \end{aligned} \tag{1.55}$$

Describing the pseudospin basis as

$$|\Uparrow\rangle = \frac{1}{\sqrt{2}}\left(|\phi_\alpha\rangle + \mathrm{i}|\phi_\beta\rangle\right), \qquad |\Downarrow\rangle = \frac{1}{\sqrt{2}}\left(\mathrm{i}|\phi_\alpha\rangle + |\phi_\beta\rangle\right), \tag{1.56}$$

the Pauli matrices are given by

$$\tau_x = -\frac{\sqrt{3}}{8}(J_x^2 - J_y^2), \quad \tau_y = -\frac{1}{8}(3J_z^2 - J^2), \quad \tau_z = \frac{\sqrt{3}}{18}\overline{J_x J_y J_z}. \tag{1.57}$$

Using these matrices, Ref. [93] constructs the following multipolar order parameters:

$$\phi_{u,s} = \langle\tau_A^+\rangle \pm \langle\tau_B^+\rangle, \qquad m_{u,s} = \langle\tau_A^z\rangle \pm \langle\tau_B^z\rangle, \tag{1.58}$$

where $A/B$ is the sublattice index, $\phi_{u,s}$ is the ferro/antiferro-quadrupolar order (FQ/AFQ) and $m_{u,s}$ is the ferro/antiferro-octupolar order (FO/AFO). By considering the symmetry-allowed Landau free energy and exploiting the Landau theory, the researchers of Ref. [93] uncovered a successive transition that occurs to the AFQ and AFQ+FO ordered phases with parasitic FQ-order parameters.

Intriguingly, this symmetry analysis was developed further, and a theory for detecting the octupole order was proposed [94]. Lattice strain has been regarded as a powerful tool for detecting quadrupolar ordered phases; however, it has been considered ineffective for

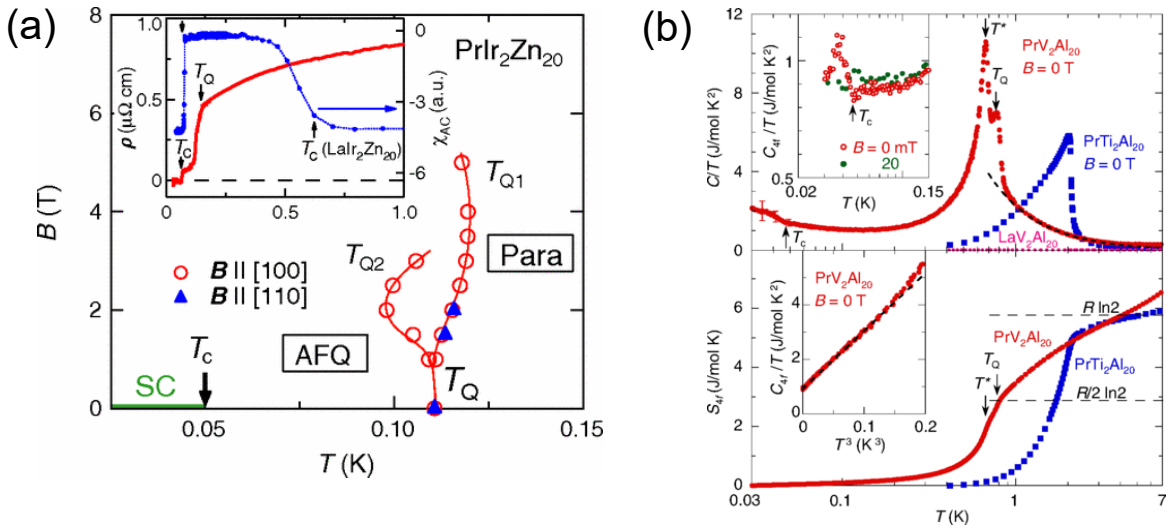


Figure 1.14. (a): $B$–$T$ phase diagram of $PrIr_2Zr_{20}$. The transition at $T_Q = 0.11$ K in the zero magnetic field splits into two transitions when magnetic fields along [100] or [110] are applied; the origin of these remains elusive. $T_c = 0.05$ K indicates a transition to the superconducting phase. The inset describes the temperature dependence of the resistivity and susceptibility, which suggests that zero resistance and perfect diamagnetism is realised below $T_c$. Reprinted with permission from [86] Copyright (2021) by the American Physical Society. (b): Temperature dependence of specific heat above $T$ and the entropy of $PrV_2Al_{20}$ and $PrTi_2Al_{20}$. In addition to the anomaly at $T_Q$, a sharp peak structure is observed in the specific heat at $T^*$ in $PrV_2Al_{20}$. The inset of the upper figure shows the temperature dependence of $C_{4f}/T$ in the zero magnetic field and $B = 20$ mT. The inset of the lower figure shows $C_{4f}/T$ versus $T^3$ in $PrV_2Al_{20}$. Here, $C_{4f}/T$ is estimated by subtracting contributions from the lattice and nuclei. Reprinted with permission from Copyright (2021) by the American Physical Society [92].

probing octupolar moments because they are odd under time-reversal. However, this difficulty is overcome by considering the time-reversal odd magnetic field, which assists the coupling between lattice strains and octupolar moments. Therefore, magnetostriction measurement can be a novel probe for detecting octupolar ordered states. In fact, it was theoretically revealed that magnetostriction in the presence of the octupolar order exhibits an unusual linear-in-field form and hysteric behaviour in a [111] magnetic field, which is consistent with unpublished experimental observations. Note that, qualitatively, quadratic-in-field magnetostriction should be observed when the quadrupolar order parameter is dominant, and thus linear-in-field magnetostriction is a unique signature that proves the existence of octupolar orders.

## 1.3 Outline of this thesis

The key points of Chapter 1 are summarised as follows:

- Quantum spin liquids are considered long-range entangled correlated paramagnets, and the lack of spontaneous symmetry breaking makes their detection arduous.
- In the $U(1)$ class of spin liquids, only the spin ice configuration based QSLs have the potential to host higher-rank multipoles.
- Multipolar ordered phases have eluded detection owing to limited experimental techniques; however, a recent proposal for a lattice-based technique has introduced a new method.

Using these points, a common feature of two seemingly unrelated quantum phases, QSLs and MPOs is revealed: both phases are difficult to experimentally detect. Considering the recent success in the lattice-based analysis, we can now wonder: *can the lattice-based technique used to probe elusive quantum phases also be used for quantum disordered phases, namely QSLs?* We believe that the best platform to investigate both QSLs and MPOs is rare-earth pyrochlore compounds, and the following two research projects will be discussed in this thesis:

1. Probing and distinguishing quantum spin liquid phases using a combination of ordinary experimental tools and a novel experimental technique known as magnetostriction measurement.
2. Pseudospin-lattice-coupling-induced phenomena in rare-earth pyrochlore materials.

The first project covers the main topic of this thesis. A dipolar-octupolar system with a $\Gamma_4 \oplus \Gamma_5$ doublet as the ground state is mainly investigated (see Section 1.2.3). First, we confirm that four distinct QSL phases can appear in the spin model of this system, where the flux degree of freedom and each multipole (dipole and octupole) play a crucial role in describing them. Then, by examining the static and dynamic properties of each QSL obtained with an ordinary experimental tool (neutron scattering), we propose that the multipolar quantum spin ice phase with a unique flux configuration is realised in $Ce_2Zr_2O_7$. To corroborate the results of the neutron scattering analysis and address its limitations, we present a new potential experimental approach. We construct a free energy formula with symmetry-allowed coupling between the lattice strain, magnetic field, and local multipolar moment. Using the obtained formula, we estimate the field dependence of the system's magnetostriction. The key finding is that a lack of direct coupling between the octupoles and magnetic fields paradoxically enables us to distinguish the octupolar-related phase from other phases. Because octupolar phases have so far been elusive, this finding is remarkable. In addition, we investigate other rare-earth pyrochlore systems for completeness and derive a comprehensive view of rare-earth pyrochlore systems.

The second project arose during the first. In the first study, we attempt to indirectly capture quantum phases by studying the effect of each quantum phase on the lattice degree of freedom. However, in the second project, we consider the effects of lattice fluctuations on the spin system and attempt to discover interesting phenomena produced

by the lattice-spin couplings. As explained in this chapter, non-Kramers pyrochlores, such as $Pr_2Zr_2O_7$, host local quadrupoles that linearly couple to quantised lattice fluctuations, phonons. Therefore, we expect the appearance of unique phonon-pseudospin-coupling-induced phenomena in non-Kramers pyrochlore materials. Motivated by this expectation, we first analyse the form of phonon-pseudospin couplings in detail and demonstrate that an emergent transverse field exists in local pseudospins. Then, we demonstrate that a unique NMR relaxation time behaviour can be observed owing to this emergent term in a [110] magnetic field. Furthermore, emergent one-dimensionality is revealed in three-dimensional frustrated magnets.

The remainder of this thesis is structured as follows: In Chapter 2, we provide detailed explanations of rare-earth pyrochlore materials and briefly describe several of our results. In Chapter 3, the main chapter of this thesis, we discuss the first project. We propose the existence of multipolar quantum spin ice and the usefulness of a novel experimental technique. The contents of Chapter 3 is published in Refs. [79] and [95]. In Chapter 4, we discuss phonon-pseudospin coupling and the emergent one-dimensionality in non-Kramers pyrochlore materials. We are currently preparing to publish the contents of Chapter 4. Finally, a summary of this thesis is provided in Chapter 5.

# Chapter 2

# Rare-earth pyrochlore materials

In Chapter 2, three types of rare-earth pyrochlore materials described in the previous chapter: (i) non-Kramers, (ii) Kramers, and (iii) dipolar-octupolar cases will be discussed. In this thesis, we study (i) non-Kramers case in Chapter 4 and (iii) dipolar-octupolar case in Chapter 3; thus experimental and theoretical progress of these cases will be intensively explained in this chapter. Additionally, the introductive topics and a part of our theoretical results for the (i) and (iii) cases will be provided.

## 2.1 Non-Kramers case

The $\Gamma_3$ non-Kramers doublet ground state can be realised in a certain rare-earth pyrochlore material. As seen in the previous chapter, $\tau_x$ and $\tau_y$ represent quadrupolar moments, and $\tau_z$ is a dipolar moment. A representative material belonging to this class is $Pr_2(TM)_2O_7$ (TM = Sn, Zr, Hf, and Ir), which has been considered a likely candidate for QSLs from both a theoretical and experimental perspective.

### 2.1.1 Theoretical study

Considering crystal symmetry and the time-reversal property of local multipolar moments, the generic nearest-neighbour pseudospin-1/2 model is represented as [96, 97]

$$H_{\rm NK} = \sum_{\langle ij \rangle} \left[ J_{zz} S_i^z S_j^z - J_{\pm}(S_i^+ S_j^- + S_i^- S_j^+) + J_{\pm\pm}(\gamma_{ij} S_i^+ S_j^+ + \gamma_{ij}^* S_i^- S_j^-) \right]. \tag{2.1}$$

Here, the summation is taken over all nearest-neighbour sites, and $\gamma$ is a $4 \times 4$ complex unimodular matrix;

$$\gamma_{\mu\nu} = \begin{cases} 1 & \boldsymbol{x}_\mu - \boldsymbol{x}_\nu \in yz \text{ plane} \\ e^{\mathrm{i}2\pi/3} & \boldsymbol{x}_\mu - \boldsymbol{x}_\nu \in xz \text{ plane} \\ e^{-\mathrm{i}2\pi/3} & \boldsymbol{x}_\mu - \boldsymbol{x}_\nu \in xy \text{ plane} \end{cases}, \tag{2.2}$$

where $\boldsymbol{x}_\mu$ ($\mu = 0, 1, 2, 3$) are vectors that connect two sites of the dual diamond lattice through the pyrochlore site with sublattice $\mu$. As in Eq. (1.18), this Hamiltonian can be mapped onto the compact $U(1)$ gauge theory on the dual diamond lattice, and the

obtained QED Hamiltonian has been investigated using the gauge mean-field theory (gMFT) [98]. Let us review the mapping procedure below.

First, the gauge charge defined on the diamond site $\boldsymbol{r}$ arises from the first Ising term by rewriting it as $(J_{zz}/2)\sum_{\boldsymbol{r}} Q_{\boldsymbol{r}}^2$ up to constant, where

$$Q_{\boldsymbol{r}} = \eta_{\boldsymbol{r}} \sum_{\boldsymbol{r}'} S^z_{(\boldsymbol{r}+\boldsymbol{r}')/2}. \tag{2.3}$$

Here, $(\boldsymbol{r}+\boldsymbol{r}')/2$ indicates that the pyrochlore site is at the centre of the vector that connects $\boldsymbol{r}$ and $\boldsymbol{r}'$, and $\boldsymbol{r}'$ is the nearest-neighbour site of $\boldsymbol{r}$. The sign factor $\eta_{\boldsymbol{r}} = 1(-1)$ if the diamond site $\boldsymbol{r}$ belongs to the $A(B)$ sublattice. Then, we introduce an operator defined on the diamond lattice, $s^z_{\boldsymbol{r}\boldsymbol{r}'} = S^z_{(\boldsymbol{r}+\boldsymbol{r}')/2}$ and the corresponding ladder operator $\Phi$. Using these operators, we obtain

$$S^+_{(\boldsymbol{r}+\boldsymbol{r}')/2} = \Phi^\dagger_{\boldsymbol{r}} s^+_{\boldsymbol{r}\boldsymbol{r}'} \Phi_{\boldsymbol{r}'}, \tag{2.4}$$

where $\boldsymbol{r} \in A$ and $\Phi^{(\dagger)}_{\boldsymbol{r}}$ are annihilation (creation) operators of a bosonic spinon that acts on the gauge charge $Q_{\boldsymbol{r}}$. Note that they satisfy the commutation relations $[\Phi^{(\dagger)}_{\boldsymbol{r}}, Q_{\boldsymbol{r}}] = (-)\Phi^{(\dagger)}_{\boldsymbol{r}}$. Employing these gauge operators, the Hamiltonian Eq. (2.1) is rewritten as

$$H_{\mathrm{QED}} = \frac{J_{zz}}{2}\sum_{\boldsymbol{r}} Q^2_{\boldsymbol{r}} - J_\pm \sum_{\boldsymbol{r},\boldsymbol{r}'\neq\boldsymbol{r}''} \Phi^\dagger_{\boldsymbol{r}'}\Phi_{\boldsymbol{r}''} s^{-\eta_{\boldsymbol{r}}}_{\boldsymbol{r}\boldsymbol{r}'} s^{\eta_{\boldsymbol{r}}}_{\boldsymbol{r}\boldsymbol{r}''} + \frac{J_{\pm\pm}}{2}\sum_{\boldsymbol{r},\boldsymbol{r}'\neq\boldsymbol{r}''} (\gamma^{\eta_{\boldsymbol{r}}}_{\mu\nu}\Phi^\dagger_{\boldsymbol{r}}\Phi^\dagger_{\boldsymbol{r}}\Phi_{\boldsymbol{r}'}\Phi_{\boldsymbol{r}''} s^{\eta_{\boldsymbol{r}}}_{\boldsymbol{r}\boldsymbol{r}'} s^{\eta_{\boldsymbol{r}}}_{\boldsymbol{r}\boldsymbol{r}''} + \mathrm{h.c.}). \tag{2.5}$$

Here, the sites $\boldsymbol{r}'$ and $\boldsymbol{r}''$ are the nearest-neighbours of site $\boldsymbol{r}$, and $\mu$ [$\nu$] is the sublattice index of the pyrochlore site at $(\boldsymbol{r}+\boldsymbol{r}')/2$ [$(\boldsymbol{r}+\boldsymbol{r}'')/2$]. This Hamiltonian is invariant under the $U(1)$ gauge transformations $\Phi_{\boldsymbol{r}} \to \Phi_{\boldsymbol{r}} e^{-\mathrm{i}\chi_{\boldsymbol{r}}}$ and $s^\pm_{\boldsymbol{r}\boldsymbol{r}'} \to s^\pm_{\boldsymbol{r}\boldsymbol{r}'} e^{\pm\mathrm{i}(\chi_{\boldsymbol{r}'}-\chi_{\boldsymbol{r}})}$.

Before providing the gMFT phase diagram of this model, we introduce a flux degree of freedom, which will be important in the next chapter. In the perturbative regime, where $J_{\pm\pm} \lesssim J_\pm \ll J_{zz}$, the effective Hamiltonian becomes the following ring exchange interaction:

$$H_{\mathrm{ring}} = -J_{\mathrm{ring}} \sum_{\hexagon} \cos(\nabla \times A) \tag{2.6}$$

with $J_{\mathrm{ring}} = \mathcal{O}(J^3_\pm/J^2_{zz})$ (cf. Eq. (1.18)–(1.22)). Thus, we expect that the flux defined for each hexagonal plaquette ($=\nabla\times A$) takes the value $\cos(\nabla\times A) = 1$ for $J_\pm > 0$ and $\cos(\nabla\times A) = -1$ for $J_\pm < 0$. The former state is known as the zero-flux state, and the latter is the $\pi$-flux state. The different flux configuration patterns describe the different QSLs. Reference [98] provides a gMFT analysis of the zero-flux state only.

Because the gMFT analysis is not a main topic of this thesis, a detailed explanation is not provided. Instead, the result is displayed in Fig. 2.1. We can see that the $U(1)$ QSL phase expands beyond the perturbative regime and exotic MPOs exist in the large $J_\pm$ or $J_{\pm\pm}$ region. Through this analysis, we have once again confirmed that rare-earth pyrochlore materials are the ideal platform for verifying MPOs and QSLs.

Inspired by the result, we evaluated the magnetostriction for each quantum phase in the previous research [80]. Our main findings are shown in Fig. 2.2, which illustrates the field dependence of the length change under an applied magnetic field [111] for the

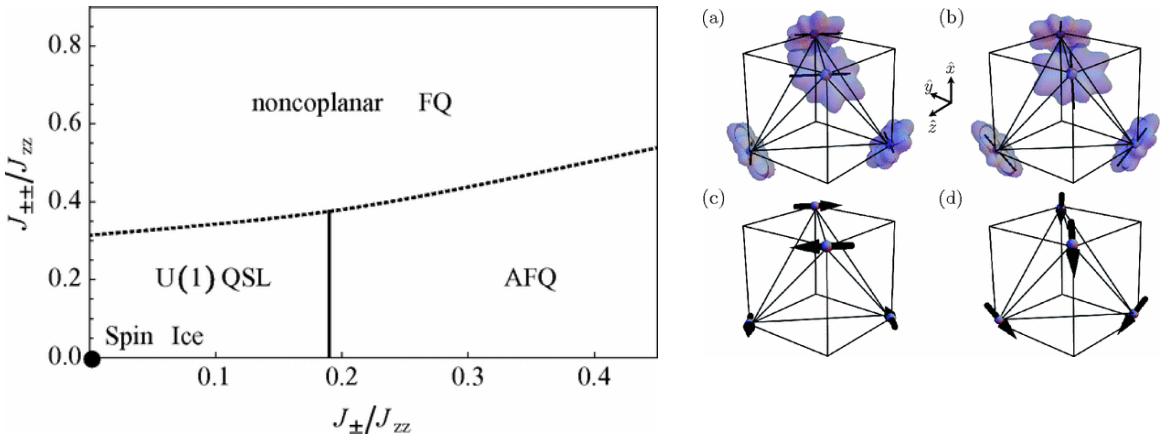


Figure 2.1. Left: Phase diagram of the $J_{\pm}$–$J_{\pm\pm}$ space. Four distinct phases are observed: classical spin ice, $U(1)$ QSLs, the antiferroquadrupolar (AFQ) order, and the ferroquadrupolar (FQ) order. Right: Schematic illustration of the (a): AFQ and (b): noncoplanar FQ orders. (c,d): Corresponding antiferromagnet and noncoplanar ferromagnet phases, where the $x$ and $y$ components of the pseudospin are regarded as the usual dipole. Reprinted with permission from Copyright (2021) by the American Physical Society [98].

$U(1)$ QSL phase ($J_{\pm}/J_{zz} = 0.02, J_{\pm\pm}/J_{zz} = 0.05$). Under this magnetic field, the system first enters the kagome ice phase, where the two-in two-out spin ice configuration is maintained within the kagome layer intrinsic to the pyrochlore lattice. Then, it becomes a trivial, fully polarised phase through an intermediate phase. The key result is that a characteristic linear-in-field dependence in the kagome ice phase and the jump behaviour in the intermediate phase are observed with length change along the (1,1,1) and (1,1,0) directions. These features are only captured for the $U(1)$ QSL ground state and are consistent with unpublished experimental results [99]. Theoretical formalisms have much in common with the contents of Chapter 3; hence, a detailed explanation will be provided there. Moreover, Appendix A contains the magnetostriction of additional MPOs.

### 2.1.2 Experimental study

A spin-ice configuration with large quantum fluctuations was reported in $Pr_2Zr_2O_7$ [100]. The neutron scattering measurements accurately captured the key properties of this material. Figure 2.3 presents a $\boldsymbol{q}$-map of inelastic and elastic neutron scattering measurements. The pinch point singularities near (111) and (002) in Fig. 2.3(b) suggest that the two-in two-out spin configuration is satisfied for each tetrahedron. Because this scattering pattern resembles the one obtained from the spin model with nearest-neighbour Ising interactions, this phase may be regarded as classical spin ice. However, the Weiss temperature is negative, which indicates that the antiferromagnetic transverse interaction term $J_{\pm}$ is not negligible. Therefore, combined with the theoretical results, we expect the $U(1)$ QSL to be realised. In fact, the inelastic scattering signature provides evidence for quantum spin dynamics. The pinch points disappear, which indicates that the excited

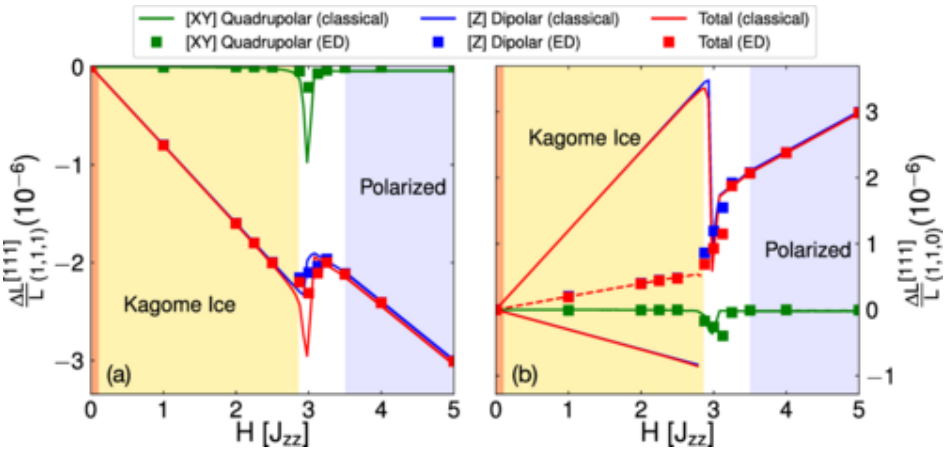


Figure 2.2. Field dependence of the length change $\Delta L/L$ under an applied magnetic field [111] for the $U(1)$ QSL phase $J_{\pm}/J_{zz} = 0.02, J_{\pm\pm}/J_{zz} = 0.05$. Left: length change along the (1,1,1) direction. Right: length change along the (1,1,0) direction. For the infinitesimal but finite field, the system enters the kagome spin ice phase, where the spin ice degeneracy only remains in the kagome layer of the pyrochlore lattice. However, the $U(1)$ QSL is stable for a small window of magnetic field strengths. This region is schematically denoted by the orange shaded region. For the large field region, the system enters a trivial, fully polarised phase (blue-shaded region). The green, blue, and red lines (squares) denote the contribution from the quadrupole, dipole, and combined to the length change, respectively, obtained through classical (exact diagonalisation) calculation. The classical (1,1,0) length change possesses two behaviours in the kagome ice phase because the length change reflects the degeneracy of the kagome ice manifold. The average over the degeneracy (red dashed line) accurately matches the exact diagonalisation result along the (1,1,0) direction. A theoretical formalism and additional pyrochlore cases will be provided in Chapter 3 and Appendix A. Adopted from our previous study [80].

states differ from the ground state owing to violation of the ice-rule and the creation of monopole excitations. Moreover, the intensity of the inelastic neutron scattering signal accounts for more than 90% of the magnetic scattering cross section. This indicates that quantum fluctuations dominate the magnetism of $Pr_2Zr_2O_7$.

At this stage, previous experiments merely assert the dominance of quantum fluctuations rather than experimentally determining the existence of $U(1)$ QSLs. To provide evidence on the presence of $U(1)$ QSLs from multiple perspectives, proposals for new experimental methods have been anticipated. Therefore, our proposal of magnetostriction as a novel probe for $U(1)$ QSLs is a powerful tool to offer further evidence. As previously mentioned, magnetostriction measurements have been conducted and the results are consistent with our theory [80, 99]. Thus, we can conclude that the ground state of $Pr_2Zr_2O_7$ is a $U(1)$ QSL.

To further corroborate the experimental realisation of the $U(1)$ spin liquid in $Pr_2Zr_2O_7$ from another perspective, let us analyse the coupling constants in Eq. (2.1). Reference

[96] provides a preliminary estimate of the coupling constants for $Pr_2(TM)_2O_7$ (TM = Sn, Zr, Hf, and Ir) using a fourth-order strong-coupling perturbation theory. Because the detailed explanation of this theory is beyond the scope of this thesis, just an overview is provided here. For Pr-based pyrochlore materials, the non-Kramers ground state doublet is described as

$$|\pm\rangle = \alpha|J_z = \pm 4\rangle \pm \beta|J_z = \pm 1\rangle - \gamma|J_z = \mp 2\rangle, \tag{2.7}$$

where $\alpha$, $\beta$, and $\gamma$ are real coefficients determined by CEF parameters, and we observe that $\alpha = \sqrt{1-\beta^2-\gamma^2}$ is dominant. For $Pr_2Zr_2O_7$, the first CEF excited state is $\Gamma_1$ singlet located at 108 K [100]. This energy scale is significantly greater than the one we are interested in; for example, $J_{zz}$ in Eq. (2.1) is predicted to be in the order of a few Kelvin [101]. Therefore, it is reasonable to neglect the CEF excited states and confine our discussion to the non-Kramers ground state doublet. Equipped with this assumption, we find that the effective quantum pseudospin-1/2 model obtained from the fourth-order perturbation theory corresponds to Eq. (2.1), and the coupling constants $J_\pm$ and $J_{\pm\pm}$ are dependent on parameters $\beta$ and $\gamma$. If $\beta = \gamma = 0$, the coupling constants $J_\pm$ and $J_{\pm\pm}$ vanish, indicating that the mixing of the $|J_z = \pm 1\rangle$ and $|J_z = \pm 2\rangle$ states in the ground state wave function contributes to additional superexchange paths and finite $J_\pm$ and $J_{\pm\pm}$. Using typical values for Slater-Koster parameters included in $\beta$ and $\gamma$, we can finally evaluate as $J_\pm/J_{zz} \sim 0.1$ and $J_{\pm\pm}/J_{zz} \sim 0.1$. When we compare this preliminary estimate of the coupling constants to the phase diagram shown in Fig. 2.1, we establish that the $U(1)$ QSL ground state is plausible. In Chapter 4, we demonstrate that the Ising anisotropy of the parameter set and resulting spin liquid phase in $Pr_2Zr_2O_7$ plays a crucial role to explain the unique experimental result of NMR relaxation time.

## 2.2 Kramers case

A trivial Kramers case with a $\Gamma_6$ doublet does not possess higher-rank multipoles. Instead, various magnetically ordered phases are reported. Only a brief comment is provided as they are not main topics in this thesis.

In addition to the Hamiltonian Eq. (2.1), another interaction term is allowed owing to the time-reversal odd nature of dipolar moments. Thus, the Hamiltonian of the usual Kramers doublet is [96, 97]

$$\begin{aligned} H_{\mathrm{K}} = \sum_{\langle ij\rangle} & J_{zz} S_i^z S_j^z - J_\pm (S_i^+ S_j^- + S_i^- S_j^+) + J_{\pm\pm}(\gamma_{ij} S_i^+ S_j^+ + \gamma_{ij}^* S_i^- S_j^-) \\ & + J_{z\pm}\left[S_i^z(\zeta_{ij} S_j^+ + \zeta_{ij}^* S_j^-) + (\zeta_{ij} S_i^+ + \zeta_{ij}^* S_i^-) S_j^z\right], \end{aligned} \tag{2.8}$$

where $\zeta = -\gamma^*$. The additional contribution to the QED Hamiltonian is described as

$$-J_{z\pm} \sum_{\boldsymbol{r},\boldsymbol{r}'\neq\boldsymbol{r}''} s^z_{\boldsymbol{r}\boldsymbol{r}'}(\gamma_{\mu\nu}^{-\eta_r} \Phi^\dagger_{\boldsymbol{r}} \Phi_{\boldsymbol{r}''} s^{\eta_r}_{\boldsymbol{r}\boldsymbol{r}''} + \mathrm{h.c.}). \tag{2.9}$$

Note that this term is also invariant under the $U(1)$ gauge transformation explained in the previous section. A similar gMFT analysis is conducted on the parameter space of $J_{z\pm}/J_{zz}$ and $J_\pm/J_{zz}$ with $J_{\pm\pm} = 0$ [102]. The phase diagram is shown in Fig. 2.4. In this

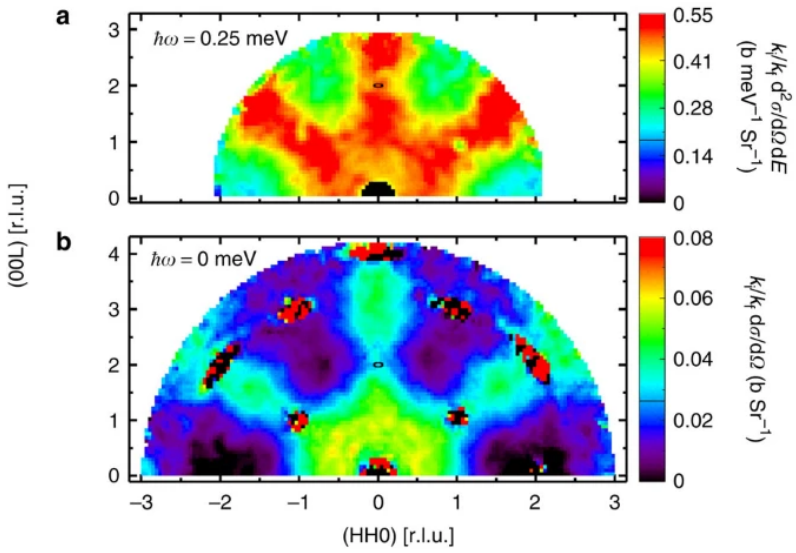


Figure 2.3. (a): Inelastic neutron scattering signal with an energy transfer of 0.25 meV in $Pr_2Zr_2O_7$. The broad scattering pattern is attributed to crystal symmetry. The pinch-point singularity unique to the spin-ice state is masked, which indicates the presence of magnetic monopoles. (b): Elastic neutron scattering signal. Pinch points are observed at (002), (111), and $(1\bar{1}1)$. The broadened nature suggests that the quantum fluctuations are not negligible in this material. Adopted from [100].

case, the $U(1)$ QSL phase is robust for finite $J_\pm$ and $J_{z\pm}$; however, we find that it is more stable against $J_{\pm\pm}$ (see Figs. 2.1 and 2.4). More interestingly, the Coulomb ferromagnetic ordered (CFM) phase is obtained and covers a wide range of the parameter region. The order parameters that characterise the CFM phase are $\langle\Phi\rangle = 0$ and $\langle s^z\rangle \neq 0$. The former condition indicates that spinons have a finite gap and are deconfined, as explained in the previous chapter, and the latter represents the presence of the Ising magnetic order.

(a)

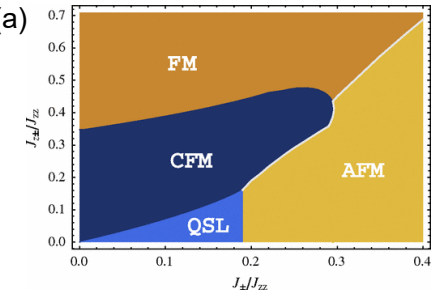


(b)

Order parameters and phases in gMFT.

| $\langle\Phi\rangle$ | $\langle s^z\rangle$ | $\langle s^\pm\rangle$ | Phase |
|---|---|---|---|
| 0 | 0 | $\neq 0$ | QSL |
| 0 | $\neq 0$ | $\neq 0$ | CFM |
| $\neq 0$ | $\neq 0$ | $\neq 0$ | FM |
| $\neq 0$ | 0 | $\neq 0$ | AFM |

Figure 2.4. (a): Phase diagram of pyrochlore materials with the Kramers doublet as the ground state. (b): Order parameters for each phase. Reprinted with permission from Copyright (2021) by the American Physical Society [102].

$Yb_2(Ti,Sn)_2O_7$ has attracted extensive experimental attention as a candidate for $U(1)$ QSLs. Despite this expectation, this material was found to enter a trivial ferromagnetic

state at the lowest temperatures. However, it was recently discovered that this seemingly trivial ferromagnetic state displays an unusual behaviour. Powder neutron diffraction experiments revealed that the magnetic moments approximately point in the same direction, along the cubic [100] axis, with a small splay angle [103]. Owing to this nature, this ordered phase is known as the splayed ferromagnetic phase (Appendix A). Moreover, a mysterious property is observed in their zero-field spin dynamics. As a primitive excitation, a gapped magnon excitation with minimum $\boldsymbol{q} = 0$ would be expected owing to large anisotropy of the exchange interactions. Contrary to this naive prediction, an almost gapless spectrum is observed in $Yb_2Ti_2O_7$, which is not well-defined in spin wave modes. The distribution of the spectrum is relatively broad with the strongest intensity at $\boldsymbol{q} = 0$, referred to as a ferromagnetic continuum [104, 105, 106]. Of particular interest is the evolution of the excitation spectrum when a magnetic field is applied. Within the strong field limit, the obtained spectrum is well explained by spin wave theory and smoothly transfers to the ferromagnetic continuum as the field is lowered without exhibiting any phase transition signatures. Below 1 T, magnon excitations merge and the spectrum deviates from semiclassical theory. An explanation for the ferromagnetic continuum could be a gapless fractionalised excitation from $U(1)$ QSLs. However, such an idea fails to explain the smooth connection between the zero-field state and the trivial high-field state; hence, this mystery is yet to be resolved.

## 2.3 Dipolar-octupolar case

The $\Gamma_4 \oplus \Gamma_5$ Kramers doublet ground state is the most important case in this thesis. As previously explained, the active multipoles are the (magnetic) dipole and octupole; thus, this system is known as a dipolar-octupolar system. In contrast with the other two cases, this state has not been the subject of much research until recently owing to difficulties in discovering higher-rank multipoles in the real materials.

### 2.3.1 Theoretical study

The general nearest-neighbour spin model in this case has a completely different form than the previous two cases. It is represented as [107, 108]

$$H_{\mathrm{DO}} = \sum_{\langle ij \rangle} J_x S_i^x S_j^x + J_y S_i^y S_j^y + J_z S_i^z S_j^z + J_{xz}(S_i^x S_j^z + S_i^z S_j^x). \tag{2.10}$$

Notably, the cross term is eliminated by a global pseudospin rotation. Then, the simple XYZ model is obtained as

$$H_{\mathrm{XYZ}} = \sum_{\langle ij \rangle} \tilde{J}_x \tau_x \tau_x + \tilde{J}_y \tau_y \tau_y + \tilde{J}_z \tau_z \tau_z. \tag{2.11}$$

Although it appears to be a simple spin model, there are two distinct QSL possibilities inherent in this system. First, we consider the case of a large $\tilde{J}_z$ limit, where $\tilde{J}_z \gg \tilde{J}_x, \tilde{J}_y$. When $\tilde{J}_x = \tilde{J}_y < 0$, a quantum Monte Carlo simulation revealed that a "usual" $U(1)$ QSL exists for $|\tilde{J}_x|/J_z \lesssim 0.1$ [109]. Note that this phase is robust against parameter

fluctuations and exists away from the $\tilde{J}_x = \tilde{J}_y$ line. The unique $U(1)$ QSL appears for the large $\tilde{J}_y$ case, where $\tilde{J}_y \gg \tilde{J}_x, \tilde{J}_z$. Here, the gauge electric field $E_{\boldsymbol{r}\boldsymbol{r}'}$ defined on a link of the dual diamond lattice is described as $\tau_i^y = \eta_{\boldsymbol{r}} E_{\boldsymbol{r}\boldsymbol{r}'}$, where $\eta_{\boldsymbol{r}} = 1(-1)$ when $\boldsymbol{r}$ is on the $A(B)$ sublattice (cf. Eq. (1.21)). This indicates that the gauge electric field is a pure octupole moment in this case, whereas in the usual $U(1)$ QSL case it is a dipole moment[1]. Owing to this feature, the former is known as an octupolar quantum spin liquid (oQSL) and the latter is a dipolar quantum spin liquid (dQSL). Although they are distinct QSL phases, it is extremely difficult to distinguish between them in experiments. For example, the $T^3$ contribution is dominant in the specific heat, which stems from gapless photon excitations in both QSLs.

A section of the phase diagram is obtained by the gMFT calculation [107]. Assuming the $\tilde{J}_\gamma$ term denotes the dominant Ising interaction, the pseudospin operators can be represented as

$$\tau_i^\gamma = s_{\boldsymbol{r}\boldsymbol{r}'}^\gamma, \qquad \tau_i^+ = \Phi_{\boldsymbol{r}}^\dagger s_{\boldsymbol{r}\boldsymbol{r}'}^+ \Phi_{\boldsymbol{r}'}. \tag{2.12}$$

Here, the site $i$ is located at the centre of the vector that connects $\boldsymbol{r}$ and $\boldsymbol{r}'$, and $\tau_i^+ = \tau_i^\alpha + \mathrm{i}\tau_i^\beta$, where $\alpha$ and $\beta$ are the two remaining directions. The XYZ models are rewritten as

$$\begin{aligned} H = &\frac{\tilde{J}_\gamma}{2} \sum_{\boldsymbol{r}} Q_{\boldsymbol{r}}^2 + \left( \frac{\tilde{J}_\alpha + \tilde{J}_\beta}{2} \right) \sum_{\boldsymbol{r}, \boldsymbol{r}' \neq \boldsymbol{r}''} \Phi_{\boldsymbol{r}'}^\dagger \Phi_{\boldsymbol{r}''} s_{\boldsymbol{r}\boldsymbol{r}'}^{-\eta_r} s_{\boldsymbol{r}\boldsymbol{r}''}^{\eta_r} \\ &+ \left( \frac{\tilde{J}_\alpha - \tilde{J}_\beta}{4} \right) \sum_{\boldsymbol{r}, \boldsymbol{r}' \neq \boldsymbol{r}''} (\Phi_{\boldsymbol{r}}^\dagger \Phi_{\boldsymbol{r}}^\dagger \Phi_{\boldsymbol{r}'} \Phi_{\boldsymbol{r}''} s_{\boldsymbol{r}\boldsymbol{r}'}^{\eta_r} s_{\boldsymbol{r}\boldsymbol{r}''}^{\eta_r} + \text{h.c.}), \end{aligned} \tag{2.13}$$

where $Q_{\boldsymbol{r}} = \eta_{\boldsymbol{r}} \sum_{\boldsymbol{r}'} \tau_{(\boldsymbol{r}+\boldsymbol{r}')/2}^\gamma$. This Hamiltonian is also invariant under the $U(1)$ gauge transformations $\Phi_{\boldsymbol{r}} \to \Phi_{\boldsymbol{r}} e^{-\mathrm{i}\chi_{\boldsymbol{r}}}$ and $s_{\boldsymbol{r}\boldsymbol{r}'}^\pm \to s_{\boldsymbol{r}\boldsymbol{r}'}^\pm e^{\pm \mathrm{i}(\chi_{\boldsymbol{r}} - \chi_{\boldsymbol{r}'})}$. A phase diagram is obtained for the unfrustrated parameter region, that is, $(\tilde{J}_\alpha + \tilde{J}_\beta)/2 < 0$. Figure 2.5 presents a section of the phase diagram for the dipolar-octupolar case. Remarkably, the $U(1)$ QSL phases are quite robust within the studied parameter region. Because QSLs are known to be more stable in the frustrated parameter region, we expect the observed QSLs to widely expand into unstudied parameter space. In addition to the QSL phases, we find the characteristic multipolar ordered state, the antiferro-octupolar (AFO) phase, and magnetically ordered state, the all-in all-out (AIAO) phase. It is interesting to observe the multipolar ordered and the spin liquid phases in the same phase diagram, as in the case of non-Kramers.

Furthermore, we explore the phase diagram of the dipolar-octupolar case under an external magnetic field. In the usual Kramers or non-Kramers cases, the emergent gauge electric fields are represented by a dipolar degree of freedom. Thus, an external magnetic field directly couples to the gauge electric field, and this coupling term results in an extremely complex spinon model. However, when $\tilde{J}_y \gg \tilde{J}_x, \tilde{J}_z$ is realized in the dipolar-octupolar case, we can conduct the gMFT analysis with a small revision. In the presence of a magnetic field, the Zeeman term is appended to the XYZ model Eq. (2.11). Here, it is described as $-\sum_i \boldsymbol{h} \cdot \hat{z}_i \tau_i^z$ because only the $z$ component of the pseudospin carries a dipolar

[1]Strictly, the octupolar moment is mixed in with the $\tau^z$ due to the global pseudospin rotation, so it is safe to say that the gauge electric field transforms under the $\Gamma_4^+$ representation of the $O_h$ point group.

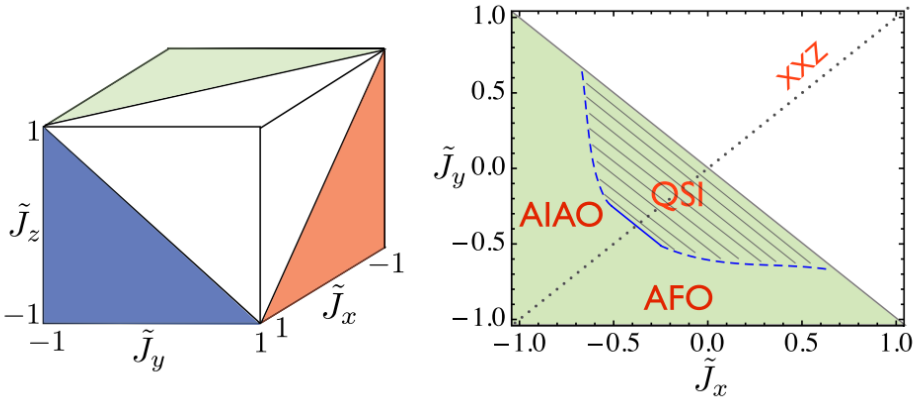


Figure 2.5. Left: Studied parameter region in the dipolar-octupolar model. The shaded region represents the unfrustrated parameter sets and can be analysed by a usual gMFT. Right: Phase diagram of the XYZ model originating from the dipolar-octupolar doublet. This is on the $\tilde{J}_z = 1$ plane; thus, quantum spin ice (QSI) represents the dQSL phase. Note that we consider the terms quantum spin ice and QSLs in the pyrochlore lattice to be the same. In addition, two ordered phases, the all-in all-out (AIAO) phase and antiferro-octupolar (AFO) phase, are found. The blue solid (dashed) line describes the phase boundary of the 2nd (1st) order transition. Note that the phase diagram for the other plane is obtained by simply relabelling the parameters. Reprinted with permission from Copyright (2021) by the American Physical Society [107].

moment and can directly couple to the magnetic field. Using the spinon representation and setting $\tilde{J}_x = \tilde{J}_z$, the full Hamiltonian becomes

$$H = \frac{\tilde{J}_y}{2} \sum_{\boldsymbol{r}} Q_{\boldsymbol{r}}^2 + \tilde{J}_x \sum_{\boldsymbol{r},\boldsymbol{r}' \neq \boldsymbol{r}''} \Phi_{\boldsymbol{r}'}^\dagger \Phi_{\boldsymbol{r}''} s_{\boldsymbol{r}\boldsymbol{r}'}^{-\eta_{\boldsymbol{r}}} s_{\boldsymbol{r}\boldsymbol{r}''}^{\eta_{\boldsymbol{r}}} - \frac{1}{2} \sum_{\langle \boldsymbol{r}\boldsymbol{r}' \rangle} \boldsymbol{h} \cdot \hat{z}_i (\Phi_{\boldsymbol{r}}^\dagger \Phi_{\boldsymbol{r}'} s_{\boldsymbol{r}\boldsymbol{r}'}^{+} + \text{h.c.}). \tag{2.14}$$

The gMFT phase diagram for various magnetic fields is depicted in Fig. 2.6. As shown, the $U(1)$ QSL is stable along all magnetic field directions. The gauge electric field $\tau^y$, which constitutes the Ising term, is not coupled to the magnetic field because it has an octupolar degree of freedom and is only affected by the external magnetic field through spinons. Reflecting this fact, the QSL is considered to be stable up to relatively large magnetic field regions. In particular, for the [110] magnetic field and small $J_\pm$, the QSL is unbroken even when subjected to a fairly large magnetic field. This is due to the relationship between the [110] magnetic field and localised pseudospins; the related phenomena will be explained in detail in Chapter 4.

Moreover, it should be emphasised that extensive theoretical research has been conducted after our publication on dipolar-octupolar systems, which is explained in detail in the next chapter [110, 111, 112].

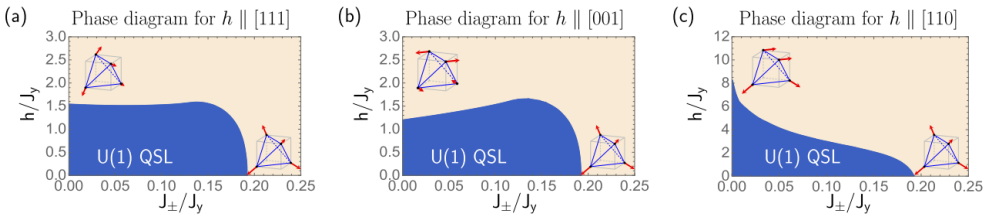


Figure 2.6. Phase diagrams of the XXZ model originating from the dipolar-octupolar doublet under magnetic fields along (a): [111], (b): [001], and (c): [110]. In our notation, $J_{\pm} = -\tilde{J}_x$. Insets are schematics of the resulting orders of the large field limit, where each order smoothly connects to the other. Reprinted with permission from Copyright (2021) by the American Physical Society [108].

### 2.3.2 Experimental study

Typical examples of dipolar-octupolar systems are Nd- and Ce-based pyrochlore materials. In the early stages of research, the Nd-based pyrochlore material $Nd_2Ir_2O_7$ was the target material [113, 114]. However, the octupolar degree of freedom in the local ground state doublet of the Nd ion had not yet been noticed. The low temperature phase of this material is known to be the all-in all-out (AIAO) phase; related materials, such as $Nd_2Sn_2O_7$, $Nd_2Hf_2O_7$, and $Nd_2Zr_2O_7$, also exhibit the AIAO phase [115, 116, 117, 118]. The observed result was consistent with the theoretical prediction; the non-Ising interaction was relatively large. However, whether the AIAO structure is constructed by dipoles or octupoles had not yet been revealed.

Several years later, a Ce-based pyrochlore material $Ce_2Zr_2O_7$ began attracting attention as a candidate for $U(1)$ QSLs with a dipolar-octupolar nature [119, 120]. Additionally, $Ce_2Sn_2O_7$ was examined and reported to exhibit no magnetic order down to $T = 20$ mK; however, at that time, the dipolar-octupolar nature of its CEF ground state had not been closely considered [121]. Returning to $Ce_2Zr_2O_7$, to confirm its dipolar-octupolar nature, a high-energy inelastic neutron scattering measurement was conducted, which revealed the single-ion properties of Ce ions. In Ref. [120], the CEF ground states were found to be well-separated from other excited states and their wave function was approximated as a pure $m_J = \pm 3/2$ state, which hosts both dipolar and octupolar moments. The inverse magnetic susceptibility of a $Ce_2Zr_2O_7$ powder sample was also measured and the neutron scattering intensity for both the powder and single crystal was obtained. Intriguingly, none of the results indicated a magnetically ordered state down to $T = 0.06$ K. In particular, no Bragg scattering nor enhancement of the Bragg peak associated with any $\boldsymbol{q} = 0$ structure was observed, which includes the AIAO phase observed in the other dipolar-octupolar pyrochlore materials explained above. To elucidate the features of the disordered state in detail, low-energy inelastic neutron scattering measurement is useful. Figure 2.7 presents the obtained results of Ref. [120] and a theoretical prediction based on the Hamiltonian of the usual Kramers case[2]. A qualitative resemblance can be observed

[2]The $U(1)$ QSLs in this model may be equivalent to the dQSL of the dipolar-octupolar case; however, this has not yet been confirmed. In addition, the theoretical prediction for the oQSL is not yet obtained.

between them, which suggests that the disordered state of $Ce_2Zr_2O_7$ is identified as a $U(1)$ QSL. Note that the other group also concludes that $Ce_2Zr_2O_7$ displays experimental signatures of a three-dimensional QSL from thermodynamic, muon spin relaxation, and neutron scattering experiments on the single crystal [119].

Now, let us estimate the coupling constants $\tilde{J}_x$, $\tilde{J}_y$, and $\tilde{J}_z$ of the XYZ model (Eq. (2.11)) for the $Ce_2Zr_2O_7$ case. One way to evaluate them is performing a fourth-order perturbation analysis on the ground state doublet $|J_z = \pm 3/2\rangle$, but we leave it as a future problem due to its extreme complexity. We naively anticipate a strong Ising anisotropy to exist (albeit we cannot identify the Ising direction) because the ground state is entirely generated from $m_J = \pm 3/2$ states and the potential superexchange pathways are restricted. Rather than performing a perturbation analysis, we provide a recent parameter estimation derived by fitting the experimental magnetization and specific heat to quantum finite temperature Lanczos method calculations [112]. In Ref. [112], they have estimated the parameters under various assumptions and found that Ising anisotropy exists in the octupole component $\tau_y$ in all situations. They have, for example, derived $(\tilde{J}_x, \tilde{J}_y, \tilde{J}_z) = (0.51, 1.01, 0.17)$ as one parameter set, where $\tilde{J}_\mu$ values are reported in Kelvin units. In Chapter 3, we show that these parameter set derived from the experiment on $Ce_2Zr_2O_7$ corresponds to a unique quantum spin liquid ground state.

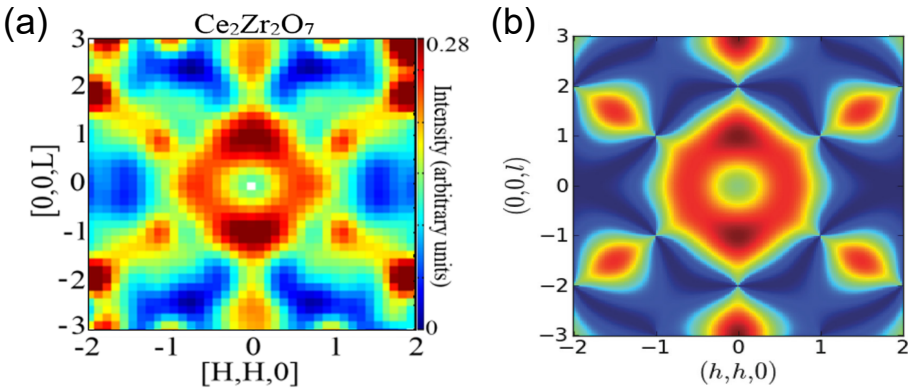


Figure 2.7. (a): Measured low-energy inelastic neutron scattering from an annealed single crystal of $Ce_2Zr_2O_7$. (b): Theoretical calculation for inelastic neutron scattering signals of the $U(1)$ QSL phase. The analysis is based on the spin Hamiltonian of the usual Kramers case at finite temperature. Reprinted with permission from Copyright (2021) by the American Physical Society [120].

## 2.4 Short summary

In this chapter, we have reviewed various type of QSLs which arise in rare-earth pyrochlore materials and some of them are distinguished based on the type of emergent gauge fields. Differences in the way the emergent gauge field couples to the external magnetic field can be observed using methods such as inelastic neutron scattering experiments. For example, in the oQSL case, the magnetic field only couples to spinons; hence,

Table 2.1: List of the difference of expected inelastic neutron scattering signals for each $U(1)$ QSL.

| Type | Inelastic neutron scattering signals |
|---|---|
| non-Kramers doublet | only gapless photon excitation |
| usual Kramers doublet | both gapless photon and gapped spinon excitations |
| dQSL in dipolar-octupolar doublet | both gapless photon and gapped spinon excitations |
| oQSL in dipolar-octupolar doublet | only gapped spinon excitations |

only the gapped excitation of the spinons will be observed, and no gapless photons will be observed. Table 2.1 summarises the differences between the inelastic neutron scattering signals of every $U(1)$ QSL reviewed throughout this chapter.

Although at least two experiments support the existence of the QSL phase in $Ce_2Zr_2O_7$, it is not clear which type of spin liquid has been realised. In the previous section, inelastic neutron scattering was identified as a tool for distinguishing the dQSL and oQSL. However, in reality, two experiments could not determine the type of QSL despite conducted inelastic neutron scattering measurements and discovering signatures of quantum spin ices. This was due to the lack of detailed research on inelastic neutron scattering based on the XYZ effective pseudospin model. To overcome this difficulty, we analyse the original XYZ model to elucidate the explicit behaviours of neutron scattering. In addition, we propose a novel technique to distinguish these QSLs by utilising multipolar-lattice couplings. In the next chapter, this theoretical proposal is explained in detail and further potential QSL phases are identified.

# Chapter 3

# Multipolar quantum spin liquid

As introduced in Section 2.3, the dipolar-octupolar system in rare-earth pyrochlore materials can host two distinct QSLs, namely the dipolar and octupolar QSLs. However, theoretical research has been limited within the unfrustrated parameter region, and other potential QSLs have not been investigated. Moreover, inelastic neutron scattering experiments have been proposed to probe the difference between the dipolar QSL (dQSL) and octupolar QSL (oQSL); however, the difference revealed in these experiments has not been specified.

In Chapter 3, we provide a classical and quantum analysis on the dipolar-octupolar system, including the parameter region, which has not previously been explored. Remarkably, we find a total of four distinct QSLs associated with the difference in the flux and multipole degrees. From our theoretical analysis of neutron scattering signals, an octupolar quantum spin liquid phase with a unique flux configuration is proposed in $Ce_2Zr_2O_7$. However, we are sceptical that inelastic neutron scattering experiments alone can distinguish between these four types of QSLs within the scope of this study. Instead, a novel probe for distinguishing QSLs known as magnetostriction is proposed. The magnetostriction experiment measures the lattice distortion under an external magnetic field, and the multipole-strain couplings play an important role in this distortion. The insensitivity of the octupolar moment to the external magnetic field results in a significant difference in the magnetostriction response of the dQSL and oQSL phases. These findings suggest that the lattice degree of freedom can be useful to detect local multipoles, including magnetic multipoles that do not interact directly with strain. In addition, these results provide a new method for probing multipoles with a rank greater than two, which is in high demand.

## 3.1 Model

We begin with the most general nearest-neighbour pseudospin-1/2 model for the dipolar-octupolar doublet in the pyrochlore lattice:

$$H_{\mathrm{DO}} = \sum_{\langle ij \rangle} J_x S_i^x S_j^x + J_y S_i^y S_j^y + J_z S_i^z S_j^z + J_{xz}(S_i^x S_j^z + S_i^z S_j^x). \tag{3.1}$$

Table 3.1: Local sublattice basis vectors

| $\alpha$ | 0 | 1 | 2 | 3 |
|---|---|---|---|---|
| $\hat{z}_\alpha$ | $\frac{1}{\sqrt{3}}(1,1,1)$ | $\frac{1}{\sqrt{3}}(1,-1,-1)$ | $\frac{1}{\sqrt{3}}(-1,1,-1)$ | $\frac{1}{\sqrt{3}}(-1,-1,1)$ |
| $\hat{x}_\alpha$ | $\frac{1}{\sqrt{6}}(-2,1,1)$ | $\frac{1}{\sqrt{6}}(-2,-1,-1)$ | $\frac{1}{\sqrt{6}}(2,1,-1)$ | $\frac{1}{\sqrt{6}}(2,-1,1)$ |
| $\hat{y}_\alpha$ | $\frac{1}{\sqrt{2}}(0,-1,1)$ | $\frac{1}{\sqrt{2}}(0,1,-1)$ | $\frac{1}{\sqrt{2}}(0,-1,-1)$ | $\frac{1}{\sqrt{2}}(0,1,1)$ |

The summation is taken over the nearest-neighbour sites, and $x, y$, and $z$ describe the local coordinate frame, which will be explained later. As shown in Section 1.2.3, the $x$ and $z$ components of the pseudospin belong to the same irreps., $\Gamma_{2u}$, although the multipole ranks are different (the $x$ component is the octupole and $z$ is the dipole). This enables the coupling between them, which corresponds to the last term of Eq. (3.1). We can eliminate the last term by introducing the transformation

$$\begin{pmatrix}\tau_x\\ \tau_z\end{pmatrix} = \begin{pmatrix}\cos\theta & -\sin\theta\\ \sin\theta & \cos\theta\end{pmatrix}\begin{pmatrix}S_x\\ S_z\end{pmatrix}, \qquad \tau_y = S_y, \tag{3.2}$$

where $2\theta = \arctan\left(\frac{2J_{xz}}{J_z - J_x}\right)$. The resulting Hamiltonian is represented by the XYZ model

$$H_{\mathrm{XYZ}} = \sum_{\langle ij\rangle} \tilde{J}_x \tau_i^x \tau_j^x + \tilde{J}_y \tau_i^y \tau_j^y + \tilde{J}_z \tau_i^z \tau_j^z, \tag{3.3}$$

where $\tilde{J}_x = J_x \cos^2\theta + J_z \sin^2\theta - 2J_{xz}\sin\theta\cos\theta$, $\tilde{J}_y = J_y$, and $\tilde{J}_z = J_x \sin^2\theta + J_z\cos^2\theta + 2J_{xz}\sin\theta\cos\theta$. Note that $\tau^x(\tau^z)$ is no longer the pure octupole (dipole) but a linear combination of the dipole and octupole[1].

Here, we introduce the local coordinate frame. As shown in the Fig. 3.1, the pyrochlore lattice has an underlying FCC Bravais lattice with four sublattices per unit cell, where the centre of each tetrahedron constitutes the Bravais lattice, and the indices 0,1,2, and 3 denote the sublattice number. The local coordinate frame differs depending on the sublattice index, and the blue vectors in the figure indicates the local $z$ axis for each sublattice. In the following explanation, we define the green (light-blue) tetrahedron as the "up" ("down") tetrahedron and its centre belongs to sublattice A (B) of the dual diamond lattice. The local sublattice basis vectors are summarised in Table 3.1.

Under an external magnetic field, only the dipolar moment can be linearly coupled via usual Zeeman coupling. In this case, the XYZ model under the field is written as

$$\begin{aligned} H_{\mathrm{XYZh}} &= \sum_{\langle ij\rangle} \tilde{J}_x \tau_i^x \tau_j^x + \tilde{J}_y \tau_i^y \tau_j^y + \tilde{J}_z \tau_i^z \tau_j^z - g_z \sum_i (\boldsymbol{h}\cdot\hat{z}_i) S_i^z \\ &= \sum_{\langle ij\rangle} \tilde{J}_x \tau_i^x \tau_j^x + \tilde{J}_y \tau_i^y \tau_j^y + \tilde{J}_z \tau_i^z \tau_j^z - \sum_i (\boldsymbol{h}\cdot\hat{z}_i)(\tilde{g}_x \tau_i^x + \tilde{g}_z \tau_i^z), \end{aligned} \tag{3.4}$$

[1]In the Ce compound case, $S^x(S^z)$ is a pure octupole (dipole) and the transformation combines the two. On the other hand, in the Nd compound case, $S^x$ already includes the dipolar components without the transformation owing to the difference in the wave function of the ground state doublets.

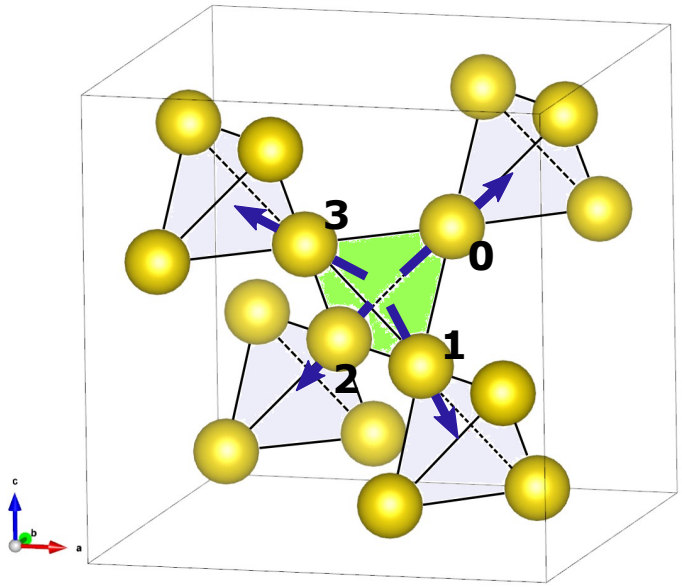


Figure 3.1. Rare-earth sites in a unit cell of the pyrochlore lattice. The centre of each tetrahedron constitute the FCC Bravais lattice, and indices 0,1,2, and 3 represent the corresponding sublattices. The local $z$ axes are defined for each sublattice and depicted as blue vectors. We define the green (light-blue) tetrahedron as the "up" ("down") tetrahedron, and its centre belongs to sublattice A (B) of the dual diamond lattice.

where $\tilde{g}_x = -g_z \sin\theta$, and $\tilde{g}_z = g_z \cos\theta$. In addition, a symmetry analysis, which will be discussed later in detail, revealed a higher-order coupling between the pure octuple $\tau^y$ and external fields. Including this higher-order coupling term, the full Hamiltonian under a magnetic field is expressed as

$$H_{\mathrm{XYZh}} = \sum_{\langle ij \rangle} \tilde{J}_x \tau_i^x \tau_j^x + \tilde{J}_y \tau_i^y \tau_j^y + \tilde{J}_z \tau_i^z \tau_j^z - \sum_i (\boldsymbol{h} \cdot \hat{z}_i)(\tilde{g}_x \tau_i^x + \tilde{g}_z \tau_i^z) + g_y \left[ (h_i^y)^3 - 3(h_i^x)^2 h_i^y \right] \tau_i^y. \tag{3.5}$$

Here, $h_i^\mu$ is the magnetic field in the local coordinate frame. Throughout this chapter, we will mainly analyse Eqs. (3.3) and (3.5).

## 3.2 Classical analysis

Before moving on to the quantum analysis, a classical analysis shall be provided. In this section, we employ representation theory analysis to derive the exact classical phase diagram for the dipolar-octupolar case. This analysis enables us to explore all potential parameter regions, and the results provide a solid starting point for the forthcoming quantum analysis. Furthermore, the spin ice states, which are the phase we are interested in, are discovered to be stable across a wide range of parameter region and to be categorised into two types in terms of multipoles.

In the non-Kramers or usual Kramers case, the classical ground state has been proven to always be a $\boldsymbol{q} = 0$ four-sublattice order, with the order parameters classified by a representation theory [122]. In this section, we can apply this method and derive an exact classical phase diagram for the dipolar-octupolar system.

### 3.2.1 Existence of a four-sublattice order

In the absence of an external field, the Hamiltonian Eq. (3.3) can be separated into the sum of tetrahedra, $H_{\mathrm{XYZ}} = \sum_m H_m$. Here, the index $m$ specifies the tetrahedron, and $H^m$ is defined as

$$H_m = \sum_{i,j\in m} \boldsymbol{\tau}_i \mathcal{J} \boldsymbol{\tau}_j = \sum_{i,j\in m} \boldsymbol{\tau}_i \begin{pmatrix} \tilde{J}_x & & \\ & \tilde{J}_y & \\ & & \tilde{J}_z \end{pmatrix} \boldsymbol{\tau}_j. \tag{3.6}$$

This decomposition is possible because the interactions within the up and down tetrahedra are related by the inversion of a single shared site. This also indicates that the interaction forms in a tetrahedron are the same regardless of the sublattice index, up and down. Assuming that $\boldsymbol{\tau}$ is the classical spin, we can construct the ground state of the system by repeating the spin configuration, which minimises the energy of $H_m$ for all tetrahedra. Because the Hamiltonians of each tetrahedron is exactly the same and every spin is shared by two tetrahedra, the state that minimises the energy of a tetrahedron simultaneously minimises the energy of all other tetrahedra; this is the classical ground state. Therefore, the classical ground state of the dipolar-octupolar system seems to be described by $\boldsymbol{q} = 0$ four-sublattice orders.

However, depending on the degeneracy type of the spin configuration for a single tetrahedron, other phases are allowed. Three cases can be considered for this problem. First, if all spins on a single tetrahedron point in a different direction in each of the classically degenerate ground states, the $\boldsymbol{q} = 0$ four-sublattice ordered state is unique and the finite $\boldsymbol{q}$ state cannot be a ground state. Second, within a set of classically degenerate ground states for a single tetrahedron, there are two or more states in which a spin on a certain site points in the same direction, the four-sublattice state is not unique, and the finite $\boldsymbol{q}$ state is possible. A good example of this case is kagome ice. Assume that the sublattice 0 points along the local $z$ axis and the other sublattices construct a two-in one-out configuration. In this case, we can separate the pyrochlore lattice into triangular layers composed of sublattice 0 and kagome layers composed of sublattices 1,2, and 3. This is also considered when the kagome ice planes accumulate along the $\boldsymbol{q} \parallel [111]$ axis, which is a ground state with finite $\boldsymbol{q}$. In the final case, two or more states exist with two spins on a certain site pointing in the same direction. The two-in two-out configuration is associated with this case, and this is not considered the $\boldsymbol{q} = 0$ ordered state. In addition, it presents a macroscopic number of degeneracies.

### 3.2.2 Representation theory

At this stage, we find that the ground state of the XYZ model in the dipolar-octupolar case is obtained by minimising the energy of a single tetrahedron. Here, we adopt a

symmetry-based analysis and derive an exact classical phase diagram [79]. First, the XYZ model of a single tetrahedron can be expressed as a 12×12 matrix,

$$H_{\mathrm{XYZ}}^{\mathrm{tet}} = \frac{1}{2}\mathcal{T}^t \begin{pmatrix} 0 & \mathcal{J} & \mathcal{J} & \mathcal{J} \\ \mathcal{J} & 0 & \mathcal{J} & \mathcal{J} \\ \mathcal{J} & \mathcal{J} & 0 & \mathcal{J} \\ \mathcal{J} & \mathcal{J} & \mathcal{J} & 0 \end{pmatrix} \mathcal{T}, \tag{3.7}$$

where $\mathcal{T}^t = (\boldsymbol{\tau}_0, \boldsymbol{\tau}_1, \boldsymbol{\tau}_2, \boldsymbol{\tau}_3)$, $\boldsymbol{\tau}_\alpha = (\tau_\alpha^x, \tau_\alpha^y, \tau_\alpha^z)$, and $\alpha$ is the sublattice index. We then explore the consequences of applying the representation theory for the point group symmetry operators to Eq. (3.7). This analysis transforms the Hamiltonian into a block diagonalised form, and the basis function set provides the order parameters that characterise the $\boldsymbol{q} = 0$ ordered states and the classical spin ice phase.

The point group symmetry of the pyrochlore lattice is $T_d$[2]. Our first aim is to obtain a character table for the $T_d$ point group using $\mathcal{T}$ as a basis for the representation matrices. The point group $T_d$ has 24 elements and 5 classes: $8 \times \hat{C}_3$, $3 \times \hat{C}_2$, $6 \times \hat{S}_4$, $6 \times \hat{\sigma}_d$, and $\hat{E}$. Thus, to obtain the character table, one element is chosen from each class, and representation matrices corresponding to them are derived. Furthermore, the generator of the $T_d$ point group is any $C_3$ rotation and any $S_4$ improper rotation, and other symmetry operators are obtained through a combination of these; hence, it is sufficient to examine the characters of these symmetry operators.

### $C_{31}^-$—$2\pi/3$ rotation about the [111] axis

Under this operator, the local axes transform as follows:

$$\begin{cases} \hat{z}_{0,1,2,3} \to \hat{z}_{0,3,1,2} \\ \hat{x}_{0,1,2,3} \to -\frac{1}{2}\hat{x}_{0,3,1,2} - \frac{\sqrt{3}}{2}\hat{y}_{0,3,1,2} \\ \hat{y}_{0,1,2,3} \to \frac{\sqrt{3}}{2}\hat{x}_{0,3,1,2} - \frac{1}{2}\hat{y}_{0,3,1,2}. \end{cases}$$

However, pseudospins $\boldsymbol{\tau}$ do not transform in this way because of their multipolar nature. Since each component of $\boldsymbol{\tau}$ is represented using the total angular momentum as $\tau^x = J_x^3 - \overline{J_x J_y J_y}$, $\tau^y = J_y^3 - \overline{J_y J_x J_x}$, and $\tau^z = J_z$, they transform in the following ways:

$$\begin{aligned}
&\tau^z \to \tau^z \\
&\tau^x \to \left(-\frac{1}{2}J_x - \frac{\sqrt{3}}{2}J_y\right)^3 - \left(-\frac{1}{2}J_x - \frac{\sqrt{3}}{2}J_y\right)\left(\frac{\sqrt{3}}{2}J_x - \frac{1}{2}J_y\right)\left(\frac{\sqrt{3}}{2}J_x - \frac{1}{2}J_y\right) \\
&\quad - \left(\frac{\sqrt{3}}{2}J_x - \frac{1}{2}J_y\right)\left(-\frac{1}{2}J_x - \frac{\sqrt{3}}{2}J_y\right)\left(\frac{\sqrt{3}}{2}J_x - \frac{1}{2}J_y\right) - \left(\frac{\sqrt{3}}{2}J_x - \frac{1}{2}J_y\right)\left(\frac{\sqrt{3}}{2}J_x - \frac{1}{2}J_y\right)\left(-\frac{1}{2}J_x - \frac{\sqrt{3}}{2}J_y\right) \\
&\quad = J_x^3 - \overline{J_x J_y J_y} = \tau^x \\
&\tau^y \to \left(\frac{\sqrt{3}}{2}J_x - \frac{1}{2}J_y\right)^3 - \left(\frac{\sqrt{3}}{2}J_x - \frac{1}{2}J_y\right)\left(-\frac{1}{2}J_x - \frac{\sqrt{3}}{2}J_y\right)\left(-\frac{1}{2}J_x - \frac{\sqrt{3}}{2}J_y\right) \\
&\quad - \left(-\frac{1}{2}J_x - \frac{\sqrt{3}}{2}J_y\right)\left(\frac{\sqrt{3}}{2}J_x - \frac{1}{2}J_y\right)\left(-\frac{1}{2}J_x - \frac{\sqrt{3}}{2}J_y\right) - \left(-\frac{1}{2}J_x - \frac{\sqrt{3}}{2}J_y\right)\left(-\frac{1}{2}J_x - \frac{\sqrt{3}}{2}J_y\right)\left(\frac{\sqrt{3}}{2}J_x - \frac{1}{2}J_y\right) \\
&\quad = J_y^3 - \overline{J_y J_x J_x} = \tau^y
\end{aligned}$$

[2]To be exact, the inversion operator $\mathcal{I}$ is also a symmetry operator; thus, $O_h = T_d \times \mathcal{I}$ is the correct point group. However, the inversion operator is often dismissed because it plays a benign role in the spin basis.

where the sublattice index is omitted for simplicity. Therefore, the representation matrix for the $C_3$ rotation operator in the basis $\mathcal{T}$ is

$$C_{31}^{-} = \begin{pmatrix} & & I \\ I & & \\ & I & \end{pmatrix}, \qquad I = \begin{pmatrix} 1 & & \\ & 1 & \\ & & 1 \end{pmatrix}. \tag{3.8}$$

From this expression, we find the character of the class $\hat{C}_3$ as $\chi(\hat{C}_3) = 3$.

### $S_{4z}$—$\pi/4$ improper rotation about the $z$ axis

In the global coordinate frame, this symmetry operator is represented as

$$S_{4z} = \begin{pmatrix} 0 & -1 & 0 \\ 1 & 0 & 0 \\ 0 & 0 & 1 \end{pmatrix} \cdot \mathcal{I},$$

where $\mathcal{I}$ is an inversion operator, which plays a benign role for spin operators. Considering this and applying the transformation of the coordinate, the local spin operators transform as

$$\begin{cases} J^z_{0,1,2,3} \to J^z_{2,0,3,1} \\ J^x_{0,1,2,3} \to \frac{1}{2}\hat{J}^x_{2,0,3,1} - \frac{\sqrt{3}}{2}\hat{J}^y_{2,0,3,1} \\ J^y_{0,1,2,3} \to -\frac{\sqrt{3}}{2}\hat{J}^x_{2,0,3,1} - \frac{1}{2}\hat{J}^y_{2,0,3,1}. \end{cases}$$

Thus, the local pseudospins transform as

$$\begin{aligned}
&\tau^z \to -\tau^z \\
&\tau^x \to \left(\frac{1}{2}J_x - \frac{\sqrt{3}}{2}J_y\right)^3 - \left(\frac{1}{2}J_x - \frac{\sqrt{3}}{2}J_y\right)\left(-\frac{\sqrt{3}}{2}J_x - \frac{1}{2}J_y\right)\left(-\frac{\sqrt{3}}{2}J_x - \frac{1}{2}J_y\right) \\
&\quad - \left(-\frac{\sqrt{3}}{2}J_x - \frac{1}{2}J_y\right)\left(\frac{1}{2}J_x - \frac{\sqrt{3}}{2}J_y\right)\left(-\frac{\sqrt{3}}{2}J_x - \frac{1}{2}J_y\right) - \left(-\frac{\sqrt{3}}{2}J_x - \frac{1}{2}J_y\right)\left(-\frac{\sqrt{3}}{2}J_x - \frac{1}{2}J_y\right)\left(\frac{1}{2}J_x - \frac{\sqrt{3}}{2}J_y\right) \\
&\quad = -J_x^3 + \overline{J_x J_y J_y} = -\tau^x \\
&\tau^y \to \left(-\frac{\sqrt{3}}{2}J_x - \frac{1}{2}J_y\right)^3 - \left(-\frac{\sqrt{3}}{2}J_x - \frac{1}{2}J_y\right)\left(\frac{1}{2}J_x - \frac{\sqrt{3}}{2}J_y\right)\left(\frac{1}{2}J_x - \frac{\sqrt{3}}{2}J_y\right) \\
&\quad - \left(\frac{1}{2}J_x - \frac{\sqrt{3}}{2}J_y\right)\left(-\frac{\sqrt{3}}{2}J_x - \frac{1}{2}J_y\right)\left(\frac{1}{2}J_x - \frac{\sqrt{3}}{2}J_y\right) - \left(\frac{1}{2}J_x - \frac{\sqrt{3}}{2}J_y\right)\left(\frac{1}{2}J_x - \frac{\sqrt{3}}{2}J_y\right)\left(-\frac{\sqrt{3}}{2}J_x - \frac{1}{2}J_y\right) \\
&\quad = J_y^3 - \overline{J_y J_x J_x} = \tau^y
\end{aligned}$$

where the sublattice index is once again omitted. Therefore, the representation matrix for the $C_3$ rotation operator in the basis $\mathcal{T}$ is

$$S_{4z} = \begin{pmatrix} & A & \\ A & & \\ & & A \\ & A & \end{pmatrix}, \qquad A = \begin{pmatrix} -1 & & \\ & 1 & \\ & & -1 \end{pmatrix}. \tag{3.9}$$

From this expression, we find the character of the class $\hat{S}_4$ as $\chi(\hat{S}_4) = 0$.

### Other operators

As mentioned above, other symmetry operators are obtained through a combination of $C_{31}^{-}$ and $S_{4z}$. For example, a $C_2$ rotation operator is obtained using $C_{2z} = S_{4z}S_{4z}$. By explicitly calculating the trace of the representation matrix of this operator, the character of the class $\hat{C}_2$ is found to be $\chi(\hat{C}_2) = 0$. The result of the character table is as follows:

| $T_d$ | $\hat{E}$ | $8\hat{C}_3$ | $3\hat{C}_2$ | $6\hat{S}_4$ | $6\hat{\sigma}_d$ |
|---|---|---|---|---|---|
| $\Gamma$ | 12 | 3 | 0 | 0 | $-2$ |

Using the method explained in Section 1.2.3, we can reduce the representation $\Gamma$ into a direct sum of irreps

$$\Gamma = \Gamma_1 \oplus 2\Gamma_2 \oplus 2\Gamma_4 \oplus \Gamma_5. \tag{3.10}$$

This means that the basis $\mathcal{T}$ is transformed into the basis functions of the irreps obtained above through a unitary transformation.

The next step involves identifying the linear combination of $\tau_\alpha^\mu$ that constitutes the basis functions of each irreps $\Gamma_n$. According to group theory, the $i$-th basis of $d$ dimensional irreps $\Gamma_n$ is obtained by operating the projection operator $\mathcal{P}$ on an arbitrary vector, which is defined as

$$\mathcal{P}^{i,(j)} = \frac{d}{g}\sum_G \langle \Gamma_n^i | G | \Gamma_n^j \rangle^* G, \tag{3.11}$$

where $g$ and $G$ are the order and elements of the point group, respectively, and $|\Gamma_n^i\rangle$ is the $i$-th basis of the irreps, which is given in a usual character table. Note that $j = 1, 2, \ldots, d$ can be chosen arbitrarily. The obtained basis functions for every $\Gamma_n$ and corresponding orders are summarised in Table 3.2. Using these basis functions, the full classical Hamiltonian is rewritten in the block-diagonalised form:

$$H_{\mathrm{XYZ}} = \frac{1}{2}\sum_n \left[ 3\tilde{J}_y M_{\Gamma_1}^2 + 3\tilde{J}_x M_{\Gamma_{2a}}^2 + 3\tilde{J}_z M_{\Gamma_{2b}}^2 - \tilde{J}_x \boldsymbol{M}_{\Gamma_{4a}}^2 - \tilde{J}_z \boldsymbol{M}_{\Gamma_{4b}}^2 - \tilde{J}_y \boldsymbol{M}_{\Gamma_5}^2 \right], \tag{3.12}$$

with the constraint $M_{\Gamma_1}^2 + M_{\Gamma_{2a}}^2 + M_{\Gamma_{2b}}^2 + \boldsymbol{M}_{\Gamma_{4a}}^2 + \boldsymbol{M}_{\Gamma_{4b}}^2 + M_{\Gamma_5}^2 = 1$, which originates from a property of classical spins $|\boldsymbol{\tau}| = 1/2$. The ground state is obtained by letting $|\boldsymbol{M}_k| = 1$ and the others equate to zero, where the coupling constant associated with the order parameter $\boldsymbol{M}_k$ is the smallest. Based on this analysis, we obtain a classical phase diagram for the dipolar-octupolar case, as shown in Fig. 3.2. In total, six distinct phases appear whose order parameters are related to the basis functions shown in Table 3.2. Although the d/o-AIAO phases are the $\boldsymbol{q} = 0$ ordered state, the d/o-CSI phases are not. In these phases, six-fold degeneracy remains within a tetrahedron and the third rule provided in the previous section is satisfied. As a result, a macroscopic number of degeneracies remain in the full system; this is one of the important properties of classical spin ices. Remarkably, the classical spin ice states, which evolve into quantum spin ices[3]

[3]Here, we do not mention symmetry of the QSL because it remains under discussion. Around the origin of each phase diagram, the existence of a $U(1)$ QSL phase is confirmed via experiments and theories. However, the symmetry of the QSL far from the origin is not clear, although quantum spin ice signatures are certainly observed. For example, at the Heisenberg limit, it is theoretically proposed that the $U(1)$ nature is absent and the probability of the $\mathbb{Z}_2$ spin liquid is suggested [123, 124].

in the quantum regime appear more stable in the unexplored frustrated parameter region. Motivated by these findings, a quantum analysis is conducted, including the area in which the interactions are frustrated.

Table 3.2: Basis functions for the magnetic orderings of the dipolar-octupolar case. Abbreviations: o-AIAO = octupolar all-in / all-out, d-AIAO = dipolar all-in / all-out, d-CSI = dipolar classical spin ice, and o-CSI = octupolar classical spin ice. Although $\tau^x$ is mainly composed of the octupolar moment, we assume that the related orders $M_{\Gamma_{2a}}$ and $M_{\Gamma_{4a}}$ belong to the dipolar phase because they transform exactly the same as the dipole $\tau^z$. The orderings are arranged into irreps of $T_d$, that is, the pyrochlore point group.

| Irreps | Basis set | Orders |
|---|---|---|
| $\Gamma_1$ | $M_{\Gamma_1} = \frac{1}{2}(\tau_0^y + \tau_1^y + \tau_2^y + \tau_3^y)$ | o-AIAO |
| $\Gamma_2$ | $M_{\Gamma_{2a}} = \frac{1}{2}(\tau_0^x + \tau_1^x + \tau_2^x + \tau_3^x)$<br>$M_{\Gamma_{2b}} = \frac{1}{2}(\tau_0^z + \tau_1^z + \tau_2^z + \tau_3^z)$ | d-AIAO |
| $\Gamma_4$ | $\boldsymbol{M}_{\Gamma_{4a}} = \frac{1}{2}\begin{pmatrix}\tau_0^x + \tau_1^x - \tau_2^x - \tau_3^x \\ \tau_0^x - \tau_1^x + \tau_2^x - \tau_3^x \\ \tau_0^x - \tau_1^x - \tau_2^x + \tau_3^x\end{pmatrix}$<br>$\boldsymbol{M}_{\Gamma_{4b}} = \frac{1}{2}\begin{pmatrix}\tau_0^z + \tau_1^z - \tau_2^z - \tau_3^z \\ \tau_0^z - \tau_1^z + \tau_2^z - \tau_3^z \\ \tau_0^z - \tau_1^z - \tau_2^z + \tau_3^z\end{pmatrix}$ | d-CSI |
| $\Gamma_5$ | $\boldsymbol{M}_{\Gamma_5} = \frac{1}{2}\begin{pmatrix}\tau_0^y + \tau_1^y - \tau_2^y - \tau_3^y \\ \tau_0^y - \tau_1^y + \tau_2^y - \tau_3^y \\ \tau_0^y - \tau_1^y - \tau_2^y + \tau_3^y\end{pmatrix}$ | o-CSI |

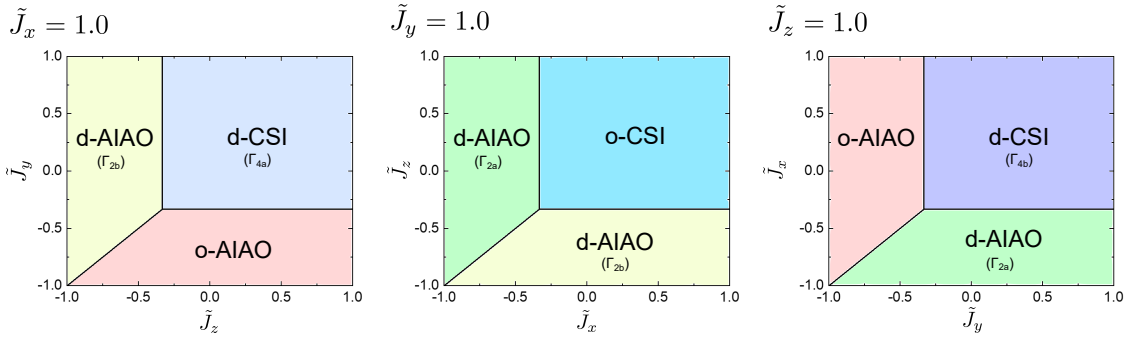


Figure 3.2. Classical phase diagram of the dipolar-octupolar system. ($\Gamma_\alpha$) describes the irreps of the order parameters.

## 3.3 Quantum analysis

Reliable methods of quantum analysis on the dipolar-octupolar system are extremely limited. For example, the aforementioned gMFT method is not easily extended to the frustrated parameter region, and quantum Monte Carlo simulations are not applicable to the frustrated parameter region because of a notorious sign problem. Owing to the difficulty of these methods, an exact diagonalisation (ED) approach was used for minority site clusters. In this section, we confirm that classical spin ices in the unfrustrated and frustrated parameter regions are distinguished in the quantum spin model and find that there are four distinct quantum spin ice phases in this model. In the following calculations, a 32-site cluster was used (Fig. 3.3), which preserves the entire crystal symmetry, and a 16-site cluster is also used, which corresponds to pyrochlore unit cells.

### 3.3.1 Quantum phase diagram

The quantum phase diagram on the $\tilde{J}_y = 1.0$ plane obtained from an ED calculation is provided in Fig. 3.4(a). The phase boundaries are denoted by points where the $\partial^2 E/\partial \tilde{J}_x$ and $\partial^2 E/\partial \tilde{J}_z$ become singular. Clear singularities appear at the boundary of the frustrated and unfrustrated parameter regions. In order to investigate the situation in detail, we illustrate in Figs. 3.4(c) and (d) the parameter dependences of the energy per site ($\epsilon = E/N$) and $\partial^2\epsilon/\partial\tilde{J}_\mu^2$ along the $\tilde{J}_z = 0$ and $\tilde{J}_x = 0$ lines, respectively. Sharp peak structures in $\partial^2\epsilon/\partial\tilde{J}_\mu^2$ at $\tilde{J}_\mu \sim \pm 0.002$ are discovered, indicating the presence of phase transitions that were not revealed in the previous classical analysis. This phase transition is explained below. Near the Ising limit ($\tilde{J}_x, \tilde{J}_z \ll \tilde{J}_y$), the low energy theory can be described by an emergent lattice $U(1)$ gauge theory defined on the dual diamond lattice

$$H_{\text{eff}} = U\boldsymbol{E}^2 + K\cos(\nabla \times A), \tag{3.13}$$

where $\boldsymbol{E}$ and $\boldsymbol{A}$ are the emergent electric and gauge fields, and are related to the Ising and transverse components of the pseudospin 1/2, respectively. Here, $K < 0$ ($K > 0$) for ferromagnetic (antiferromagnetic) transverse interactions and $U$ is taken to be a large constant. As we have mentioned before, these regimes are often called unfrustrated ($K < 0$) and frustrated ($K > 0$) regimes, respectively. The argument $\nabla \times A$ in (3.13)

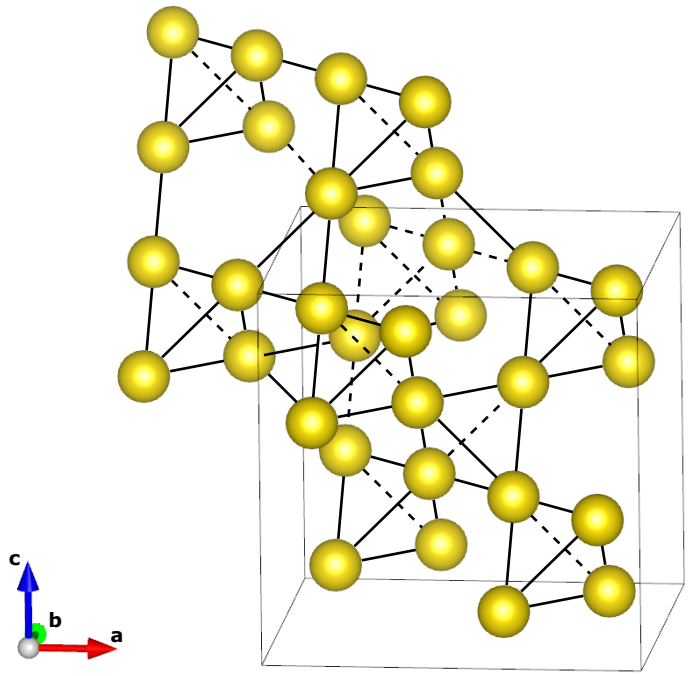


Figure 3.3. Schematic illustration of a 32-site symmetric cluster of the pyrochlore lattice. The periodic conditions are imposed along the $[\bar{1}10]$, $[\bar{1}01]$, and [011] axes.

represents the emergent gauge flux penetrating a hexagonal loop in the dual diamond lattice, and $K < 0$ ($K > 0$) would favour 0 ($\pi$) flux configurations in the corresponding ground states. Therefore, the QSL in the unfrustrated (frustrated) region is called the 0-flux ($\pi$-flux) QSL. The gauge flux degree of freedom stems from quantum spins; thus, this phase transition was invisible within the classical analysis. As seen in Figs. 3.4(c) and (d), the classical spin ice (CSI) state (which should be found in the Ising limit) is stable within a quite small window ($-0.002 \lesssim \tilde{J}_\mu \lesssim 0.002$). According to the preceding description, the phase transition at $\tilde{J}_\mu \simeq -0.002$ ($\tilde{J}_\mu \simeq 0.002$) corresponds to the transition to the 0-flux ($\pi$-flux) QSL phase. These QSLs are discriminated experimentally, as we will demonstrate later. We should highlight that the names 0-flux and $\pi$-flux QSLs are based on the preceding perturbative analysis, and we do not explicitly compute the amplitude of the gauge field on the dual diamond lattice because it is not capturable in the ED calculation. The energy gain $\Delta$ can be defined as the amount of energy gained as a result of optimal flux configurations.

In addition, we find the $\pi$-flux oQSL phase expands across a wide range in the parameter region. This result is consistent with the rough estimation of gMFT for the non-Kramers case [98]. In the non-Kramers case, a gMFT calculation reveals that the critical point is $J_\pm/J_z \sim 0.19$ for the unfrustrated case and $J_\pm/J_z \sim 4.13$ for the frustrated case. Moreover, from our ED calculation, the stability of the $U(1)$ QSL in the frustrated parameter region is confirmed; remarkably, this can also be true far from the perturbative regime. Another possibility is that the quantum spin ice originating from the classical

spin ice scheme ($U(1)$ QSL) smoothly connects another QSL on the pyrochlore lattice, which is observed in the Heisenberg model. The existence of the $U(1)$ nature far from the origin is still under discussion; hence, it is still unclear whether quantum spin ices in the non-perturbative and frustrated parameter regions are identified as $U(1)$ QSLs. Thus, we do not explicitly mention the symmetry of QSLs here. Note that the quantum spin ice signatures are observed even in the non-perturbative region. Furthermore, the parameter region, where the 0-flux oQSL phase exists, which is also found in the gMFT calculation, is much smaller than that of gMFT. This indicates that 0-flux oQSL phase is not robust against fluctuations. However, the present results still indicate that the spin liquid state exists stably in a wider range than the perturbative region.

Because phase diagrams on other planes are obtained by simply relabelling the coordinates, 0- and $\pi$-flux dQSLs can also be found. Therefore, the dipolar-octupolar system has potential to exhibit four distinct QSLs in total. Although Ce-based compounds present numerous signatures indicating the realisation of the QSL phase, the type of QSL to which it belongs is yet unknown. Furthermore, previous theoretical research has focussed only on the difference between dipolar and octupolar QSLs and did not pay attention to the differences between flux configurations. Hence, it is important to discover clear differences between these four QSLs.

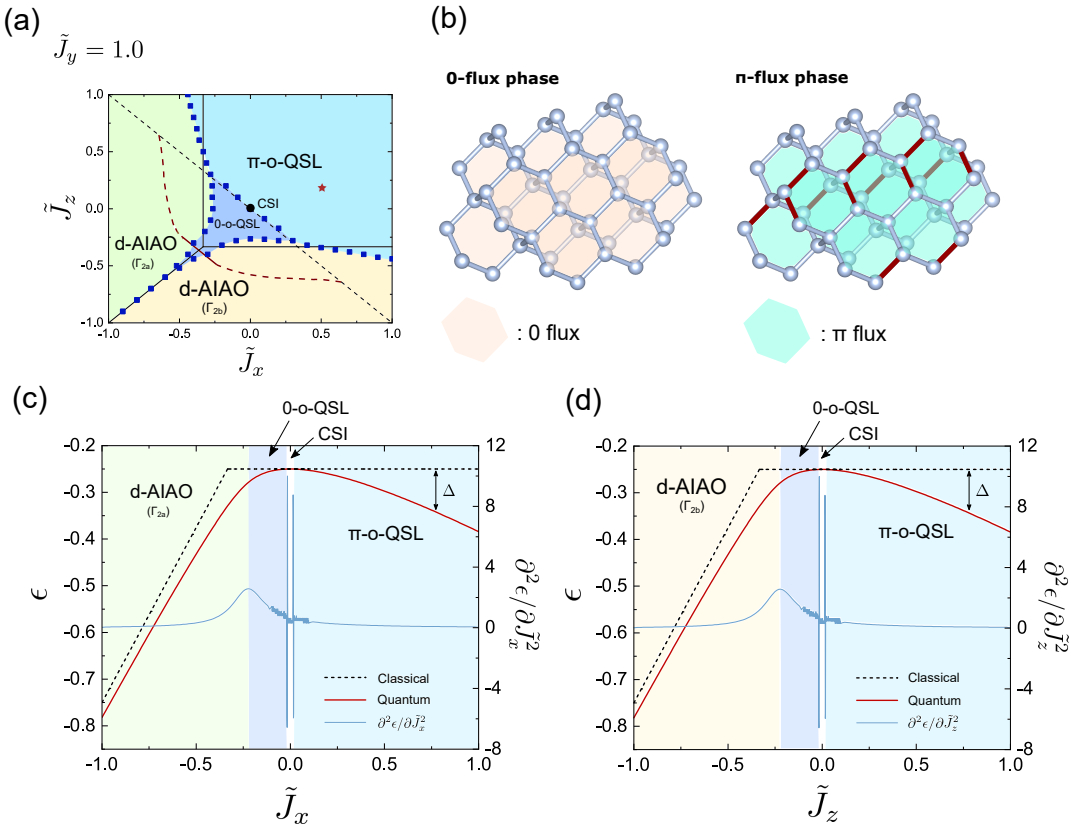


Figure 3.4. (a): Quantum phase diagram for the dipolar-octupolar system. The phase boundaries are determined by the singular points of the second derivative of the ground state energy in the 16-site cluster ED calculation. The black-dashed line represents the boundary between the frustrated and unfrustrated parameter regions, and the red line is the phase boundary obtained in the gMFT calculation [107]. The red star indicates the parameter set that is considered to be realised in $Ce_2Zr_2O_7$ (see Section 2.3.2). Note that the phase diagrams for other planes are obtained by relabelling the coupling constant and considering the order parameters. (b): The schematics of the 0-flux and $\pi$-flux configurations. The lattice represents the dual diamond lattice, and the thick red lines carry the emergent lattice gauge field $A_{\boldsymbol{r}\boldsymbol{r}'} = \pi$. $(\nabla \times A)_{\hexagon} = 0$ $(\pi)$ mod $2\pi$ is satisfied for all hexagons in the 0 $(\pi)$-flux phase. The energy per site $\epsilon = E/N$ and the second derivative $\partial^2\epsilon/\partial\tilde{J}_\mu^2$ along (c): the $\tilde{J}_z = 0$ and (d): $\tilde{J}_x = 0$ line. The black-dashed, red-solid, and blue-solid lines indicate the classical energy, the quantum energy, and the second derivative, respectively.

### 3.3.2 Static properties of each QSL and other MPOs

Now the quantum phase diagram for the dipolar-octupolar system has been revealed, we must elucidate the physical properties of each phase. First, we attempt to discover several differences that characterise the distinct flux configurations. As shown in Fig. 3.4, a gauge field with $A_{\boldsymbol{rr'}} = \pi$ appears on some bond of the diamond lattice only in the $\pi$-flux phase. Considering the spins are located at the centre of the bond, we expect spins on the bond with $A_{\boldsymbol{rr'}} = \pi$ and $A_{\boldsymbol{rr'}} = 0$ to be different. Because there are a macroscopic number of gauge field configurations that satisfy $(\nabla \times A)_{\hexagon} = \pi \bmod 2\pi$, it will not be possible to compare a single spin and discover an intriguing signal. However, it will be possible for the finite gauge fields to provide the static spin correlations with a certain effect. Motivated by this prediction, we calculate the diagonal pseudospin correlation:

$$\tilde{S}^{\alpha\alpha} = \frac{1}{N} \sum_{i,j} e^{\mathrm{i}\boldsymbol{q}\cdot\boldsymbol{R}_i - \boldsymbol{R}_j} \langle S_i^{\alpha} S_j^{\alpha} \rangle, \tag{3.14}$$

where $\alpha$ is the local coordinate frame. This quantity is explored using two methods: a classical Monte Carlo calculation on $4 \times L \times L \times L$ ($L = 8$) sites and an exact diagonalisation (ED) on the 32-site cluster with full point group symmetry. The Monte Carlo simulation was performed by my collaborator Emily Z. Zhang.

Figure 3.5 displays the local diagonal pseudospin correlation of the octupolar spin ices. The first, second, third, and fourth rows correspond to the result of the ED calculation for the $\pi$-flux oQSL ($\pi$-oQSL), classical Monte Carlo calculation for the $\pi$-oQSL, ED calculation for the 0-flux oQSL (0-oQSL), and classical Monte Carlo calculation for the 0-oQSL, respectively. The following parameter sets were employed: $(\tilde{J}_x, \tilde{J}_y, \tilde{J}_z) = (0.5, 1.0, 0.25)$ for the $\pi$-oQSL phase, and $(\tilde{J}_x, \tilde{J}_y, \tilde{J}_z) = (-0.1, 1.0, -0.1)$ for the 0-oQSL phase. The white hexagons in each plot represent the Brillouin zone. From the classical Monte Carlo results, we can find sharp pinch point structures in the $\boldsymbol{q}$-map of $\tilde{S}^{yy}$ for both flux patterns, which characterises the spin ice states, as seen in Figs. 3.5(e) and (k). We expect gapless photon excitation to emerge from these $\boldsymbol{q}$ locations in its quantum counterpart. No significant difference is observed between the pinch point structures of the 0-flux and $\pi$-flux phases. In contrast, the results of $\tilde{S}^{xx}$ and $\tilde{S}^{zz}$ (Figs. 3.5(d), (f), (j), and (l)) exhibit a clear difference, which yields a distinct neutron scattering signature, as will be explained later. In Figs. 3.5(d) and (f), the $\pi$-oQSL phase has a weak intensity at the $\Gamma_0$ point ($\boldsymbol{q} = (0, 0, 0)$) and exhibits peaks at the $\Gamma_1$ ($\boldsymbol{q} = (0, 0, 4\pi)$) and $\Gamma_2$ ($\boldsymbol{q} = (\pm 4\pi, \pm 4\pi, 0)$) points; their contrast is prominent in $\tilde{S}^{xx}$. Conversely, as shown in Figs. 3.5(j) and (l), the 0-oQSL phase has a peak at the $\Gamma_0$ point, and the intensity at the $\Gamma_1$ and $\Gamma_2$ points is relatively weak. Considering the emergent gauge fields are related to $\tau_i^{+/-}$, it is reasonable to observe that a difference in flux configuration yields a difference in the diagonal pseudospin correlations whose components are not related to the spin ice configuration. Figures 3.5 (a–c) and (g–i) show the quantum results, which support the classical Monte Carlo results, although the pinch point structures are not clear due to the quantum fluctuations and the size effect. However, the enhanced signals are still observed around the corresponding momentum positions. Whether these behaviours are due to finite size effects or quantum effects obscuring the pinch point must be clarified experimentally and in future theories.

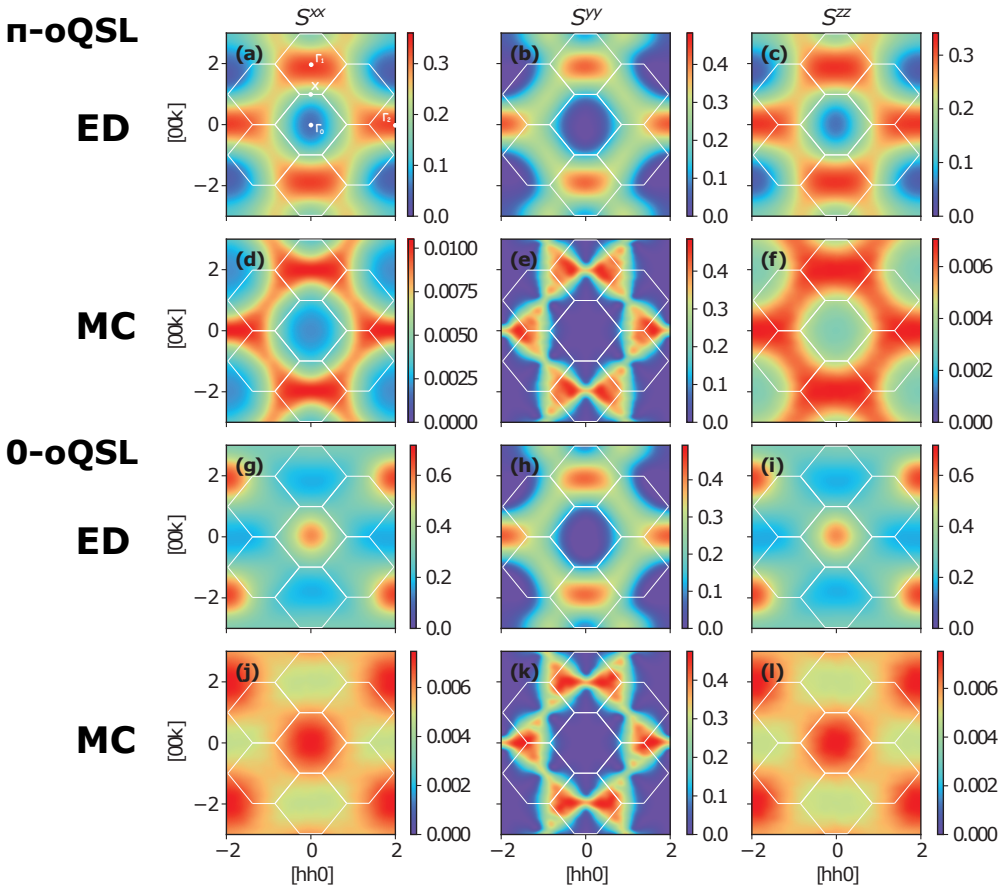


Figure 3.5. Diagonal pseudospin correlation for octupolar spin ice phases obtained from the classical Monte Carlo calculation and the exact diagonalisation on the 32-site cluster. The following parameter sets were employed: $(\tilde{J}_x, \tilde{J}_y, \tilde{J}_z) = (0.5, 1.0, 0.25)$ for the $\pi$-oQSL phase and $(\tilde{J}_x, \tilde{J}_y, \tilde{J}_z) = (-0.1, 1.0, -0.1)$ for the 0-oQSL phase. (a–c): the exact diagonalisation (ED) results for the $\pi$-oQSL phase, (d–f): the classical Monte Carlo (MC) results for the $\pi$-oQSL phase, (g–i) the ED results for the 0-oQSL phase, and (j–l): the MC results for the 0-oQSL phase. The white hexagons in each plot represent the Brillouin zone. The pinch point singularities observed in (e) and (k) characterise the realisation of the spin ice state.

Figure 3.6 presents the local diagonal pseudospin correlations of the dipolar spin ices. The first, second, third, and fourth rows correspond to the result of ED calculation for the $\pi$-flux dQSL ($\pi$-dQSL), classical Monte Carlo calculation for the $\pi$-dQSL, ED calculation for the 0-flux dQSL (0-dQSL), and classical Monte Carlo calculation for the 0-dQSL, respectively. The following parameter sets were employed: $(\tilde{J}_x, \tilde{J}_y, \tilde{J}_z) = (0.25, 0.5, 1.0)$ for the $\pi$-dQSL phase and $(\tilde{J}_x, \tilde{J}_y, \tilde{J}_z) = (-0.1, -0.1, 1.0)$ for the 0-dQSL phase. In dipolar spin ice cases, we find pinch point singularities in the $z$ component of correlations for both flux configurations, and this resemblance yields a similar neutron scattering signature and makes it difficult to distinguish between them. Other properties are understood in a similar way to the octupolar spin ices by relabelling the coordinates.

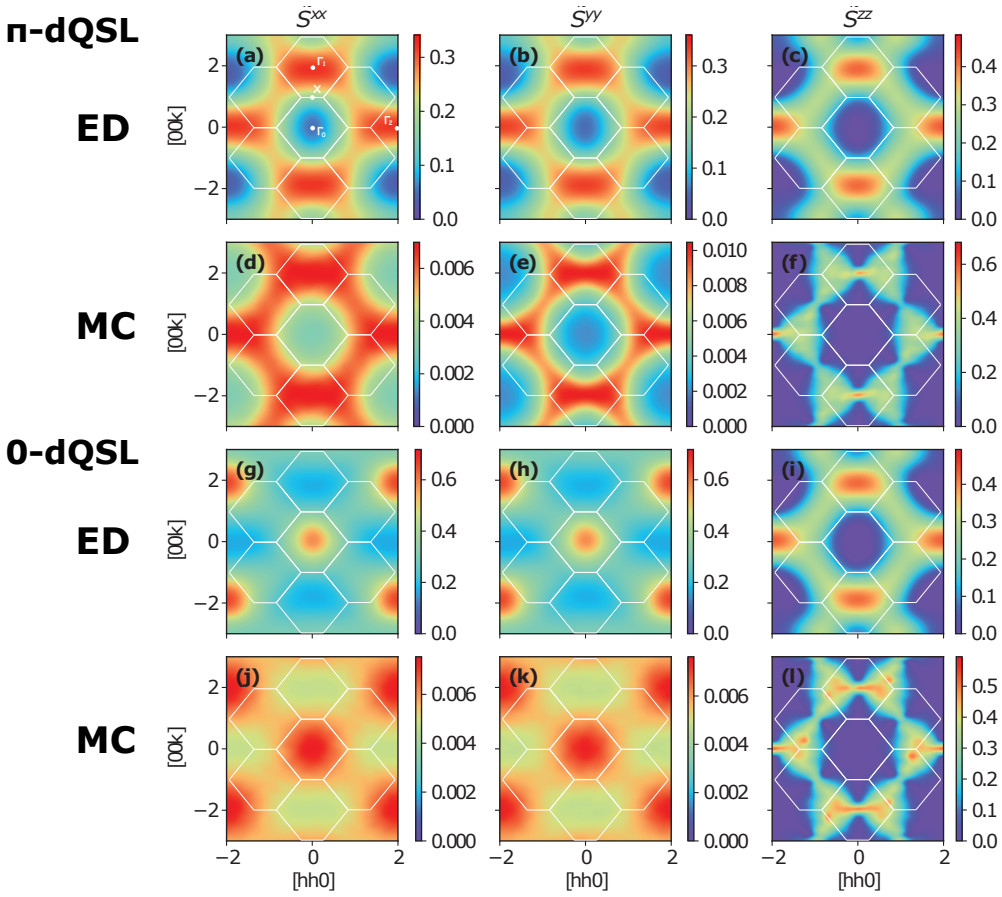


Figure 3.6. Diagonal pseudospin correlation for dipolar spin ice phases obtained from the classical Monte Carlo calculation and the exact diagonalisation on the 32-site cluster. The following parameter sets were employed: $(\tilde{J}_x, \tilde{J}_y, \tilde{J}_z) = (0.25, 0.5, 1.0)$ for the $\pi$-dQSL phase and $(\tilde{J}_x, \tilde{J}_y, \tilde{J}_z) = (-0.1, -0.1, 1.0)$ for the 0-dQSL phase. (a–c): the exact diagonalisation (ED) results for the $\pi$-dQSL phase, (d–f): the classical Monte Carlo (MC) results for the $\pi$-dQSL phase, (g–i) the ED results for the 0-dQSL phase, and (j–l): the MC results for the 0-dQSL phase. The white hexagons in each plot represent the Brillouin zone. The pinch point singularities observed in (f) and (i) characterise the realisation of the spin ice state.

For completeness, we explore the local diagonal pseudospin correlations of the ordered phases, namely, X-AIAO (d-AIAO ($\Gamma_{2a}$)), Y-AIAO (o-AIAO), and Z-AIAO (d-AIAO ($\Gamma_{2b}$)). Figure 3.7 depicts the ED and classical Monte Carlo results for the Y-AIAO phase, and those for other phases are obtained by relabelling the index. For example, the results of the X-AIAO phase are obtained by relabelling as $(x, y, z) \to (z, x, y)$. Supported by the $\boldsymbol{q} = 0$ nature of the ordered states, the intensity distribution of the o-AIAO phase shown in Fig. 3.7 exhibits an especially sharp intensity of the pseudospin correlation at $\boldsymbol{q} = 0$ for $\tilde{S}^{yy}$, which was not observed in the spin ice phases. This behaviour characterises the pseudospin correlation property of the ordered phases. However, the $\boldsymbol{q}$ dependence of $\tilde{S}^{zz}$ looks similar to that of the $\pi$-oQSL phase. As we will describe

below, this indicates the QSL phase and the ordered phase are indistinguishable by a neutron scattering measurement alone although they are apparently distinguishable by verifying the existence of anomalies in the specific heat and susceptibility measurements. In addition, an inconsistency between classical and quantum calculations is found for the $\boldsymbol{q}$ dependence of $\tilde{S}^{xx}$. The reason for this is not clearly understood and needs to be compared with the results of other calculations, but intuitively, the results of the classical calculation are reasonable because the $\tau^x$ coupling ($\tilde{J}_x$) is antiferromagnetic and we would expect low intensities at the zone centre as seen in the $\pi$-oQSL case. Another possibility is that, owing to quantum effects, what is actually observed is the ED results.

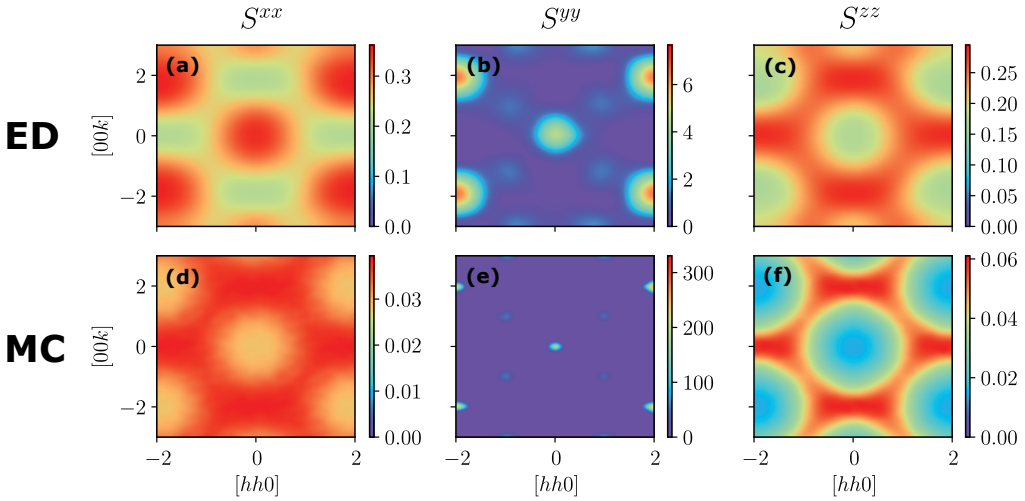


Figure 3.7. Diagonal pseudospin correlation for the o-AIAO phase obtained from (a–c): the exact diagonalisation on the 32-site cluster and (d–f): the classical Monte Carlo calculation. Note that the results for d-AIAO phases are obtained by simply relabelling the index, as appropriate. The parameter set was chosen as $(\tilde{J}_x, \tilde{J}_y, \tilde{J}_z) = (0.2, -0.75, 1.0)$.

Some may assume that these signals are detectable using a neutron scattering measurement; however, this is incorrect. Since neutron spins are considered dipolar moments or external fields, they cannot couple to the $y$ component of the pseudospin, and $\tilde{S}^{yy}$ is invisible in neutron scattering measurements. Furthermore, in the limit of $J_{xz} \to 0$, that is, the dipolar-octupolar coupling within the same irreps is negligible, $\tilde{S}^{xx}$ is also invisible. Therefore, only $\tilde{S}^{zz}$ can contribute to the neutron scattering signals. In other words, we should define the neutron scattering structure factor as

$$S(\boldsymbol{q}) = \frac{1}{N} \sum_{\mu\nu} \left( \delta_{\mu\nu} - \frac{q_\mu q_\nu}{q^2} \right) \langle M^\mu(-\boldsymbol{q}) M^\nu(\boldsymbol{q}) \rangle. \tag{3.15}$$

Here, $\mu$ and $\nu$ represent the global coordinate frame, the dipolar-based magnetization $\boldsymbol{M}(\boldsymbol{q}) = \sum_i e^{\mathrm{i}\boldsymbol{q}\cdot\boldsymbol{R}_i} \hat{z}_i \tau_i^z$, and $N$ is the number of sites. In the local coordinate frame, this is represented as

$$S(\boldsymbol{q}) = \frac{1}{N} \sum_{i,j} \left[ \hat{z}_i \cdot \hat{z}_j - \frac{(\hat{z}_i \cdot \boldsymbol{q})(\hat{z}_j \cdot \boldsymbol{q})}{q^2} \right] e^{-\mathrm{i}\boldsymbol{q}\cdot(\boldsymbol{R}_i - \boldsymbol{R}_j)} \langle \tau_i^z \tau_j^z \rangle. \tag{3.16}$$

Figure 3.8 shows the $\boldsymbol{q}$ dependences of this neutron scattering structure factor for every QSL, which are then compared to experimental values. Figures 3.8(a–d) present the ED results for the $\pi$-oQSL, $\pi$-dQSL, 0-oQSL, and 0-dQSL phases, and Figs. 3.8(e–h) present the classical Monte Carlo results for the $\pi$-oQSL, $\pi$-dQSL, 0-oQSL, and 0-dQSL phases, respectively. As is the case for diagonal pseudospin correlation, the classical calculations demonstrate that the $\pi$- and 0-flux oQSLs display distinct behaviours in the neutron scattering structure factor, and thus they are distinguishable in the experiment. However, on a classical level, it is almost impossible to identify the difference between the $\pi$- and 0-flux dQSLs; although, their pseudospin correlation is completely different. Moreover, considering the experimental resolution, we expect that it is difficult to differentiate them against the $\pi$-oQSL phase. This is because the main differences in the pseudospin correlation of these phases are found in $\tilde{S}^{xx}$ and $\tilde{S}^{yy}$, which do not couple to neutron spins. Thus, neutron scattering signals for the $\pi$-oQSL, $\pi$-dQSL, and 0-oQSL phases resemble one another. This situation is partially solved by examining the quantum ED results. The $\pi$-oQSL phase exhibits a similar rod-like distribution to the classical result; however, we find intensity peaks at the X points of the Brillouin zone ($\boldsymbol{q} = (0, 0, \pm 2\pi)$), which was not found in the classical calculation. Therefore, we can conclude that the rod-like neutron scattering behaviour and the particularly high intensity at the X points are important properties of the $\pi$-oQSL phase. Meanwhile, the $\pi$-dQSL and 0-dQSL phases exhibit somewhat different behaviours from the $\pi$-oQSL phase. Although the remnants of rod-like behaviour are still captured in the ED results, they are divided into high-intensity and low-intensity regions. In other words, the difference in scattering intensity becomes conspicuous in the quantum calculation. Points with strong scattering intensities are concentrated at the $\Gamma$ points, and peak behaviours cannot be found at the X points. This fact enables us to distinguish the $\pi$-oQSL phase from $\pi$- and 0-dQSLs. Unfortunately, it is difficult to distinguish between the $\pi$- and 0-dQSL phases because of their similar neutron scattering intensity distributions. We will see that the limitation of these ordinary experiments (neutron scattering measurement) can be resolved by introducing a novel experimental probe, the magnetostriction measurement, in the latter half of this chapter.

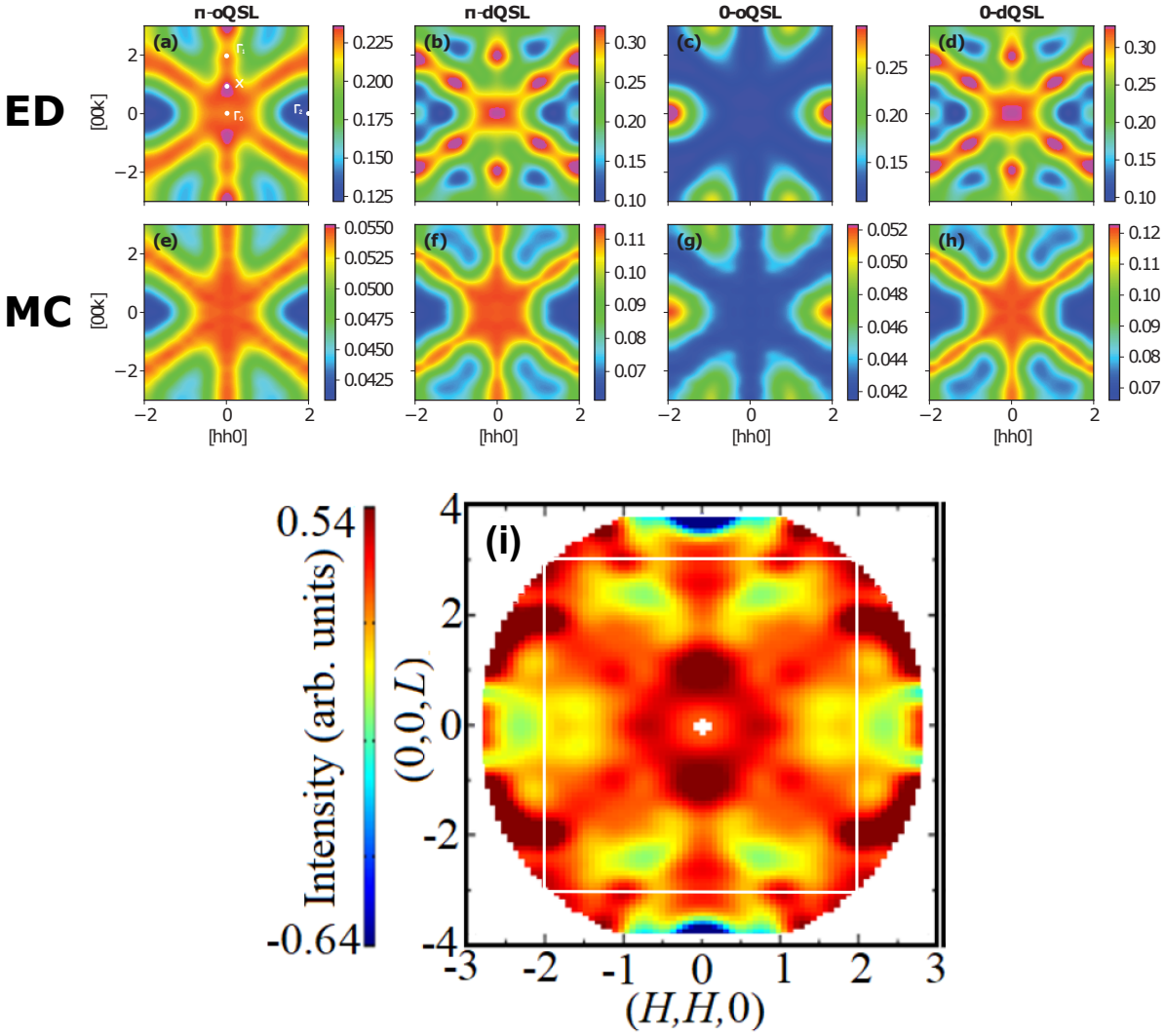


Figure 3.8. Neutron structure factor of four distinct spin ices obtained from (a–d): the exact diagonalisation and (e–h): the classical Monte Carlo calculation. In the ED results, particularly high intensity regions are depicted by the purple-shaded regions. The experimental data shows the subtraction of scattering intensity at $T = 2$ K from that at $T = 60$ mK, with an integration in energy transfer $E = [0, 0.15]$ meV [111]. The white square represents the region in which the corresponding theoretical results are provided. Rod-like behaviours along the [001], [111], and [11$\bar{1}$] directions with a strong scattering intensity are observed in the $\pi$-oQSL, $\pi$-dQSL, 0-oQSL phases, and the experiment. Among them, the quantum (ED) result for the $\pi$-oQSL is in good agreement with the experiment because a particularly strong scattering intensity is identified at the X points ($\boldsymbol{q} = (0, 0, \pm 2\pi)$).

For completeness, Fig. 3.9 shows the $\boldsymbol{q}$-map of the neutron scattering structure factors of the ordered phases. As expected from the local pseudospin correlation results, distinct behaviours can be found for each ordered phase. We note that the discrepancy in the

results for the X-AIAO phase is due to the inconsistency in the local spin correlations. If we assume the ED results are what is actually observed, these results suggest that neutron scattering measurement can be utilised to identify the type of AIAO state . For example, in $Nd_2Zr_2O_7$, which has an AIAO order below $T_N \sim 0.4$ K [117, 125], a strong sharp neutron scattering intensity is observed at $\Gamma_2 = (4\pi, 4\pi, 0)$ [126]. This scattering structure is unique to the Z-AIAO phase, and we can conclude that the all-in all-out configuration is constituted by usual dipolar moments.

Finally, let us compare the theoretical results to recent neutron scattering measurements on $Ce_2Zr_2O_7$, which is a candidate material of QSLs. Figure 3.8(i) shows the subtraction of the scattering intensity at $T = 2$ K from that at $T = 60$ mK, with an integration in energy transfer $E = [0, 0.15]$ meV [111]. The rod-like intensity distribution and peak structures can be found at the X points, which indicates that the $\pi$-oQSL phase is realised in this system. For the quantum calculation, Fig. 3.8(a) effectively describes the experimental result, including the peak structures. Quantum spin ice composed of multipoles had not yet been identified; this identification of *multipolar quantum spin ice* is the main result of the first half of this chapter.

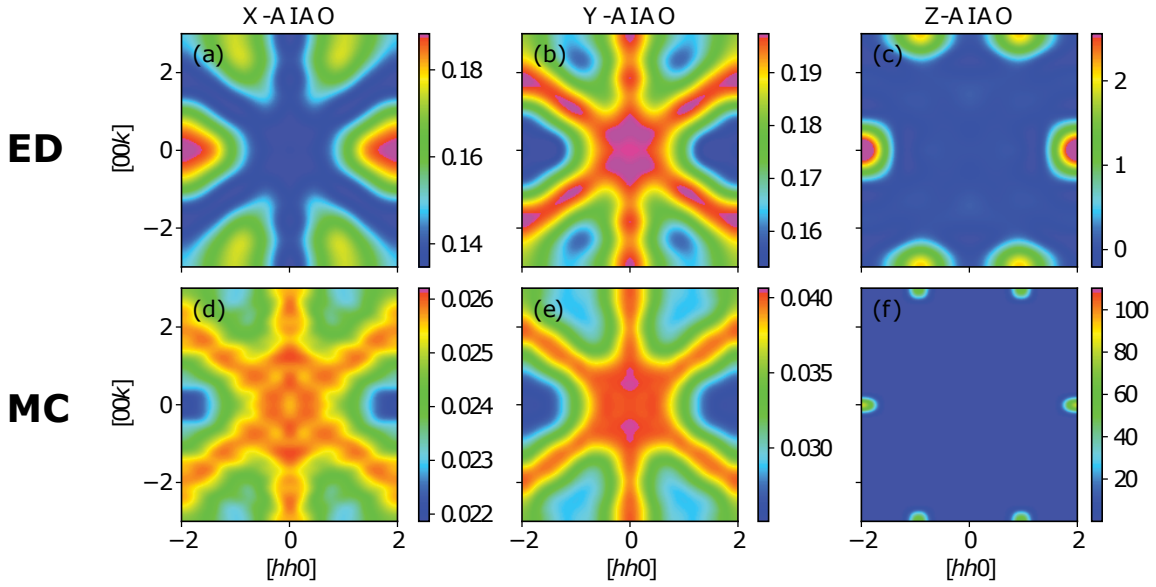


Figure 3.9. Neutron structure factor of three ordered phases (X-, Y-, and Z-AIAO phases) obtained from (a–c): the exact diagonalisation on the 32-site cluster and (d–f): the classical Monte Carlo calculation.

### 3.3.3 Dynamic properties of each QSL

To capture the dynamic properties of the system, the following dynamic structure factors represented in the local coordinate frame are calculated:

$$S(\boldsymbol{q},\omega) = \frac{1}{2\pi N}\sum_{i,j}\int_{-\infty}^{\infty} dt \left[\hat{z}_i \cdot \hat{z}_j - \frac{(\hat{z}_i \cdot \boldsymbol{q})(\hat{z}_j \cdot \boldsymbol{q})}{q^2}\right] e^{-\mathrm{i}\boldsymbol{q}\cdot(\boldsymbol{R}_i - \boldsymbol{R}_j)+\mathrm{i}\omega t}\langle \tau_i^z(t)\tau_j^z(0)\rangle. \quad (3.17)$$

Before moving on to the results, we should first provide the method to calculate them.

### Molecular dynamics

To examine the classical limit, finite temperature Monte Carlo (MC) techniques have been employed to obtain the spin correlations [127, 128]. Firstly, a combination of simulated annealing and parallel tempering for $5 \times 10^6$ MC sweeps has been used. Fixing the magnitude of the classical pseudospins $\boldsymbol{\tau} = (\tau^x, \tau^y, \tau^z)$ to be $\tau = 1/2$, we have allowed the system to thermalize to a temperature of $T = 0.06|\tilde{J}|$, where $\tilde{J} = \tilde{J}_y$ in the octupolar case, and $\tilde{J} = \tilde{J}_x$ in the dipolar case. Then, another $10^6$ MC sweeps have been performed with measurements recorded every 10 steps.

Now, the method of classical Molecular Dynamics (MD) is used to capture the dynamics of these systems. The spins are evolved according to the semi-classical Landau-Lifshitz-Gilbert equations of motion [129],

$$\frac{d}{dt}\boldsymbol{\tau}_i = -\boldsymbol{\tau}_i \times \frac{\partial H}{\partial \boldsymbol{\tau}_i}, \tag{3.18}$$

and we allow the system to evolve for a long but finite time of $t = 60/|\tilde{J}|$, with step sizes of $\delta t = 0.05/|\tilde{J}|$ to obtain $\tau_i^\mu(t)\tau_j^\nu(0)$. This process is repeated for every measurement from the MC simulations, and the results are averaged over to yield $\langle \tau_i^\mu(t)\tau_j^\nu(0)\rangle$. Finally, we numerically integrate over these time-evolved spins to obtain the energy- and momentum-dependent dynamical structure factors. In order to more accurately compare the classical-quantum correspondence in the spin dynamics, our classical MD results are re-scaled by a factor of $\beta\omega$ [127].

### Dynamical function in exact diagonalisation

Here, we limit our discussion within zero temperature. First, we start from defining two operators: $\mathcal{A}_{\boldsymbol{q}}^\mu = N^{-1/2}\sum_i e^{\mathrm{i}\boldsymbol{q}\cdot\boldsymbol{R}_i}\hat{z}_i^\mu\tau_i^z$ and $\mathcal{B}_{\boldsymbol{q}} = N^{-1/2}\sum_i e^{\mathrm{i}\boldsymbol{q}\cdot\boldsymbol{R}_i}(\hat{z}_i\cdot\boldsymbol{q}/q)\tau_i^z$. Then, Eq. (3.17) is rewritten as

$$S(\boldsymbol{q},\omega) = \frac{1}{2\pi}\int_{-\infty}^{\infty} e^{\mathrm{i}\omega t}(\langle \mathcal{A}_{\boldsymbol{q}}^{\mu\dagger}(t)\mathcal{A}_{\boldsymbol{q}}^\mu(0)\rangle - \langle \mathcal{B}_{\boldsymbol{q}}^\dagger(t)\mathcal{B}_{\boldsymbol{q}}(0)\rangle), \tag{3.19}$$

where the summation is taken over $\mu = x, y, z$. It is known from linear response theory that the correlation function $C(\boldsymbol{q},\omega) = \frac{1}{2\pi}\int_{-\infty}^{\infty} e^{\mathrm{i}\omega t}\langle \hat{A}^\dagger(t)\hat{B}(0)\rangle$ and retarded Green's function $G_{AB}^R(\boldsymbol{q},\omega) = \sum_n \frac{\langle 0|\hat{A}^\dagger|n\rangle\langle n|\hat{B}|0\rangle}{\omega+\mathrm{i}\delta-E_n} = \langle 0|\hat{A}^\dagger\frac{1}{\omega+\mathrm{i}\delta-H}\hat{B}|0\rangle$ are related via the fluctuation-dissipation theorem as

$$C(\boldsymbol{q},\omega) = -2\mathrm{Im}G_{AB}^R(\boldsymbol{q},\omega). \tag{3.20}$$

Therefore, the final form of the dynamic structure factor is

$$S(\boldsymbol{q},\omega) = -\frac{1}{\pi}\mathrm{Im}\left[-\langle\Phi_0|\mathcal{B}_{\boldsymbol{q}}^\dagger\frac{1}{\omega+\mathrm{i}\delta-H}\mathcal{B}_{\boldsymbol{q}}|\Phi_0\rangle + \sum_\mu\langle\Phi_0|\mathcal{A}_{\boldsymbol{q}}^{\mu\dagger}\frac{1}{\omega+\mathrm{i}\delta-H}\mathcal{A}_{\boldsymbol{q}}^\mu|\Phi_0\rangle\right], \tag{3.21}$$

where $|\Phi_0\rangle$ is the ED ground state. This result indicates that the dynamical structure factor is obtained by employing the Lanczos algorithm initialised with the excited states $\mathcal{A}^{\mu}_{\boldsymbol{q}}|\Phi_0\rangle$ and $\mathcal{B}_{\boldsymbol{q}}|\Phi_0\rangle$. However, because intuitive implementation of this can cause a truncation error [130, 131], this calculation was performed using a sophisticated shifted Krylov method in a numerical library K$\omega$ with the quantum lattice model solver package H$\Phi$ [132].

The method is briefly explained below [133]. First, let us introduce the vectors

$$|\nu(z)\rangle_X = \frac{1}{z-H}X_{\boldsymbol{q}}|\Phi_0\rangle, \qquad |\mu\rangle_X = X_{\boldsymbol{q}}|\Phi_0\rangle, \tag{3.22}$$

where $X_{\boldsymbol{q}} = \mathcal{A}^{\mu}_{\boldsymbol{q}}, \mathcal{B}_{\boldsymbol{q}}$. Then,

$$S(\boldsymbol{q},\omega) = -\frac{1}{\pi}\mathrm{Im}[-\langle\mu|\nu(\omega+\mathrm{i}\delta)\rangle_B + \sum_{\mu}\langle\mu|\nu(\omega+\mathrm{i}\delta)\rangle_{A^{\mu}}]. \tag{3.23}$$

To calculate $|\nu(z)\rangle_X$, we solve the equation $(z-H)|\nu(z)\rangle_X = |\mu\rangle$. This linear equation can be solved by an iterative procedure, such as the conjugate gradient (CG) method. At each $i$-th step, the CG algorithm searches for an approximate solution $|\nu(z)\rangle_{X,i}$, which minimises the norm of the residual vector $(z-H)|\nu(z)\rangle_{X,i} - |\mu\rangle$ within a Krylov subspace, $\mathrm{span}\{|\mu\rangle, (z-H)|\mu\rangle, \ldots, (z-H)^{n-1}|\mu\rangle\}$. Owing to the shift invariance in the Krylov subspace, we can obtain $|\nu(z')\rangle$ from $|\nu(z)\rangle$ with the complexity of $\mathcal{O}(N^0)$, where $N$ is the dimension of the Hamiltonian. This invariance gave the shifted Krylov method its name and enables us to calculate $|\nu(\omega+\mathrm{i}\delta)\rangle$ for various $\omega$ with reasonable computational resources. In the following calculations, we use $\delta = 0.05$ and the number of iterations $N = 1000$.

### Results and discussion

Figure 3.10 presents the dynamical structure factors of four distinct spin ices along the [001] direction obtained from the ED and classical Monte Carlo calculations. In the ED results, only the accessible momentum points, namely the $\Gamma_0$, X, and $\Gamma_1$ points, are depicted.

As shown in Figs. 3.10(a) and (e), the $\pi$-oQSL phase displays a gapped excitation spectrum with the gap $\Delta/J_y \sim 0.6$. The classical result (Fig. 3.10(e)) does not show the momentum dependence of the excitation spectrum, whereas the quantum result (Fig. 3.10(a)) clearly presents a strong intensity at the X point, as is expected from the equal-time neutron structure factor provided in the previous section. The gapped nature is consistent with the prediction in Table 2.1. In octupolar quantum spin ices, the gauge photon cannot be captured by the neutron's moment due to the inherent octupolar nature. Thus, gapless gauge photon excitation is invisible, and only gapped spinon excitations are observed.

In contrast with the $\pi$-oQSL phase, (nearly) gapless excitation spectra are observed in the $\pi$-dQSL phase, as shown in Figs. 3.10(b) and (f). We expect that the tiny gap in the ED result stems from a finite size effect, and the gap becomes smaller as the system size increases. In fact, the result of the classical calculation, which was performed on a lattice

with 2048 sites, supports this prediction. Moreover, we find the intensity is strong at the Γ points. We can attribute the gapless excitation signature to gauge photon excitation of the $U(1)$ QSL; however, further theoretical and experimental research is required to determine this $U(1)$ nature.

The classical and quantum results show a discrepancy for the 0-oQSL, as shown in Figs. 3.10(c) and (g), despite the fact that they both possess a gapped excitation unique to octupolar spin ices. The excitation gap of the ED result is $\Delta/J_y \sim 1.0$, whereas that of the classical result is $\Delta/J_y \sim 0.6$. The reason for this difference is not clear; however, it indicates the failure of classical calculations in differentiating flux configurations. Thus, we expect the excitation energy of the magnetic gauge charges to differ depending on the ground state flux configuration.

Lastly, Figs. 3.10(d) and (h) present the dynamic structure factor results of the 0-dQSL phase. As well as the π-dQSL, the gapless excitation spectrum is captured, which is attributed to the gauge charge degree of freedom. The band-like spectrum obtained in the classical result shown in Fig. 3.10(h) is a unique signature of this phase. However, this discreteness is concealed in the quantum calculation, and thus it is undetectable in real experiments. Therefore, it will be difficult to distinguish between the flux configurations of dipolar quantum spin ices when examining the excitation spectra as well as the static properties. This limitation of neutron scattering is partially resolved by introducing a novel experimental probe, magnetostriction, which will be described in the subsequent sections.

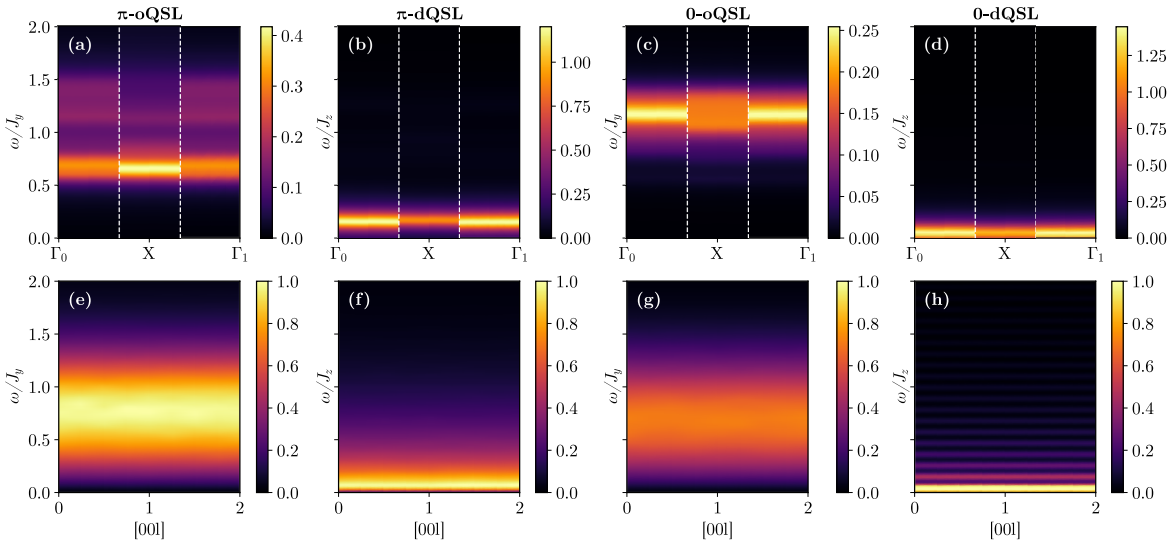


Figure 3.10. Dynamical structure factor of four distinct spin ices along the [001] direction obtained from (a–d): exact diagonalisation and (e–h): classical Monte Carlo calculation. In the ED results, only the accessible momentum points, namely the $\Gamma_0$, X, and $\Gamma_1$ points, are displayed.

## 3.4 Novel probes for QSLs in the dipolar-octupolar system

So far, the responses of each spin liquid phase to basic experiments has been investigated. However, these are not sufficient to completely identify the type of spin liquid. Therefore, it becomes necessary to discover the unique characteristics of each spin liquid using further experiments. Here, we extend our theory of magnetostriction, which has been proven to be a powerful tool to detect a quantum spin liquid phase in a non-Kramers case (Section 2.1.1), to the present dipolar-octupolar system. Detailed explanations for magnetostriction are provided in this section, and results for the non-Kramers and usual Kramers cases, which are not the main topics of this thesis, are summarised in Appendix A.

### 3.4.1 Symmetry-allowed pseudospin-strain couplings

#### Elastic energy

Before discussing these couplings, the symmetry-constrained elastic energy is considered. As explained in Section 3.2, the pyrochlore lattice hosts a symmetry with a point group $O_h$. This cubic nature of the underlying Bravais lattice constrains the elastic energy to

$$\mathcal{F}_{\text{lattice}} = \frac{c_B}{2}\epsilon_B^2 + \frac{c_{11}-c_{12}}{2}\left(\epsilon_\mu^2+\epsilon_\nu^2\right) + \frac{c_{44}}{2}\left(\epsilon_{xy}^2+\epsilon_{yz}^2+\epsilon_{zx}^2\right). \tag{3.24}$$

Here, the crystal deformation is described by the components of the strain tensor in the global coordinate frame $\epsilon_{ij}$, and $c_{ij}$ is the elastic modulus tensor describing the stiffness of the crystal. $c_B$ is defined as the bulk modulus, $\epsilon_B \equiv \epsilon_{xx}+\epsilon_{yy}+\epsilon_{zz}$ is the volume expansion of the crystal, and $\epsilon_\mu \equiv \epsilon_{xx}-\epsilon_{yy}$ and $\epsilon_\nu \equiv (2\epsilon_{zz}-\epsilon_{xx}-\epsilon_{yy})/\sqrt{3}$ are the cubic normal mode lattice strains.

#### Notations and symmetries

Since we will consider elastic strain tensors, magnetic fields, and local moments on each sublattice, we specify the notation here to clearly identify in which sublattice basis we are considering each quantity,

$$\tau^\alpha_{x,y,z}, \quad h^\alpha_{x,y,z}, \quad \epsilon^\alpha_{ij}, \tag{3.25}$$

where $i,j = x,y,z$ are the usual components of the cubic strain tensor, and $\alpha = 0,1,2,3$ refers to the sublattice index. Here, $\tau^\alpha_{x,y,z}$, $h^\alpha_{x,y,z}$, and $\epsilon^\alpha_{ij}$ denote the local pseudospin-1/2 moment (i.e. local coordinate frame), magnetic field component and the elastic strain tensor component in the sublattice $\alpha$ basis, respectively. We can also define the same quantities in the global coordinate frame $\{(1,0,0),(0,1,0),(0,0,1)\}$ as $\tau_{x,y,z}, h_{x,y,z}$ and $\epsilon_{ij}$, i.e. without the sublattice superscript.

Next, the transformation of the relevant quantities from the local coordinate frame to the global axes is presented. The vector-like quantities, such as the magnetic field and pseudospins, are transformed using $\boldsymbol{h}^\alpha = \mathcal{P}_\alpha^{-1}\boldsymbol{h}$ and $\boldsymbol{\tau}^\alpha = \mathcal{P}_\alpha^{-1}\boldsymbol{\tau}$, and the tensor-strain is transformed using $\overleftrightarrow{\epsilon}^\alpha = \mathcal{P}_\alpha^{-1}\overleftrightarrow{\epsilon}\mathcal{P}_\alpha$. Here, $\mathcal{P}_\alpha$ is the matrix for sublattice–$\alpha$ to

change the basis, that is, its columns contain the basis vectors of the given sublattice, as denoted in Table 3.1. As an example, the local-to-global magnetic field transformations are presented below (transformations of the strain components are more complex and struggle to fit on the page).

$$\begin{aligned}
\begin{pmatrix} h_x^{(0)} \\ h_y^{(0)} \\ h_z^{(0)} \end{pmatrix} &= \begin{pmatrix} \frac{-2h_x+h_y+h_z}{\sqrt{6}} \\ \frac{h_z-h_y}{\sqrt{2}} \\ \frac{h_x+h_y+h_z}{\sqrt{3}} \end{pmatrix} \qquad \begin{pmatrix} h_x^{(1)} \\ h_y^{(1)} \\ h_z^{(1)} \end{pmatrix} = \begin{pmatrix} -\frac{2h_x+h_y+h_z}{\sqrt{6}} \\ \frac{h_y-h_z}{\sqrt{2}} \\ \frac{h_x-h_y-h_z}{\sqrt{3}} \end{pmatrix} \\
\begin{pmatrix} h_x^{(2)} \\ h_y^{(2)} \\ h_z^{(2)} \end{pmatrix} &= \begin{pmatrix} \frac{2h_x+h_y-h_z}{\sqrt{6}} \\ -\frac{h_y+h_z}{\sqrt{2}} \\ -\frac{h_x-h_y+h_z}{\sqrt{3}} \end{pmatrix} \qquad \begin{pmatrix} h_x^{(3)} \\ h_y^{(3)} \\ h_z^{(3)} \end{pmatrix} = \begin{pmatrix} \frac{2h_x-h_y+h_z}{\sqrt{6}} \\ \frac{h_y+h_z}{\sqrt{2}} \\ -\frac{h_x+h_y-h_z}{\sqrt{3}} \end{pmatrix}
\end{aligned} \tag{3.26}$$

Recall that $h_{x,y,z}$ are magnetic field components in the global coordinate frame.

As the third step, we consider the local symmetry of rare-earth ions. Although the point group symmetry of the overall lattice is $O_h$, the local point group symmetry of the rare-earth site is described by the $D_{3d}$ point group. It can be generated by the following two symmetry operators written in an orthonormal basis ($\mathbb{R}^3$ basis):

$$S_6^- = \begin{pmatrix} 1/\sqrt{2} & \sqrt{3}/2 & 0 \\ -\sqrt{3}/2 & 1/2 & 0 \\ 0 & 0 & -1 \end{pmatrix}, \quad C_{21}' = \begin{pmatrix} -1 & 0 & 0 \\ 0 & 1 & 0 \\ 0 & 0 & -1 \end{pmatrix}, \tag{3.27}$$

where $S_6^-$ is an improper rotation about the $z$-axis by $\pi/3$, and $C_{21}'$ is a $\pi$ rotation about the $y$-axis. Using these generators, we can transform the pseudospin-1/2 quantities as follows:

$$\begin{aligned}
\tau_x^\alpha &\xrightarrow{S_6^-} \tau_x^\alpha & \tau_x^\alpha &\xrightarrow{C_{21}'} -\tau_x^\alpha \\
\tau_y^\alpha &\xrightarrow{S_6^-} \tau_y^\alpha & \tau_y^\alpha &\xrightarrow{C_{21}'} \tau_y^\alpha \\
\tau_z^\alpha &\xrightarrow{S_6^-} \tau_z^\alpha & \tau_z^\alpha &\xrightarrow{C_{21}'} -\tau_z^\alpha
\end{aligned} \tag{3.28}$$

$$\begin{aligned}
h_x^\alpha &\xrightarrow{S_6^-} -\frac{1}{2}h_x^\alpha - \frac{\sqrt{3}}{2}h_y^\alpha & h_x^\alpha &\xrightarrow{C_{21}'} h_x^\alpha \\
h_y^\alpha &\xrightarrow{S_6^-} \frac{\sqrt{3}}{2}h_x^\alpha - \frac{1}{2}h_y^\alpha & h_y^\alpha &\xrightarrow{C_{21}'} -h_y^\alpha \\
h_z^\alpha &\xrightarrow{S_6^-} h_z^\alpha & h_z^\alpha &\xrightarrow{C_{21}'} -h_z^\alpha.
\end{aligned} \tag{3.29}$$

Note that the inversion operator included in $S_6^-$ behaves as an identical operator for pseudovectors, such as spins and magnetic fields. Finally, the elastic tensor transforms in the usual manner, that is, $\overleftrightarrow{\epsilon}^\alpha \to A\overleftrightarrow{\epsilon}^\alpha A^T$, where $A$ is the symmetry element.

### Octupolar-strain couplings

First, we consider the coupling between the octupolar component $\tau_y$ and strains. Owing to the time reversal odd nature of the octupolar moment, they cannot directly

couple to the strains. However, in the presence of magnetic fields, field-assisted strain-moment couplings are possible. Their general form can be expressed as

$$\mathcal{F}^{\alpha}_{\text{octupolar}-\text{strain}} = \sum_{\mu=x,y,z} \sum_{\nu,\gamma=x,y,z} \mathcal{C}_{\mu\nu\gamma} \tau^{\alpha}_{y} h^{\alpha}_{\mu} \epsilon^{\alpha}_{\nu\gamma}, \tag{3.30}$$

where $\mathcal{C}_{\mu\nu\gamma}$ are the phenomenological coupling constants. Considering the above point group symmetry, terms that are invariant under the symmetry operators $S_6^-$ and $C'_{21}$ remain. Thus, $D_{3d}$ symmetry-constrained octupolar-strain coupling is described as

$$\mathcal{F}^{\alpha}_{\text{octupolar}-\text{strain}} = \tau^{\alpha}_{y} \left[ \mathcal{C}_0 \left( 2h^{\alpha}_{x} \epsilon^{\alpha}_{xy} + h^{\alpha}_{y} (\epsilon^{\alpha}_{xx} - \epsilon^{\alpha}_{yy}) \right) + \mathcal{C}_1 \left( h^{\alpha}_{y} \epsilon^{\alpha}_{xz} - h^{\alpha}_{x} \epsilon^{\alpha}_{yz} \right) \right], \tag{3.31}$$

where Einstein summation notation is introduced for the sublattice index $\alpha = 0, 1, 2, 3$, and $\mathcal{C}_{0,1}$ are phenomenological coupling constants, which are independent of the choice in sublattice (as each sublattice is physically equivalent to the others, the only difference is that they are rotated with respect to each other). Combining all sublattices, we obtain

$$\mathcal{F}_{\text{octupolar}-\text{strain}} = \mathcal{F}_{\text{octupolar}-\text{strain},\mathcal{C}_0} + \mathcal{F}_{\text{octupolar}-\text{strain},\mathcal{C}_1} \tag{3.32}$$

and

$$\begin{aligned}
\mathcal{F}_{\text{octupolar}-\text{strain},\mathcal{C}_0} = \mathcal{C}'_0 \{ & [(2\epsilon_{xy} - 2\epsilon_{zx} - \epsilon_{yy} + \epsilon_{zz}) h_x + (2\epsilon_{yz} - 2\epsilon_{xy} - \epsilon_{zz} + \epsilon_{xx}) h_y \\
& + (2\epsilon_{zx} - 2\epsilon_{yz} - \epsilon_{xx} + \epsilon_{yy}) h_z] \tau^{(0)}_{y} \\
& + [(-2\epsilon_{xy} + 2\epsilon_{zx} - \epsilon_{yy} + \epsilon_{zz}) h_x + (-2\epsilon_{yz} - 2\epsilon_{xy} + \epsilon_{zz} - \epsilon_{xx}) h_y \\
& + (2\epsilon_{zx} + 2\epsilon_{yz} + \epsilon_{xx} - \epsilon_{yy}) h_z] \tau^{(1)}_{y} \\
& + [(2\epsilon_{xy} + 2\epsilon_{zx} + \epsilon_{yy} - \epsilon_{zz}) h_x + (-2\epsilon_{yz} + 2\epsilon_{xy} - \epsilon_{zz} + \epsilon_{xx}) h_y \\
& + (-2\epsilon_{zx} - 2\epsilon_{yz} + \epsilon_{xx} - \epsilon_{yy}) h_z] \tau^{(2)}_{y} \\
& + [(-2\epsilon_{xy} - 2\epsilon_{zx} + \epsilon_{yy} - \epsilon_{zz}) h_x + (2\epsilon_{yz} + 2\epsilon_{xy} + \epsilon_{zz} - \epsilon_{xx}) h_y \\
& + (-2\epsilon_{zx} + 2\epsilon_{yz} - \epsilon_{xx} + \epsilon_{yy}) h_z] \tau^{(3)}_{y} \},
\end{aligned} \tag{3.33}$$

$$\begin{aligned}
\mathcal{F}_{\text{octupolar}-\text{strain},\mathcal{C}_1} = \mathcal{C}'_1 \{ & [(\epsilon_{xy} - \epsilon_{zx} + \epsilon_{yy} - \epsilon_{zz}) h_x + (\epsilon_{yz} - \epsilon_{xy} + \epsilon_{zz} - \epsilon_{xx}) h_y \\
& + (\epsilon_{zx} - \epsilon_{yz} + \epsilon_{xx} - \epsilon_{yy}) h_z] \tau^{(0)}_{y} \\
& + [(-\epsilon_{xy} + \epsilon_{zx} + \epsilon_{yy} - \epsilon_{zz}) h_x + (-\epsilon_{yz} - \epsilon_{xy} - \epsilon_{zz} + \epsilon_{xx}) h_y \\
& + (\epsilon_{zx} + \epsilon_{yz} - \epsilon_{xx} + \epsilon_{yy}) h_z] \tau^{(1)}_{y} \\
& + [(\epsilon_{xy} + \epsilon_{zx} - \epsilon_{yy} + \epsilon_{zz}) h_x + (-\epsilon_{yz} + \epsilon_{xy} + \epsilon_{zz} - \epsilon_{xx}) h_y \\
& + (-\epsilon_{zx} - \epsilon_{yz} - \epsilon_{xx} + \epsilon_{yy}) h_z] \tau^{(2)}_{y} \\
& + [(-\epsilon_{xy} - \epsilon_{zx} - \epsilon_{yy} + \epsilon_{zz}) h_x + (\epsilon_{yz} + \epsilon_{xy} - \epsilon_{zz} + \epsilon_{xx}) h_y \\
& + (-\epsilon_{zx} + \epsilon_{yz} + \epsilon_{xx} - \epsilon_{yy}) h_z] \tau^{(3)}_{y} \},
\end{aligned} \tag{3.34}$$

where $\mathcal{C}'_0 = \sqrt{2}\mathcal{C}_0/3$, $\mathcal{C}'_1 = \mathcal{C}_1/3$, and all physical quantities except for pseudospins are represented in a global coordinate frame using the transformation described above.

### Dipolar-strain couplings

A similar analysis is also applicable to dipolar-strain couplings. Because $\tau_x$ and $\tau_z$ are symmetrically equivalent, it is sufficient to only consider the coupling between $\tau_x$ and stains. Again, the general coupling form is represented as

$$\mathcal{F}^{\alpha}_{\text{dipolar}-\text{strain}} = \sum_{\mu=x,y,z} \sum_{\nu,\gamma=x,y,z} \mathcal{C}_{ijk} \tau^{\alpha}_{x} h^{\alpha}_{\mu} \epsilon^{\alpha}_{\nu\gamma}, \tag{3.35}$$

and $D_{3d}$ symmetry-constrained dipolar-strain coupling is described as

$$\begin{aligned} \mathcal{F}^{\alpha}_{\text{dipolar}-\text{strain}} = \tau^{\alpha}_{x} \big[ \mathcal{C}_{2x} \left( h^{\alpha}_{x} (\epsilon^{\alpha}_{yy} - \epsilon^{\alpha}_{zz}) + 2 h^{\alpha}_{y} \epsilon^{\alpha}_{xy} \right) + \mathcal{C}_{3x} \left( h^{\alpha}_{x} \epsilon^{\alpha}_{xz} + h^{\alpha}_{y} \epsilon^{\alpha}_{yz} \right) \\ + \mathcal{C}_{4x} h^{\alpha}_{z} \left( \epsilon^{\alpha}_{xx} + \epsilon^{\alpha}_{yy} \right) + \mathcal{C}_{5x} h^{\alpha}_{z} \epsilon^{\alpha}_{zz} \big], \end{aligned} \tag{3.36}$$

where the summation is taken over $\alpha$, and $\mathcal{C}_{2x,3x,4x,5x}$ are phenomenological coupling constants independent of the sublattice indices. Taking the summation over the sublattices, we obtain

$$\begin{aligned} \mathcal{F}^{x}_{\text{dipolar}-\text{strain}} = \mathcal{F}^{x}_{\text{dipolar}-\text{strain},\mathcal{C}_{2x}} + \mathcal{F}^{x}_{\text{dipolar}-\text{strain},\mathcal{C}_{3x}} \\ + \mathcal{F}^{x}_{\text{dipolar}-\text{strain},\mathcal{C}_{4x}} + \mathcal{F}^{x}_{\text{dipolar}-\text{strain},\mathcal{C}_{5x}}. \end{aligned} \tag{3.37}$$

The explicit forms of each term are listed below.

$$\begin{aligned} \mathcal{F}_{\text{dipolar}-\text{strain},\mathcal{C}_{2x}} = \mathcal{C}'_{2x} \{ & [(-2\epsilon_{xx} + \epsilon_{yy} + \epsilon_{zz} + 2(\epsilon_{xy} - 2\epsilon_{yz} + \epsilon_{zx})) h_x \\ & + (\epsilon_{xx} - 2\epsilon_{yy} + \epsilon_{zz} + 2(\epsilon_{xy} + \epsilon_{yz} - 2\epsilon_{zx})) h_y \\ & + (\epsilon_{xx} + \epsilon_{yy} - 2\epsilon_{zz} - 2(2\epsilon_{xy} - \epsilon_{yz} - \epsilon_{zx})) h_z ] \tau^{(0)}_{x} \\ & [(-2\epsilon_{xx} + \epsilon_{yy} + \epsilon_{zz} - 2(\epsilon_{xy} + 2\epsilon_{yz} + \epsilon_{zx})) h_x \\ & + (-\epsilon_{xx} + 2\epsilon_{yy} - \epsilon_{zz} + 2(\epsilon_{xy} - \epsilon_{yz} - 2\epsilon_{zx})) h_y \\ & + (-\epsilon_{xx} - \epsilon_{yy} + 2\epsilon_{zz} - 2(2\epsilon_{xy} + \epsilon_{yz} - \epsilon_{zx})) h_z ] \tau^{(1)}_{x} \\ & [(2\epsilon_{xx} - \epsilon_{yy} - \epsilon_{zz} + 2(\epsilon_{xy} - 2\epsilon_{yz} - \epsilon_{zx})) h_x \\ & + (\epsilon_{xx} - 2\epsilon_{yy} + \epsilon_{zz} - 2(\epsilon_{xy} + \epsilon_{yz} + 2\epsilon_{zx})) h_y \\ & + (-\epsilon_{xx} - \epsilon_{yy} + 2\epsilon_{zz} - 2(2\epsilon_{xy} - \epsilon_{yz} + \epsilon_{zx})) h_z ] \tau^{(2)}_{x} \\ & [(2\epsilon_{xx} - \epsilon_{yy} - \epsilon_{zz} - 2(\epsilon_{xy} + 2\epsilon_{yz} - \epsilon_{zx})) h_x \\ & + (\epsilon_{xx} + 2\epsilon_{yy} - \epsilon_{zz} - 2(\epsilon_{xy} - \epsilon_{yz} + 2\epsilon_{zx})) h_y \\ & + (\epsilon_{xx} + \epsilon_{yy} - 2\epsilon_{zz} - 2(2\epsilon_{xy} + \epsilon_{yz} + \epsilon_{zx})) h_z ] \tau^{(3)}_{x} \} \end{aligned} \tag{3.38}$$

$$\begin{aligned}\mathcal{F}_{\text{dipolar}-\text{strain},\mathcal{C}_{3x}} = \mathcal{C}'_{3x}\{&[(2\epsilon_{xx}-\epsilon_{yy}-\epsilon_{zz}+\epsilon_{xy}-2\epsilon_{yz}+\epsilon_{zx})h_x\\ &+(-\epsilon_{xx}+2\epsilon_{yy}-\epsilon_{zz}+\epsilon_{xy}+\epsilon_{yz}-2\epsilon_{zx})h_y\\ &+(-\epsilon_{xx}-\epsilon_{yy}+2\epsilon_{zz}-2\epsilon_{xy}+\epsilon_{yz}+\epsilon_{zx})h_z]\tau_x^{(0)}\\ &[(2\epsilon_{xx}-\epsilon_{yy}-\epsilon_{zz}-\epsilon_{xy}-2\epsilon_{yz}-\epsilon_{zx})h_x\\ &+(\epsilon_{xx}-2\epsilon_{yy}+\epsilon_{zz}+\epsilon_{xy}-\epsilon_{yz}-2\epsilon_{zx})h_y\\ &+(\epsilon_{xx}+\epsilon_{yy}-2\epsilon_{zz}-2\epsilon_{xy}-\epsilon_{yz}+\epsilon_{zx})h_z]\tau_x^{(1)}\\ &[(-2\epsilon_{xx}+\epsilon_{yy}+\epsilon_{zz}+\epsilon_{xy}-2\epsilon_{yz}-\epsilon_{zx})h_x\\ &+(-\epsilon_{xx}+2\epsilon_{yy}-\epsilon_{zz}-\epsilon_{xy}-\epsilon_{yz}-2\epsilon_{zx})h_y\\ &+(\epsilon_{xx}+\epsilon_{yy}-2\epsilon_{zz}-2\epsilon_{xy}+\epsilon_{yz}-\epsilon_{zx})h_z]\tau_x^{(2)}\\ &[(-2\epsilon_{xx}+\epsilon_{yy}+\epsilon_{zz}-\epsilon_{xy}-2\epsilon_{yz}+\epsilon_{zx})h_x\\ &+(\epsilon_{xx}-2\epsilon_{yy}+\epsilon_{zz}-\epsilon_{xy}+\epsilon_{yz}-2\epsilon_{zx})h_y\\ &+(-\epsilon_{xx}-\epsilon_{yy}+2\epsilon_{zz}-2\epsilon_{xy}-\epsilon_{yz}-\epsilon_{zx}))h_z]\tau_x^{(3)}\}\end{aligned} \tag{3.39}$$

$$\begin{aligned}\mathcal{F}_{\text{dipolar}-\text{strain},\mathcal{C}_{4x}} = \mathcal{C}'_{4x}\{&[(\epsilon_{xx}+\epsilon_{yy}+\epsilon_{zz}-\epsilon_{xy}-\epsilon_{yz}-\epsilon_{zx})(h_x+h_y+h_z)]\tau_x^{(0)}\\ &+[(\epsilon_{xx}+\epsilon_{yy}+\epsilon_{zz}+\epsilon_{xy}-\epsilon_{yz}+\epsilon_{zx})(h_x-h_y-h_z)]\tau_x^{(1)}\\ &-[(\epsilon_{xx}+\epsilon_{yy}+\epsilon_{zz}+\epsilon_{xy}+\epsilon_{yz}-\epsilon_{zx})(h_x-h_y+h_z)]\tau_x^{(2)}\\ &-[(\epsilon_{xx}+\epsilon_{yy}+\epsilon_{zz}-\epsilon_{xy}+\epsilon_{yz}+\epsilon_{zx})(h_x+h_y-h_z)]\tau_x^{(3)}\}\end{aligned} \tag{3.40}$$

$$\begin{aligned}\mathcal{F}_{\text{dipolar}-\text{strain},\mathcal{C}_{5x}} = \mathcal{C}'_{5x}\{&[(\epsilon_{xx}+\epsilon_{yy}+\epsilon_{zz}+2\epsilon_{xy}+2\epsilon_{yz}+2\epsilon_{zx})(h_x+h_y+h_z)]\tau_x^{(0)}\\ &+[(\epsilon_{xx}+\epsilon_{yy}+\epsilon_{zz}-2\epsilon_{xy}+2\epsilon_{yz}-2\epsilon_{zx})(h_x-h_y-h_z)]\tau_x^{(1)}\\ &-[(\epsilon_{xx}+\epsilon_{yy}+\epsilon_{zz}-2\epsilon_{xy}-2\epsilon_{yz}+2\epsilon_{zx})(h_x-h_y+h_z)]\tau_x^{(2)}\\ &-[(\epsilon_{xx}+\epsilon_{yy}+\epsilon_{zz}-2\epsilon_{xy}-2\epsilon_{yz}-2\epsilon_{zx})(h_x+h_y-h_z)]\tau_x^{(3)}\}\end{aligned} \tag{3.41}$$

Here, $\mathcal{C}'_{2x} = \sqrt{6}\mathcal{C}_{2x}/9$, $\mathcal{C}'_{3x} = \sqrt{3}\mathcal{C}_{3x}/9$, $\mathcal{C}'_{4x} = 2\sqrt{3}\mathcal{C}_{4x}/9$, and $\mathcal{C}'_{5x} = \sqrt{3}\mathcal{C}_{5x}/9$. The couplings between $\tau_z$ and the strains are represented in exactly the same form, with coupling constants $\mathcal{C}_{2z,3z,4z,5z}$.

### 3.4.2 General magnetostriction expressions

Based on the above results, the total energy is represented as follows:

$$\mathcal{F}_{\text{total}} = \mathcal{F}_{\text{lattice}} + \mathcal{F}_{\text{octupolar}-\text{strain}} + \mathcal{F}^x_{\text{dipolar}-\text{strain}} + \mathcal{F}^z_{\text{dipolar}-\text{strain}}. \tag{3.42}$$

In this section, the steps to obtain general length change expressions are presented and the length change along particular cubic directions is evaluated. Before doing so, the extremised lattice normal modes ($\epsilon^*_{ij}$) are first computed using all free energy terms that involve the elastic strain tensors (Eq. (3.42)). Extremising $\mathcal{F}_{\text{total}}$ with respect to the

normal modes ($\delta\mathcal{F}_{\text{total}}/\delta\epsilon_{ij}$) yields $\epsilon^*_{ij}$. Their explicit forms are highly complex, and thus they are not shown here.

Inserting the extremised strain into the length change formula given by

$$\left(\frac{\Delta L}{L}\right)^{\hat{n}}_{\boldsymbol{\ell}} = \sum_{j,k=x,y,z} \epsilon_{jk}\hat{\ell}_j\hat{\ell}_k \tag{3.43}$$

yields the magnetostriction along a direction $\boldsymbol{\ell}$ in the presence of an external magnetic field $\boldsymbol{h} = h\hat{n}$. The complete expression for the various experimentally relevant magnetic fields and length change cubic directions are provided in Appendix B. Presented here are the magnetostriction expressions for the length change along the $\boldsymbol{\ell} = (1,1,1)$ direction under a parallel magnetic field $\hat{n} = [111]$:

$$\begin{aligned}\left(\frac{\Delta L}{L}\right)^{[111]}_{(1,1,1)} = \frac{h}{27c_B}\Big[&(\mathcal{C}_{5z} + 2\mathcal{C}_{4z})\left(3\tau_z^{(0)} - \tau_z^{(1)} - \tau_z^{(2)} - \tau_z^{(3)}\right)\\ &+ (\mathcal{C}_{5x} + 2\mathcal{C}_{4x})\left(3\tau_x^{(0)} - \tau_x^{(1)} - \tau_x^{(2)} - \tau_x^{(3)}\right)\Big]\\ + \frac{4}{27c_{44}}h\Bigg[&\left(8\sqrt{2}\mathcal{C}_{2x} - 4\mathcal{C}_{3x}\right)\left(\tau_x^{(1)} + \tau_x^{(2)} + \tau_x^{(3)}\right)\\ &+ (\mathcal{C}_{5x} - \mathcal{C}_{4x})\left(9\tau_x^{(0)} + \tau_x^{(1)} + \tau_x^{(2)} + \tau_x^{(3)}\right)\\ &+ \left(8\sqrt{2}\mathcal{C}_{2z} - 4\mathcal{C}_{3z}\right)\left(\tau_z^{(1)} + \tau_z^{(2)} + \tau_z^{(3)}\right)\\ &+ (\mathcal{C}_{5z} - \mathcal{C}_{4z})\left(9\tau_z^{(0)} + \tau_z^{(1)} + \tau_z^{(2)} + \tau_z^{(3)}\right)\Bigg]\end{aligned} . \tag{3.44}$$

### 3.4.3 Magnetostriction for 0-flux QSLs

In this section, we analyse the magnetostriction of 0-flux QSLs, namely the 0-dQSL and 0-oQSL, using the formulae obtained in the previous section. Here, the moments of each sublattice are estimated from two ways: a classical mean-field calculation and the exact diagonalisation method on the XYZh Hamiltonian Eq. (3.5). Before presenting the result, Table 3.3 shows the coupling between the external magnetic fields and pseudospin moments under the three considered magnetic field directions: [111], [110], and [001]. Note that the pure octupolar moment $\tau_y$ only couples to the magnetic field along the [110] direction. For $g$-factors in the magnetic field coupling terms, we take $g_z = 1.0$, $g_x = 0.01$, and $g_y = 4.0 \times 10^{-4}$. The diminutive nature of $g_y$ emphasises the perturbatively weak nature of the cubic-in-$h$ coupling. The tiny value of $g_x$ indicates limited mixing between the pure dipole $S_z$ and octupole $S_x$, which allows an isolated study of the dipolar-dominant and octupolar-dominant phases.

As a main result of this section, Figure 3.11 depicts the classical and magnetostriction behaviours of the two 0-flux QSLs parallel to a [111] magnetic field with their respective order parameter evolutions.

Table 3.3: Direct coupling of multipolar moments to magnetic fields along the $\boldsymbol{h} = \frac{h}{\sqrt{3}}(1,1,1)$, $\boldsymbol{h} = \frac{h}{\sqrt{2}}(1,1,0)$, and $\boldsymbol{h} = h(0,0,1)$ directions.

| | | Coupling to sublattice $\alpha$ | | | |
|---|---|---|---|---|---|
| | | 0 | 1 | 2 | 3 |
| [111] | $\tau_\alpha^y$ | 0 | 0 | 0 | 0 |
| | $\tau_\alpha^{x,z}$ | $h$ | $-h/3$ | $-h/3$ | $-h/3$ |
| [110] | $\tau_\alpha^y$ | 0 | $-h^3$ | $h^3$ | 0 |
| | $\tau_\alpha^{x,z}$ | $\sqrt{2/3}h$ | 0 | 0 | $-\sqrt{2/3}h$ |
| [001] | $\tau_\alpha^y$ | 0 | 0 | 0 | 0 |
| | $\tau_\alpha^{x,z}$ | $h/\sqrt{3}$ | $-h/\sqrt{3}$ | $-h/\sqrt{3}$ | $h/\sqrt{3}$ |

Through a comparison to magnetostriction experiments on familiar rare-earth Pr- and Ce-based heavy fermion compounds, the magnitudes of the coupling constants $\mathcal{C}_i$ are estimated. We adopt $\mathcal{C}_0 = 0.27 \times 10^{-7}, \mathcal{C}_1 = -0.8 \times 10^{-7}, \mathcal{C}_{2x} = 4.0 \times 10^{-7}, \mathcal{C}_{3x} = -8.0 \times 10^{-7}, \mathcal{C}_{4x} = 1.2 \times 10^{-6}, \mathcal{C}_{5x} = -2.6 \times 10^{-7}, \mathcal{C}_{2z} = 0.5 \times 10^{-7}, \mathcal{C}_{3z} = -0.7 \times 10^{-7}, \mathcal{C}_{4z} = 0.43 \times 10^{-7}$, and $\mathcal{C}_{5z} = 0.51 \times 10^{-7}$. The scale of the above coupling constants results in magnetostriction behaviours on the physical scale of $\Delta L/L \sim 10^{-6}$. The order of magnitude of the pseudospin-$x$ coupling terms aids in highlighting the importance of quantum fluctuations in the 0-dQSL and 0-oQSL. If these are chosen to be comparable, magnetostriction is dominated by the pseudospin-$z$ and provides a jump feature similar to what is seen in magnetostriction studies on non-Kramers pyrochlore systems under a [111] field (Section 2.1.1). Note that the elastic constants are taken as unity $c_B = c_{44} = c_{11} - c_{12} = 1.0$. The precise values of the coupling constants can be determined by employing these theoretical predictions in conjunction with future experimental measurements on Ce-based pyrochlore materials—for example, by fitting the experimentally measured length changes along the various directions and field orientations proposed later.

As seen in Figs. 3.11(a) and (b), there is a clear discrepancy between the two QSLs. The classical 0-dQSL experiences a sharply decreasing jump discontinuity at $h_a \sim 3J_z$ followed by a drop, and then a sharp kink in the length change at $h_b \sim 3.5J_z$, as seen in Fig. 3.11(a). From the quantum mechanical ED results, the 0-dQSL is in agreement with its classical result in that it displays a similar drop at approximately the same magnetic field strength. However, the magnitude of the drop is enhanced in ED compared to its classical counterpart, which indicates the importance of quantum fluctuations in enhancement of 0-dQSL magnetostriction. The underlying physics of the 0-dQSL magnetostriction behaviour can be understood in terms of a metamagnetic transition from kagome ice, that is, a classically two-in two-out configuration with sublattice 0 fixed to $+1/2$, to the fully polarised three-in one-out phase, as shown in the corresponding order parameter evolution in Fig. 3.11(c). This transition is accompanied by the brief appearance and disappearance of an island of $\langle \tau_{x,y} \rangle \neq 0$, which accounts for the aforementioned sharp nonanalytic kinks in Fig. 3.11(a) at $h_a$ and $h_b$. In the quantum model, the meta-

magnetic transition is more gradual and lacks the sharp discontinuous features of the classical island, which is expected from a finite-sized cluster. Nevertheless, this creates the (enhanced by quantum fluctuations) dip feature in the magnetostriction. Indeed, the analogous physics is responsible for the similar magnetostriction results obtained for the non-Kramers QSL in $Pr_2Zr_2O_7$ (Section 2.1.1).

In contrast, the classical 0-oQSL undergoes a monotonic (negative) increase in the length change with a single continuous kink at $h_c \sim 3J_y$, as shown in Fig. 3.11(b). The origin of the kink is the ultimate demise of pseudospin-$y$ and the completed polarisation of pseudospin-$z$, which is encouraged by the [111] magnetic field, as shown by the order parameter evolution in Fig. 3.11(d). Indeed, because the magnitude of pseudospin-$y$ diminishes with increasing field, the pseudospin-$y$ expectation values of two sublattices ($\alpha_1$ and $\alpha_2$) are positive, whereas the pseudospin-$y$ expectation values of the remaining two sublattices ($\alpha_3$ and $\alpha_4$) are negative. In other words, $\langle \tau_y^{(\alpha_1,\alpha_2)} \rangle > 0$ and $\langle \tau_y^{(\alpha_3,\alpha_4)} \rangle < 0$. This sign structure is reminiscent of the octupolar spin ice two-in, two-out degeneracy. Thus, the increasing pseudospin-$z$ in conjunction with the disappearing pseudospin-$y$ indicates a polarised dipole (pseudospin-$z$) coexisting with octupole (pseudospin-$y$) spin-ice correlations for $h < h_c$. In the magnetostriction of the quantum model, there is an overall monotonic (negative) increase in the length change that is analogous to the classical behaviour. Interestingly, as seen in Fig. 3.11(b), the classical kink at $h_c$ is smoothened out in the quantum model, which can be understood from ED order parameter evolution under the magnetic field: the transition into the fully polarised state is smoother/broadened out in the ED order parameters in Fig. 3.11(d). Moreover, nonanalytic kinks exist in the order parameter at an order of magnitude smaller than the classical $h_c$. The early locations of the ED kinks suggest the fragility of the 0-oQSL to quantum fluctuations in the presence of the field.

The key difference between the 0-dQSL and 0-oQSL is caused by the ability of the pseudospin degree of freedom responsible for forming the classical ice manifold to couple directly to the magnetic field (Table 3.3). This leads to different phases appearing in the low-field window, and subsequently, distinct magnetostriction signatures of the parent QSL phase. Despite this difference, both QSLs retain remnants of their parent classical spin ice degeneracy in the low-field window, which is reflected in particular length change directions. For completeness, Fig. 3.12 presents the classical magnetostriction behaviours under the [111] field along the (1,1,0) and (0,0,1) directions, where the retained classical degeneracy is reflected. The observed directions provide the clearest differences between the 0-dQSL and 0-oQSL phases. As shown, the degeneracy of the kagome ice regime for 0-dQSL and the dampened degeneracy of the 0-dQSL are reflected in the classical solutions. Since the [111] magnetic field does not couple to the $\tau_y$ octupolar moment, we are unable to extract the ED pseudospin-$y$ expectation values required for the $\boldsymbol{\ell} = (1,1,0), (0,0,1)$ directions; hence, only the classical solutions are presented. Once again, the 0-dQSL classically demonstrates a more dramatic peak in the magnetostriction, while the 0-oQSL classically has more kink-like features. This is the general discriminating feature between the 0-flux QSLs: the 0-oQSL possesses a gentler behaviour in its magnetostriction compared with the sharp features of the 0-dQSL. To contrast, and emphasise the uniqueness of, the length change behaviours of the QSLs, the magnetostriction of neighbouring multipolar ordered phases are also examined in the following section. Considering an array

of commonly accessible (in cubic materials) magnetic field and length change directions, these findings highlight the anisotropic (and distinct) nature of magnetostriction for the various possible ordered phases.

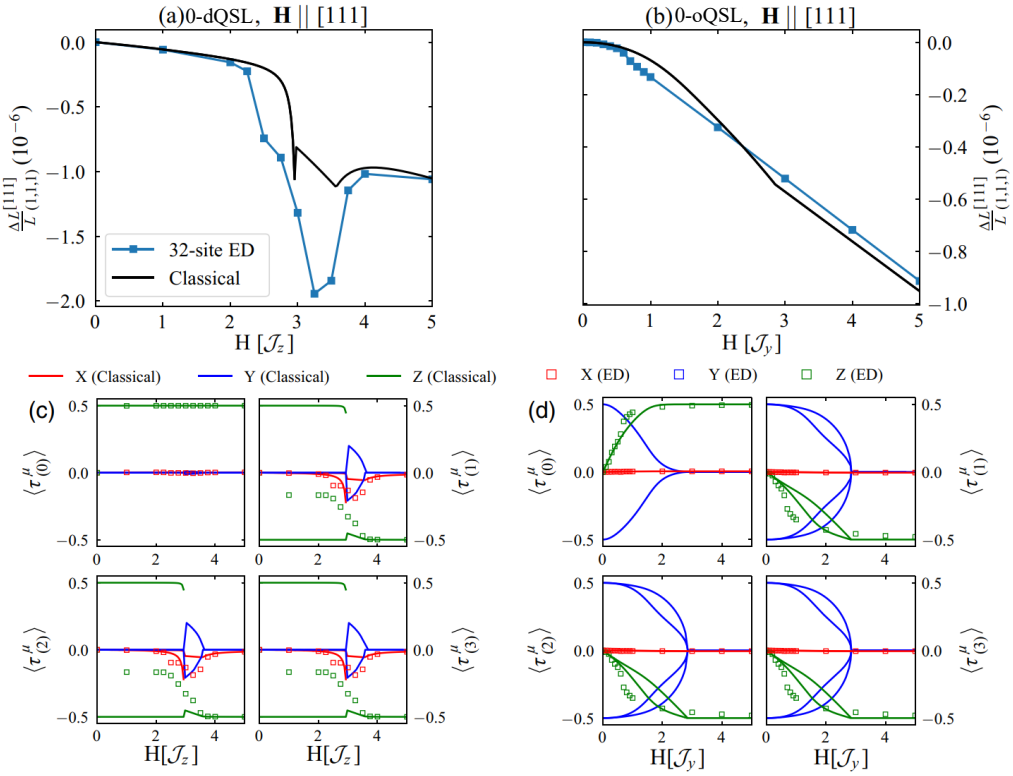


Figure 3.11. Magnetostriction along the $\boldsymbol{\ell} = (1,1,1)$ direction and order parameter evolution under the $\hat{\boldsymbol{n}} = [111]$ magnetic field for the 0-flux dipolar QSL (0-dQSL) and octupolar QSL (0-oQSL). (a), (b): relative length change, $\Delta L/L$ for the 0-dQSL and 0-oQSL, respectively, along the $\boldsymbol{\ell} = (1,1,1)$ and $\hat{\boldsymbol{n}} = [111]$ magnetic field. Solid lines (squares) indicate classical (32-site exact diagonalisation) magnetostrictions and order parameters. The superimposed magnetostriction ED result in (a) indicates an enhancement by quantum fluctuations. (c): 0-dQSL order parameter evolution. The 0-dQSL develops (both classically and quantum mechanically) into the kagome ice phase within the low-field limit. Upon increasing the field, the kagome ice undergoes a metamagnetic transition in $\langle \tau_z \rangle$ and is accompanied by an "island" of the finite $x$ and $y$ components of the pseudospins for sublattices 1,2, and 3 that survives for a small window of magnetic field strengths. The first (second) discontinuity in (a) reflects the appearance (disappearance) of this island. (d): 0-oQSL order parameter evolution. The 0-oQSL steadily collapses with increasing field strength and is accompanied by the gradual increase in $\langle \tau_z \rangle$ into a fully polarised phase. The single classical kink at $h_c \sim 3J_y$ in (b) is the critical field value, where $\langle \tau_y \rangle$ on all sublattices has collapsed to zero.

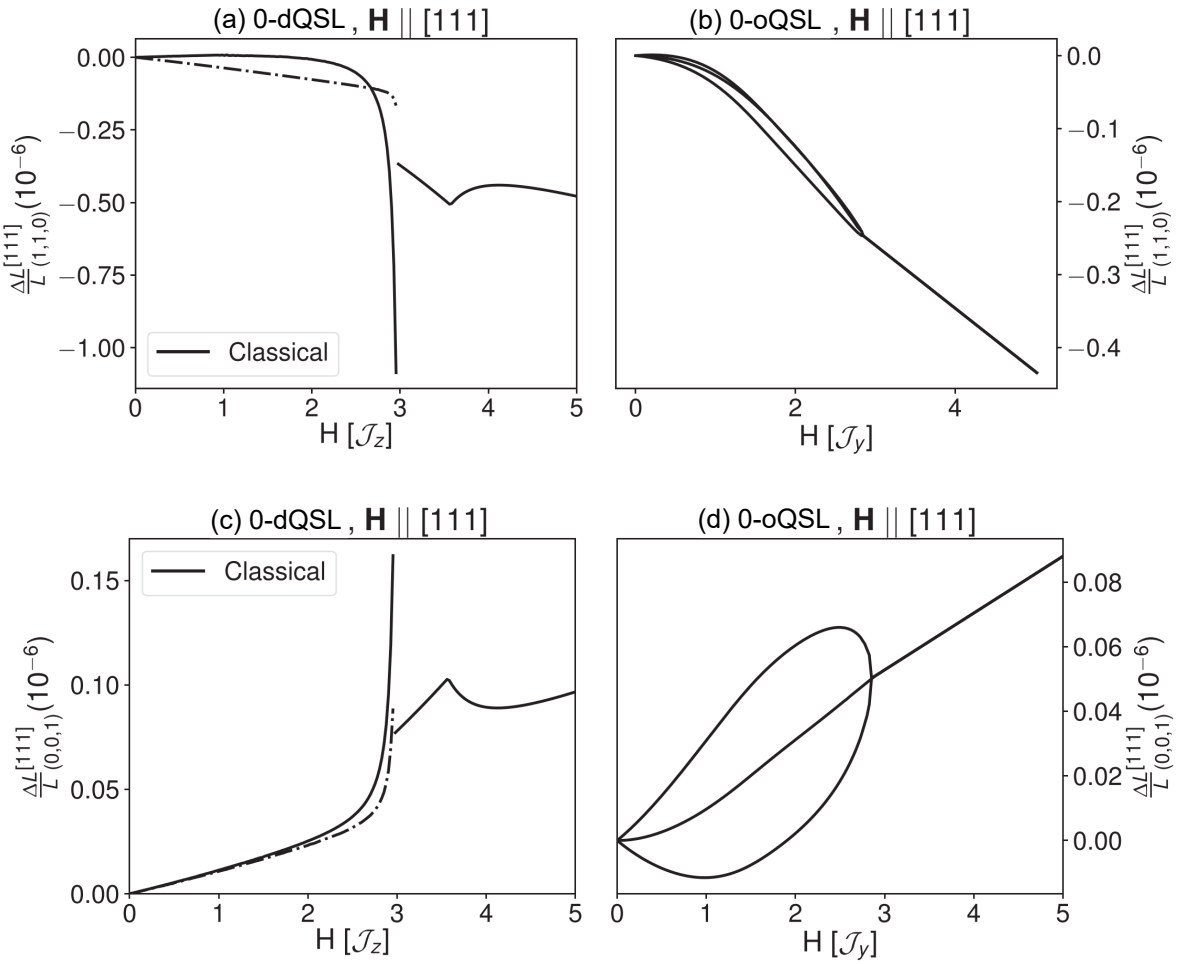


Figure 3.12. Length change $\Delta L/L$ along the $\boldsymbol{\ell} = (1,1,0), (0,0,1)$ directions for a magnetic field applied along the $\hat{\boldsymbol{n}} = [111]$ direction for the 0-dQSL and 0-oQSL. Solid lines indicate classical magnetostrictions. (a): 0-dQSL along $\boldsymbol{\ell} = (1,1,0)$, (b): 0-oQSL along $\boldsymbol{\ell} = (1,1,0)$, (c): 0-dQSL $\boldsymbol{\ell} = (0,0,1)$, and (d): 0-oQSL $\boldsymbol{\ell} = (0,0,1)$. The 0-dQSL reflects the kagome ice degeneracy and the 0-oQSL reflects the dampened degeneracy, as described in the main text. The degenerate 0-dQSL solutions are denoted by dashed lines for clarity.

### 3.4.4 Magnetostriction for AIAO ordered phases

To contrast the length change behaviours of the 0-flux QSLs, we verify these behaviours for the all-in all-out ordered phases. The obtained results can be used to determine the type of multipole that comprises the AIAO configuration in Nd-based pyrochlore materials. However, the main purpose is to reveal the uniqueness of the QSL length change behaviour; hence, Fig. 3.13 presents the results of the classical calculations only. Note that degenerate branches exist for the AIAO magnetostriction behaviours, which reflects the degeneracy of the AIAO phase. Clearly, this is not observed in all length change directions because it requires particular combinations of pseudospin configurations to ap-

pear in the length change expressions, such as $\sim h(3\tau_x^{(1)}+3\tau_x^{(2)}+2\tau_x^{(3)})$, $\sim h(3\tau_x^{(0)}+\tau_x^{(3)})$, $\sim h(3\tau_z^{(1)}+3\tau_z^{(2)}+2\tau_z^{(3)})$, $\sim h(3\tau_z^{(0)}+\tau_z^{(3)})$, and $\sim h(\tau_y^{(1)}-\tau_y^{(2)})$.

As shown in Figs. 3.13(a), (d), and (g), every AIAO phase exhibits a distinct length change behaviour from that of 0-flux QSLs. Neither dip nor kink behaviours found in the 0-flux QSL phases are observed in AIAO ordered phases, which supports the uniqueness of the length change behaviour of 0-flux QSLs. More interestingly, each AIAO phase exhibits a different behaviour. Under a [111] magnetic field, X- and Y-AIAO phases present a monotonic quadratic-in-$h$ length change behaviour at low field and no discontinuity is observed, as shown in Figs. 3.13(a) and (d). Although the multipole symmetries are different, they are considered octupolar AIAO phases, and these mild length change behaviours are an important property for octupolar AIAO phases. Indeed, in the Z-AIAO phase, that is, a dipolar AIAO phase, we find several kinks in the length change behaviour, and each sector exhibits a linear-in-$h$ behaviour in Figs. 3.13(g), which indicates the distinguishability between the dipolar AIAO and octupolar AIAO phases. For different magnetic field directions, we can find clear difference between the dipolar and octupolar AIAO phases, as shown in Fig. 3.13(b), (c), (e), (f), (h), and (i). In particular, while octupolar AIAOs exhibit a gentle length change behaviour under the [110] field, the dipolar AIAO exhibits a clear jump structure in all accessible length change directions. In experiments, linear-in-$h$ length change behaviour, and the observation of kink or jump structures, will evidence the realisation of the dipolar AIAO phase. In contrast, the observation of quadratic-in-$h$ length change behaviour for small $h$ and the lack of nonanalytic behaviour under the [111] and [110] fields indicates the realisation of octupolar AIAO phases.

As is the case for 0-flux QSLs, the key difference between dipolar and octupolar AIAO phases is caused by the ability of the pseudospin degree of freedom responsible for forming the all-in all-out configuration to directly couple to the magnetic field. This results in the qualitative difference in the length change behaviour within the low-field window. Unfortunately, distinguishing between X- and Y-AIAO phases is difficult because quantitative differences in Figs. 3.13(a–f) are caused by an arbitrary choice of the coupling constants $\mathcal{C}_i$. Note that, in a realistic system with multiple domains, an average is expected over the degenerate branches.

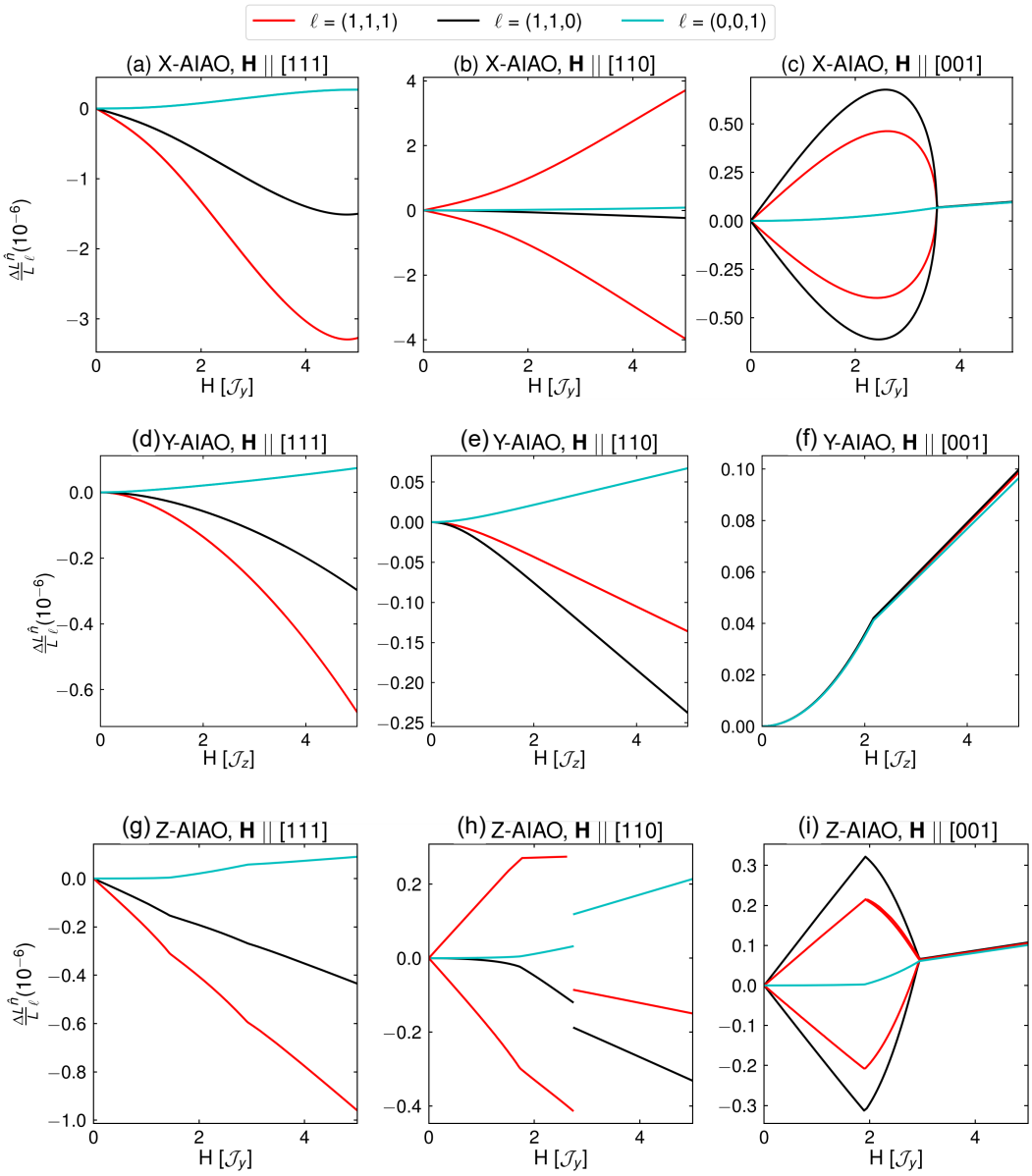


Figure 3.13. Length change $\Delta L/L$ for a magnetic field applied along the $\hat{\boldsymbol{n}} = [111], [110]$, and $[001]$ directions for X-, Y-, and Z-AIAO phases, where the $x$, $y$, and $z$ components of the pseudospin constitute the all-in all-out configuration, respectively. Depicted are the three common experimentally accessible cubic length change directions along $\boldsymbol{\ell} = (1,1,1), (1,1,0), (0,0,1)$, in red, black, and cyan, respectively. In several of these results, classically degenerate branches are observed at the low and intermediate fields, reflecting the degeneracy of the all-in all-out nature of these phases. In a realistic system with multiple domains, an average is expected over the degenerate branches. Moreover, quantum fluctuations can enhance the discontinuity or change the transition points; however, the overall properties are not expected to be altered.

### 3.4.5 Magnetostriction for $\pi$-flux QSLs

At this stage, we have analysed the length change behaviours of classically distinguishable phases, namely 0-flux QSLs and AIAO ordered phases. As shown in the first half of this chapter, the most promising candidate for the QSL phase in $Ce_2Zr_2O_7$ is the $\pi$-oQSL. Therefore, it is vital to ascertain whether magnetostriction is also useful for distinguishing between $\pi$-flux QSLs and other phases because this would offer another way to check for $\pi$-flux QSL realisation in actual materials.

Figure 3.14 presents the quantum magnetostriction behaviours of the two $\pi$-flux QSLs parallel to a [111] magnetic field; their respective order parameter evolutions are also shown. Here, only the quantum results are presented because the classical $\pi$-flux QSL phase results do not capture their unique features because they do not appear in the classical phase diagram. From these results, we can find a clear difference in the length change behaviours of other phases, such as 0-flux QSLs and AIAO ordered phases. However, the length changes of the $\pi$-dQSL and $\pi$-oQSL phases display a resemblance, which reveals the difficulty in distinguishing between them using magnetostriction experiments. Of particular interest is that both phases exhibit several jumps in the length change behaviour accompanied by stable plateaus in the order parameter evolution.

As shown in Fig. 3.14(b), the $\pi$-dQSL gradually develops into the kagome ice phase, similar to the case of the 0-dQSL in the small field region. Upon increasing the magnetic field, it experiences two sharp transitions at $h_a \sim 2.0$ and $h_b \sim 3.5$ accompanied by the plateaus in $\tau_z$ for sublattices 1, 2, and 3. The critical field $h_a$, in which the kagome ice phase collapses, is almost identical to that in the 0-dQSL phase. Finally, at $h_c \sim 4.0$, the system enters a fully polarised phase. The underlying physics can be described as follows: the $\pi$-flux phases exhibit partially polarised phases as intermediate phases, which is not described by the metamagnetic transition observed in 0-flux QSLs. In the parameter region $h_a < h < h_b$, we estimate that 25% of tetrahedra enter the fully polarised phase and 62.5% are in the fully polarised phase within the parameter region $h_b < h < h_c$. Although the reason why such behaviours are found only in $\pi$-QSLs is elusive, it is possible that the flux configuration plays an important role in determining the stability of partially polarised phases for an intermediate field strength.

The order parameter evolution and the resulting length change behaviour of the $\pi$-oQSL are similar to those of the $\pi$-dQSL, as shown in Figs. 3.14(a) and (b). The key difference between the $\pi$-dQSL and $\pi$-oQSL phases is the absence of a stable kagome ice state in the low-field window. Instead, the early locations of transition into partially polarised phases are captured. Such instability of the oQSL is also found in the 0-flux case, which can be an important property of oQSL phases regardless of the flux configurations. In contrast with the $\pi$-dQSL phase, the plateau-like order parameter evolution in $\tau_z$ for sublattices 1, 2, and 3 displays a subtle field dependence whose origin has yet to be revealed. Unfortunately, the difference between the $\pi$-dQSL and $\pi$-oQSL does not yield distinct behaviours in the magnetostriction; therefore, we cannot determine the QSL type when a length change with several jump structures is observed. However, once again, it must be emphasised that the multiple jump structures are unique to $\pi$-flux QSLs. Therefore, the 0-dQSL and $\pi$-dQSL, which were proven to be almost indistinguishable via neutron scattering, can be distinguished by this novel probe for detecting

quantum phases: magnetostriction measurement. The key message in this chapter is as follows: *the combination of an ordinary probe (neutron scattering measurement) and a novel probe (magnetostriction measurement) reveals the existence of new type of QSL, namely multipolar quantum spin liquids.*

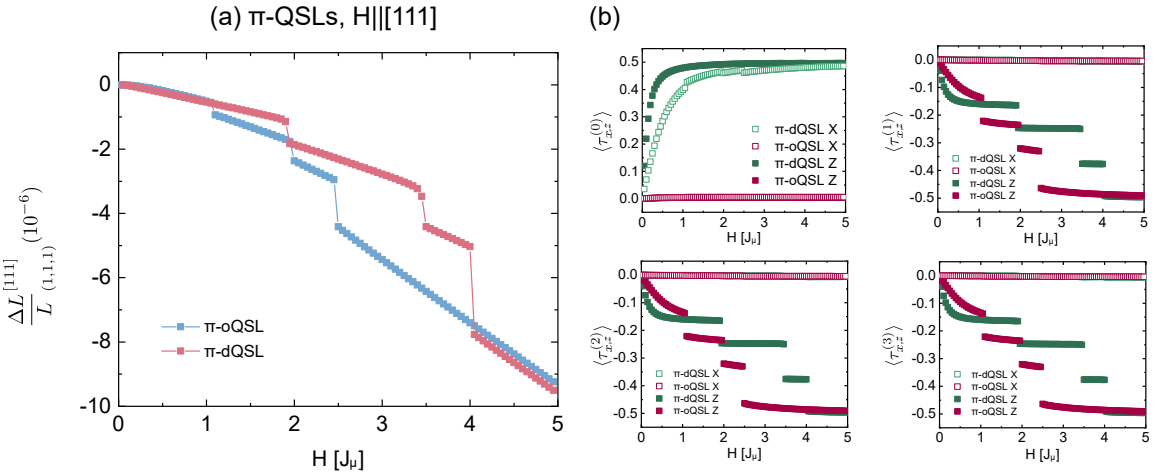


Figure 3.14. Magnetostriction along the $\boldsymbol{\ell} = (1,1,1)$ direction and order parameter evolution under the $\hat{\boldsymbol{n}} = [111]$ magnetic field for the $\pi$-flux dipolar QSL ($\pi$-dQSL) and octupolar QSL ($\pi$-oQSL). (a): relative length change, $\Delta L/L$, for the $\pi$-dQSL and $\pi$-oQSL, respectively, along $\boldsymbol{\ell} = (1,1,1)$ and the $\hat{\boldsymbol{n}} = [111]$ magnetic field. Squares indicate 16-site exact diagonalisation magnetostrictions and order parameters. Multiple jump structures in the length change behaviours are unique properties of $\pi$-flux QSLs. (b): $\pi$-QSL order parameter evolution. The $\pi$-dQSL gradually develops into the kagome ice phase in the small-field region. Upon increasing the field, the kagome ice undergoes two sudden transitions in $\langle \tau_z^{(1,2,3)} \rangle$ at approximately $h_a \sim 2.0$ and $h_b \sim 3.5$ accompanied by $h$-independent $\tau_z^{(1,2,3)}$. From the values of these plateaus, we estimate that 25% (62.5%) of tetrahedra are in the fully polarised phase for $h_a < h < h_b$ ($h_b < h < h_c$). Then, at approximately $h_c \sim 4.0$, the system enters a fully polarised phase. The $\pi$-oQSL also exhibits a similar behaviour except for the stable kagome ice state. In addition, the meaning of the value of $\tau_z$ in the plateaus is unclear. Resemblance in the length change behaviour stems from the similarity in order parameter evolution.

## 3.5 Conclusion

In this chapter, we analysed the dipolar-octupolar Kramers system in rare-earth pyrochlore materials and revealed the existence of four types of QSLs, that is, the dipolar and octupolar QSLs with 0 and $\pi$ flux. The flux degree of freedom was concealed due to the difficulty in accessing the frustrated parameter region; however, this was made clear by exploiting the exact diagonalisation method on the 32-site cluster. In addition, we studied the physical properties, the static and dynamic structure factors, of four QSLs

from classical and quantum viewpoints. As a result, we found strong evidence for the realisation of the $\pi$ flux octupolar QSL phase in $Ce_2Zr_2O_7$. This is the first observation of a multipolar quantum spin liquid and has the potential to exhibit exotic phenomena owing to its multipolar nature. Its field dependence and novel responses are expected to be of experimental interest in future studies.

In the latter half of this chapter, a novel probe was proposed to complete the experimental identification method for QSLs. In the first half, it had become clear that distinguishing between the 0-dQSL and $\pi$-dQSL using conventional experimental methods alone, such as neutron scattering experiments, was a difficult task. Therefore, we have shown that they are distinguishable using magnetostriction experiments, which have been successful in distinguishing MPOs or QSLs in other $f$ electron systems. In this theory, magnetic-field-supported strain-pseudospin coupling plays an important role and enables us to capture the different length change behaviours under an external magnetic field depending on the types of QSLs. These results suggest that the lattice degree of freedom is also useful in detecting multipoles with time-reversal even nature, which do not directly interact with the strains. Furthermore, importantly, magnetostriction measurement can be a new promising experimental method for detecting multipoles with ranks greater than two, which has been in high demand.

As a concluding remark, it is once again emphasised that this is the first time that a multipolar quantum spin liquid has been found in which the local multipoles are frustrated and constitute the quantum spin liquid. This discovery opens a new door for the study of quantum spin liquids and will broaden the scope of future research in terms of peculiar responses and practical applications.

# Chapter 4

# Field-revealed one-dimensionality in non-Kramers pyrochlore materials

In the previous chapter, we discussed the effect of spin configuration on the lattice degree of freedom and the usefulness of magnetostriction to probe various quantum phases, including multipolar QSLs and MPOs. In this chapter, we will discuss the effect of the lattice degree of freedom on the spin system. Quantised lattice fluctuations, phonons, can linearly couple to the local quadrupolar moment in the non-Kramers doublet ground state owing to its time-reversal even nature. First, this phonon-pseudospin coupling is shown to result in an effective transverse field to the local quadrupoles. Then, the realisation of an emergent one-dimensional transverse field Ising model is proposed for a particular external magnetic field, that is, the field along the [110] direction.

On the experimental side, an unusual NMR relaxation time behaviour is observed in the non-Kramers pyrochlore material $Pr_2Zr_2O_7$ under the [110] magnetic field. We demonstrate that these behaviours can be described by the finite temperature quantum phase transition of the one-dimensional transverse field Ising model. Because the anomalies associated with this transition are usually concealed in specific heat and susceptibility measurements, only NMR relaxation time measurement provides strong evidence of emergent one-dimensionality in three-dimensional frustrated magnets.

## 4.1 Introduction

As revealed previously, to develop a deep understanding of rare-earth pyrochlore materials, it is crucial that the lattice degree of freedom is considered. In particular, non-Kramers pyrochlore materials possess local quadrupolar moments that can linearly couple to lattice dislocations; thus, exploring their phonon-pseudospin interactions is of particular importance. However, interesting phonon-induced phenomena have not been reported and are currently not being actively studied. Motivated by these circumstances, we will reveal the explicit form of phonon-pseudospin couplings in non-Kramers pyrochlore systems and suggest that this coupling plays an important role in describing the peculiar behaviour of NMR relaxation time $T_1$ under an external magnetic field along the [110] direction in $Pr_2Zr_2O_7$, which is an unpublished experimental result.

The extremely large [110] magnetic field separates the three-dimensional pyrochlore lattice into two types of one-dimensional chains. Let us consider the following nearest-neighbour pseudospin 1/2 model under an external field along the [110] direction:

$$H_{\text{spin}} = J \sum_{\langle ij \rangle} S_i^z S_j^z - \sum_i \boldsymbol{h} \cdot \hat{z}_\alpha S_i^z. \tag{4.1}$$

Here, we ignore the $J_\pm$ and $J_{\pm\pm}$ terms in Eq. (2.1) for simplicity, $\alpha$ represents the sublattice index to which site $i$ belongs, and $\boldsymbol{h} \parallel [110]$. As we mentioned in Section 2.1.2, the Ising anisotropy exits in the Pr-based pyrochlore materials; and thus, ignoring the transverse term $J_\pm$ and $J_{\pm\pm}$ is not far from reality. From Table 3.1, we find $\boldsymbol{h} \cdot \hat{z}_\alpha = 0$ for sublattices 1 and 2, which means the one-dimensional chains constituted by sublattices 0 and 3 become fully polarised (forced ferromagnetic chain) and the other one-dimensional chains constituted by sublattices 1 and 2 remain decoupled within the strong field limit (decoupled chain) [134]. A schematic of this situation is shown in Fig. 4.1.

In Fig. 4.1(a), we can see that the forced ferromagnetic and decoupled chains accumulate alternately along the crystal $c$ direction. Because only the nearest-neighbour interactions are considered, the chain-chain couplings within the same $ab$ plane are negligible; however, those between different $ab$ planes (chain-chain coupling between different types of chains) are finite. Bearing this in mind, we can identify the ground state spin configuration of each chain within the strong field limit, as shown in Fig. 4.1(b). The spins in the forced ferromagnetic chain can couple to the external field and point in the $+\hat{z}_0$ and $-\hat{z}_3$ directions, where $\hat{z}_\alpha$ is the local $z$ axis of sublattice $\alpha$ defined in Table 3.1. As a result, net magnetisation along the [110] axis remains in the forced ferromagnetic chains. In the decoupled chain, although the spins exhibit a similar configuration to those in the forced ferromagnetic chain, as shown in Fig. 4.1(b), their origin is different. Because the spins cannot couple to the external field, their configuration is determined by the Ising term in Eq. (4.1). Remembering that this interaction yields the two-in two-out constraint to a single tetrahedron and each tetrahedron is constructed from two atoms of the forced ferromagnetic chain (one points inwards and the other points outwards from the tetrahedron) and two atoms of the decoupled chain, we find two possible spin configurations as the ground states: $(+\hat{z}_1, -\hat{z}_2)$ and $(-\hat{z}_1, +\hat{z}_2)$. This indicates that the decoupled chain is regarded as a one-dimensional antiferromagnetic Ising chain, where the local $z$ axis is dependent on the sublattice index. Note that this robustness of the two-in two-out configuration relates to the robustness of the $U(1)$ QSL in the dipolar-octupolar system under a field along the [110] direction (Fig. 2.6(c)).

The uniqueness of the [110] field direction also appears in the experimental signatures. For instance, the NMR study on Zr sites of $Pr_2Zr_2O_7$ for a variety of magnetic field directions revealed an unusual temperature dependence of the spin-lattice relaxation time $T_1$. As shown in Fig. 4.1(a), the Zr atom is surrounded by six Pr ions and monitors the local (pseudo)spin susceptibility via transferred hyperfine interactions. In particular, under the [110] magnetic field, four sites out of the six belong to the forced ferromagnetic chain and the remaining two sites belong to the decoupled chain. Figure 4.2 presents the experimental results of the temperature dependences of $1/T_1$. For the magnetic field along the [111] and [100] directions, $1/T_1$ drastically reduces at low temperatures. More precisely, these "drop" behaviours are observed for $H > 2$ T under the [111] magnetic field

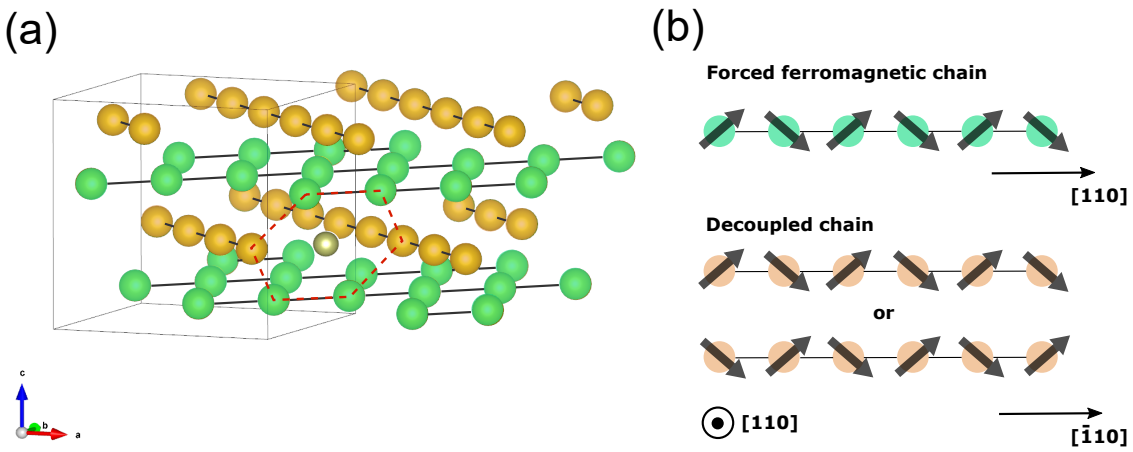


Figure 4.1. Schematic illustration of the separation of the pyrochlore lattice into two types of one-dimensional chains under a strong [110] magnetic field. (a): Chain decomposition of the rare-earth sites in the pyrochlore lattice. The orange (green) spheres represent the sites that belong to sublattices 0 and 3 (1 and 2) and constitute the forced ferromagnetic (decoupled) chains. The gold sphere is one of the Zr atoms of $Pr_2Zr_2O_7$, and the internal field at this Zr site originates from nearest-neighbour Pr sites, that is, the sites on the red-dashed hexagon. (b): Spin configuration under the strong [110] magnetic field of the forced ferromagnetic and decoupled chains. The spins in the forced ferromagnetic chain point in the $+\hat{z}_0$ and $-\hat{z}_3$ directions owing to usual Zeeman coupling, where $\hat{z}_\alpha$ is the local $z$ axis of sublattice $\alpha$ defined in Table 3.1. Meanwhile, the spin configurations in the decoupled chain are determined only by the Ising interaction because of the lack of Zeeman coupling. There are two possible spin configurations within a single tetrahedron that maintain the ice rule: spins pointing to $(+\hat{z}_1, -\hat{z}_2)$ and $(-\hat{z}_1, +\hat{z}_2)$.

and are observed in magnetic fields as small as 0.5 T in the [100] direction. Meanwhile, for the [110] magnetic field, $1/T_1$ reaches its minimum at approximately $T = 5$ K and then increases with decreasing temperature. This "up-and-down" behaviour is unique to this field direction and is associated with the emergent one-dimensionality described above.

Several of these behaviours can be explained by a simple analysis. For example, the "drop" behaviours are described in the context of a gapped spin system. Under the field along the [111] direction, the system enters into the kagome ice state. Then, at approximately $h/J \sim 2.0$, it becomes a fully polarised state [135]. In the high field region, the singlet fully polarised ground state has an excitation gap $\Delta$ corresponding to the required energy for spin-flipping. Analogous to the NMR relaxation time behaviour of $s$-wave superconductivity, we expect the relation $1/T_1 \propto \exp(-\Delta/k_B T)$ in this strong field regime. In fact, the "drop" behaviour for $h > 2$ T and the [111] field direction can be accurately fitted by this relation, and the increasing $\Delta$ with increasing field is consistent with this scenario. In addition, it is reasonable to assume that the phase transition to the fully polarised state occurs at approximately 2 T because $J$ is of the order of a few Tesla, and hence the drop is only observed for $h > 2$ T. A similar scenario is also applicable to

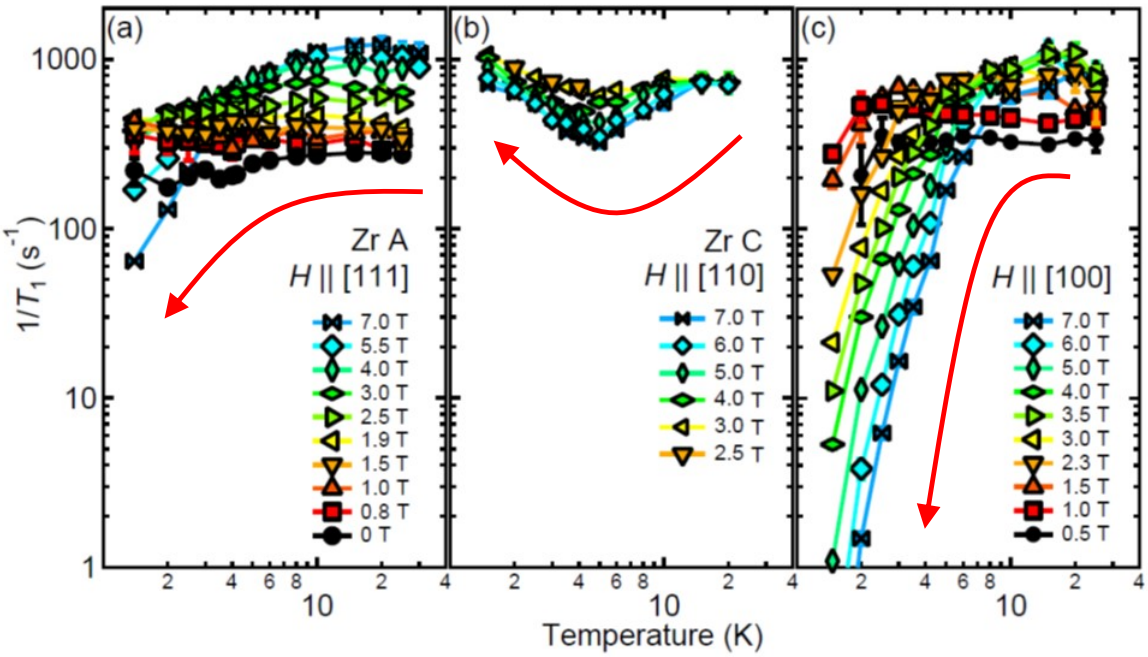


Figure 4.2. Temperature dependences of the inverse of the spin-lattice relaxation time $1/T_1$ for various magnetic field directions, (a): along the [111] direction, (b): [110] direction, and (c): [100] direction. For the [111] and [100] field directions, $1/T_1$ drastically decreases with decreasing temperature, whereas $1/T_1$ reaches its minimum at approximately 5 K before increasing for the [110] field direction. This uniqueness can be attributed to emergent one-dimensionality under the [110] magnetic field. Note that this experimental data is unpublished and obtained from a private communication with Dr. Hikaru Takeda.

the "drop" behaviour under the [100] magnetic field. In this case, the system does not experience the kagome ice state; hence, the "drop" signature is observable for fields as small as 0.5 T.

Unfortunately, the other features cannot be described by a simple analysis. In particular, the origin of the unique "up-and-down" relaxation time behaviour for the [110] field remains elusive because it cannot be explained by simply considering chain decoupling. The key purposes of this chapter are as follows:

1. To consider the phonon degree of freedom and construct the phonon-pseudospin coupling Hamiltonian.

2. To describe the up-and-down behaviour in the spin-lattice relaxation time $T_1$ under the [110] magnetic field.

To begin with, we consider phonon-spin coupling of non-Kramers pyrochlore systems in the subsequent section.

## 4.2 Phonon-pseudospin coupling

In this section, a Hamiltonian, including the phonon degree of freedom, is constructed by considering a generalised spring model and point charge approximation. Two different models are proposed depending on the considered assumptions; however, only one of them is discussed here. The second model is described in Appendix C for future research.

### 4.2.1 Phonon part

We start from the following generalised model for atomic oscillations

$$H_{\mathrm{ph}} = \sum_{j,\alpha,\mu} \frac{\hat{p}^2_{j\alpha\mu}}{2m_\alpha} + \frac{1}{2} \sum_{\substack{j\alpha\mu \\ j',\beta,\nu}} \phi(j\alpha\mu; j'\beta\nu) \hat{u}_{j\alpha\mu} \hat{u}_{j'\beta\nu}, \tag{4.2}$$

where $j$ and $j'$ are the unit cell indices, $\alpha$ and $\beta$ are the sublattice indices, and $\mu, \nu = x, y, z$ denote the direction of displacement. $\hat{u}_{j\alpha\mu}$ and $\hat{p}_{j\alpha\mu}$ are the $\mu$ components of the position and momentum operators at site $(j, \alpha)$, respectively. Note that $\hat{u}$ is measured from the equilibrium position, that is, $\hat{u}$ denotes the deviation from the equilibrium position. $\phi(j\alpha\mu; j'\beta\nu)$ is the coupling constant and satisfies $\phi(j\alpha\mu; j'\beta\nu) = \phi(j'\beta\nu; j\alpha\mu)$. Because it is reported that the dislocation of Pr ions is significant in $Pr_2Zr_2O_7$ [9, 136], we consider a situation in which only the nearest-neighbour Pr ions couple with each other through certain coupling constants. Applying the Fourier transformation

$$\hat{u}_{j\alpha\mu} = \frac{1}{\sqrt{N}} \sum_{\boldsymbol{q}} e^{\mathrm{i}\boldsymbol{q}\cdot\boldsymbol{R}_j} \hat{u}_{\alpha\mu}(\boldsymbol{q}) \qquad \hat{p}_{j\alpha\mu} = \frac{1}{\sqrt{N}} \sum_{\boldsymbol{q}} e^{-\mathrm{i}\boldsymbol{q}\cdot\boldsymbol{R}_j} \hat{p}_{\alpha\mu}(\boldsymbol{q}), \tag{4.3}$$

we find that Eq. (4.2) becomes

$$\begin{aligned}
H_{\mathrm{ph}} &= \sum_{\boldsymbol{q}} \sum_{\alpha,\mu} \frac{\hat{p}_{\alpha\mu}(-\boldsymbol{q}) \hat{p}_{\alpha\mu}(\boldsymbol{q})}{2m_\alpha} + \frac{1}{2} \sum_{\boldsymbol{q}} \sum_{\substack{\alpha,\mu \\ \beta,\nu}} \tilde{\phi}_{\alpha\mu,\beta\nu}(\boldsymbol{q}) \hat{u}_{\alpha\mu}(-\boldsymbol{q}) \hat{u}_{\beta\nu}(\boldsymbol{q}) \\
&= \frac{1}{2} \sum_{\boldsymbol{q}} \sum_{\alpha,\mu} \frac{\hat{p}_{\alpha\mu}(-\boldsymbol{q})}{\sqrt{m_\alpha}} \frac{\hat{p}_{\alpha\mu}(\boldsymbol{q})}{\sqrt{m_\alpha}} + \frac{1}{2} \sum_{\boldsymbol{q}} \sum_{\substack{\alpha,\mu \\ \beta,\nu}} \frac{\tilde{\phi}_{\alpha\mu,\beta\nu}(\boldsymbol{q})}{\sqrt{m_\alpha m_\beta}} \sqrt{m_\alpha} \hat{u}_{\alpha\mu}(-\boldsymbol{q}) \sqrt{m_\beta} \hat{u}_{\beta\nu}(\boldsymbol{q}) \\
&= \frac{1}{2} \sum_{\boldsymbol{q}} \left[ \tilde{\boldsymbol{p}}(-\boldsymbol{q}) \cdot \tilde{\boldsymbol{p}}(\boldsymbol{q}) + \tilde{\boldsymbol{u}}^\dagger(\boldsymbol{q}) \mathcal{D}(\boldsymbol{q}) \tilde{\boldsymbol{u}}(\boldsymbol{q}) \right] \\
&= \frac{1}{2} \sum_{\boldsymbol{q}} \sum_{s} \left[ |\mathcal{P}_s(\boldsymbol{q})|^2 + \omega_s^2(\boldsymbol{q}) |\mathcal{U}_s(\boldsymbol{q})|^2 \right].
\end{aligned} \tag{4.4}$$

Here, $\tilde{u}_{\alpha\mu} = \sqrt{m_\alpha} \hat{u}_{\alpha\mu}$ and $\tilde{p}_{\alpha\mu} = \hat{p}_{\alpha\mu} / \sqrt{m_\alpha}$ are the new conjugate operator pair and are represented in vector form in the third line. $\omega_s(\boldsymbol{q})$ is the $s$-th eigenvalue of the dynamical matrix $\mathcal{D}_{\alpha\mu,\beta\nu}(\boldsymbol{q}) = \tilde{\phi}_{\alpha\mu,\beta\nu}(\boldsymbol{q}) / \sqrt{m_\alpha m_\beta}$, and $\mathcal{U}_s(\boldsymbol{q})$ is the $s$-th component of the eigenstate of $\mathcal{D}$, that is, $\overrightarrow{\mathcal{U}} = U^\dagger(\boldsymbol{q}) \tilde{\boldsymbol{u}}(\boldsymbol{q})$, where $U$ is the unitary operator, which diagonalises the

dynamical matrix $\mathcal{D}$. Because this Hamiltonian can be regarded as a set of independent harmonic oscillators, we can introduce the usual bosonic phonon operators:

$$\mathcal{U}_s(\boldsymbol{q}) = \sqrt{\frac{\hbar}{2\omega_s^2(\boldsymbol{q})}}\left(a_{s\boldsymbol{q}} + a_{s,-\boldsymbol{q}}^\dagger\right), \qquad \mathcal{P}_s(\boldsymbol{q}) = \mathrm{i}\sqrt{\frac{\hbar\omega_s^2(\boldsymbol{q})}{2}}\left(-a_{s,-\boldsymbol{q}} + a_{s,\boldsymbol{q}}^\dagger\right). \tag{4.5}$$

Equipped with these results, the phonon part of the Hamiltonian is simplified as

$$H_{\mathrm{ph}} = \sum_{\boldsymbol{q}}\sum_{s}\hbar\omega_s(\boldsymbol{q})\left(a_{s\boldsymbol{q}}^\dagger a_{s\boldsymbol{q}} + \frac{1}{2}\right). \tag{4.6}$$

### 4.2.2 Phonon-pseudospin interaction

We assume that the main contribution of phonon-pseudospin interactions originates from the modified crystal electric field (CEF) owing to the dislocation of the Pr ions. Moreover, there is an in-plane instability in the Pr location; thus, we consider dislocation within the local $xy$ plane and its effect using point charge approximation [96]. The $D_{3d}$ symmetric CEF is composed of three types of ions: two oxygen ions at the A sites (red spheres), six iridium ions in a hexagonal arrangement (gold spheres), and six oxygen ions at the B sites (blue spheres), as shown in Fig. 4.3. Here, the yellow sphere at the centre denotes the equilibrium position of the Pr ion, and $\boldsymbol{u} = (u\cos\alpha, u\sin\alpha, 0)$ indicates the deviation from the origin within the local $xy$ plane.

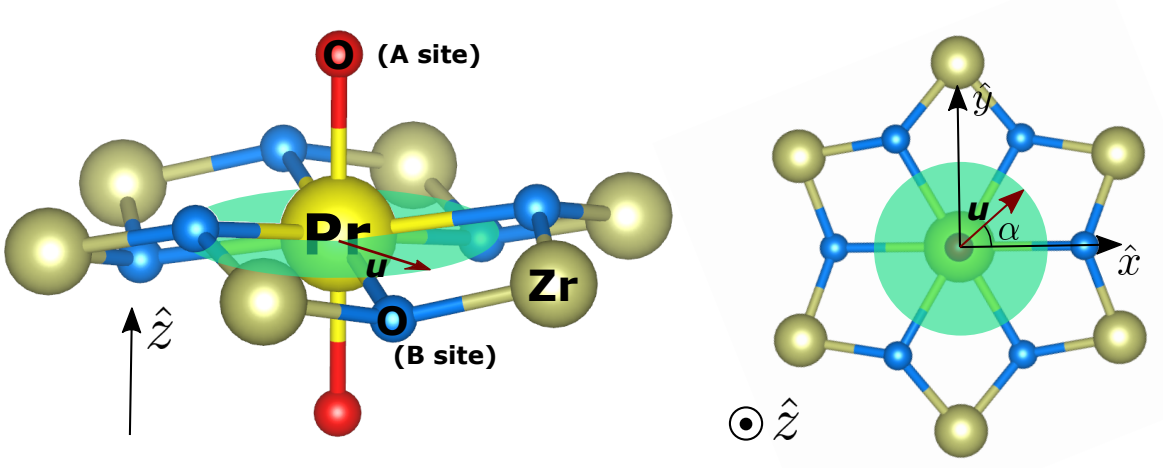


Figure 4.3. Site configuration of the $D_{3d}$ symmetric crystal electric field. The yellow sphere denotes the Pr ion, the two red spheres represent the oxygen ions at the A sites, the six blue spheres represent the oxygen ions at the B sites, and the six gold spheres denote the Zr ions. The green ellipse indicates the local $xy$ plane, and the red vector is the deviation from the equilibrium position. The right panel shows this view from the local $z$ axis. Note that this configuration, including the direction of the local $x, y$ and $z$, is independent of the sublattice index introduced in the previous chapter.

**CEF from the oxygen ions at the A sites**

Without the deviation, the oxygen ions at the A sites are located at $(0,0,\pm\frac{\sqrt{3}a}{8})$, where $a$ is the lattice constant. When the Pr ion shifts to $(u\cos\alpha, u\sin\alpha, 0)$, their relative positions become $(-u\cos\alpha, -u\sin\alpha, \pm\frac{\sqrt{3}a}{8})$. In the spherical coordinate frame, they are represented as $\boldsymbol{R}_1 = (r_{\mathrm{O,A}}, \theta_0, \pi+\alpha)$ and $\boldsymbol{R}_2 = (r_{\mathrm{O,A}}, \pi-\theta_0, \pi+\alpha)$, where $r_{\mathrm{O,A}} = \left(u^2 + \frac{3}{64}a^2\right)^{-1/2}$ and $\theta_0 = \cos^{-1}\left(\frac{\sqrt{3}a}{8r_{\mathrm{O,A}}}\right)$.

In general, the potential energy at $\boldsymbol{r} = (r,\theta,\phi)$ arising from the ions with electric charge $Ze$ residing at $\boldsymbol{R}_i = (R_i, \theta_i, \phi_i)$ is given by [78]

$$V_{\mathrm{CEF}}(r,\theta,\phi) = \sum_i \sum_{k=0}^{\infty} \sum_{m=-k}^{k} r^k \gamma_{km}^i C_m^{(k)}(\theta,\phi), \tag{4.7}$$

where

$$\gamma_{km}^i = \sqrt{\frac{4\pi}{2k+1}} \frac{Ze^2}{R_i^{k+1}} \sum_i Y_{km}^*(\theta_i,\phi_i), \qquad C_m^{(k)} = \sqrt{\frac{4\pi}{2k+1}} Y_{km}(\theta,\phi). \tag{4.8}$$

Note that $Y_{km}(\theta,\phi)$ denotes the spherical harmonics.

In the present case, we find

$$\begin{aligned} \gamma_{km} &= \sqrt{\frac{4\pi}{2k+1}} \frac{2e^2}{r_{\mathrm{O,A}}^{k+1}} \left[Y_{km}^*(\theta_0, \pi+\alpha) + Y_{km}^*(\pi-\theta_0, \pi+\alpha)\right] \\ &= \sqrt{\frac{4\pi}{2k+1}} \frac{2e^2}{r_{\mathrm{O,A}}^{k+1}} \left[(-1)^m + (-1)^k\right] Y_{km}^*(\theta_0, \alpha), \end{aligned} \tag{4.9}$$

which yields

$$\begin{aligned} V_{\mathrm{CEF}}^{\mathrm{O,A}}(\boldsymbol{r}) &= \sum_{k=0}^{\infty} \sum_{m=-k}^{k} V_{\mathrm{CEF}}^{\mathrm{O,A}(k,m)}(\boldsymbol{r}) \\ &= \sum_{k=0}^{\infty} \sum_{m=-k}^{k} \sqrt{\frac{4\pi}{2k+1}} \frac{2e^2}{r_{\mathrm{O,A}}^{k+1}} r^k \left[(-1)^m + (-1)^k\right] Y_{km}^*(\theta_0,\alpha) C_m^{(k)}(\theta,\phi). \end{aligned} \tag{4.10}$$

To consider the CEF effect on $f$ electrons with $l = 3, m_l = -3,-2,\ldots,3$, we next calculate $\langle lm'|V_{\mathrm{CEF}}^{\mathrm{O,A}}(\boldsymbol{r})|lm\rangle$. For $f$ electrons, the even $k$ (with $k \le 6$) gives the finite matrix element. Using Eq. (4.10), we can find that the matrix elements are finite only when $m'-m$ is even. Expanding the spherical harmonics up to the second order with regard to $\delta = u/a$, we finally obtain $V_{\mathrm{CEF}}^{\mathrm{O,A}}(\boldsymbol{r}) = V_{\mathrm{CEF}}^{\mathrm{O,A}(0)}(\boldsymbol{r}) + V_{\mathrm{CEF}}^{\mathrm{O,A}(2)}(\boldsymbol{r})$, where

$$\begin{aligned} &V_{\mathrm{CEF}}^{\mathrm{O,A}(0)}(\boldsymbol{r})_{(\pm3,\pm3)} = \mathcal{V}_3^{\mathrm{O,A}}, \qquad V_{\mathrm{CEF}}^{\mathrm{O,A}(0)}(\boldsymbol{r})_{(\pm2,\pm2)} = \mathcal{V}_2^{\mathrm{O,A}} \\ &V_{\mathrm{CEF}}^{\mathrm{O,A}(0)}(\boldsymbol{r})_{(\pm1,\pm1)} = \mathcal{V}_1^{\mathrm{O,A}}, \qquad V_{\mathrm{CEF}}^{\mathrm{O,A}(0)}(\boldsymbol{r})_{(\pm0,\pm0)} = \mathcal{V}_0^{\mathrm{O,A}} \\ &V_{\mathrm{CEF}}^{\mathrm{O,A}(2)}(\boldsymbol{r})_{(3,1)} = \left(V_{\mathrm{CEF}}^{\mathrm{O,A}(2)}(\boldsymbol{r})_{(1,3)}\right)^* = V_{\mathrm{CEF}}^{\mathrm{O,A}(2)}(\boldsymbol{r})_{(-1,-3)} = \left(V_{\mathrm{CEF}}^{\mathrm{O,A}(2)}(\boldsymbol{r})_{(-3,-1)}\right)^* = \mathcal{U}_3^{\mathrm{O,A}}\delta^2 e^{-2\mathrm{i}\alpha} \\ &V_{\mathrm{CEF}}^{\mathrm{O,A}(2)}(\boldsymbol{r})_{(2,0)} = \left(V_{\mathrm{CEF}}^{\mathrm{O,A}(2)}(\boldsymbol{r})_{(0,2)}\right)^* = V_{\mathrm{CEF}}^{\mathrm{O,A}(2)}(\boldsymbol{r})_{(0,-2)} = \left(V_{\mathrm{CEF}}^{\mathrm{O,A}(2)}(\boldsymbol{r})_{(-2,0)}\right)^* = \mathcal{U}_2^{\mathrm{O,A}}\delta^2 e^{-2\mathrm{i}\alpha} \\ &V_{\mathrm{CEF}}^{\mathrm{O,A}(2)}(\boldsymbol{r})_{(1,-1)} = \left(V_{\mathrm{CEF}}^{\mathrm{O,A}(2)}(\boldsymbol{r})_{(-1,1)}\right)^* = \mathcal{U}_1^{\mathrm{O,A}}\delta^2 e^{-2\mathrm{i}\alpha}. \end{aligned} \tag{4.11}$$

Here, $V_{\rm CEF}^{\rm O,A}(\boldsymbol{r})_{(m',m)}$ denotes $\langle lm'|V_{\rm CEF}^{\rm O,A}(\boldsymbol{r})|lm\rangle$, and $\mathcal{V}$ and $\mathcal{U}$ are real parameters that complexly depend on the expectation value of the power $r$, $\bar{r^p} = \int |R_{4f}(r)|^2 r^p r^2 dr$. Note that $\mathcal{U}/\mathcal{V}$ is of the order of $10^2$.

**CEF from the Zr ions**

We can employ a similar analysis for the CEF induced by the Zr ions. With the in-plane deviation of the Pr ions, the relative positions of the Zr site are represented as

$$
\begin{aligned}
&\boldsymbol{R}_1 = (R_1, \pi/2, \phi_1), \quad R_1 = \frac{a}{2}\left[1 - 4\delta\sin\left(\alpha + \frac{\pi}{3}\right) + 4\delta^2\right]^{1/2}, \quad \phi = \tan^{-1}\left[\frac{1-4\delta\sin\alpha}{\sqrt{3}-4\delta\cos\alpha}\right],\\
&\boldsymbol{R}_2 = (R_2, \pi/2, \phi_2), \quad R_2 = \frac{a}{2}\left[1 - 4\delta\sin\alpha + 4\delta^2\right]^{1/2}, \qquad\quad \phi = \tan^{-1}\left[\frac{1-2\delta\sin\alpha}{-2\delta\cos\alpha}\right],\\
&\boldsymbol{R}_3 = (R_3, \pi/2, \phi_3), \quad R_3 = \frac{a}{2}\left[1 - 4\delta\sin\left(\alpha - \frac{\pi}{3}\right) + 4\delta^2\right]^{1/2}, \quad \phi = \tan^{-1}\left[\frac{1-4\delta\sin\alpha}{-\sqrt{3}-4\delta\cos\alpha}\right],\\
&\boldsymbol{R}_4 = (R_4, \pi/2, \phi_4), \quad R_4 = \frac{a}{2}\left[1 + 4\delta\sin\left(\alpha + \frac{\pi}{3}\right) + 4\delta^2\right]^{1/2}, \quad \phi = \tan^{-1}\left[\frac{-1-4\delta\sin\alpha}{-\sqrt{3}-4\delta\cos\alpha}\right],\\
&\boldsymbol{R}_5 = (R_5, \pi/2, \phi_5), \quad R_5 = \frac{a}{2}\left[1 + 4\delta\sin\alpha + 4\delta^2\right]^{1/2}, \qquad\quad \phi = \tan^{-1}\left[\frac{-1-4\delta\sin\alpha}{-2\delta\cos\alpha}\right],\\
&\boldsymbol{R}_6 = (R_6, \pi/2, \phi_6), \quad R_6 = \frac{a}{2}\left[1 + 4\delta\sin\left(\alpha - \frac{\pi}{3}\right) + 4\delta^2\right]^{1/2}, \quad \phi = \tan^{-1}\left[\frac{-1-4\delta\sin\alpha}{\sqrt{3}-4\delta\cos\alpha}\right].
\end{aligned}
\tag{4.12}
$$

Therefore, the CEF from the Zr ions is

$$
V_{\rm CEF}^{\rm Zr}(\boldsymbol{r}) = -\sum_{i=1}^{6}\sum_{k=0}^{\infty}\sum_{m=-k}^{k}\sqrt{\frac{4\pi}{2k+1}}\frac{4e^2}{R_i}\left(\frac{r}{R_i}\right)^k Y_{km}^*(\pi/2,\phi_i)C_m^{(k)}(\theta,\phi). \tag{4.13}
$$

Similar to the previous case, the matrix elements $\langle lm'|V_{\rm CEF}^{\rm Zr}(\boldsymbol{r})|lm\rangle$ are finite only when $k \leq 6$, and $m'-m$ are even. Each matrix element of $\langle lm'|V_{\rm CEF}^{\rm Zr}(\boldsymbol{r})|lm\rangle = \langle lm'|V_{\rm CEF}^{\rm Zr(0)}(\boldsymbol{r})|lm\rangle + \langle l,m'|V_{\rm CEF}^{\rm Zr(2)}(\boldsymbol{r})|lm\rangle$ is expressed as follows:

$$
\begin{aligned}
&V_{\rm CEF}^{\rm Zr(0)}(\boldsymbol{r})_{(\pm3,\pm3)} = \mathcal{V}_3^{\rm Zr}, \qquad V_{\rm CEF}^{\rm Zr(0)}(\boldsymbol{r})_{(\pm2,\pm2)} = \mathcal{V}_2^{\rm Zr}, \qquad V_{\rm CEF}^{\rm Zr(0)}(\boldsymbol{r})_{(\pm1,\pm1)} = \mathcal{V}_1^{\rm Zr},\\
&V_{\rm CEF}^{\rm Zr(0)}(\boldsymbol{r})_{(\pm0,\pm0)} = \mathcal{V}_0^{\rm Zr}, \quad V_{\rm CEF}^{\rm Zr(0)}(\boldsymbol{r})_{(3,-3)} = \left(V_{\rm CEF}^{\rm Zr(0)}(\boldsymbol{r})_{(-3,3)}\right)^* = \mathcal{V}_6^{\rm Zr},\\
&V_{\rm CEF}^{\rm Zr(2)}(\boldsymbol{r})_{(3,1)} = \left(V_{\rm CEF}^{\rm Zr(2)}(\boldsymbol{r})_{(1,3)}\right)^* = V_{\rm CEF}^{\rm Zr(2)}(\boldsymbol{r})_{(-1,-3)} = \left(V_{\rm CEF}^{\rm Zr(2)}(\boldsymbol{r})_{(-3,-1)}\right)^* = \mathcal{U}_3^{\rm Zr}\delta^2 e^{-2{\rm i}\alpha},\\
&V_{\rm CEF}^{\rm Zr(2)}(\boldsymbol{r})_{(2,0)} = \left(V_{\rm CEF}^{\rm Zr(2)}(\boldsymbol{r})_{(0,2)}\right)^* = V_{\rm CEF}^{\rm Zr(2)}(\boldsymbol{r})_{(0,-2)} = \left(V_{\rm CEF}^{\rm Zr(2)}(\boldsymbol{r})_{(-2,0)}\right)^* = \mathcal{U}_2^{\rm Zr}\delta^2 e^{-2{\rm i}\alpha},\\
&V_{\rm CEF}^{\rm Zr(2)}(\boldsymbol{r})_{(1,-1)} = \left(V_{\rm CEF}^{\rm Zr(2)}(\boldsymbol{r})_{(-1,1)}\right)^* = \mathcal{U}_1^{\rm Zr}\delta^2 e^{-2{\rm i}\alpha},\\
&V_{\rm CEF}^{\rm Zr(2)}(\boldsymbol{r})_{(3,-1)} = \left(V_{\rm CEF}^{\rm Zr(2)}(\boldsymbol{r})_{(-1,3)}\right)^* = V_{\rm CEF}^{\rm Zr(2)}(\boldsymbol{r})_{(1,-3)} = \left(V_{\rm CEF}^{\rm Zr(2)}(\boldsymbol{r})_{(-3,1)}\right)^* = \mathcal{U}_4^{\rm Zr}\delta^2 e^{2{\rm i}\alpha},\\
&V_{\rm CEF}^{\rm Zr(2)}(\boldsymbol{r})_{(2,-2)} = \left(V_{\rm CEF}^{\rm Zr(2)}(\boldsymbol{r})_{(-2,2)}\right)^* = \mathcal{U}_5^{\rm Zr}\delta^2 e^{2{\rm i}\alpha}.
\end{aligned}
\tag{4.14}
$$

### CEF from the oxygen ions at the B sites

As shown in the left panel of Fig. 4.3, oxygen ions at the B sites do not reside on the local $xy$ plane. Three of them reside on the $z = z_0$ plane and the others are on the $z = -z_0$ plane, which reduces the CEF symmetry from $D_{6d}$ to $D_{3d}$. Their equilibrium positions are represented using the parameter $\eta$ as $\boldsymbol{R}_1^0 = (\sqrt{6}a(\frac{1}{8}-\eta), 0, \sqrt{3}\eta a), \boldsymbol{R}_2^0 = (\frac{\sqrt{6}a}{2}(\frac{1}{8}-\eta), \frac{3\sqrt{2}a}{2}(\frac{1}{8}-\eta), -\sqrt{3}\eta a), \boldsymbol{R}_2^0 = (-\frac{\sqrt{6}a}{2}(\frac{1}{8}-\eta), \frac{3\sqrt{2}a}{2}(\frac{1}{8}-\eta), \sqrt{3}\eta a), \boldsymbol{R}_4^0 = -\boldsymbol{R}_1^0, \boldsymbol{R}_5^0 = -\boldsymbol{R}_2^0$, and $\boldsymbol{R}_6^0 = -\boldsymbol{R}_3^0$. Although their relative positions in the presence of Pr ion deviation is not presented owing to their extreme complexity, we obtain the CEF from the oxygen ions at the B sites as

$$V_{\mathrm{CEF}}^{\mathrm{O,B}}(\boldsymbol{r}) = \sum_{i=1}^{6}\sum_{k=0}^{\infty}\sum_{m=-k}^{k}\sqrt{\frac{4\pi}{2k+1}}\frac{2e^2}{R_i}\left(\frac{r}{R_i}\right)^k Y_{km}^*(\theta_i,\phi_i)\, C_m^{(k)}(\theta,\phi), \tag{4.15}$$

where $\boldsymbol{R}_i = (R_i, \theta_i, \phi_i)$ are the oxygen ions' relative locations in the presence of Pr ion deviation. Of particular importance is the finite nature of the matrix elements $\langle lm'|V_{\mathrm{CEF}}^{\mathrm{O,B}}(\boldsymbol{r})|lm\rangle$ for odd $m'-m$, which contrasts with the above two cases. Then, each matrix element of $\langle lm'|V_{\mathrm{CEF}}^{\mathrm{O,B}}(\boldsymbol{r})|lm\rangle = \langle lm'|V_{\mathrm{CEF}}^{\mathrm{O,B}(0)}(\boldsymbol{r})|lm\rangle + \langle lm'|V_{\mathrm{CEF}}^{\mathrm{O,B}(2)}(\boldsymbol{r})|lm\rangle$ is obtained. However, these are not shown here owing to space limitation. Instead, the combined CEF effect is provided in the next section.

### Dislocation-induced emergent transverse field

Combining all three CEF effects, we can derive the total CEF Hamiltonian as $V_{\mathrm{CEF}} = V_{\mathrm{CEF}}^{(0)} + V_{\mathrm{CEF}}^{(2)}$, where $V_{\mathrm{CEF}}^{(i)}$ indicates the $i$-th order term in terms of $\delta = u/a$. The explicit form is

$$\begin{aligned}
&V_{\mathrm{CEF}}^{(0)} = \sum_{m',m}\sum_{\sigma} V_{\mathrm{CEF},(m',m)}^{(0)} f_{m'\sigma}^{\dagger} f_{m\sigma},\\
&V_{\mathrm{CEF},(\pm3,\pm3)}^{(0)} = \mathcal{V}_3, \quad V_{\mathrm{CEF},(\pm2,\pm2)}^{(0)} = \mathcal{V}_2, \quad V_{\mathrm{CEF},(\pm1,\pm1)}^{(0)} = \mathcal{V}_1,\\
&V_{\mathrm{CEF},(0,0)}^{(0)} = \mathcal{V}_0, \quad V_{\mathrm{CEF},(3,-3)}^{(0)} = \left(V_{\mathrm{CEF},(-3,3)}^{(0)}\right)^* = \mathcal{V}_4,\\
&V_{\mathrm{CEF},(3,0)}^{(0)} = \left(V_{\mathrm{CEF},(0,3)}^{(0)}\right)^* = -V_{\mathrm{CEF},(0,-3)}^{(0)} = -\left(V_{\mathrm{CEF},(-3,0)}^{(0)}\right)^* = \mathcal{V}_5,\\
&V_{\mathrm{CEF},(2,-1)}^{(0)} = \left(V_{\mathrm{CEF},(-1,2)}^{(0)}\right)^* = -V_{\mathrm{CEF},(1,-2)}^{(0)} = -\left(V_{\mathrm{CEF},(-2,1)}^{(0)}\right)^* = \mathcal{V}_6,
\end{aligned} \tag{4.16}$$

$$
\begin{aligned}
&V^{(2)}_{\mathrm{CEF}} = \sum_{m',m}\sum_{\sigma} V^{(2)}_{\mathrm{CEF},(m',m)} f^{\dagger}_{m'\sigma} f_{m\sigma},\\
&V^{(2)}_{\mathrm{CEF},(3,2)} = \left(V^{(2)}_{\mathrm{CEF},(2,3)}\right)^{*} = -V^{(2)}_{\mathrm{CEF},(-2,-3)} = -\left(V^{(2)}_{\mathrm{CEF},(-3,-2)}\right)^{*} = \mathcal{U}_0\delta^2 e^{2\mathrm{i}\alpha}\\
&V^{(2)}_{\mathrm{CEF},(3,1)} = \left(V^{(2)}_{\mathrm{CEF},(1,3)}\right)^{*} = V^{(2)}_{\mathrm{CEF},(-1,-3)} = \left(V^{(2)}_{\mathrm{CEF},(-3,-1)}\right)^{*} = \mathcal{U}_1\delta^2 e^{-2\mathrm{i}\alpha}\\
&V^{(2)}_{\mathrm{CEF},(3,-1)} = \left(V^{(2)}_{\mathrm{CEF},(-1,3)}\right)^{*} = V^{(2)}_{\mathrm{CEF},(1,-3)} = \left(V^{(2)}_{\mathrm{CEF},(-3,1)}\right)^{*} = \mathcal{U}_2\delta^2 e^{2\mathrm{i}\alpha}\\
&V^{(2)}_{\mathrm{CEF},(3,-2)} = \left(V^{(2)}_{\mathrm{CEF},(-2,3)}\right)^{*} = -V^{(2)}_{\mathrm{CEF},(2,-3)} = -\left(V^{(2)}_{\mathrm{CEF},(-3,2)}\right)^{*} = \mathcal{U}_3\delta^2 e^{-2\mathrm{i}\alpha}\\
&V^{(2)}_{\mathrm{CEF},(2,1)} = \left(V^{(2)}_{\mathrm{CEF},(1,2)}\right)^{*} = -V^{(2)}_{\mathrm{CEF},(-1,-2)} = -\left(V^{(2)}_{\mathrm{CEF},(-2,-1)}\right)^{*} = \mathcal{U}_4\delta^2 e^{2\mathrm{i}\alpha}\\
&V^{(2)}_{\mathrm{CEF},(2,0)} = \left(V^{(2)}_{\mathrm{CEF},(0,2)}\right)^{*} = V^{(2)}_{\mathrm{CEF},(0,-2)} = \left(V^{(2)}_{\mathrm{CEF},(-2,0)}\right)^{*} = \mathcal{U}_5\delta^2 e^{-2\mathrm{i}\alpha}\\
&V^{(2)}_{\mathrm{CEF},(2,-2)} = \left(V^{(2)}_{\mathrm{CEF},(-2,2)}\right)^{*} = \mathcal{U}_6\delta^2 e^{2\mathrm{i}\alpha}\\
&V^{(2)}_{\mathrm{CEF},(1,0)} = \left(V^{(2)}_{\mathrm{CEF},(0,1)}\right)^{*} = -V^{(2)}_{\mathrm{CEF},(0,-1)} = -\left(V^{(2)}_{\mathrm{CEF},(-1,0)}\right)^{*} = \mathcal{U}_7\delta^2 e^{2\mathrm{i}\alpha}\\
&V^{(2)}_{\mathrm{CEF},(1,-1)} = \left(V^{(2)}_{\mathrm{CEF},(-1,1)}\right)^{*} = \mathcal{U}_8\delta^2 e^{-2\mathrm{i}\alpha}
\end{aligned}
\tag{4.17}
$$

where $f^{\dagger}_{m\sigma}$ ($f_{m\sigma}$) is a creation (annihilation) operator of the $f$ electron with a magnetic quantum number $m$ and spin $\sigma$, and $\mathcal{V}_i$ and $\mathcal{U}_i$ are real crystal field parameters. It is once again emphasised that $\mathcal{U}/\mathcal{V}$ is of the order of $10^2$.

As shown in Section 1.2.3, the ground state $J$-multiplet of the Pr ion is the $J = 4$ nine-fold state. To examine the CEF splitting of the ground state $J$-multiplet, we must calculate the matrix element with regard to the basis functions $|JM\rangle$ ($J = 4, M = -4, -3, \ldots, 4$). Employing the $LS$-coupling scheme, the states $|JM\rangle$ are expanded by Clebsch–Gordan coefficients as

$$
\begin{aligned}
&|JM\rangle\\
&= \sum_{m_L,m_S} \langle L=5, m_L; S=1, m_S|JM\rangle |L=5, m_L; S=1, m_S\rangle\\
&= \sum_{\substack{m_{\ell_1},\sigma_1\\ m_{\ell_2},\sigma_2}} \langle \ell_1=3, m_{\ell_1}; \ell_2=3, m_{\ell_2}|L=5, m_{\ell_1}+m_{\ell_2}\rangle \langle s_1=1/2, \sigma_1; s_2=1/2, \sigma_2|S=1, \sigma_1+\sigma_2\rangle\\
&\qquad \langle L=5, m_{\ell_1}+m_{\ell_2}; S=1, \sigma_1+\sigma_2|JM\rangle f^{\dagger}_{m_{\ell_1}\sigma_1} f^{\dagger}_{m_{\ell_2}\sigma_2}|0\rangle\\
&\equiv \sum_{\substack{m_{\ell_1},m_{\ell_2}\\ \sigma_1,\sigma_2}} \mathcal{C}^{M}_{m_{\ell_1},m_{\ell_2},\sigma_1,\sigma_2} f^{\dagger}_{m_{\ell_1}\sigma_1} f^{\dagger}_{m_{\ell_2}\sigma_2}|0\rangle.
\end{aligned}
\tag{4.18}
$$

Using this result, we obtain

$$\langle JM'|V_{\mathrm{CEF}}|JM\rangle = \sum_{\substack{m'_{\ell_1},m'_{\ell_2}\\ \sigma'_1,\sigma'_2}} \sum_{\substack{m_{\ell_1},m_{\ell_2}\\ \sigma_1,\sigma_2}} \sum_{\alpha,\beta,\sigma} \mathcal{C}^{M'}_{m'_{\ell_1},m'_{\ell_2},\sigma'_1,\sigma'_2} V_{\mathrm{CEF},(\alpha,\beta)} \mathcal{C}^{M}_{m_{\ell_1},m_{\ell_2},\sigma_1,\sigma_2} \langle 0| f_{m'_{\ell_2}\sigma_2} f_{m'_{\ell_1}\sigma_1} f^\dagger_{\alpha\sigma} f_{\beta\sigma} f^\dagger_{m_{\ell_1}\sigma_1} f^\dagger_{m_{\ell_2}\sigma_2} |0\rangle, \tag{4.19}$$

and

$$\begin{aligned}
\langle 0| f_{m'_{\ell_2}\sigma_2} f_{m'_{\ell_1}\sigma_1} f^\dagger_{\alpha\sigma} f_{\beta\sigma} f^\dagger_{m_{\ell_1}\sigma_1} f^\dagger_{m_{\ell_2}\sigma_2} |0\rangle &= \delta_{\beta,m_{\ell_1}}\delta_{\sigma,\sigma_1}\langle f_{m'_{\ell_2}\sigma_2} f_{m'_{\ell_1}\sigma_1} f^\dagger_{\alpha\sigma} f^\dagger_{m_{\ell_2}\sigma_2}\rangle \\
&\quad - \delta_{\beta,m_{\ell_2}}\delta_{\sigma,\sigma_2}\langle f_{m'_{\ell_2}\sigma_2} f_{m'_{\ell_1}\sigma_1} f^\dagger_{\alpha\sigma} f^\dagger_{m_{\ell_1}\sigma_1}\rangle \\
&= \delta_{\beta,m_{\ell_1}}\delta_{\sigma,\sigma_1}\delta_{\alpha,m'_{\ell_1}}\delta_{\sigma,\sigma'_1}\delta_{m'_{\ell_2},m_{\ell_2}}\delta_{\sigma'_2,\sigma_2} \\
&\quad - \delta_{\beta,m_{\ell_1}}\delta_{\sigma,\sigma_1}\delta_{\alpha,m'_{\ell_2}}\delta_{\sigma,\sigma'_2}\delta_{m'_{\ell_1},m_{\ell_2}}\delta_{\sigma'_1,\sigma_2} \\
&\quad - \delta_{\beta,m_{\ell_2}}\delta_{\sigma,\sigma_2}\delta_{\alpha,m'_{\ell_1}}\delta_{\sigma,\sigma'_1}\delta_{m'_{\ell_2},m_{\ell_1}}\delta_{\sigma'_2,\sigma_1} \\
&\quad + \delta_{\beta,m_{\ell_2}}\delta_{\sigma,\sigma_2}\delta_{\alpha,m'_{\ell_2}}\delta_{\sigma,\sigma'_2}\delta_{m'_{\ell_1},m_{\ell_1}}\delta_{\sigma'_1,\sigma_1},
\end{aligned} \tag{4.20}$$

which yields

$$\begin{aligned}
\langle JM'|V_{\mathrm{CEF}}|JM\rangle = \sum_{\alpha,\beta,\gamma}\sum_{\sigma,\sigma'} V_{\mathrm{CEF},(\alpha,\beta)} \Big[ &\mathcal{C}^{M'}_{\alpha,\gamma,\sigma,\sigma'}\mathcal{C}^{M}_{\beta,\gamma,\sigma,\sigma'} - \mathcal{C}^{M'}_{\gamma,\alpha,\sigma,\sigma'}\mathcal{C}^{M}_{\beta,\gamma,\sigma',\sigma} \\
&- \mathcal{C}^{M'}_{\alpha,\gamma,\sigma,\sigma'}\mathcal{C}^{M}_{\gamma,\beta,\sigma',\sigma} + \mathcal{C}^{M'}_{\gamma,\alpha,\sigma,\sigma'}\mathcal{C}^{M}_{\gamma,\beta,\sigma,\sigma'} \Big].
\end{aligned} \tag{4.21}$$

To analyse the effect of the dislocation-induced CEF on the local pseudospins, we treat $V^{(2)}_{\mathrm{CEF}}$ as a perturbation of the $D_{3d}$ symmetric CEF, $V^{(0)}_{\mathrm{CEF}}$. Diagonalising the Hamiltonian $\langle JM'|V^{(0)}_{\mathrm{CEF}}|JM\rangle$ reveals that the nine-fold $J = 4$ is separated into three doublets and three singlets, and the ground state is known to be the doublet [137]. The wave function of the ground state doublet is described as

$$|\pm\rangle = p|M = \pm 4\rangle \pm q|M = \pm 1\rangle + r|M = \mp 2\rangle, \tag{4.22}$$

where $p, q$, and $r$ are real parameters, which depend on the CEF parameters. Describing these states as $|\sigma\rangle = \sum_M \mathcal{C}^{\sigma}_{M}|JM\rangle$, where $\sigma = +, -$, we find that the first-order perturbative calculation using Eqs. (4.17) results in

$$\langle \sigma'|V^{(2)}_{\mathrm{CEF}}|\sigma\rangle = \sum_{M',M} \mathcal{C}^{\sigma'}_{M'}\mathcal{C}^{\sigma}_{M}\langle JM'|V^{(2)}_{\mathrm{CEF}}|JM\rangle = \begin{pmatrix} 0 & -\Gamma\delta^2 e^{2\mathrm{i}\alpha} \\ -\Gamma\delta^2 e^{-2\mathrm{i}\alpha} & 0 \end{pmatrix}. \tag{4.23}$$

Here, the parameter $\Gamma$ is real and complexly depends on the CEF parameters $\mathcal{U}$. Importantly, this result indicates that Pr ion dislocation induces the effective transverse field to the local pseudospin. Combined with the result of the previous section, we can derive

the total Hamiltonian as

$$\begin{aligned} H &= H_{\text{spin}} + H_{\text{ph}} + H_{\text{s-p}} \\ &= J\sum_{\langle ij\rangle} S_i^z S_j^z - \sum_i \boldsymbol{h}\cdot\hat{z}_\alpha S_i^z + \sum_{\boldsymbol{q}}\sum_s \hbar\omega_s(\boldsymbol{q})\left(a_{s\boldsymbol{q}}^\dagger a_{s\boldsymbol{q}} + \frac{1}{2}\right) \\ &\quad - \Delta_0 \sum_i \left[(u_{i,x}^2 - u_{i,y}^2)S_i^x - 2u_{i,x}u_{i,y}S_i^y\right]. \end{aligned} \tag{4.24}$$

Equation (4.23) is reformulated using the relations $u_x = u\cos\alpha$, $u_y = u\sin\alpha$, and $\Delta_0 = \Gamma/a^2$, and the site dependence of the deviation is assumed. An intriguing feature of this Hamiltonian is that, if the phonon part is removed and only the phonon-pseudospin coupling is considered, the aforementioned decoupled chain under an external [110] magnetic field can be regarded as an emergent one-dimensional transverse field Ising chain. We demonstrate that this treatment succeeds in explaining the unique $T_1$ behaviour of the NMR experiment throughout the rest of this chapter.

## 4.3 Benchmark calculations

In this section, several benchmark calculations are provided before describing the characteristic features of the NMR relaxation time under the [110] magnetic field. In the following calculation, we only consider the effect of phonons via phonon-pseudospin coupling for simplicity. Then, under the [110] magnetic field, the Hamiltonian of the decoupled chain is

$$H = J\sum_{\langle ij\rangle} S_i^z S_j^z - \Delta_0 \sum_i \left[(u_{i,x}^2 - u_{i,y}^2)S_i^x - 2u_{i,x}u_{i,y}S_i^y\right]. \tag{4.25}$$

Let us define $\alpha_i$ as the angle that specifies the direction of deviation of the Pr ion at site $i$. The complex transverse field term can be simplified by applying frame rotation about the $\hat{z}_i$ axis by angle $2\alpha_i$, which yields

$$H = J\sum_{\langle ij\rangle} \tilde{S}_i^z \tilde{S}_j^z - \Delta_0 u^2 \sum_i \tilde{S}_i^x. \tag{4.26}$$

Here, we assume that the amplitude of the deviation $u^2 = u_x^2 + u_y^2$ is independent of the site indices. Clearly, this is nothing more than a transverse field Ising model with the field $\Gamma = \Delta_0 u^2$. Because the lattice deviation is mainly caused by thermal fluctuations, we expect that the emergent transverse field $\Gamma$ depends on the temperature $T$ and becomes stronger as $T$ increases. Thus, the $T$ dependence of $\Gamma$ is first estimated by examining the thermal average $\langle u^2\rangle$.

Employing the notations in Section 4.2.1, the $\mu$ direction deviation of the Pr ion at unit cell $i$ with sublattice $\alpha$ is represented as

$$\begin{aligned} u_{i\alpha\mu} &= \frac{1}{\sqrt{N}}\sum_{\boldsymbol{q},s} \frac{1}{\sqrt{m_{\text{Pr}}}} e^{\mathrm{i}\boldsymbol{q}\cdot\boldsymbol{R}_i} U(\boldsymbol{q})_{\alpha\mu,s}\mathcal{U}_s(\boldsymbol{q}) \\ &= \frac{1}{\sqrt{N}}\sum_{\boldsymbol{q},s} e^{\mathrm{i}\boldsymbol{q}\cdot\boldsymbol{R}_i} U(\boldsymbol{q})_{\alpha\mu,s}\sqrt{\frac{\hbar}{2m_{\text{Pr}}\omega_s(\boldsymbol{q})}}(a_{s\boldsymbol{q}} + a_{s,-\boldsymbol{q}}^\dagger) \end{aligned} \tag{4.27}$$

where $m_{\rm Pr}$ is the mass of the Pr ion. Now, we focus on the acoustic modes $s = 0, 1, 2$ and assume that their dispersions are represented as $\omega_s(\boldsymbol{q}) = c_s|\boldsymbol{q}|$. We find

$$\begin{aligned}\langle u_{i\alpha}^2\rangle &= \sum_{\mu=x,y}\langle u_{i\alpha\mu}^2\rangle \\ &\sim \frac{1}{N}\sum_{\boldsymbol{q},\mu}\sum_{s=0,1,2}|U(\boldsymbol{q})_{\alpha\mu,s}|^2\frac{\hbar}{2m_{\rm Pr}c_s|\boldsymbol{q}|}\langle(a_{s\boldsymbol{q}}+a_{s,-\boldsymbol{q}}^\dagger)(a_{s,-\boldsymbol{q}}+a_{s\boldsymbol{q}}^\dagger)\rangle \\ &= \frac{1}{N}\sum_{\boldsymbol{q},\mu}\sum_{s=0,1,2}|U(\boldsymbol{q})_{\alpha\mu,s}|^2\frac{\hbar}{m_{\rm Pr}c_s|\boldsymbol{q}|}\langle a_{s\boldsymbol{q}}^\dagger a_{s\boldsymbol{q}}+\frac{1}{2}\rangle \\ &= \frac{1}{N}\sum_{\boldsymbol{q},\mu}\sum_{s=0,1,2}|U(\boldsymbol{q})_{\alpha\mu,s}|^2\frac{\hbar}{2m_{\rm Pr}c_s|\boldsymbol{q}|}\coth\frac{\beta\hbar c_s|\boldsymbol{q}|}{2}.\end{aligned} \tag{4.28}$$

Here, we assume that, at low temperatures, the $\boldsymbol{q} = 0$ contribution is important and remove the $q$-dependence of $U(\boldsymbol{q})_{\alpha\mu,s}$. Then, we obtain

$$\begin{aligned}\langle u_{i\alpha}^2\rangle &\simeq \frac{v_0}{2\pi^2}\sum_{\mu,s}\int dq\ q^2|U(\boldsymbol{q}=0)_{\alpha\mu,s}|^2\frac{\hbar}{2m_{\rm Pr}c_s|\boldsymbol{q}|}\coth\frac{\beta\hbar c_s|\boldsymbol{q}|}{2} \\ &= \frac{v_0}{2\pi^2}\sum_{\mu,s}\frac{1}{(\beta\hbar c_s)^2}\frac{\hbar}{2m_{\rm Pr}c_s}|U(\boldsymbol{q}=0)_{\alpha\mu,s}|^2\int_0^{\Theta_D/T}dx\ x\coth\frac{x}{2} \\ &\propto T^2,\end{aligned} \tag{4.29}$$

where $v_0$ is the volume of the unit cell and $\Theta_D$ is the Debye temperature which specify the cutoff of the integral. Because the temperature region we are interested in (a few Kelvin) is a finite temperature, but sufficiently smaller than the Debye temperature, the upper limit of the integral is approximated as infinity; therefore no temperature-dependent contribution from the integral is assumed. From this assumption, we can conclude that the main $T$ dependence of $\Gamma$ is approximated as $\Gamma \propto T^2$ at low temperatures. Following this estimation, we analyse the Hamiltonian defined on a one-dimensional decoupled chain

$$H = J\sum_{\langle ij\rangle}\tilde{S}_i^z\tilde{S}_j^z - \Gamma\sum_i\tilde{S}_i^x \tag{4.30}$$

with the temperature-dependent effective transverse field $\Gamma = \rho T^2$, where $\rho$ is a phenomenological parameter.

Here, we briefly estimate the amplitude of $\Gamma$. If we adopt the simplest phonon Hamiltonian on a one-dimensional chain as the starting point, that is,

$$H_{\rm ph} = \sum_{j,\mu}\frac{|\hat{p}_{j\mu}^2|}{2M} + \frac{K_\mu}{2}(u_{j\mu}-u_{j+1,\mu})^2 \tag{4.31}$$

we find $U(\boldsymbol{q})_{\alpha\mu,s} = 1$ without any approximation. Inserting the experimentally obtained values, Debye temperature $\Theta_D = 452$ K, $c_s = 3700$ m/s, and the lattice constant $a = 7.665 \times 10^{-10}$ m, we find that $\langle u^2\rangle \sim 3.57 \times 10^{-22}$ m$^2$ at 5 K [138]. From the CEF experiment, the order of the $\mathcal{V}$ parameters is approximately 10 meV; thus, the order of

the $\mathcal{U}$ parameters is approximately 1000 meV. Because the order of $\Gamma$ is $\Gamma \sim \mathcal{O}(\mathcal{U}\langle u^2\rangle/a^2)$, we can estimate that $\Gamma$ is of the order of a few Kelvin.

As is well known from the Jordan–Wigner transformation analysis, the one-dimensional transverse field Ising model Eq. (4.30) reveals a quantum phase transition (QPT) at $\Gamma = J/2$ for zero temperature (Appendix D). Based on this fact, we expect that the unique behaviour of the NMR relaxation time under the [110] field is associated with the "finite-temperature" QPT. In other words, at 5 K, where $1/T_1$ takes its minimum value, the relation $\Gamma = \rho T^2 = J/2$ is satisfied. In fact, because the amplitude of $J$ is also evaluated to be a few Kelvin, this scenario is not unrealistic. To corroborate this expectation, we must confirm the absence of anomalies in the physical quantities related to the "finite-temperature" QPT because such anomalies are not observed experimentally.

### 4.3.1 Specific heat

Here, the temperature dependence of the specific heat is provided for the non-Kramers pyrochlore model with a temperature-dependent transverse field:

$$H = J\sum_{\langle ij\rangle} S_i^z S_j^z - \sum_i \boldsymbol{h}\cdot\hat{z}_\alpha S_i^z - \Gamma\sum_i S_i^x, \tag{4.32}$$

where the summation is taken over all pyrochlore sites, and $\Gamma = \rho T^2$. Figure 4.4(a) shows the $T$ dependence of the specific heat under the strong [110] magnetic field. In this case, we expect that the forced ferromagnetic and decoupled chains emerge where the effective transverse field Ising model is realised (Eq. (4.30)). Thus, the QPT on the decoupled chains will be observed at finite temperatures. The calculation was conducted on the 16-site cluster of the pyrochlore lattice by employing the microcanonical TPQ method (mTPQ). The gray (blue) dashed (solid) line represents the result for $\Gamma = 0.0$ ($\Gamma = \rho T^2$), where $J = 1.0$ and $\rho = 0.02$. In this parameter set, the finite temperature QPT should occur at $T = 5.0$ K. As shown in Fig. 4.4(a), QPT signatures are not observed, and we find that the effect of the transverse field is almost negligible. This is consistent with the experimental results, in which no anomalies associated with the QPT are observed. We expect that such an anomaly is concealed by thermal fluctuations.

Remarkably, the presence of the QPT induced by the effective transverse field is proposed in the absence of external magnetic fields [139]. Motivated by this proposal, we examine the $T$ dependence of the specific heat without a magnetic field. In this case, a benign effect of the transverse field is found and traces of the QPT are not observed. From these results, we can conclude that the "finite temperature" QPT is concealed due to thermal fluctuations and is not captured within the usual physical quantity.

### 4.3.2 Magnetic susceptibility

Because it is often the case that the magnetic susceptibility is more sensitive to fluctuations, and effective transverse field is applied to examine the effect. Figure 4.5 presents the temperature dependence of the inverse susceptibility of Eq. (4.32). As in Fig. 4.4, the gray (blue) dashed (solid) line represents the results for $\Gamma = 0.0$ ($\Gamma = \rho T^2$), where $J = 1.0$ and $\rho = 0.02$. Whether the effective transverse magnetic field exists or not, a

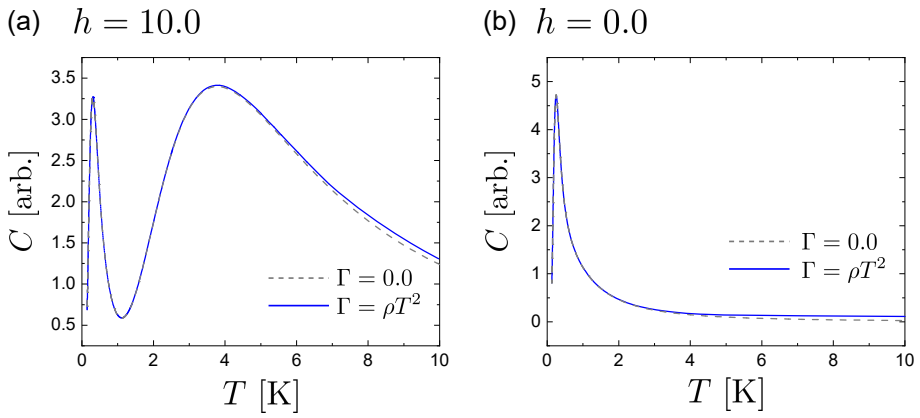


Figure 4.4. Temperature dependence of the specific heat for Eq. (4.32) with $J = 1.0$ and $\rho = 0.02$. The strength of the applied magnetic field along the [110] direction is (a): $h = 10.0$ (strong limit) and (b): $h = 0.0$. The gray (blue) dashed (solid) line represents the result for $\Gamma = 0.0$ ($\Gamma = \rho T^2$). We find that the effect of the transverse field is almost negligible in both cases.

Curie-Weiss behaviour can be found for a wide range of temperatures. If we consider the phonon-pseudospin coupling as an effective transverse field, its contribution to the susceptibility is approximated by the Van-Vleck-like behaviour as $1/\chi \propto \Gamma \propto T^2$. Thus, we expect an additional $T^2$ contribution to the Curie-Weiss-type inverse magnetic susceptibility. However, in this case, its effect is tiny enough to ignore and the effect on the overall magnetic susceptibility is limited. Naturally, no anomalies associated with the finite temperature QPT are observed.

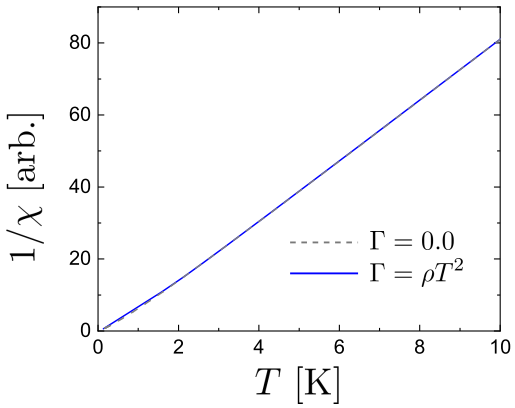


Figure 4.5. Temperature dependence of the inverse susceptibility for Eq. (4.32) with $J = 1.0$ and $\rho = 0.02$. The gray (blue) dashed (solid) line represents the results for $\Gamma = 0.0$ ($\Gamma = \rho T^2$). The Curie-Weiss behaviour is observed for a wide range of temperatures, and a significant transverse field effect is not observed, as expected.

## 4.4 NMR relaxation time

Thus far, we have verified that the effective transverse magnetic field and accompanying quantum transition do not affect physical quantities such as specific heat and magnetic susceptibility. In this section, it is proposed that the finite temperature QPT has an influence on the NMR relaxation time and can explain the experimental signatures. As shown in Fig. 4.1 and 4.6, the Zr ions are surrounded by six Pr ions on a hexagon, and the internal field is constructed from them. When the external field is sufficiently strong, only the Pr spins in the decoupled chain introduce fluctuations to the internal field. Because the fluctuations perpendicular to the external field contribute the relaxation time $1/T_1$, we will focus on this value.

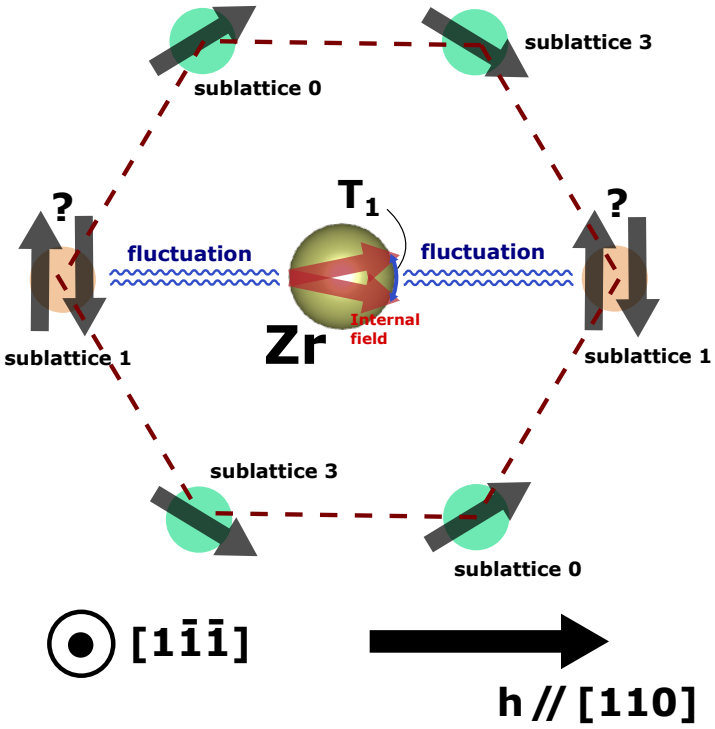


Figure 4.6. Schematic illustration of the NMR measurement for Zr ions in $Pr_2Zr_2O_7$ under a strong magnetic field along the [110] direction. The internal field at the Zr site is constructed from six Pr ions on the surrounding hexagon. Within the strong field limit, the internal field fluctuations perpendicular to the field's direction, which relate to the relaxation time $T_1$, are introduced by the decoupled chain.

We begin from the phonon-pseudospin coupling model of the decoupled chain under an external field along the [110] direction:

$$H = J\sum_j \sigma_j^z\sigma_{j+1}^z - \Gamma\sum_j \sigma_j^x \tag{4.33}$$

with $\Gamma = \rho T^2$. Here, we rewrite Eq. (4.30) using Pauli matrices and consider the rotation

about the local $y$ axis by angle $\pi/2$. The Hamiltonian in this new coordinate frame is

$$H = J\sum_j \tilde{\sigma}_j^x \tilde{\sigma}_{j+1}^x - \Gamma \sum_j \tilde{\sigma}_j^z. \tag{4.34}$$

This transverse field Ising model can be exactly solved with the Jordan–Wigner transformation (Appendix D) which yields

$$H = \sum_{k>0} \left( c_k^\dagger \; c_{-k} \right) \begin{pmatrix} 2J\cos k - 2\Gamma & 2\mathrm{i}J\sin k \\ -2\mathrm{i}J\sin k & -2J\cos k + 2\Gamma \end{pmatrix} \begin{pmatrix} c_k \\ c_{-k}^\dagger \end{pmatrix}, \tag{4.35}$$

where $c_k^\dagger (c_k)$ is the creation (annihilation) operator of a spinon with momentum $k$. We can derive the matrix form of Green's function from the formula $\mathcal{G}(k, \mathrm{i}\epsilon_\lambda)(\mathrm{i}\epsilon_\lambda - H(k)) = 1$. The explicit form is represented as

$$\mathcal{G}(k, \mathrm{i}\epsilon_\lambda) = \frac{1}{(\mathrm{i}\epsilon_\lambda)^2 - E_k^2} \begin{pmatrix} \mathrm{i}\epsilon_\lambda + 2(J\cos k - \Gamma) & 2\mathrm{i}J\sin k \\ -2\mathrm{i}J\sin k & \mathrm{i}\epsilon_\lambda - 2(J\cos k - \Gamma) \end{pmatrix}, \tag{4.36}$$

where $E_k = 2\sqrt{(J\cos k - \Gamma)^2 + J^2 \sin^2 k}$.

Let us calculate the NMR relaxation time using these formulae. The longitudinal relaxation rate, $1/T_1$, is given by

$$\frac{1}{T_1} = T \lim_{\omega \to 0} \sum_{j,j' \in \mathrm{hex}} \frac{\mathrm{Im}\chi_{jj'}^\perp(\omega + \mathrm{i}\delta)}{\omega}. \tag{4.37}$$

Here, $\chi_{jj'}^\perp(\omega + \mathrm{i}\delta)$ is obtained using the analytic continuation $\chi_{jj'}^\perp(\mathrm{i}\omega_\lambda)|_{\mathrm{i}\omega_\lambda \to \omega + \mathrm{i}\delta}$. Note that $\chi_{jj'}^\perp(\mathrm{i}\omega_\lambda) = \int_0^\beta d\tau e^{\mathrm{i}\omega_\lambda \tau} \chi_{jj'}^\perp(\tau)$, where $\chi_{jj'}^\perp(\tau) = \sum_\mu \langle \sigma_j^\mu(\tau) \sigma_{j'}^\mu(0) \rangle$, and the summation over $\mu$ is taken for two perpendicular axes to the external field direction [110] ($[1, -1, -1]$ and $[-1, 1, -2]$). When sites $j$ and $j'$ belong to the decoupled chain, considering the basis rotation introduced in Section 4.3 and at the beginning of this section, we obtain

$$\begin{aligned}
&\chi_{jj'}^\perp(\tau) \\
&= \langle \tilde{\sigma}_j^x(\tau) \tilde{\sigma}_{j'}^x(0) \rangle \\
&+ \left\langle \left[ \sin\left(2\alpha_j + \frac{\pi}{3}\right) \tilde{\sigma}_j^y + \cos\left(2\alpha_j + \frac{\pi}{3}\right) \tilde{\sigma}_j^z \right]_\tau \left[ \sin\left(2\alpha_{j'} + \frac{\pi}{3}\right) \tilde{\sigma}_{j'}^y + \cos\left(2\alpha_{j'} + \frac{\pi}{3}\right) \tilde{\sigma}_{j'}^z \right]_0 \right\rangle \\
&\to \langle \tilde{\sigma}_j^x(\tau) \tilde{\sigma}_{j'}^x(0) \rangle + \frac{1}{2} \delta_{jj'} \langle \tilde{\sigma}_j^y(\tau) \tilde{\sigma}_{j'}^y(0) + \tilde{\sigma}_j^z(\tau) \tilde{\sigma}_{j'}^z(0) \rangle.
\end{aligned} \tag{4.38}$$

In the final line, an average is taken over $\alpha_j$ and $\alpha_{j'}$. Because spins in forced ferromagnetic chains do not contribute to the NMR relaxation time within the strong field limit, we only need to consider this value. Henceforth, we focus on the final term $\chi_{jj'}^{zz}(\tau) = \frac{1}{2}\delta_{jj'} \langle \tilde{\sigma}_j^z(\tau) \tilde{\sigma}_{j'}^z(0) \rangle$ because it is analytically calculated and accurately describes

the experimental signatures. Then, we can evaluate the longitudinal relaxation time as

$$\begin{aligned}\frac{1}{T_1} &= T\lim_{\omega\to 0}\frac{1}{\omega}\mathrm{Im}\left[\int_0^\beta d\tau e^{\mathrm{i}\omega_\lambda\tau}\langle\tilde{\sigma}_s^z(\tau)\tilde{\sigma}_s^z(0)\rangle\right]_{\mathrm{i}\omega_\lambda\to\omega+\mathrm{i}\delta} \\ &= T\lim_{\omega\to 0}\frac{1}{\omega}\mathrm{Im}\left[\sum_q \underbrace{\frac{1}{N}\int_0^\beta d\tau e^{\mathrm{i}\omega_\lambda\tau}\langle\tilde{\sigma}_q^z(\tau)\tilde{\sigma}_{-q}^z(0)\rangle}_{\equiv\chi^{zz}(q,i\omega_\lambda)}\right]_{\mathrm{i}\omega_\lambda\to\omega+\mathrm{i}\delta}\end{aligned} \tag{4.39}$$

where the subscript $s$ denotes the site index of the decoupled chain. Because there are two sites that belong sublattice 1 in the hexagon, the factor $1/2$ in $\chi_{jj'}^{zz}(\tau)$ is cancelled out after the summation $\sum_{j,j'\in\mathrm{hex}}$. Applying a Fourier transformation with regard to the space and imaginary time, we find

$$\begin{aligned}\chi^{zz}(q,i\omega_\lambda) &= \frac{1}{N}\int_0^\beta d\tau e^{\mathrm{i}\omega_\lambda\tau}\langle\tilde{\sigma}_q^z(\tau)\tilde{\sigma}_{-q}^z(0)\rangle \\ &= \frac{1}{N}\int_0^\beta d\tau e^{\mathrm{i}\omega_\lambda\tau}\sum_{k,k'}\langle(2c_k^\dagger c_{k+q}-1)_\tau(2c_{k'}^\dagger c_{k'-q}-1)_0\rangle \\ &= \frac{4}{N}\int_0^\beta d\tau e^{\mathrm{i}\omega_\lambda\tau}\sum_k\langle c_k^\dagger(\tau)c_k(0)\rangle\langle c_{k+q}(\tau)c_{k+q}^\dagger(0)\rangle - \langle c_k^\dagger(\tau)c_{-k}^\dagger(0)\rangle\langle c_{k+q}(\tau)c_{-k-q}(0)\rangle \\ &= \frac{4}{N}\int_0^\beta d\tau e^{\mathrm{i}\omega_\lambda\tau}\sum_k \mathcal{G}_{22}(-k,\tau)\mathcal{G}_{11}(k+q,\tau) - \mathcal{G}_{21}(-k,\tau)\mathcal{G}_{12}(k+q,\tau) \\ &= -\frac{4k_BT}{N}\sum_{k,n}\mathcal{G}_{11}(k+q,\mathrm{i}\epsilon_n+\mathrm{i}\omega_\lambda)\mathcal{G}_{11}(k,\mathrm{i}\epsilon_n) - \mathcal{G}_{12}(k+q,\mathrm{i}\epsilon_n+\mathrm{i}\omega_\lambda)\mathcal{G}_{12}(k,\mathrm{i}\epsilon_n).\end{aligned} \tag{4.40}$$

The summation over the Matsubara frequency can be replaced by the integral along pass $C$ (Fig. 4.7) as follows:

$$\begin{aligned}&\chi^{zz}(q,i\omega_\lambda) \\ &= \frac{4}{N}\sum_k\oint_C\frac{dz}{2\pi\mathrm{i}}f(z)\left[\mathcal{G}_{11}(k+q,z+\mathrm{i}\omega_\lambda)\mathcal{G}_{11}(k,z) - \mathcal{G}_{12}(k+q,z+\mathrm{i}\omega_\lambda)\mathcal{G}_{12}(k,z)\right] \\ &= \frac{4}{N}\sum_k\int_{-\infty}^{\infty}\frac{d\epsilon}{2\pi\mathrm{i}}f(\epsilon)\left[\mathcal{G}_{11}(k+q,\epsilon+\mathrm{i}\omega_\lambda)\mathcal{G}_{11}(k,\epsilon+\mathrm{i}\delta) - \mathcal{G}_{11}(k+q,\epsilon+\mathrm{i}\omega_\lambda)\mathcal{G}_{11}(k,\epsilon-\mathrm{i}\delta)\right. \\ &\qquad + \mathcal{G}_{11}(k+q,\epsilon+\mathrm{i}\delta)\mathcal{G}_{11}(k,\epsilon-\mathrm{i}\omega_\lambda) - \mathcal{G}_{11}(k+q,\epsilon-\mathrm{i}\delta)\mathcal{G}_{11}(k,\epsilon-\mathrm{i}\omega_\lambda) \\ &\qquad - \mathcal{G}_{12}(k+q,\epsilon+\mathrm{i}\omega_\lambda)\mathcal{G}_{12}(k,\epsilon+\mathrm{i}\delta) + \mathcal{G}_{12}(k+q,\epsilon+\mathrm{i}\omega_\lambda)\mathcal{G}_{12}(k,\epsilon-\mathrm{i}\delta) \\ &\qquad \left.-\mathcal{G}_{12}(k+q,\epsilon+\mathrm{i}\delta)\mathcal{G}_{12}(k,\epsilon-\mathrm{i}\omega_\lambda) + \mathcal{G}_{12}(k+q,\epsilon-\mathrm{i}\delta)\mathcal{G}_{12}(k,\epsilon-\mathrm{i}\omega_\lambda)\right],\end{aligned} \tag{4.41}$$

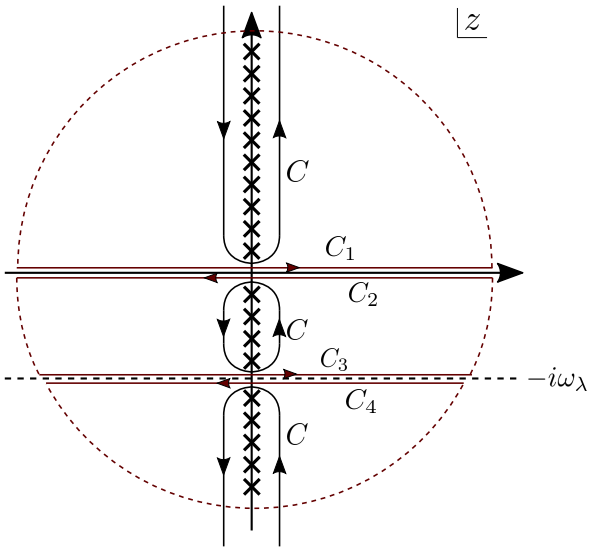


Figure 4.7. Pass of the integral. The integral along the original pass $C$ is divided into four contributions, the integral along $C_1, C_2, C_3$, and $C_4$, because the contribution from the arc (red dashed line) is zero.

where $f(z) = 1/(e^{\beta z}+1)$. From Eq. (4.36), the 11 and 12 components of Green's function are represented as

$$\mathcal{G}_{11}(k, \mathrm{i}\epsilon_\lambda) = \frac{|u_k|^2}{\mathrm{i}\epsilon_\lambda - E_k} + \frac{|v_k|^2}{\mathrm{i}\epsilon_\lambda + E_k}, \quad \mathcal{G}_{12}(k, \mathrm{i}\epsilon_\lambda) = \frac{u_k v_k^*}{\mathrm{i}\epsilon_\lambda - E_k} - \frac{u_k v_k^*}{\mathrm{i}\epsilon_\lambda + E_k}. \tag{4.42}$$

Here,

$$u_k = \sqrt{\frac{1}{2}\left(1 + \frac{2(J\cos k - \Gamma)}{E_k}\right)}, \quad v_k = -\mathrm{i}\frac{J\sin k}{|J\sin k|}\sqrt{\frac{1}{2}\left(1 - \frac{2(J\cos k - \Gamma)}{E_k}\right)}. \tag{4.43}$$

Then, defining the retarded (advanced) Green's function as $G^R(k,\epsilon) = \mathcal{G}(k, \mathrm{i}\epsilon_\lambda \to \epsilon + \mathrm{i}\delta)$ ($G^A(k,\epsilon) = \mathcal{G}(k, \mathrm{i}\epsilon_\lambda \to \epsilon - \mathrm{i}\delta)$), we obtain

$$\begin{aligned}
&\chi^{zz}(q, i\omega_\lambda) \\
&= \frac{4}{N}\sum_k \int_{-\infty}^{\infty} \frac{d\epsilon}{2\pi\mathrm{i}} f(\epsilon) \left[ G_{11}^R(k+q, \epsilon+\mathrm{i}\omega_\lambda) G_{11}^R(k,\epsilon) - G_{11}^R(k+q,\epsilon+\mathrm{i}\omega_\lambda) G_{11}^A(k,\epsilon) \right. \\
&\qquad + G_{11}^R(k+q,\epsilon) G_{11}^A(k,\epsilon-\mathrm{i}\omega_\lambda) - G_{11}^A(k+q,\epsilon) G_{11}^A(k,\epsilon-\mathrm{i}\omega_\lambda) \\
&\qquad - G_{12}^R(k+q,\epsilon+\mathrm{i}\omega_\lambda) G_{12}^R(k,\epsilon) + G_{12}^R(k+q,\epsilon+\mathrm{i}\omega_\lambda) G_{12}^A(k,\epsilon) \\
&\qquad \left. - G_{12}^R(k+q,\epsilon) G_{12}^A(k,\epsilon-\mathrm{i}\omega_\lambda) + G_{12}^A(k+q,\epsilon) G_{12}^A(k,\epsilon-\mathrm{i}\omega_\lambda) \right].
\end{aligned} \tag{4.44}$$

Then,

$$
\begin{aligned}
&\lim_{\omega\to 0}\frac{\mathrm{Im}\chi^{zz}(q,\omega+\mathrm{i}\delta)}{\omega}\\
&=-\frac{4}{N}\sum_k\int_{-\infty}^{\infty}\frac{d\epsilon}{2\pi}f(\epsilon)\left\{\mathrm{Re}\left[\frac{\partial}{\partial\epsilon}G^R_{11,k+q}(\epsilon)G^R_{11,k}(\epsilon)+G^A_{11,k+q}(\epsilon)\frac{\partial}{\partial\epsilon}G^A_{11,k}(\epsilon)\right]\right.\\
&\qquad\left.-\mathrm{Re}\left[\frac{\partial}{\partial\epsilon}G^R_{11,k+q}(\epsilon)G^A_{11,k}(\epsilon)+G^R_{11,k+q}(\epsilon)\frac{\partial}{\partial\epsilon}G^A_{11,k}(\epsilon)\right]\right\}\\
&=-\frac{4}{N}\sum_k\int_{-\infty}^{\infty}\frac{d\epsilon}{2\pi}f(\epsilon)\left\{\mathrm{Re}\left[\frac{\partial}{\partial\epsilon}G^R_{11,k+q}(\epsilon)G^R_{11,k}(\epsilon)+G^R_{11,k+q}(\epsilon)\frac{\partial}{\partial\epsilon}G^R_{11,k}(\epsilon)\right]\right.\\
&\qquad\left.-\mathrm{Re}\left[\frac{\partial}{\partial\epsilon}G^R_{11,k+q}(\epsilon)G^A_{11,k}(\epsilon)+G^R_{11,k+q}(\epsilon)\frac{\partial}{\partial\epsilon}G^A_{11,k}(\epsilon)\right]\right\}\\
&=\frac{4}{N}\sum_k\int_{-\infty}^{\infty}\frac{d\epsilon}{2\pi}f'(\epsilon)\mathrm{Re}\left[G^R_{11,k+q}(\epsilon)\left[G^R_{11,k}(\epsilon)-G^A_{11,k}(\epsilon)\right]\right]\\
&=\frac{4}{N}\sum_k\frac{\beta}{4\cosh^2\frac{\beta E_k}{2}}\frac{\delta}{(E_{k+q}-E_k)^2+\delta^2}(|u_{k+q}|^2|u_k|^2+|v_{k+q}|^2|v_k|^2-2u_{k+q}v^*_{k+q}u_kv^*_k)\\
&=\frac{4}{N}\sum_k\frac{\beta}{4\cosh^2\frac{\beta E_k}{2}}\frac{\delta}{(E_{k+q}-E_k)^2+\delta^2}(u_{k+q}u_k-v_{k+q}v_k)^2.
\end{aligned}
\tag{4.45}
$$

During this calculation, we employ $\pi\delta(x)\simeq\delta/(x^2+\delta^2)$. From this, we obtain

$$
\begin{aligned}
\frac{1}{T_1}&=\frac{1}{N}\sum_{k,q}\frac{1}{\cosh^2\frac{\beta E_k}{2}}\frac{\delta}{(E_{k+q}-E_k)^2+\delta^2}(u_{k+q}u_k-v_{k+q}v_k)^2\\
&=\frac{1}{N}\sum_{k,k'}\frac{1}{\cosh^2\frac{\beta E_k}{2}}\frac{\delta}{(E_k-E_{k'})^2+\delta^2}(u_ku_{k'}-v_kv_{k'})^2.
\end{aligned}
\tag{4.46}
$$

Now that we have derived the formula to calculate the NMR relaxation time, Fig. 4.8 presents the temperature dependences of $1/T_1$. The parameter $\rho=0.02$ was chosen, the QPT occurs at 5 K, and the values are normalised by the value at the QPT point.

Figure 4.8(a) shows the coupling constant dependence of the relaxation time behaviour. Below the QPT point and the low-temperature region, $1/T_1$ exhibits the power-law behaviour, $1/T_1\sim T^{-\alpha}$ and $\alpha$ decreases as the coupling constant increases. At the QPT point ($T=5$ K), $1/T_1$ reaches its minimum, which is observed in the experiment shown in Fig. 4.2(b). Above the QPT temperature, $1/T_1$ again increases; however, in this case, the rising slope is sharper when $J$ is greater, which is the opposite behaviour to the low-temperature region. Furthermore, in contrast with to the low-temperature region, the relaxation time is almost independent of the temperature for $T\gtrsim 8$ K. In the experiment shown in Fig. 4.2(b), $1/T_1$ is proportional to $T^{-\alpha}$ with $\alpha=0.8$–$1.0$ for the low-temperature region and becomes almost independent of the temperature for $T>10$ K, and the $J=0.5$ case behaves in a way that supports this.

Figure 4.8(b) describes the $\delta$ dependence of the relaxation time behaviour. We expect that impurities in the system affect the value of $\delta$. In the low-temperature region, we

find the power-law behaviour $1/T_1 \sim T^{-\alpha}$ and $\alpha$ decreases as $\delta$ decreases. In the high-temperature region, we again observe the opposite behaviour to the low-temperature region. The slope near the critical point is sharper when $\delta$ is small. Of particular importance in these results is that $1/T_1$ reaches its minimum value at the finite QPT point regardless of the choice of $J$ and $\delta$. Therefore, we can conclude that the unique behaviour of the temperature dependence of the NMR relaxation time is associated with the finite temperature QPT. Although the QPT is not captured by specific heat and susceptibility measurements, NMR measurements, which are sensitive to fluctuations, are able to reveal this.

The phase diagram of the one-dimensional transverse field Ising model helps to explain these results. Figure 4.9(a) is the $\Gamma$–$T$ phase diagram of the *usual* one-dimensional transverse field Ising model. The quantum phase transition occurs at the critical field $\Gamma = \Gamma_c$ when $T = 0$. Meanwhile, at finite temperatures, the region of quantum criticality is enlarged and transitions to the renormalized classical and quantum disordered phases are viewed as crossovers, as shown in Fig. 4.9(a) by the green-dashed lines. These crossover lines are determined by $T = |\Delta|$, where $\Delta$ is the spinon excitation gap. On these crossover lines, we naively expect the spinon fluctuation to increase as well as the QPT point ($T = 0$, $\Gamma = \Gamma_c$) and that this will enhance the nuclear spin relaxation, resulting in a small $T_1$. In other words, for finite temperatures, $1/T_1$ will become large towards the crossover areas. As a result, $1/T_1$ will be smaller on the finite temperature QPT line ($\Gamma = \Gamma_c$) in the middle of quantum critical zone than near the crossover regions (around the green dashed lines). Figure 4.9(b) depicts the value of $1/T_1$ on the $\Gamma$–T plane for the case $J = 0.5$ and $\delta = 1.0 \times 10^{-4}$. Because the effective transverse field in our situation is temperature dependent, $\Gamma$ and $T$ moves along the black-dashed line. White-dashed and red-solid lines indicate the crossover lines and the finite temperature QPT line, respectively. As predicted before, the value of $1/T_1$ gets smaller on the finite temperature QPT line than in the surrounding region. As the temperature is reduced in the current model, the parameters $(\Gamma, T)$ cross the finite temperature QPT line at 5 K; therefore, the inverse of the relaxation time $1/T_1$ behaves as if it is the smallest at 5 K. These scenarios are unaffected by the choice of $J$ or $\delta$.

Lastly, the effect of other terms in Eq. (4.38) is discussed. These terms appear in the NMR relaxation time calculation for the usual one-dimensional transverse field Ising model and have been extensively investigated in previous studies [140, 141]. In the low-temperature region of the usual transverse field Ising model, a previous study revealed that $1/T_1 \sim T^{-1}e^{\Delta/T}$, where $\Delta$ is the spinon excitation gap. This indicates that $1/T_1$ increases more rapidly than $T^{-1}$ as the temperature decreases. However, in the experiment shown in Fig. 4.2(b), $1/T_1 \sim T^{-0.8}$–$T^{-1}$ at the low temperature region. Thus, we expect that the contributions from $\langle\sigma^x(\tau)\sigma^x(0)\rangle$ and $\langle\sigma^y(\tau)\sigma^y(0)\rangle$ are not significant and the contribution from the term we have been focusing on is dominant. The NMR relaxation time behaviour for the quantum disordered regime ($\Gamma > J$) is only known for low temperatures ($1/T_1 \sim e^{-\Delta/T}$). In our case, the quantum disordered regime is reachable only for $T > 5$ K (relatively high temperature) and it is unclear whether the $1/T_1 \sim e^{-\Delta/T}$ behaviour is observed. In any case, this contribution can be predicted to be sub-dominant for the same reasons explained earlier.

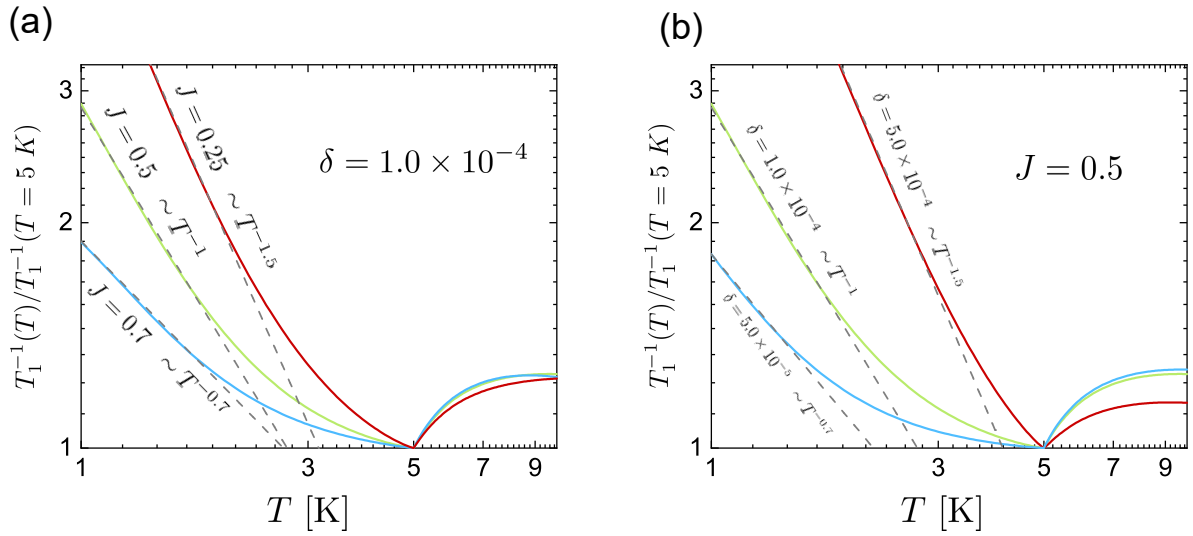


Figure 4.8. Temperature dependences of the inverse of the NMR relaxation time $1/T_1$. (a): Coupling constant $J$ dependence, and (b): $\delta$ dependence. The power-law behaviour varies depending on the parameter; however, all cases exhibit the behaviour of taking a minimum at the QPT point (5 K). The values in this figure are normalised by the value of the QPT point.

## 4.5 Conclusion

In this chapter, we analysed the phonon-pseudospin coupling effect on non-Kramers pyrochlore materials and revealed that the unique NMR relaxation time behaviour is described by considering its effect. Recent experiment studies in the temperature dependence of the NMR relaxation time for various field directions have clarified that the unique up-and-down behaviour is observed under the [110] magnetic field. Here, it is proposed that this behaviour is associated with the finite temperature quantum phase transition in the one-dimensional transverse field Ising chain.

In the first half of this chapter, we derived an explicit form of the phonon-pseudospin coupling of non-Kramers pyrochlore materials by employing point charge approximation. As is expected from the time-reversal even nature of the lattice deviation and the local quadrupolar moment, the resultant coupling form is represented as an effective transverse field. We clarified that, combined with one-dimensionality under the strong [110] magnetic field, this phonon-pseudospin coupling yields an emergent transverse field Ising model in the pyrochlore lattice.

Equipped with this result, we have investigated the temperature dependence of the NMR relaxation time in the latter half of this chapter. We derived an analytical form of the relaxation time by focussing on the $zz$ correlation. Remarkably, this term accurately describes the experimental result, and the unique up-and-down behaviour for $1/T_1$ has been obtained regardless of the choice in parameters. These results indicate that the NMR experiment succeeds in capturing evidence for the finite temperature quantum phase transition of an emergent transverse field Ising model. However, other experiments, such as specific heat and susceptibility measurements, cannot find any anomalies associated

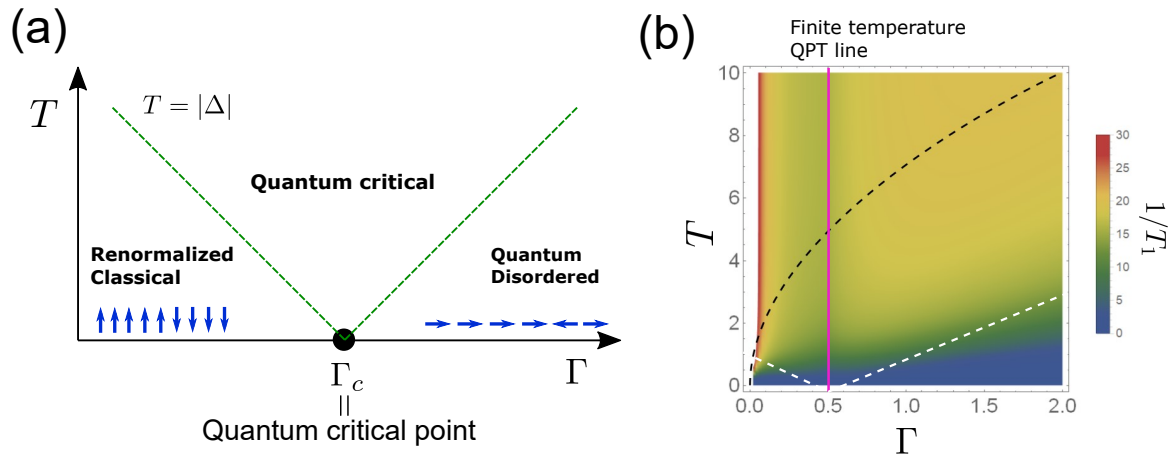


Figure 4.9. (a): $\Gamma$–$T$ phase diagram of the one-dimensional transverse field Ising model. At $T = 0$, the quantum phase transition occurs at the critical field $\Gamma_c$. Meanwhile, at finite temperatures, the quantum critical region expands and the transition is considered to be a crossover. Here, the green dashed line $T = |\Delta|$ indicates the crossover, where $\Delta$ is the spinon excitation gap. (b): Colour map of $1/T_1$ on the $\Gamma$–$T$ plane. The parameters $J = 0.5$ and $\delta = 1.0 \times 10^{-4}$ are chosen. Because the effective transverse field depends on the temperature, $\Gamma$ and $T$ moves along the black dashed line. The white dashed and red solid lines are the crossover in Fig. (a) and the finite temperature QPT line, respectively.

with this phase transition.

As a concluding remark, potential future prospects are provided. In the intermediate field region, chain-chain couplings are expected between the decoupled chains as a result of fluctuations in forced ferromagnetic chains. Though the NMR experiment has not been conducted for this regime, it might be possible to corroborate our scenario by taking such an interaction into account in this theory and comparing the result to future experiments.

# Chapter 5

# Summary

In this dissertation, various multipolar related phenomena in rare-earth pyrochlore materials were studied. Multipolar moments have attracted great attention as an emergent degree of freedom induced by the strong spin-orbit entanglement of rare-earth ions. Combined with other factors such as geometrical frustration and lattice fluctuation, they present a variety of interesting phenomena.

In Chapter 2, we classified rare-earth pyrochlore materials based on the ground state doublet; (i): non-Kramers, (ii): usual Kramers, and (iii): dipolar-octupolar. Among these, the non-Kramers and dipolar-octupolar cases possess a local multipolar moment and are expected to exhibit a number of intriguing multipolar related phenomena.

In Chapter 3, we focussed on the dipolar-octupolar system and proposed the existence of four different quantum spin liquid regimes, namely 0-flux octupolar quantum spin liquid (0-oQSL) and 0-flux dipolar quantum spin liquid (0-dQSL) in the unfrustrated parameter regime, and $\pi$-flux octupolar quantum spin liquid ($\pi$-oQSL) and $\pi$-flux dipolar quantum spin liquid ($\pi$-dQSL) in the frustrated parameter regime. In previous research, the flux degree of freedom was not considered because of the difficulty in accessing the frustrated parameter region. However, this study succeeded in capturing it by employing the exact diagonalisation (ED) method on a 32-site cluster. Analysing the equal-time and dynamical neutron structure factors using the ED calculation and classical Monte Carlo simulation and comparing the obtained results with the experimental signatures from $Ce_2Zr_2O_7$, we revealed that the $\pi$-oQSL phase is realised in real materials. This is completely different from the usual quantum spin ice phase in that the spin ice state is constructed by octupoles. This multipolar quantum spin ice discovery was one of the main results of this chapter. During the analysis of neutron scattering profiles, we noticed that it was not sufficient to distinguish all four quantum spin regimes. To tackle this problem, we extended the theory of magnetostriction to the present case, and showed that it is useful to distinguish between the four quantum spin liquids. This result indicates that the combination of ordinary and novel experimental techniques is required to uncover the intriguing properties of the dipolar-octupolar system.

In Chapter 4, the interaction between the multipolar moment and the lattice fluctuation, that is, phonons was discussed. Furthermore, by considering this phonon-pseudospin interaction with the effect of an external field, the nature of the peculiar NMR relaxation time behaviour observed in the [110] field direction was revealed. In non-Kramers py-

rochlore materials, the $x$ and $y$ components of the pseudospin consist of time-reversal even quadrupoles and can linearly couple with phonons. Because of this property, the phonon-pseudospin coupling can be regarded as an effective transverse field. In addition, applying the strong [110] magnetic field, we found that the pyrochlore lattice is divided into a series of forced ferromagnetic and decoupled chains. Considering the phonon-pseudospin coupling on the decoupled chains, the possible emergent one-dimensional transverse field Ising model was proposed in a three-dimensional frustrated magnet. Then, based on this proposal, we investigated the temperature dependences of the NMR relaxation time under the strong [110] magnetic field. The possibility of the unique NMR relaxation time behaviour in this situation corresponding to the finite temperature quantum phase transition of the transverse field Ising model was revealed. This was the main finding of this chapter.

To summarise this dissertation, future prospects are presented. Although we have clarified the existence a variety of quantum spin ices, the majority of their features remain unknown. For example, investigating the transport properties in multipolar quantum spin ice will be an interesting topic. The combination of the multipolar nature and spin liquid nature may result in unique transport behaviours. In addition, the phonon-pseudospin coupling discussed in Chapter 4 will have some influence on the transport properties of rare-earth pyrochlore materials. Because the phonon transport has not yet been studied in detail, this will also be a fascinating research direction.

# Appendix A

# Magnetostriction of non-Kramers and Kramers pyrochlores

## A.1 Model

As shown in Section 2.1, the symmetry-allowed generic nearest-neighbour pseudospin 1/2 model for non-Kramers pyrochlore materials is represented as

$$H_{\mathrm{NK}} = \sum_{\langle ij \rangle} \left[ J_{zz} S_i^z S_j^z - J_{\pm}(S_i^+ S_j^- + S_i^- S_j^+) + J_{\pm\pm}(\gamma_{ij} S_i^+ S_j^+ + \gamma_{ij}^* S_i^- S_j^-) \right], \tag{A.1}$$

where the summation is taken over all the nearest-neighbour sites $i$ and $j$. For the usual Kramers case, the time-reversal odd nature of pseudospins allows another coupling term, which yields

$$\begin{aligned} H_{\mathrm{K}} = \sum_{\langle ij \rangle} & J_{zz} S_i^z S_j^z - J_{\pm}(S_i^+ S_j^- + S_i^- S_j^+) + J_{\pm\pm}(\gamma_{ij} S_i^+ S_j^+ + \gamma_{ij}^* S_i^- S_j^-) \\ & + J_{z\pm} \left[ S_i^z (\zeta_{ij} S_j^+ + \zeta_{ij}^* S_j^-) + (\zeta_{ij} S_i^+ + \zeta_{ij}^* S_i^-) S_j^z \right], \end{aligned} \tag{A.2}$$

where the unimodular $4 \times 4$ matrix $\gamma$ is defined as

$$\gamma_{\mu\nu} = \begin{cases} 1 & \boldsymbol{x}_\mu - \boldsymbol{x}_\nu \in yz \text{ plane} \\ e^{\mathrm{i}2\pi/3} & \boldsymbol{x}_\mu - \boldsymbol{x}_\nu \in xz \text{ plane} \\ e^{-\mathrm{i}2\pi/3} & \boldsymbol{x}_\mu - \boldsymbol{x}_\nu \in xy \text{ plane} \end{cases}, \tag{A.3}$$

and $\zeta = -\gamma^*$. Note that pseudospin $S_i^\mu$ is represented in the local coordinate frame introduced in Section 3.1.

Under an applied magnetic field, the magnetic dipole moment couples at a linear order and to the quadrupolar moments at a quadratic order. The explicit form of the Zeeman

term is described as

$$H_{\mathrm{mag,NK}} = -\sum_t \sum_{\alpha=0}^{3} \boldsymbol{h}\cdot\hat{z}_\alpha S^z_{t\alpha} + \delta_1(h^x_\alpha h^z_\alpha S^x_{t\alpha} + h^y_\alpha h^z_\alpha S^y_{t\alpha}) + \delta_2\Gamma_2([(h^y_\alpha)^2 - (h^x_\alpha)^2]S^x_{t\alpha} + 2h^x_\alpha h^y_\alpha S^y_{t\alpha})$$
$$H_{\mathrm{mag,K}} = -\sum_t \sum_{\alpha=0}^{3} \boldsymbol{h}\cdot\left[\hat{z}_\alpha S^z_{t\alpha} + \frac{g_\perp}{g_z}(\hat{x}_\alpha S^x_{t\alpha} + \hat{y}_\alpha S^y_{t\alpha})\right]. \tag{A.4}$$

Here, $t$ indicates the index for the "up" tetrahedra, and $S^\mu_{t\alpha}$ is the $S^\mu$ moment on sublattice $\alpha$ of tetrahedron $t$. As a typical example, we take the estimated $g$-factor values of $Yb_2Ti_2O_7$: $(g_\perp, g_z) = (4.18, 1.77)$ [142].

## A.2 Classical analysis

As in the dipolar-octupolar case, the classical Hamiltonians (A.1) and (A.2) can be separated into the sum of the tetrahedra, $H_{\mathrm{NK/K}} = \sum_m H_m^{\mathrm{NK/K}}$, and $H_m$ can be rewritten in a block-diagonalised form using the basis of irreducible representations. The results are as follows:

$$H_{\mathrm{NK}} = \frac{1}{2}\sum_m \left[3J_{zz}M^2_{\Gamma_2} - 6J_\pm \boldsymbol{M}^2_{\Gamma_3} - J_{zz}\boldsymbol{M}^2_{\Gamma_{4a}} + (2J_\pm - 4J_{\pm\pm})\boldsymbol{M}^2_{\Gamma_{4b}} + (2J_\pm + 4J_{\pm\pm})\boldsymbol{M}^2_{\Gamma_5}\right],$$
$$H_{\mathrm{K}} = \frac{1}{2}\sum_m \left[3J_{zz}M^2_{\Gamma_2} - 6J_\pm \boldsymbol{M}^2_{\Gamma_3} - J_{zz}\boldsymbol{M}^2_{\Gamma_{4a}} + (2J_\pm - 4J_{\pm\pm})\boldsymbol{M}^2_{\Gamma_{4b}} + (2J_\pm + 4J_{\pm\pm})\boldsymbol{M}^2_{\Gamma_5}\right.$$
$$\left. -8J_{z\pm}\boldsymbol{M}_{\Gamma_{4a}}\cdot\boldsymbol{M}_{\Gamma_{4b}}\right], \tag{A.5}$$

with the constraint $M^2_{\Gamma_2} + \boldsymbol{M}^2_{\Gamma_3} + \boldsymbol{M}^2_{\Gamma_{4a}} + \boldsymbol{M}^2_{\Gamma_{4b}} + \boldsymbol{M}^2_{\Gamma_5} = 1$. The ground state is obtained by letting $|\boldsymbol{M}_k| = 1$ and the others equate to zero, where the coupling constant associated with the order parameter $\boldsymbol{M}_k$ is the smallest. The basis sets are provided in Table A.1, and the classical phase diagram is presented in Fig. A.1.

These classical non-Kramers/Kramers phase diagrams provide a variety of possible phases: in the non-Kramers case, a classical two-in two-out spin ice phase with $\Gamma_4$ symmetry, a coplanar antiferroquadrupolar ($\mathrm{cAFQ_L}$) phase with $\Gamma_5$ symmetry, another coplanar antiferroquadrupolar ($\overline{\mathrm{cAFQ}}_{\mathrm{L}}$) phase with $\Gamma_4$ symmetry, and a ferroquadrupolar ($\mathrm{FQ_L}$) phase with $\Gamma_3$ symmetry; in the Kramers case, a spin ice (SI) phase with $\Gamma_4$ symmetry, a splayed ferromagnet (SFM) phase with $\Gamma_4$ symmetry, a Palmer-Chalker (PC) phase with $\Gamma_5$ symmetry, and a one-dimensional manifold of states with $\Gamma_3$ symmetry. Key differences between Kramers and non-Kramers ions are (i) $J_{z\pm} \neq 0$, which causes mixing between the spin-ice and splayed ferromagnet phases and (ii) in Kramers ions, the magnetic field can couple at a linear order to the $xy$ components of the pseudospins. These differences are a consequence of the pseudospin components being mere dipole moments and are thus odd under time reversal.

Although these discussions are based on a classical analysis, they strongly indicate that quantum phases have origins in classical phases from parton mean-field theory (gMFT), as

explained in Section 2.1 and 2.2. Indeed, in gMFT, the classical SI phase gets promoted to a $U(1)$ QSL phase, which is characterised by the existence of deconfined bosonic spinons coupled to a $U(1)$ gauge field [69]. The other classically ordered phases get promoted to Higgs phases in gMFT, where the bosonic monopole condenses, thus eliminating the emergent gauge field.

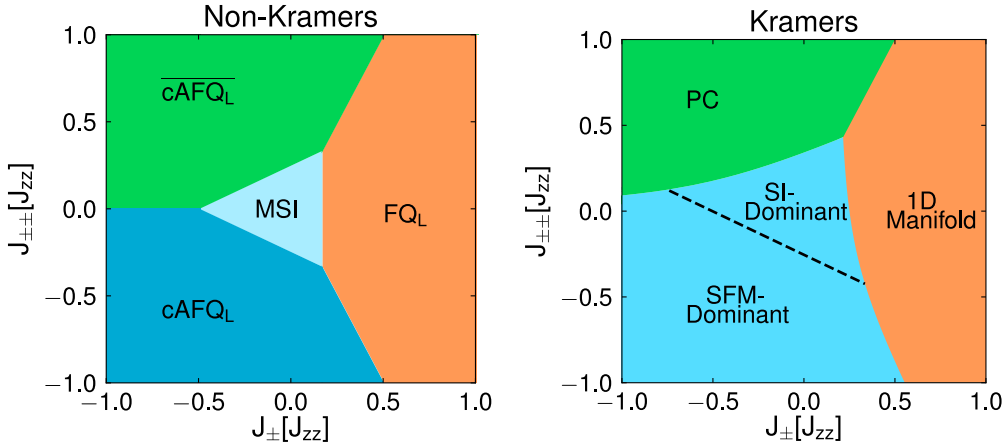


Figure A.1. (a): Classical phase diagram of non-Kramers ions. The depicted phases are classical spin ice (CSI), coplanar antiferroquadrupolar ($\text{cAFQ}_\text{L}$), a second coplanar antiferroquadrupolar ($\overline{\text{cAFQ}_\text{L}}$), and ferroquadrupolar ($\text{FQ}_\text{L}$). The subscript L is to indicate orderings in the local basis. $\text{cAFQ}_\text{L}$ and $\overline{\text{cAFQ}_\text{L}}$ are related by a local $C_{4z}$ rotation on each sublattice. (b): Classical phase diagram for the Kramers case ($J_{z\pm} = 0.25J_{zz}$). The depicted phases are spin ice (SI), splayed ferromagnet (SFM), Palmer-Chalker (PC), and the one-dimensional manifold of states. The black dashed line indicates an equal mixing of the SI and SFM phases and separates the SI-dominating phase and SFM-dominating phase.

Table A.1: Basis states for the magnetic orderings of Kramers and non-Kramers ions. Abbreviations: AIAO = all-in / all-out, PC = Palmer-Chalker, SI = spin ice, one-dimensional (1D) manifold of states, SFM = splayed ferromagnet, MSI= multipolar spin ice, $\mathrm{cAFQ_L}$, $\overline{\mathrm{cAFQ_L}}$ = coplanar anti-ferroquadrupolar, and $\mathrm{FQ_L}$ = ferro-quadrupolar. The two types of coplanar anti-ferroquadrupolar orders are related by a local $C_{4z}$ symmetry. The orderings are arranged into irreps of $T_d$, that is, the pyrochlore point group.

| Name | Kramers case | Order | non-Kramers case | Order |
|---|---|---|---|---|
| $\Gamma_2$ | $M_{\Gamma_2} = \frac{1}{2}(S_0^z + S_1^z + S_2^z + S_3^z)$ | AIAO | $M_{\Gamma_2} = \frac{1}{2}(S_0^z + S_1^z + S_2^z + S_3^z)$ | AIAO |
| $\Gamma_3$ | $\boldsymbol{M}_{\Gamma_3} = \frac{1}{2}\begin{pmatrix} S_0^x + S_1^x + S_2^x + S_3^x \\ S_0^y + S_1^y + S_2^y + S_3^y \end{pmatrix}$ | 1D Manifold | $\boldsymbol{M}_{\Gamma_3} = \frac{1}{2}\begin{pmatrix} S_0^x + S_1^x + S_2^x + S_3^x \\ S_0^y + S_1^y + S_2^y + S_3^y \end{pmatrix}$ | $\mathrm{FQ_L}$ |
| $\Gamma_5$ | $\boldsymbol{M}_{\Gamma_5} = \begin{pmatrix} \frac{1}{2}\left(S_0^y + S_1^y - S_2^y - S_3^y\right) \\ \frac{1}{4}(-\sqrt{3}S_0^x - S_0^y + \sqrt{3}S_1^x + S_1^y - \sqrt{3}S_2^x - S_2^y + \sqrt{3}S_3^x + S_3^y) \\ \frac{1}{4}(\sqrt{3}S_0^x - S_0^y - \sqrt{3}S_1^x + S_1^y - \sqrt{3}S_2^x + S_2^y + \sqrt{3}S_3^x - S_3^y) \end{pmatrix}$ | PC | $\boldsymbol{M}_{\Gamma_5} = \begin{pmatrix} \frac{1}{2}\left(S_0^x + S_1^x - S_2^x - S_3^x\right) \\ \frac{1}{4}\left(-S_0^x + \sqrt{3}S_0^y + S_1^x - \sqrt{3}S_1^y - S_2^x + \sqrt{3}S_2^y + S_3^x - \sqrt{3}S_3^y\right) \\ \frac{1}{4}\left(-S_0^x - \sqrt{3}S_0^y + S_1^x + \sqrt{3}S_1^y + S_2^x + \sqrt{3}S_2^y - S_3^x - \sqrt{3}S_3^y\right) \end{pmatrix}$ | $\mathrm{cAFQ_L}$ |
| $\Gamma_{4,a}$ | $\boldsymbol{M}_{T_1,A} = \frac{1}{2}\begin{pmatrix} S_0^z + S_1^z - S_2^z - S_3^z \\ S_0^z - S_1^z + S_2^z - S_3^z \\ S_0^z - S_1^z - S_2^z + S_3^z \end{pmatrix}$ | SI | $\boldsymbol{M}_{T_1,A} = \frac{1}{2}\begin{pmatrix} S_0^z + S_1^z - S_2^z - S_3^z \\ S_0^z - S_1^z + S_2^z - S_3^z \\ S_0^z - S_1^z - S_2^z + S_3^z \end{pmatrix}$ | MSI |
| $\Gamma_{4,b}$ | $\boldsymbol{M}_{T_1,B} = \begin{pmatrix} \frac{1}{2}\left(S_0^x + S_1^x - S_2^x - S_3^x\right) \\ \frac{1}{4}\left(-S_0^x + \sqrt{3}S_0^y + S_1^x - \sqrt{3}S_1^y - S_2^x + \sqrt{3}S_2^y + S_3^x - \sqrt{3}S_3^y\right) \\ \frac{1}{4}\left(-S_0^x - \sqrt{3}S_0^y + S_1^x + \sqrt{3}S_1^y + S_2^x + \sqrt{3}S_2^y - S_3^x - \sqrt{3}S_3^y\right) \end{pmatrix}$ | SFM | $\boldsymbol{M}_{T_1,B} = \begin{pmatrix} \frac{1}{2}\left(S_0^y + S_1^y - S_2^y - S_3^y\right) \\ \frac{1}{4}(-\sqrt{3}S_0^x - S_0^y + \sqrt{3}S_1^x + S_1^y - \sqrt{3}S_2^x - S_2^y + \sqrt{3}S_3^x + S_3^y) \\ \frac{1}{4}(\sqrt{3}S_0^x - S_0^y - \sqrt{3}S_1^x + S_1^y - \sqrt{3}S_2^x + S_2^y + \sqrt{3}S_3^x - S_3^y) \end{pmatrix}$ | $\overline{\mathrm{cAFQ_L}}$ |

## A.3 Magnetostriction

In this section, we first examine the coupling of the local pseudospin moments to the elastic normal modes and then derive the magnetostriction expression for the non-Kramers/Kramers case. As shown in Section 3.4.1, the cubic nature of the underlying Bravais lattice constrains the elastic energy to the form

$$\mathcal{F}_{\text{lattice}} = \frac{c_B}{2}\epsilon_B^2 + \frac{c_{11}-c_{12}}{2}\left(\epsilon_\mu^2+\epsilon_\nu^2\right) + \frac{c_{44}}{2}\left(\epsilon_{xy}^2+\epsilon_{yz}^2+\epsilon_{zx}^2\right), \tag{A.6}$$

where the crystal deformation is described by the components of the strain tensor in the global coordinate frame $\epsilon_{ij}$, and $c_{ij}$ is the elastic modulus tensor describing the stiffness of the crystal. $c_B$ is defined as the bulk modulus, $\epsilon_B \equiv \epsilon_{xx}+\epsilon_{yy}+\epsilon_{zz}$ is the volume expansion of the crystal, and $\epsilon_\mu \equiv \epsilon_{xx}-\epsilon_{yy}$ and $\epsilon_\nu \equiv (2\epsilon_{zz}-\epsilon_{xx}-\epsilon_{yy})/\sqrt{3}$ are cubic normal mode lattice strains.

### A.3.1 Quadrupolar-strain coupling in the non-Kramers case

Because non-Kramers $xy$ pseudospin components are time-reversal even quadrupolar moments, they can linearly couple to elastic strains. Therefore, the general form is represented as

$$\mathcal{F}^\alpha_{\text{quad-strain}} = \sum_{\mu=x,y}\sum_{\nu,\gamma=x,y,z} \mathcal{C}_{\mu\nu\gamma} S^\alpha_\mu \epsilon^\alpha_{\nu\gamma}. \tag{A.7}$$

Here, pseudospins and strains are described in the local basis, and the superscript $\alpha$ indicates the sublattice index. Considering the point group symmetry introduced in Section 3.4.1, the majority of coupling constants $\mathcal{C}_{\mu\nu\gamma}$ are zero and the $D_{3d}$ symmetry constrained quadrupolar-strain coupling becomes

$$\mathcal{F}_{\text{quad-strain}} = -k_1\left[S^\alpha_x(\epsilon^\alpha_{xx}-\epsilon^\alpha_{yy}) - 2S^\alpha_y\epsilon^\alpha_{xy}\right] - k_2\left[S^\alpha_x\epsilon^\alpha_{xz}+S^\alpha_y\epsilon^\alpha_{yz}\right], \tag{A.8}$$

in which Einstein summation notation is introduced for $\alpha$, and $k_{1,2}$ are phenomenological coupling constants.

### A.3.2 Dipolar-strain coupling

The $z$ pseudospin component contains the time-reversal odd magnetic dipole moment and can only couple to the elastic strain in the presence of a time-reversal breaking external magnetic field $\boldsymbol{h}$ to yield

$$\mathcal{F}^\alpha_{\text{dipolar}-\text{strain}} = \sum_{\mu=x,y,z}\sum_{\nu,\gamma=x,y,z} \mathcal{C}_{\mu\nu\gamma} S^\alpha_z h^\alpha_\mu \epsilon^\alpha_{\nu\gamma}. \tag{A.9}$$

In addition, point group symmetry reduces the degrees of the coupling constant, which results in

$$\begin{aligned}\mathcal{F}_{\text{dipolar}-\text{strain},z} =& -g_1 S^\alpha_z\left[(\epsilon^\alpha_{xx}-\epsilon^\alpha_{yy})h^\alpha_z - 2\epsilon^\alpha_{xy}h^\alpha_y\right] - g_2 S^\alpha_z\left[\epsilon^\alpha_{xz}h^\alpha_x+\epsilon^\alpha_{yz}h^\alpha_y\right]\\ &- g_3 S^\alpha_z h^\alpha_z\left[\epsilon^\alpha_{xx}+\epsilon^\alpha_{yy}\right] - g_4 S^\alpha_z h^\alpha_z \epsilon^\alpha_{zz},\end{aligned} \tag{A.10}$$

where $g_{1,2,3,4}$ are coupling constants, and we once again employ Einstein summation notation for $\alpha$. Note that this expression is common to both non-Kramers and Kramers cases.

In the Kramers case, the $x$ and $y$ components also contain the time-reversal odd magnetic dipole moment; thus, additional dipolar-strain couplings are found as

$$\begin{aligned}\mathcal{F}_{\mathrm{dipolar-strain},xy} =& -n_0\left[S_x^\alpha h_x^\alpha \epsilon_{xx}^\alpha + S_y^\alpha h_y^\alpha \epsilon_{yy}^\alpha + (S_x^\alpha h_y^\alpha + S_y^\alpha h_x^\alpha)\epsilon_{xy}^\alpha\right]\\ &-n_1\left[S_x^\alpha h_x^\alpha \epsilon_{yy}^\alpha + S_y^\alpha h_y^\alpha \epsilon_{xx}^\alpha - (S_x^\alpha h_y^\alpha + S_y^\alpha h_x^\alpha)\epsilon_{xy}^\alpha\right]\\ &-n_2\left[(S_y^\alpha h_y^\alpha - S_x^\alpha h_x^\alpha)\epsilon_{xz}^\alpha + (S_x^\alpha h_y^\alpha + S_y^\alpha h_x^\alpha)\epsilon_{yz}^\alpha\right] - n_3\left[(S_x^\alpha h_x^\alpha + S_y^\alpha h_y^\alpha)\epsilon_{zz}^\alpha\right]\\ &-n_4\left[S_x^\alpha(\epsilon_{xx}^\alpha - \epsilon_{yy}^\alpha) - 2S_y^\alpha \epsilon_{xy}^\alpha\right] h_z^\alpha - n_5\left[S_x^\alpha \epsilon_{xz}^\alpha + S_y^\alpha \epsilon_{yz}^\alpha\right],\end{aligned} \tag{A.11}$$

where $n_{0,1,2,3,4,5}$ are phenomenological coupling constants.

### A.3.3 General magnetostriction expressions

Now that we have obtained free energy expressions for the non-Kramers and Kramers cases, general magnetostriction expressions can be derived for these cases by following the strategy described in Section 3.4.1 and 3.4.2. Present here is an important expression for magnetostriction, that is, the length change along the $\boldsymbol{\ell} = (1,1,1)$ direction under $\boldsymbol{h} = \frac{h}{\sqrt{3}}(1,1,1)$.

$$\begin{aligned}\left(\frac{\Delta L}{L}\right)^{[111]}_{(1,1,1),\mathrm{NK}} =& \frac{4}{3c_{44}}(2k_1+k_2)\left[\frac{1}{\sqrt{3}}\left(2S_x^{(1)} - S_x^{(2)} - S_x^{(3)}\right) + \left(S_y^{(2)} - S_y^{(3)}\right)\right]\\ &+\frac{(g_3+g_4)}{3\sqrt{3}c_B}h\left[3S_z^{(0)} - S_z^{(1)} - S_z^{(2)} - S_z^{(3)}\right]\\ &-\frac{2\sqrt{3}}{27c_{44}}h\Big[(3g_3-6g_4)\left(9S_z^{(0)} + S_z^{(1)} + S_z^{(2)} + S_z^{(3)}\right)\\ &+(32g_1+16g_2)\left(S_z^{(1)} + S_z^{(2)} + S_z^{(3)}\right)\Big],\end{aligned} \tag{A.12}$$

$$\begin{aligned}\left(\frac{\Delta L}{L}\right)^{[111]}_{(1,1,1),\mathrm{K}} =& -h\left[\frac{1}{\sqrt{3}}\left(2S_x^{(1)} - S_x^{(2)} - S_x^{(3)}\right) + \left(S_y^{(2)} - S_y^{(3)}\right)\right]\tilde{n}\\ &+\frac{(g_3+g_4)}{3\sqrt{3}c_B}h\left[3S_z^{(0)} - S_{(1)}^{z} - S_z^{(2)} - S_z^{(3)}\right]\\ &-\frac{2\sqrt{3}}{27c_{44}}h\Big[(3g_3-6g_4)\left(9S_z^{(0)} + S_z^{(1)} + S_z^{(2)} + S_z^{(3)}\right)\\ &+(32g_1+16g_2)\left(S_z^{(1)} + S_z^{(2)} + S_z^{(3)}\right)\Big].\end{aligned} \tag{A.13}$$

Here, subscripts NK and K represent the non-Kramers and Kramers cases, respectively, and $\tilde{n} = \sqrt{3}\frac{\left(2c_B\left(5\sqrt{2}n_0-3\sqrt{2}n_1-4n_2-2\sqrt{2}n_3+4n_4+\sqrt{2}n_5\right)+\sqrt{2}c_{44}(n_0+n_1+n_3)\right)}{27c_{44}c_B}$ is a collection of constants. Note that the couplings from Eqs. (A.8) and (A.10) have been redefined for brevity, that is, $g_1 = \frac{g_1}{\sqrt{6}}$, $g_2 = \frac{g_2}{2\sqrt{3}}$, $g_3 = \frac{2g_3}{3\sqrt{3}}$, $g_4 = \frac{g_4}{3\sqrt{3}}$, $k_1 = \frac{k_1}{\sqrt{3}}$, and $k_2 = \frac{k_2}{\sqrt{6}}$. Because the $z$ couplings of the Kramers case have the same form as in the non-Kramers case, the length change arising from the $z$ dipole moment is identical. The $xy$ contribution is also similar; however, in the Kramers case, it is associated with a magnetic field strength, $h$.

A striking observation of these formulae is that uniform ferro-like ordering of the $xy$ local moments results in vanishing length change contributions from the quadrupolar (non-Kramers) or dipolar (Kramers) moments. This scenario occurs when $J_{\pm\pm} = 0$ and only $J_{zz}, J_{\pm} > 0$. To have nonvanishing contributions from the $xy$ moments, the $\boldsymbol{\ell} = (1,1,1)$ length change clearly requires the assistance of finite $J_{\pm\pm}$ to provide nonuniformity to the ordering on each sublattice.

### A.3.4 Magnetostriction of MPOs in the non-Kramers case

Because the length change behaviour of the QSL phase in the non-Kramers case has already been provided in Section 2.1, presented here is the length change behaviour of MPO phases and the uniqueness of the jump behaviour found in Fig. 2.2. Figure A.2 illustrates the length change behaviour for four distinct MPO phases that can be realized in non-Kramers pyrochlore materials. We take $J_{zz} = 1.0$ in this study. For the $\mathrm{cAFQ_L}$ magnetostriction, $J_{\pm}/J_{zz} = -0.5$ and $J_{\pm\pm}/J_{zz} = -0.5$. For the $\overline{\mathrm{cAFQ_L}}$ magnetostriction, $J_{\pm}/J_{zz} = -0.5$ and $J_{\pm\pm}/J_{zz} = 0.5$. For $\mathrm{FQ_{L+}}$, $J_{\pm}/J_{zz} = 0.72$ and $J_{\pm\pm}/J_{zz} = 0.5$. For $\mathrm{FQ_{L-}}$, $J_{\pm}/J_{zz} = 0.72$ and $J_{\pm\pm}/J_{zz} = -0.5$. As for the phenomenological coupling constants, we take $g_1 = g_2 = -\frac{9}{4\sqrt{3}} \times 10^{-7}, g_3 = 14\sqrt{3} \times 10^{-7}, g_4 = 4\sqrt{3} \times 10^{-7}, k_1 = -4.5\sqrt{3} \times 10^{-7}, k_2 = 2.6\sqrt{3} \times 10^{-7}$, and $c_B = c_{44} = c_{11} - c_{12} = 1.0$. Finally, we take $\delta_1 = 7.5 \times 10^{-4}$ and $-\delta_2 = 8.8 \times 10^{-5}$ to emphasize the perturbative nature of the quadratic-in-$h$ magnetic field coupling. The numerical values of the pseudospin-lattice couplings are taken with comparison to an experimental study on a Pr-based heavy fermion compound, $\mathrm{PrIr_2Zn_{20}}$ [143]. $\mathrm{PrIr_2Zn_{20}}$ has similarities to $\mathrm{Pr_2Zr_2O_7}$ in that both of their interesting phenomena arise from the $f_2$ electrons in Pr ions. Taking the above coupling constants yields magnetostriction behaviours that are of the same scale as the reported study. Indeed, the physical scale of $(\Delta L/L) \sim 10^{-6}$ for the relative length change has also been observed in other $f$ electron heavy fermion compounds as well as Kitaev materials under pressure during recent magnetostriction studies [144, 145, 146]. The actual value or ratio of the coupling constants will be determined by employing the proposed length change behaviours in conjunction with experimental measurements. As an example, by subtracting the leading linear-in-$h$ scaling behaviour from the experimental length change measurements for the [111] field and (1,1,1) direction allows the determination of $(2k_1+k_2)$ in Eq. (A.12) and subsequently $(k_1-k_2)$ from the (1,1,0) length change (the formula is not shown) because we have numerically computed the pseudospin configurations. Additional length change measurements are required to subsequently extract the remaining $g_{1,2,3,4}$ couplings.

To successfully understand the length change behaviour of MPOs in the non-Kramers

case, Eq. (A.12) is rewritten in the following form:

$$\left(\frac{\Delta L}{L}\right)^{[111]}_{(1,1,1),\mathrm{NK}} = \mathcal{Q}_0\left[M^x_{\Gamma_5}+M^y_{\Gamma_5}+M^z_{\Gamma_5}\right]-h\mathcal{C}_0 M_{\Gamma_2}-h\mathcal{C}_1(M^x_{\Gamma_4,a}+M^y_{\Gamma_4,a}+M^z_{\Gamma_4,a}), \quad \text{(A.14)}$$

where the constants are collected under $\mathcal{Q}_0 = \frac{8(2k_1+k_2)}{3\sqrt{3}c_{44}}$, $\mathcal{C}_0 = \frac{4\sqrt{3}(-8g_1+4g_2-3g_3+6g_4)}{9c_{44}}$, and $\mathcal{C}_1 = \frac{8\sqrt{3}(4g_1+2g_2-3g_3+6g_4)}{27c_{44}} + \frac{2(g_3+g_4)}{3\sqrt{3}c_B}$. Figure A.2 depicts the magnetostriction behaviour of MPOs in the non-Kramers case for $\boldsymbol{\ell} = (1,1,1)$. The vertical dashed lines indicate jump discontinuous behaviours in the ordering. Specifically, both the $\mathrm{cAFQ_L}$ and $\overline{\mathrm{cAFQ_L}}$ phases have jump discontinuous behaviours, which correspond to $S_z^{(0)}$ becoming fully polarised. $\mathrm{cAFQ_L}$ also has the distinction of having a finite length change in the absence of an external field[1]. This is apparent from Eq. (A.14), where the $\mathrm{cAFQ_L}$ order parameter is present even at zero magnetic field. The $\mathrm{FQ_{L\pm}}$ states do not possess any nonanalytic behaviours in their length changes. Indeed, the local moments undergo a smooth and gradual change into the fully polarised state. Note that the $\mathrm{FQ_{L+}}$ and $\mathrm{FQ_{L-}}$ behaviours are related by local $C_{4z}$ rotation of the pseudospins, where the $\pm$ denote $J_{\pm\pm} > 0$ and $J_{\pm\pm} < 0$, respectively. These different parameter options for the classically same phase[2] highlight the independence of the qualitative magnetostriction features on the precise value of the exchange couplings.

Because of these characteristics, each MPO has its own distinct signature that allows it to be identified individually as well as distinguished from the classical and quantum spin ice phase (Fig. 2.2). The $\mathrm{FQ_{L\pm}}$ states are the easiest to identify because they possess a smooth change in the length change; this gradual change is not present in classical or quantum spin ices nor the other MPOs. $\mathrm{cAFQ_L}$ can also be distinguished as it is the only non-Kramers phase that has a finite length change in the absence of an external field. The length change of $\overline{\mathrm{cAFQ_L}}$ and classical and quantum spin ices share several characteristics as both possess a jump discontinuity in the total length change. However, the lack of a jump or peak in the quadrupolar contribution of $\overline{\mathrm{cAFQ_L}}$ qualitatively distinguishes this phase from the classical and quantum spin ices. Furthermore, the length change of the classical and quantum spin ices has a dominant linear-in-$h$ scaling behaviour before the jump, whereas $\overline{\mathrm{cAFQ_L}}$ has an overarching nonlinear scaling before $S_z$ becomes fully polarised. These differences demonstrate the uniqueness of the non-Kramers classical and quantum spin ices and the MPO magnetostriction signatures.

[1]Here, the length change is not measured from the length at zero magnetic field but from the length when the system is disordered. Therefore, it is possible that the order itself can induce the lattice distortion without a magnetic field.

[2]These phases can be distinguished by considering spin wave excitation.

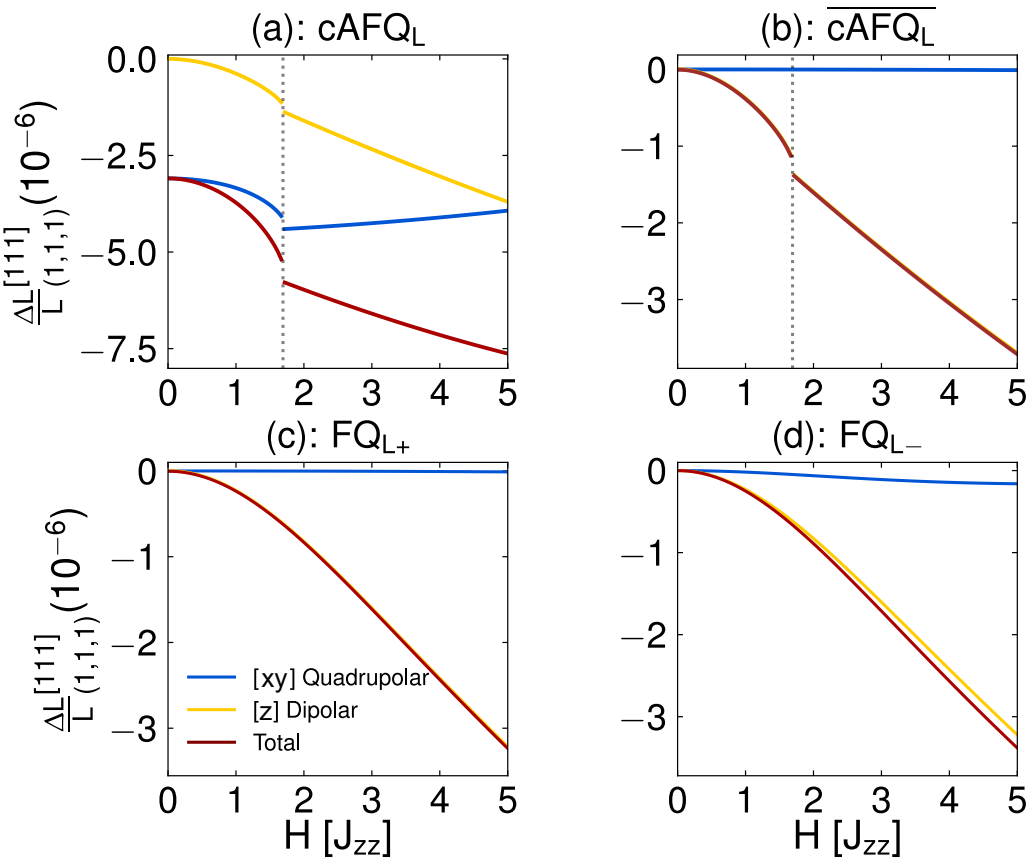


Figure A.2. Length change along the (1,1,1) direction under an applied [111] magnetic field for the various classical MPOs of non-Kramers ions: (a) coplanar antiferroquadrupolar ($\mathrm{cAFQ_L}$), (b) a second coplanar antiferroquadrupolar ($\overline{\mathrm{cAFQ_L}}$), and (c) and (d) ferroquadrupolar ($\mathrm{FQ_{L\pm}}$), where the $\pm$ denote $J_{\pm\pm} > 0$ and $J_{\pm\pm} < 0$, respectively. The dashed vertical lines indicate regions of discontinuity in the length change arising from $S_z^{(0)}$ becoming fully polarised. The blue, yellow, and red curves denote the length change arising from the $xy$ pseudospin (quadrupolar), $z$ pseudospin (dipole), and combined contributions, respectively.

### A.3.5 Magnetostriction of Kramers ions

For completeness, we investigate the magnetostriction of Kramers ions. Fig. A.3 shows the length change along the (1,1,1) direction under an applied [111] magnetic field for various classically magnetically ordered phases of Kramers ions, where we set $J_{z\pm} = 0.25$ and $\tilde{n} = 1.0 \times 10^{-7}$ in Eq. (A.13). Because of the aforementioned mixing of the SI and SFM phases, the behaviour is presented for the choice of $J_\pm$, $J_{\pm\pm}$, $J_{z\pm}$, which yields a dominant SI (SFM) behaviour over SFM (SI). For SI-dominant magnetostriction, $J_\pm/J_{zz} = 0.02$ and $J_{\pm\pm}/J_{zz} = 0.05$. For SFM-dominant magnetostriction, $J_\pm/J_{zz} = -0.5$ and $J_{\pm\pm}/J_{zz} = -0.5$. For PC magnetostriction, $J_\pm/J_{zz} = -0.5$ and $J_{\pm\pm}/J_{zz} = 0.5$. For

1D$_+$, $J_\pm/J_{zz} = 0.72$ and $J_{\pm\pm}/J_{zz} = 0.5$. For 1D$_-$, $J_\pm/J_{zz} = 0.72$ and $J_{\pm\pm}/J_{zz} = -0.5$. Once again, 1D$_+$ and 1D$_-$ behaviours are related by local $C_{4z}$ rotation of the pseudospins, where the $\pm$ denote $J_{\pm\pm} > 0$ and $J_{\pm\pm} < 0$, respectively.

In this case, we can also rewrite the Eq. (A.13) in the following form:

$$\left(\frac{\Delta L}{L}\right)^{[111]}_{(1,1,1),K} = -\frac{2\tilde{n}}{\sqrt{3}}h\left[M^x_{\Gamma_{4,b}} + M^y_{\Gamma_{4,b}} + M^z_{\Gamma_{4,b}}\right] - h\left[\mathcal{C}_0 M_{\Gamma_2} + \mathcal{C}_1(M^x_{\Gamma_{4,a}} + M^y_{\Gamma_{4,a}} + M^z_{\Gamma_{4,a}})\right]. \tag{A.15}$$

In all Kramers ion behaviours, at $h = 0$, the total length change vanishes, as indicated by Eq. (A.15). Moreover, all phases possess a monotonically increasing $xy$ contribution to the length change. For the SI-dominant phase in Fig. A.3(a), two points of discontinuity are observed. The first arises due to $S^{(0)}_z$ becoming fully polarised in the $-\hat{z}_0$ direction, and the second is a result of $S^{(0)}_z$ becoming polarised in the $+\hat{z}_0$ direction. This discontinuity also appears in the $xy$ behaviour. The second discontinuity can be loosely associated with the discontinuity in the NK case, in that $S^{(0)}_z$ becomes fully polarised in both. However, because the magnetic field coupling involves $S^{(0\text{-}3)}_{x,y}$ as well as the presence of the finite $J_{z\pm}$ term, it is not a direct comparison. The SFM-dominant phase in Fig. A.3(b) possesses a single discontinuity, which (just as the second discontinuity point of the SI-dominant phase) is associated with $S^{(0)}_z$ becoming fully polarised. The broad maximum in the $z$ contribution arises from the gradual change in the sign of $S^{(0)}_z$ from $S^{(0)}_z < 0$ in the SFM-like phase to the fully polarised value $S^{(0)}_z = 1/2$. The PC phase in Fig. A.3 (c) also possesses two discontinuous points. The first is associated with $S^{(0)}_z$ becoming fully polarised, and the second is where $S^{(1)}_y \to 0$. From numerical minimisation, the second discontinuity appears to be continuous. Finally, the two 1D manifold states in Figs. A.3(d) and A.3(e) have a single discontinuity that is again associated with $S^{(0)}_z$ becoming fully polarised.

There is a lack of clear difference between the various Kramers magnetically ordered phases. In fact, only the SI-dominant phase appears to be distinct, with the dipole contribution flipping sign after discontinuity. This suggests that, unlike the non-Kramers case, magnetostriction is less suited to Kramers ions.

Specific contrasts can be drawn between the associated Kramers and non-Kramers cases. For instance, the 1D manifold states in the Kramers case have a discontinuity, whereas the corresponding FQ$_\mathrm{L}$ states of non-Kramers ions undergo a smooth length change under an increasing magnetic field. Analogously, SFM and cAFQ$_\mathrm{L}$ can be distinguished because SFM has a vanishing length change at zero field, whereas it is finite for cAFQ$_\mathrm{L}$. Finally, PC and $\overline{\text{cAFQ}_\mathrm{L}}$ can be differentiated because PC has two discontinuous points in the length change, whereas $\overline{\text{cAFQ}_\mathrm{L}}$ has only one. Such key differences in the length change behaviours of Kramers and non-Kramers ions highlight the broad applicability of magnetostriction in pyrochlore materials. Furthermore, since Kramers ions are more commonly examined with conventional magnetic ordering probes (most notably, neutron scattering), magnetostriction can serve as useful corroborating evidence. This contrasts with the non-Kramers case, which has a shortage of available probes, and each MPO possesses distinct features (Fig. A.2) that allow them to be individually identified (and distinguished from non-Kramers classical and quantum spin ices). Therefore, this comparison also serves to emphasise the suitability of magnetostriction to non-Kramers

ions.

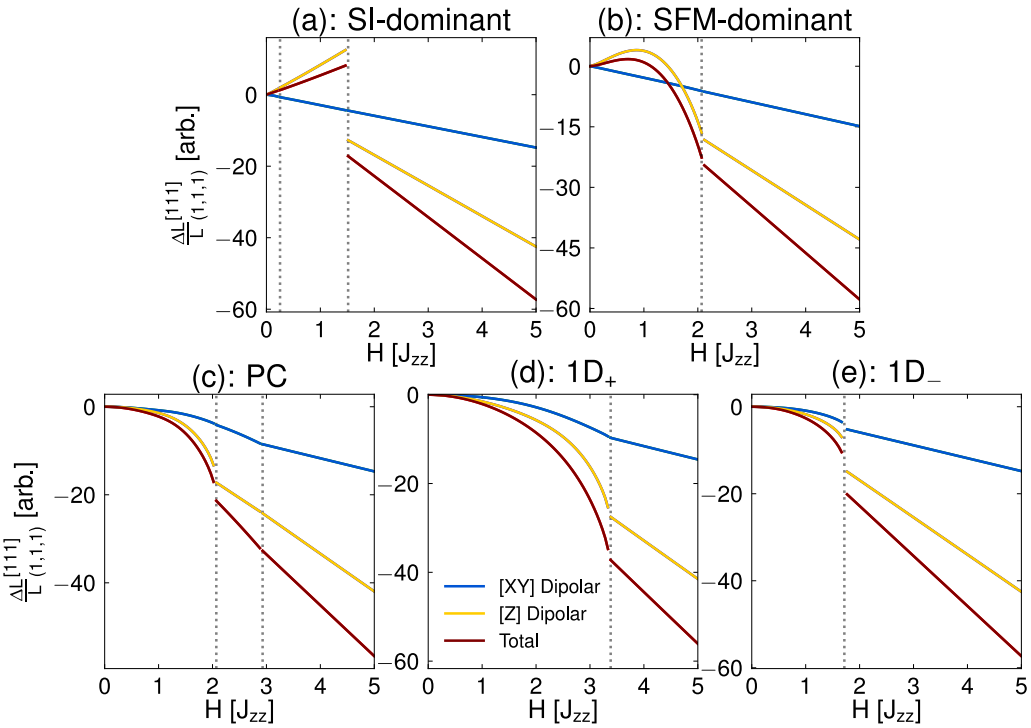


Figure A.3. Length change along the (1,1,1) direction under an applied [111] magnetic field for various classically magnetically ordered phases of non-Kramers ions: (a) spin-dominant (SI), (b) splayed ferromagnetic dominant (SFM-dominant), (c) Palmer-Chalker (PC), (d) and (e) one-dimensional (1D±), where the ± denote $J_{\pm\pm} > 0$ and $J_{\pm\pm} < 0$, respectively. The dashed vertical lines indicate regions of discontinuity in the length change, which is closely linked to the discontinuity in the pseudospin expectation values. The blue, yellow, and red curves denote the length change arising from the $xy$ pseudospin (quadrupolar), $z$ pseudospin (dipole), and combined contributions, respectively.

## A.4 Summary

To summarise this appendix, a novel experimental tool known as the measurement of magnetostriction is useful for distinguishing MPOs as well as the multipolar quantum spin ice phases described in the main text. In particular, the five distinct classical phases, including MPOs and a spin ice in non-Kramers ions, display completely different length change behaviours. This indicates that experimentally elusive phases are now exposed to detection through magnetostriction measurements. This means that magnetostriction can serve as a novel alternative to ultrasonic measurement.

In terms of future studies, it would be interesting to examine finite-temperature length-change behaviours, such as thermal expansion, and identify the nature of the

finite-field quantum kagome ice state in the generic pyrochlore model (in addition to its possible connection to the resonating plaquette state in the simplified XXZ model [109, 147]). Such studies would provide insight into the nontrivial fractionalised excitations predicted in quantum spin ice, such as the emergent monopoles and photons. Furthermore, in the context of $Pr_2Zr_2O_7$, an important future study would be to examine and incorporate the impacts of disorder [136, 148] in the context of magnetostriction. Finally, it would also be interesting to examine magnetostriction in other frustrated lattices (with different symmetries) that are candidates for QSLs. It would be fascinating to explore whether those systems also possess strong magnetostriction signatures for their proposed QSL and/or any nearby ordered phases.

# Appendix B

# Complete set of magnetostriction expressions

## B.1 Magnetic field along [111] direction

In this section, we provide the magnetostriction expression for field along [111] direction.

$$\begin{aligned}\left(\frac{\Delta L}{L}\right)^{[111]}_{(1,1,1)} &= \frac{h}{27c_B}\left[(\mathcal{C}_{5z}+2\mathcal{C}_{4z})\left(3\tau_z^{(0)}-\tau_z^{(1)}-\tau_z^{(2)}-\tau_z^{(3)}\right)+(\mathcal{C}_{5x}+2\mathcal{C}_{4x})\left(3\tau_x^{(0)}-\tau_x^{(1)}-\tau_x^{(2)}-\tau_x^{(3)}\right)\right]\\ &+\frac{4}{27c_{44}}h\Bigg[\left(8\sqrt{2}\mathcal{C}_{2x}-4\mathcal{C}_{3x}\right)\left(\tau_x^{(1)}+\tau_x^{(2)}+\tau_x^{(3)}\right)+(\mathcal{C}_{5x}-\mathcal{C}_{4x})\left(9\tau_x^{(0)}+\tau_x^{(1)}+\tau_x^{(2)}+\tau_x^{(3)}\right)\\ &\quad+\left(8\sqrt{2}\mathcal{C}_{2z}-4\mathcal{C}_{3z}\right)\left(\tau_z^{(1)}+\tau_z^{(2)}+\tau_z^{(3)}\right)+(\mathcal{C}_{5z}-\mathcal{C}_{4z})\left(9\tau_z^{(0)}+\tau_z^{(1)}+\tau_z^{(2)}+\tau_z^{(3)}\right)\Bigg]\end{aligned} \tag{B.1}$$

$$\begin{aligned}\left(\frac{\Delta L}{L}\right)^{[111]}_{(1,1,0)} &= \frac{h}{27c_B}\left[(\mathcal{C}_{5z}+2\mathcal{C}_{4z})\left(3\tau_z^{(0)}-\tau_z^{(1)}-\tau_z^{(2)}-\tau_z^{(3)}\right)+(\mathcal{C}_{5x}+2\mathcal{C}_{4x})\left(3\tau_x^{(0)}-\tau_x^{(1)}-\tau_x^{(2)}-\tau_x^{(3)}\right)\right]\\ &+\frac{1}{18\sqrt{3}(c_{11}-c_{22})}h\Bigg[\left(\sqrt{6}\mathcal{C}_{2x}+\sqrt{3}\mathcal{C}_{3x}\right)\left(\tau_x^{(1)}+\tau_x^{(2)}-2\tau_x^{(3)}\right)\\ &\quad+\left(\sqrt{6}\mathcal{C}_{2z}+\sqrt{3}\mathcal{C}_{3z}\right)\left(\tau_z^{(1)}+\tau_z^{(2)}-2\tau_z^{(3)}\right)\Bigg]\\ &-\frac{2}{9c_{44}}h\Bigg[(\mathcal{C}_{4x}-\mathcal{C}_{5x})\left(3\tau_x^{(0)}+\tau_x^{(1)}+\tau_x^{(2)}-\tau_x^{(3)}\right)+\left(\mathcal{C}_{3x}-2\sqrt{2}\mathcal{C}_{2x}\right)\left(\tau_x^{(1)}+\tau_x^{(2)}+2\tau_x^{(3)}\right)\\ &\quad+(\mathcal{C}_{4z}-\mathcal{C}_{5z})\left(3\tau_z^{(0)}+\tau_z^{(1)}+\tau_z^{(2)}-\tau_z^{(3)}\right)+\left(\mathcal{C}_{3z}-2\sqrt{2}\mathcal{C}_{2z}\right)\left(\tau_z^{(1)}+\tau_z^{(2)}+2\tau_z^{(3)}\right)\Bigg]\\ &+\left[\frac{(\sqrt{2}\mathcal{C}_0-\mathcal{C}_1)}{6\sqrt{3}(c_{11}-c_{22})}+\frac{2\left(2\sqrt{6}\mathcal{C}_0+\sqrt{3}\mathcal{C}_1\right)}{9c_{44}}\right]h\left(\tau_y^{(1)}-\tau_y^{(2)}\right)\end{aligned} \tag{B.2}$$

$$\left(\frac{\Delta L}{L}\right)^{[111]}_{(0,0,1)} = \frac{h}{27c_B}\left[(\mathcal{C}_{5z}+2\mathcal{C}_{4z})\left(3\tau_z^{(0)}-\tau_z^{(1)}-\tau_z^{(2)}-\tau_z^{(3)}\right)+(\mathcal{C}_{5x}+2\mathcal{C}_{4x})\left(3\tau_x^{(0)}-\tau_x^{(1)}-\tau_x^{(2)}-\tau_x^{(3)}\right)\right]$$
$$-\frac{1}{9\sqrt{3}(c_{11}-c_{22})}h\Bigg[\left(\sqrt{6}\mathcal{C}_{2x}+\sqrt{3}\mathcal{C}_{3x}\right)\left(\tau_x^{(1)}+\tau_x^{(2)}-2\tau_x^{(3)}\right)$$
$$+\left(\sqrt{6}\mathcal{C}_{2z}+\sqrt{3}\mathcal{C}_{3z}\right)\left(\tau_z^{(1)}+\tau_z^{(2)}-2\tau_z^{(3)}\right)+\left(3\sqrt{2}\mathcal{C}_0-3\mathcal{C}_1\right)\left(\tau_y^{(1)}-\tau_y^{(2)}\right)\Bigg] \tag{B.3}$$

## B.2 Magnetic field along [110] direction

In this section, we provide the magnetostriction expression for field along [110] direction.

$$\left(\frac{\Delta L}{L}\right)^{[110]}_{(1,1,1)} = \frac{\sqrt{2}}{9\sqrt{3}c_B}h\left[(\mathcal{C}_{5z}+2\mathcal{C}_{4z})\left(\tau_z^{(0)}-\tau_z^{(3)}\right)+(\mathcal{C}_{5x}+2\mathcal{C}_{4x})\left(\tau_x^{(0)}-\tau_x^{(3)}\right)\right]$$
$$+\frac{2}{27c_{44}}h\Bigg[-2\sqrt{6}\left(\mathcal{C}_{4x}-\mathcal{C}_{5x}\right)\left(3\tau_x^{(0)}+\tau_x^{(3)}\right)+\sqrt{3}\left(4\mathcal{C}_{2x}-\sqrt{2}\mathcal{C}_{3x}\right)\left(3\tau_x^{(1)}+3\tau_x^{(2)}+2\tau_x^{(3)}\right)$$
$$-2\sqrt{6}\left(\mathcal{C}_{4z}-\mathcal{C}_{5z}\right)\left(3\tau_z^{(0)}+\tau_z^{(3)}\right)+\sqrt{3}\left(4\mathcal{C}_{2z}-\sqrt{2}\mathcal{C}_{3z}\right)\left(3\tau_z^{(1)}+3\tau_z^{(2)}+2\tau_z^{(3)}\right)$$
$$+\left(12\mathcal{C}_0+3\sqrt{2}\mathcal{C}_1\right)\left(\tau_y^{(1)}-\tau_y^{(2)}\right)\Bigg] \tag{B.4}$$

$$\left(\frac{\Delta L}{L}\right)^{[110]}_{(1,1,0)} = \frac{\sqrt{2}}{9\sqrt{3}c_B}h\left[(\mathcal{C}_{5z}+2\mathcal{C}_{4z})\left(\tau_z^{(0)}-\tau_z^{(3)}\right)+(\mathcal{C}_{5x}+2\mathcal{C}_{4x})\left(\tau_x^{(0)}-\tau_x^{(3)}\right)\right]$$
$$+\frac{1}{12\sqrt{3}(c_{11}-c_{22})}h\Bigg[\left(2\mathcal{C}_{2x}+\sqrt{2}\mathcal{C}_{3x}\right)\left(\tau_x^{(0)}-\tau_x^{(3)}\right)+\left(2\mathcal{C}_{2z}+\sqrt{2}\mathcal{C}_{3z}\right)\left(\tau_z^{(0)}-\tau_z^{(3)}\right)$$
$$+\left(2\sqrt{3}\mathcal{C}_0-\sqrt{6}\mathcal{C}_1\right)\left(\tau_y^{(1)}-\tau_y^{(2)}\right)\Bigg]$$
$$+\frac{1}{9c_{44}}h\Bigg[\sqrt{3}\left(-4\mathcal{C}_{2x}+\sqrt{2}\mathcal{C}_{3x}-2\sqrt{2}\mathcal{C}_{4x}+2\sqrt{2}\mathcal{C}_{5x}\right)\left(\tau_x^{(0)}-\tau_x^{(3)}\right)$$
$$+\sqrt{3}\left(-4\mathcal{C}_{2z}+\sqrt{2}\mathcal{C}_{3z}-2\sqrt{2}\mathcal{C}_{4z}+2\sqrt{2}\mathcal{C}_{5z}\right)\left(\tau_z^{(0)}-\tau_z^{(3)}\right)+\left(12\mathcal{C}_0+3\sqrt{2}\mathcal{C}_1\right)\left(\tau_y^{(1)}-\tau_y^{(2)}\right)\Bigg] \tag{B.5}$$

$$\left(\frac{\Delta L}{L}\right)^{[110]}_{(0,0,1)} = \frac{\sqrt{2}}{9\sqrt{3}c_B}h\left[(\mathcal{C}_{5z}+2\mathcal{C}_{4z})\left(\tau_z^{(0)}-\tau_z^{(3)}\right)+(\mathcal{C}_{5x}+2\mathcal{C}_{4x})\left(\tau_x^{(0)}-\tau_x^{(3)}\right)\right] + \frac{1}{6\sqrt{3}(c_{11}-c_{22})}h\Bigg[\left(-2\mathcal{C}_{2x}-\sqrt{2}\mathcal{C}_{3x}\right)\left(\tau_x^{(0)}-\tau_x^{(3)}\right)+\left(-2\mathcal{C}_{2z}-\sqrt{2}\mathcal{C}_{3z}\right)\left(\tau_z^{(0)}-\tau_z^{(3)}\right) + \left(-2\sqrt{3}\mathcal{C}_0+\sqrt{6}\mathcal{C}_1\right)\left(\tau_y^{(1)}-\tau_y^{(2)}\right)\Bigg] \tag{B.6}$$

## B.3 Magnetic field along [001] direction

In this section, we provide the magnetostriction expression for field along [001] direction.

$$\begin{aligned}\left(\frac{\Delta L}{L}\right)^{[001]}_{(1,1,1)} &= \frac{1}{9\sqrt{3}c_B}h\left[(2\mathcal{C}_{4x}+\mathcal{C}_{5x})\left(\tau_x^{(0)}-\tau_x^{(1)}-\tau_x^{(2)}+\tau_x^{(3)}\right)+(2\mathcal{C}_{4z}+\mathcal{C}_{5z})\left(\tau_z^{(0)}-\tau_z^{(1)}-\tau_z^{(2)}+\tau_z^{(3)}\right)\right]\\ &- \frac{4}{27c_{44}}h\Bigg[\left(\sqrt{3}\mathcal{C}_{4x}-\sqrt{3}\mathcal{C}_{5x}\right)\left(3\tau_x^{(0)}+\tau_x^{(1)}+\tau_x^{(2)}-\tau_x^{(3)}\right)\\ &-\left(2\sqrt{6}\mathcal{C}_{2x}-\sqrt{3}\mathcal{C}_{3x}\right)\left(\tau_x^{(1)}+\tau_x^{(2)}+2\tau_x^{(3)}\right)+\left(\sqrt{3}\mathcal{C}_{4z}-\sqrt{3}\mathcal{C}_{5z}\right)\left(3\tau_z^{(0)}+\tau_z^{(1)}+\tau_z^{(2)}-\tau_z^{(3)}\right)\\ &-\left(2\sqrt{6}\mathcal{C}_{2z}-\sqrt{3}\mathcal{C}_{3z}\right)\left(\tau_z^{(1)}+\tau_z^{(2)}+2\tau_z^{(3)}\right)+\left(6\sqrt{2}\mathcal{C}_0+3\mathcal{C}_1\right)\left(\tau_y^{(1)}-\tau_y^{(2)}\right)\Bigg]\end{aligned} \tag{B.7}$$

$$\begin{aligned}\left(\frac{\Delta L}{L}\right)^{[001]}_{(1,1,0)} &= \frac{1}{9\sqrt{3}c_B}h\left[(2\mathcal{C}_{4x}+\mathcal{C}_{5x})\left(\tau_x^{(0)}-\tau_x^{(1)}-\tau_x^{(2)}+\tau_x^{(3)}\right)+(2\mathcal{C}_{4z}+\mathcal{C}_{5z})\left(\tau_z^{(0)}-\tau_z^{(1)}-\tau_z^{(2)}+\tau_z^{(3)}\right)\right]\\ &+ \frac{1}{6\sqrt{3}(c_{11}-c_{12})}h\Bigg[\left(-\sqrt{2}\mathcal{C}_{2x}-\mathcal{C}_{3x}\right)\left(\tau_x^{(0)}-\tau_x^{(1)}-\tau_x^{(2)}+\tau_x^{(3)}\right)\\ &\qquad+\left(-\sqrt{2}\mathcal{C}_{2z}-\mathcal{C}_{3z}\right)\left(\tau_z^{(0)}-\tau_z^{(1)}-\tau_z^{(2)}+\tau_z^{(3)}\right)\Bigg]\\ &- \frac{2}{3\sqrt{3}c_{44}}h\Bigg[\left(-2\sqrt{2}\mathcal{C}_{2x}+\mathcal{C}_{3x}+\mathcal{C}_{4x}-\mathcal{C}_{5x}\right)\left(\tau_x^{(0)}+\tau_x^{(1)}+\tau_x^{(2)}+\tau_x^{(3)}\right)\\ &\qquad+\left(-2\sqrt{2}\mathcal{C}_{2z}+\mathcal{C}_{3z}+\mathcal{C}_{4z}-\mathcal{C}_{5z}\right)\left(\tau_z^{(0)}+\tau_z^{(1)}+\tau_z^{(2)}+\tau_z^{(3)}\right)\Bigg]\end{aligned} \tag{B.8}$$

$$\left(\frac{\Delta L}{L}\right)^{[001]}_{(0,0,1)} = \frac{1}{9\sqrt{3}c_B} h \left[ (2\mathcal{C}_{4x} + \mathcal{C}_{5x}) \left( \tau_x^{(0)} - \tau_x^{(1)} - \tau_x^{(2)} + \tau_x^{(3)} \right) + (2\mathcal{C}_{4z} + \mathcal{C}_{5z}) \left( \tau_z^{(0)} - \tau_z^{(1)} - \tau_z^{(2)} + \tau_z^{(3)} \right) \right]$$
$$+ \frac{1}{3\sqrt{3}(c_{11} - c_{12})} h \Bigg[ \left( \sqrt{2}\mathcal{C}_{2x} + \mathcal{C}_{3x} \right) \left( \tau_x^{(0)} - \tau_x^{(1)} - \tau_x^{(2)} + \tau_x^{(3)} \right)$$
$$+ \left( \sqrt{2}\mathcal{C}_{2z} + \mathcal{C}_{3z} \right) \left( \tau_z^{(0)} - \tau_z^{(1)} - \tau_z^{(2)} + \tau_z^{(3)} \right) \Bigg] \tag{B.9}$$

# Appendix C

# Phonon-pseudospin coupling within the long wavelength limit

## C.1 Assumption

In this appendix, another phonon-pseudospin coupling model is provided based on a different assumption from the one used in the main text. Here, we only focus on the acoustic phonon mode from the beginning. First, the properties of acoustic phonon modes in a one-dimensional atomic chain are reviewed for simplicity. Figure C.1(a) illustrates the relative deviation of atoms observed from a certain atom (yellow circle) corresponding to the acoustic phonon mode within the long wavelength limit. The green (blue) vectors represent the deviations of the longitudinal (transverse) mode. Comparing the atoms on the left with those on the right with respect to the central atom, we can see that the direction of relative displacement is reversed. In addition, the magnitude of the displacement increases as the atoms move away from the centre.

Let us extend these observations to our case. First, we assume that the direction of deviation of the central Pr ion is specified by two angles $\theta_0$ and $\phi_0$, where $\theta_0$ is the polar angle and $\phi_0$ is the azimuthal angle in the local coordinate frame. Here, we consider the coupling between the local pseudospin and the acoustic phonon associated with this set up within the long wavelength limit. Figure C.1(b) shows the configuration of the relative lattice dislocation in this case. Sites that are point-symmetrical with respect to the Pr ion will each be displaced in the opposite direction; the magnitude of the displacement is proportional to $\boldsymbol{r}_i \cdot \boldsymbol{q}$, where $\boldsymbol{r}_i$ denotes the equilibrium position of each site and $\boldsymbol{q}$ is the direction of phonon propagation. Equipped with these assumptions, we derive the phonon-pseudospin coupling by employing the point charge approximation in the next section.

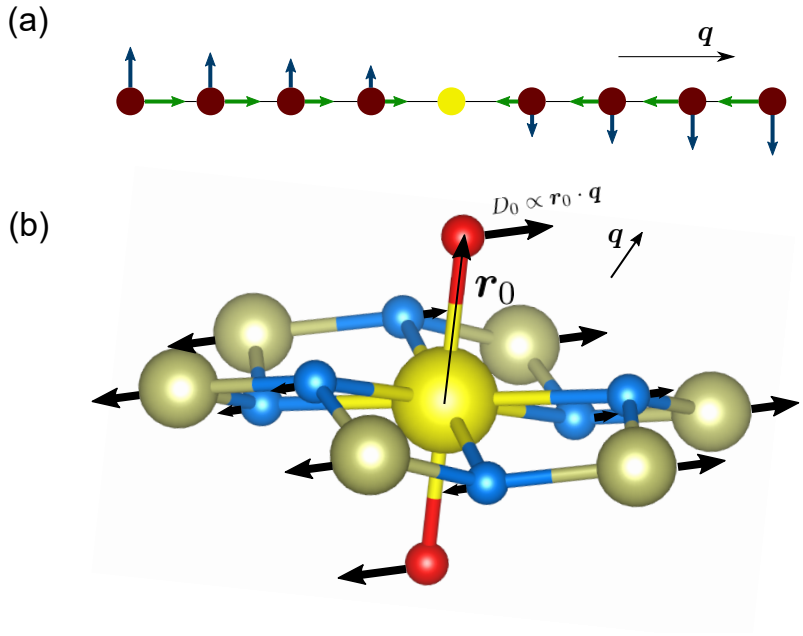


Figure C.1. (a): Schematic illustration of the lattice deviation of the one-dimensional chain corresponding to the acoustic phonon modes within the long wavelength limit. The green (blue) vectors represent the deviations of the longitudinal (transverse) mode. $\boldsymbol{q}$ denotes the direction of phonon propagation. (b): Relative deviation of each site of the pyrochlore lattice, measured from the central Pr site (yellow sphere), corresponding to the acoustic phonon modes within the long wavelength limit. The magnitude of the displacement is proportional to $\boldsymbol{r}_i \cdot \boldsymbol{q}$, where $\boldsymbol{r}_i$ denotes the equilibrium position of each site. For instance, the deviation magnitude of an oxygen atom at $\boldsymbol{r}_0$ is represented as $D_0 \propto \boldsymbol{r}_0 \cdot \boldsymbol{q}$.

## C.2 Point charge approximation and crystal electric field

We begin by considering the crystal electric field (CEF) of oxygen ions at the A sites (red spheres in Fig. C.1(b)) using the assumptions described above. Their relative positions are represented as $\boldsymbol{R}_1^{\mathrm{O,A}} = (D_0 \sin\theta_0 \cos\phi_0, D_0 \sin\theta_0 \sin\phi_0, \frac{\sqrt{3}a}{8} + D_0 \cos\theta_0)$ and $\boldsymbol{R}_2^{\mathrm{O,A}} = -\boldsymbol{R}_1^{\mathrm{O,A}}$. In the spherical coordinate frame, we obtain $\boldsymbol{R}_1^{\mathrm{O,A}} = (R, \theta, \phi)$ and $\boldsymbol{R}_2^{\mathrm{O,A}} = (R, \pi - \theta, \pi + \phi)$, where

$$R = \frac{\sqrt{3}a}{8}\left[1 - \frac{16}{\sqrt{3}}\delta_0 \cos\theta_0 + \frac{64}{3}\delta_0^2\right]^{\frac{1}{2}}, \theta = \cos^{-1}\left[\frac{1 - \frac{8}{\sqrt{3}}\delta_0 \cos\theta_0}{\left[1 - \frac{16}{\sqrt{3}}\delta_0 \cos\theta_0 + \frac{64}{3}\delta_0^2\right]^{\frac{1}{2}}}\right], \phi = \phi_0. \tag{C.1}$$

Here, we define $\delta_0 = D_0/a$. From these relations, we find that $\gamma_{km}$ in Eq. (4.8) is represented as

$$\gamma_{km} = \sqrt{\frac{4\pi}{2k+1}}\frac{2e^2}{R^{k+1}}\left[Y^*_{km}(\theta,\phi_0) + Y^*_{km}(\pi-\theta,\pi+\phi_0)\right]. \tag{C.2}$$

Therefore, the CEF potential induced by oxygen ions at the A sites is given by

$$V^{\mathrm{O,A}}_{\mathrm{CEF}}(\boldsymbol{r}) = \sum_{k=0}^{\infty}\sum_{m=-k}^{k}\sqrt{\frac{4\pi}{2k+1}}\frac{2e^2}{R^{k+1}}r^k\left[Y^*_{km}(\theta,\phi_0) + Y^*_{km}(\pi-\theta,\pi+\phi_0)\right]C^{(k)}_m(\theta,\phi). \tag{C.3}$$

As in the main text, we consider the matrix elements $\langle lm'|V^{\mathrm{O,A}}_{\mathrm{CEF}}(\boldsymbol{r})|lm\rangle$. However, because the first order term in $\delta_0 = D_0/a$ is finite in this case, we expand the CEF potential to $V^{\mathrm{O,A}}_{\mathrm{CEF}}(\boldsymbol{r}) = V^{\mathrm{O,A(0)}}_{\mathrm{CEF}}(\boldsymbol{r}) + V^{\mathrm{O,A(1)}}_{\mathrm{CEF}}(\boldsymbol{r})$. Note that the 0th order term is the same as the one provided in the main text. The explicit form of the matrix elements $V^{\mathrm{O,A(1)}}_{\mathrm{CEF}}(\boldsymbol{r})_{(m',m)} = \langle lm'|V^{\mathrm{O,A(1)}}_{\mathrm{CEF}}(\boldsymbol{r})|lm\rangle$ is provided below.

$$\begin{aligned}
V^{\mathrm{O,A(1)}}_{\mathrm{CEF},(3,2)} &= \left[V^{\mathrm{O,A(1)}}_{\mathrm{CEF},(2,3)}\right]^* = -V^{\mathrm{O,A(1)}}_{\mathrm{CEF},(-2,-3)} = \left[-V^{\mathrm{O,A(1)}}_{\mathrm{CEF},(-3,-2)}\right]^* = \mathcal{A}_1\delta_0\sin\theta_0 e^{-\mathrm{i}\phi_0}\\
V^{\mathrm{O,A(1)}}_{\mathrm{CEF},(2,1)} &= \left[V^{\mathrm{O,A(1)}}_{\mathrm{CEF},(1,2)}\right]^* = -V^{\mathrm{O,A(1)}}_{\mathrm{CEF},(-1,-2)} = \left[-V^{\mathrm{O,A(1)}}_{\mathrm{CEF},(-2,-1)}\right]^* = \mathcal{A}_2\delta_0\sin\theta_0 e^{-\mathrm{i}\phi_0}\\
V^{\mathrm{O,A(1)}}_{\mathrm{CEF},(1,0)} &= \left[V^{\mathrm{O,A(1)}}_{\mathrm{CEF},(0,1)}\right]^* = -V^{\mathrm{O,A(1)}}_{\mathrm{CEF},(0,-1)} = \left[-V^{\mathrm{O,A(1)}}_{\mathrm{CEF},(-1,0)}\right]^* = \mathcal{A}_3\delta_0\sin\theta_0 e^{-\mathrm{i}\phi_0}.
\end{aligned} \tag{C.4}$$

Here, the position dependence $\boldsymbol{r}$ was removed, and $\mathcal{A}_i$ is a real parameter.

Next, we consider the CEF constructed by transition metal ions (gold spheres in Fig. C.1(b)). Their relative positions in the spherical coordinate frame are represented as $\boldsymbol{R}^{\mathrm{TM}}_1 = (R_1,\theta_1,\phi_1)$, $\boldsymbol{R}^{\mathrm{TM}}_2 = (R_2,\theta_2,\phi_2)$, $\boldsymbol{R}^{\mathrm{TM}}_3 = (R_3,\theta_3,\phi_3)$, $\boldsymbol{R}^{\mathrm{TM}}_4 = -\boldsymbol{R}^{\mathrm{TM}}_1$, $\boldsymbol{R}^{\mathrm{TM}}_5 = -\boldsymbol{R}^{\mathrm{TM}}_2$, and $\boldsymbol{R}^{\mathrm{TM}}_6 = -\boldsymbol{R}^{\mathrm{TM}}_3$, where

$$\begin{aligned}
R_1 &= \frac{a}{2}\left[1+4\delta_1\sin\theta_0\sin\left(\phi_0+\frac{\pi}{3}\right)+4\delta_1^2\right]^{\frac{1}{2}}, \theta_1 = \cos^{-1}\left[\frac{2\delta_1\cos\theta_0}{\left[1+4\delta_1\sin\theta_0\sin\left(\phi_0+\frac{\pi}{3}\right)+4\delta_1^2\right]^{\frac{1}{2}}}\right]\\
\phi_1 &= \tan^{-1}\left[\frac{1+4\delta_1\sin\theta_0\sin\phi_0}{\sqrt{3}+4\delta_1\sin\theta_0\cos\phi_0}\right],\\
R_2 &= \frac{a}{2}\left[1+4\delta_2\sin\theta_0\sin\phi_0+4\delta_2^2\right]^{\frac{1}{2}}, \theta_2 = \cos^{-1}\left[\frac{2\delta_1\cos\theta_0}{\left[1+4\delta_2\sin\theta_0\sin\phi_0+4\delta_2^2\right]^{\frac{1}{2}}}\right],\\
\phi_2 &= \tan^{-1}\left[\frac{1+2\delta_2\sin\theta_0\sin\phi_0}{2\delta_2\sin\theta_0\cos\phi_0}\right]\\
R_3 &= \frac{a}{2}\left[1+4\delta_3\sin\theta_0\sin\left(\phi_0-\frac{\pi}{3}\right)+4\delta_3^2\right]^{\frac{1}{2}}, \theta_3 = \cos^{-1}\left[\frac{2\delta_3\cos\theta_0}{\left[1+4\delta_3\sin\theta_0\sin\left(\phi_0-\frac{\pi}{3}\right)+4\delta_3^2\right]^{\frac{1}{2}}}\right],\\
\phi_3 &= \tan^{-1}\left[\frac{1+4\delta_3\sin\theta_0\sin\phi_0}{-\sqrt{3}+4\delta_3\sin\theta_0\cos\phi_0}\right].
\end{aligned} \tag{C.5}$$

Here, $\delta_i = D_i/a$, and $D_i$ is the magnitude of deviation of each ion. Using these relations, we obtain the CEF potential from the transition metal ions to be

$$V_{\rm CEF}^{\rm TM}(\boldsymbol{r}) = -\sum_{i=1,2,3}\sum_{k=0}^{\infty}\sum_{m=-k}^{k}\sqrt{\frac{4\pi}{2k+1}}\frac{4e^2}{R_i^{k+1}}r^k\left[Y_{km}^*(\theta_i,\phi_i)+Y_{km}^*(\pi-\theta_i,\pi+\phi_i)\right]C_m^{(k)}(\theta,\phi). \tag{C.6}$$

The matrix elements $\langle l'm|V_{\rm CEF}^{\rm TM}(\boldsymbol{r})|lm\rangle$ are calculated from this result. Expanding this with regard to $\delta_i$, the first order term of the matrix element, that is, $\langle l'm|V_{\rm CEF}^{\rm TM(1)}(\boldsymbol{r})|lm\rangle$ is represented as

$$\begin{aligned}
&V_{{\rm CEF},(m,m-1)}^{\rm TM(1)} = \left[V_{{\rm CEF},(m-1,m)}^{\rm TM(1)}\right]^* = -V_{{\rm CEF},(-m+1,-m)}^{\rm TM(1)} = \left[-V_{{\rm CEF},(-m,-m+1)}^{\rm TM(1)}\right]^* \\
&= \mathcal{A}_{(m,m-1)}^{\rm TM}\cos\theta_0\left[\delta_1 e^{-{\rm i}\pi/6}+\delta_2 e^{-{\rm i}\pi/2}+\delta_3 e^{-{\rm i}5\pi/6}\right], \\
&V_{{\rm CEF},(m,m-2)}^{\rm TM(1)} = \left[V_{{\rm CEF},(m-2,m)}^{\rm TM(1)}\right]^* = V_{{\rm CEF},(-m+2,-m)}^{\rm TM(1)} = \left[V_{{\rm CEF},(-m,-m+2)}^{\rm TM(1)}\right]^* \\
&= \mathcal{A}_{(m,m-2)}^{\rm TM}\sin\theta_0\left[\delta_1 e^{-{\rm i}\pi/3}\cos(\phi_0-\frac{\pi}{6})+\delta_2 e^{-{\rm i}\pi}\cos(\phi_0-\frac{\pi}{2})+\delta_3 e^{-{\rm i}5\pi/3}\cos(\phi_0-\frac{5\pi}{6})\right] \\
&+\mathcal{A}_{(m,m-2)}^{\prime\rm TM}{\rm i}\sin\theta_0\left[\delta_1 e^{-{\rm i}\pi/3}\sin(\phi_0-\frac{\pi}{6})+\delta_2 e^{-{\rm i}\pi}\sin(\phi_0-\frac{\pi}{2})+\delta_3 e^{-{\rm i}5\pi/3}\sin(\phi_0-\frac{5\pi}{6})\right], \\
&V_{{\rm CEF},(m,m-3)}^{\rm TM(1)} = \left[V_{{\rm CEF},(m-3,m)}^{\rm TM(1)}\right]^* = -V_{{\rm CEF},(-m+3,-m)}^{\rm TM(1)} = \left[-V_{{\rm CEF},(-m,-m+3)}^{\rm TM(1)}\right]^* \\
&= \mathcal{A}_{(m,m-3)}^{\rm TM}\cos\theta_0\left[\delta_1 e^{-{\rm i}\pi/2}+\delta_2 e^{-{\rm i}3\pi/2}+\delta_3 e^{-{\rm i}5\pi/2}\right], \\
&V_{{\rm CEF},(m,m-4)}^{\rm TM(1)} = \left[V_{{\rm CEF},(m-4,m)}^{\rm TM(1)}\right]^* = V_{{\rm CEF},(-m+4,-m)}^{\rm TM(1)} = \left[V_{{\rm CEF},(-m,-m+4)}^{\rm TM(1)}\right]^* \\
&= \mathcal{A}_{(m,m-4)}^{\rm TM}\sin\theta_0\left[\delta_1 e^{-{\rm i}2\pi/3}\cos(\phi_0-\frac{\pi}{6})+\delta_2 e^{-{\rm i}2\pi}\cos(\phi_0-\frac{\pi}{2})+\delta_3 e^{-{\rm i}10\pi/3}\cos(\phi_0-\frac{5\pi}{6})\right] \\
&+\mathcal{A}_{(m,m-4)}^{\prime\rm TM}{\rm i}\sin\theta_0\left[\delta_1 e^{-{\rm i}2\pi/3}\sin(\phi_0-\frac{\pi}{6})+\delta_2 e^{-{\rm i}2\pi}\sin(\phi_0-\frac{\pi}{2})+\delta_3 e^{-{\rm i}10\pi/3}\sin(\phi_0-\frac{5\pi}{6})\right], \\
&V_{{\rm CEF},(m,m-5)}^{\rm TM(1)} = \left[V_{{\rm CEF},(m-5,m)}^{\rm TM(1)}\right]^* = -V_{{\rm CEF},(-m+5,-m)}^{\rm TM(1)} = \left[-V_{{\rm CEF},(-m,-m+5)}^{\rm TM(1)}\right]^* \\
&= \mathcal{A}_{(m,m-5)}^{\rm TM}\cos\theta_0\left[\delta_1 e^{-{\rm i}5\pi/6}+\delta_2 e^{-{\rm i}5\pi/2}+\delta_3 e^{-{\rm i}25\pi/6}\right], \\
&V_{{\rm CEF},(m,m-6)}^{\rm TM(1)} = \left[V_{{\rm CEF},(m-6,m)}^{\rm TM(1)}\right]^* = V_{{\rm CEF},(-m+6,-m)}^{\rm TM(1)} = \left[V_{{\rm CEF},(-m,-m+6)}^{\rm TM(1)}\right]^* \\
&= \mathcal{A}_{(m,m-6)}^{\rm TM}\sin\theta_0\left[\delta_1\cos(\phi_0-\frac{\pi}{6})+\delta_2\cos(\phi_0-\frac{\pi}{2})+\delta_3\cos(\phi_0-\frac{5\pi}{6})\right] \\
&+\mathcal{A}_{(m,m-6)}^{\prime\rm TM}{\rm i}\sin\theta_0\left[\delta_1\sin(\phi_0-\frac{\pi}{6})+\delta_2\sin(\phi_0-\frac{\pi}{2})+\delta_3\sin(\phi_0-\frac{5\pi}{6})\right],
\end{aligned} \tag{C.7}$$

where the position dependence $\boldsymbol{r}$ was removed, and $\mathcal{A}_{(m',m)}^{\rm TM}$ and $\mathcal{A}_{(m',m)}^{\prime\rm TM}$ are real parameters.

Lastly, we analyse the CEF potential induced by oxygen atoms at the B sites (blue spheres in Fig. C.1(b)). Only the first order term in $\delta_i$ of the matrix element is provided

below to avoid overcomplication.

$$
\begin{aligned}
&V^{\mathrm{O,B}(1)}_{\mathrm{CEF},(m,m-1)} = \left[V^{\mathrm{O,B}(1)}_{\mathrm{CEF},(m-1,m)}\right]^* = -V^{\mathrm{O,B}(1)}_{\mathrm{CEF},(-m+1,-m)} = \left[-V^{\mathrm{O,B}(1)}_{\mathrm{CEF},(-m,-m+1)}\right]^* \\
&= \mathcal{A}^{\mathrm{O,B}}_{(m,m-1)} \cos\theta_0 \left[\delta_4 + \delta_5 e^{-\mathrm{i}2\pi/3} + \delta_6 e^{-\mathrm{i}4\pi/3}\right] \\
&+ \mathcal{A}'^{\mathrm{O,B}}_{(m,m-1)} \sin\theta_0 \left[\delta_4 \cos\phi_0 + \delta_5 e^{-\mathrm{i}2\pi/3} \cos(\phi_0 - \frac{2\pi}{3}) + \delta_6 e^{-\mathrm{i}4\pi/3} \cos(\phi_0 - \frac{4\pi}{3})\right] \\
&+ \mathcal{A}''^{\mathrm{O,B}}_{(m,m-1)} \mathrm{i} \sin\theta_0 \left[\delta_4 \sin\phi_0 + \delta_5 e^{-\mathrm{i}2\pi/3} \sin(\phi_0 - \frac{2\pi}{3}) + \delta_6 e^{-\mathrm{i}4\pi/3} \sin(\phi_0 - \frac{4\pi}{3})\right] \\
&V^{\mathrm{O,B}(1)}_{\mathrm{CEF},(m,m-2)} = \left[V^{\mathrm{O,B}(1)}_{\mathrm{CEF},(m-2,m)}\right]^* = V^{\mathrm{O,B}(1)}_{\mathrm{CEF},(-m+2,-m)} = \left[V^{\mathrm{O,B}(1)}_{\mathrm{CEF},(-m,-m+2)}\right]^* \\
&= \mathcal{A}^{\mathrm{O,B}}_{(m,m-2)} \cos\theta_0 \left[\delta_4 + \delta_5 e^{-\mathrm{i}4\pi/3} + \delta_6 e^{-\mathrm{i}2\pi/3}\right] \\
&+ \mathcal{A}'^{\mathrm{O,B}}_{(m,m-2)} \sin\theta_0 \left[\delta_4 \cos\phi_0 + \delta_5 e^{-\mathrm{i}4\pi/3} \cos(\phi_0 - \frac{2\pi}{3}) + \delta_6 e^{-\mathrm{i}2\pi/3} \cos(\phi_0 - \frac{4\pi}{3})\right] \\
&+ \mathcal{A}''^{\mathrm{O,B}}_{(m,m-2)} \mathrm{i} \sin\theta_0 \left[\delta_4 \sin\phi_0 + \delta_5 e^{-\mathrm{i}4\pi/3} \sin(\phi_0 - \frac{2\pi}{3}) + \delta_6 e^{-\mathrm{i}2\pi/3} \sin(\phi_0 - \frac{4\pi}{3})\right] \\
&V^{\mathrm{O,B}(1)}_{\mathrm{CEF},(m,m-3)} = \left[V^{\mathrm{O,B}(1)}_{\mathrm{CEF},(m-3,m)}\right]^* = -V^{\mathrm{O,B}(1)}_{\mathrm{CEF},(-m+3,-m)} = \left[-V^{\mathrm{O,B}(1)}_{\mathrm{CEF},(-m,-m+3)}\right]^* \\
&= \mathcal{A}^{\mathrm{O,B}}_{(m,m-3)} \cos\theta_0 \left[\delta_4 + \delta_5 + \delta_6\right] \\
&+ \mathcal{A}'^{\mathrm{O,B}}_{(m,m-3)} \sin\theta_0 \left[\delta_4 \cos\phi_0 + \delta_5 \cos(\phi_0 - \frac{2\pi}{3}) + \delta_6 \cos(\phi_0 - \frac{4\pi}{3})\right] \\
&+ \mathcal{A}''^{\mathrm{O,B}}_{(m,m-3)} \mathrm{i} \sin\theta_0 \left[\delta_4 \sin\phi_0 + \delta_5 \sin(\phi_0 - \frac{2\pi}{3}) + \delta_6 \sin(\phi_0 - \frac{4\pi}{3})\right] \\
&V^{\mathrm{O,B}(1)}_{\mathrm{CEF},(m,m-4)} = \left[V^{\mathrm{O,B}(1)}_{\mathrm{CEF},(m-4,m)}\right]^* = V^{\mathrm{O,B}(1)}_{\mathrm{CEF},(-m+4,-m)} = \left[V^{\mathrm{O,B}(1)}_{\mathrm{CEF},(-m,-m+4)}\right]^* \\
&= \mathcal{A}^{\mathrm{O,B}}_{(m,m-4)} \cos\theta_0 \left[\delta_4 + \delta_5 e^{-\mathrm{i}2\pi/3} + \delta_6 e^{-\mathrm{i}4\pi/3}\right] \\
&+ \mathcal{A}'^{\mathrm{O,B}}_{(m,m-4)} \sin\theta_0 \left[\delta_4 \cos\phi_0 + \delta_5 e^{-\mathrm{i}2\pi/3} \cos(\phi_0 - \frac{2\pi}{3}) + \delta_6 e^{-\mathrm{i}4\pi/3} \cos(\phi_0 - \frac{4\pi}{3})\right] \\
&+ \mathcal{A}''^{\mathrm{O,B}}_{(m,m-4)} \mathrm{i} \sin\theta_0 \left[\delta_4 \sin\phi_0 + \delta_5 e^{-\mathrm{i}2\pi/3} \sin(\phi_0 - \frac{2\pi}{3}) + \delta_6 e^{-\mathrm{i}4\pi/3} \sin(\phi_0 - \frac{4\pi}{3})\right] \\
&V^{\mathrm{O,B}(1)}_{\mathrm{CEF},(m,m-5)} = \left[V^{\mathrm{O,B}(1)}_{\mathrm{CEF},(m-5,m)}\right]^* = V^{\mathrm{O,B}(1)}_{\mathrm{CEF},(-m+5,-m)} = \left[V^{\mathrm{O,B}(1)}_{\mathrm{CEF},(-m,-m+5)}\right]^* \\
&= \mathcal{A}^{\mathrm{O,B}}_{(m,m-5)} \cos\theta_0 \left[\delta_4 + \delta_5 e^{-\mathrm{i}4\pi/3} + \delta_6 e^{-\mathrm{i}2\pi/3}\right] \\
&+ \mathcal{A}'^{\mathrm{O,B}}_{(m,m-5)} \sin\theta_0 \left[\delta_4 \cos\phi_0 + \delta_5 e^{-\mathrm{i}4\pi/3} \cos(\phi_0 - \frac{2\pi}{3}) + \delta_6 e^{-\mathrm{i}2\pi/3} \cos(\phi_0 - \frac{4\pi}{3})\right] \\
&+ \mathcal{A}''^{\mathrm{O,B}}_{(m,m-5)} \mathrm{i} \sin\theta_0 \left[\delta_4 \sin\phi_0 + \delta_5 e^{-\mathrm{i}4\pi/3} \sin(\phi_0 - \frac{2\pi}{3}) + \delta_6 e^{-\mathrm{i}2\pi/3} \sin(\phi_0 - \frac{4\pi}{3})\right] \\
&V^{\mathrm{O,B}(1)}_{\mathrm{CEF},(m,m-6)} = \left[V^{\mathrm{O,B}(1)}_{\mathrm{CEF},(m-6,m)}\right]^* = -V^{\mathrm{O,B}(1)}_{\mathrm{CEF},(-m+6,-m)} = \left[-V^{\mathrm{O,B}(1)}_{\mathrm{CEF},(-m,-m+6)}\right]^* \\
&= \mathcal{A}^{\mathrm{O,B}}_{(m,m-6)} \cos\theta_0 \left[\delta_4 + \delta_5 + \delta_6\right] \\
&+ \mathcal{A}'^{\mathrm{O,B}}_{(m,m-6)} \sin\theta_0 \left[\delta_4 \cos\phi_0 + \delta_5 \cos(\phi_0 - \frac{2\pi}{3}) + \delta_6 \cos(\phi_0 - \frac{4\pi}{3})\right] \\
&+ \mathcal{A}''^{\mathrm{O,B}}_{(m,m-6)} \mathrm{i} \sin\theta_0 \left[\delta_4 \sin\phi_0 + \delta_5 \sin(\phi_0 - \frac{2\pi}{3}) + \delta_6 \sin(\phi_0 - \frac{4\pi}{3})\right].
\end{aligned}
\tag{C.8}
$$

We note once more that $\delta_i = D_i/a$, $D_i$ is the magnitude of deviation of each site, and $\mathcal{A}^{\mathrm{O,B}}_{(m',m)}$, $\mathcal{A}'^{\mathrm{O,B}}_{(m',m)}$, and $\mathcal{A}''^{\mathrm{O,B}}_{(m',m)}$ are real parameters.

Following the same procedure as in the main text and projecting the total CEF, which is the first order in $\delta$, that is, $V^{(1)}_{\mathrm{CEF}} = V^{\mathrm{O,A(1)}}_{\mathrm{CEF}} + V^{\mathrm{TM(1)}}_{\mathrm{CEF}} + V^{\mathrm{O,B(1)}}_{\mathrm{CEF}}$, to the local doublet, we again find that the effective interaction is described as a transverse field, $(\Delta S^+ + \Delta^* S^-)$. However, the amplitude of the effective transverse field is different. Assuming the normalised deviation $\delta_i$ is proportional to $\boldsymbol{r}_i \cdot \boldsymbol{q}$, as explained in the previous section, we obtain

$$\Delta = \Delta_0[q_x u_x - q_y u_y + \mathrm{i}(q_x u_y + u_x q_y)] + \Delta_1 \left[q_z(u_x - \mathrm{i}u_y)\right] + \Delta_2 \left[u_z(q_x - \mathrm{i}q_y)\right], \tag{C.9}$$

where $u_\mu$ denotes the deviation of the Pr ion along the local $\mu$ axis from its equilibrium position. Therefore, the phonon-pseudospin interaction is represented as

$$H_{\text{s-p}} = S^x \left[\Delta_0(q_x u_x - q_y u_y) + \Delta_1 q_z u_x + \Delta_2 q_x u_z\right] + S_y \left[-\Delta_0(q_x u_y + u_x q_y) + \Delta_1 q_z u_y + \Delta_2 q_y u_z\right]. \tag{C.10}$$

We note that the parameter $\Delta_i$ is real. This coupling form will be utilised in the analysis of phonon transport properties in non-Kramers pyrochlore materials.

# Appendix D

# Jordan–Wigner transformation

In this appendix, we review the exact solution of the one-dimensional transverse field Ising model by employing the Jordan–Wigner transformation. The starting point is

$$H = J\sum_{j=0}^{N-1}\sigma_j^x\sigma_{j+1}^x - \Gamma\sum_{j=0}^{N-1}\sigma_j^z, \tag{D.1}$$

where $N$ represents the number of sites. Applying the Jordan–Wigner transformation ($\boldsymbol{S} = \boldsymbol{\sigma}/2$ and $S^{\pm} = S^x \pm \mathrm{i}S^y$):

$$\begin{cases} S_j^+ = \prod_{i=0}^{j-1}(1-2c_i^\dagger c_i)c_j^\dagger = (-1)^{\sum_{i=0}^{j-1}c_i^\dagger c_i}c_j^\dagger \\ S_j^- = \prod_{i=0}^{j-1}(1-2c_i^\dagger c_i)c_j = (-1)^{\sum_{i=0}^{j-1}c_i^\dagger c_i}c_j \\ S_j^z = c_j^\dagger c_j - \frac{1}{2} \end{cases}, \tag{D.2}$$

we obtain

$$H = J\sum_{j=0}^{N-2}(c_j^\dagger - c_j)(c_{j+1}^\dagger + c_{j+1}) + J(-1)^{\mathrm{F+P}}(c_0^\dagger + c_0)(c_{N-1}^\dagger - c_{N-1}) - 2\Gamma\sum_{j=0}^{N-1}\left(c_j^\dagger c_j - \frac{1}{2}\right). \tag{D.3}$$

Here, $(-1)^{\mathrm{F}} = \prod_{j=0}^{N-1}(1-2c_j^\dagger c_j)$ is known as the fermion parity and is a conserved quantity. Additionally, $P = 0$ ($P = 1$) when the boundary condition is periodic (antiperiodic). Henceforth, we only consider the periodic boundary condition, that is, the $P = 0$ case.

First, we assume $F = 0$. Carefully considering the boundary condition of the fermion operators, we find $k$ can take $k = \frac{2m+1}{N}\pi$ ($m \in \mathbb{Z}$) and $-\pi \le k \le \pi$, namely

$$k = \begin{cases} -\pi + \frac{\pi}{N}, -\pi + \frac{3\pi}{N}, \ldots, -\frac{\pi}{N}, \frac{\pi}{N}, \ldots, \pi - \frac{3\pi}{N}, \pi - \frac{\pi}{N} & N : \text{even} \\ -\pi, -\pi + \frac{2\pi}{N}, \ldots, -\frac{\pi}{N}, \frac{\pi}{N}, \ldots, \pi - \frac{2\pi}{N}, \pi & N : \text{odd} \end{cases}. \tag{D.4}$$

When the number of sites $N$ is even, the Fourier transformation

$$c_j^\dagger = \frac{1}{\sqrt{N}}\sum_k e^{-\mathrm{i}kj}c_k^\dagger, \quad c_j = \frac{1}{\sqrt{N}}\sum_k e^{\mathrm{i}kj}c_k, \tag{D.5}$$

yields

$$\begin{aligned} H &= \sum_{k>0} \begin{pmatrix} c_k^\dagger & c_{-k} \end{pmatrix} \begin{pmatrix} 2J\cos k - 2\Gamma & 2\mathrm{i}J\sin k \\ -2\mathrm{i}J\sin k & -2J\cos k + 2\Gamma \end{pmatrix} \begin{pmatrix} c_k \\ c_{-k}^\dagger \end{pmatrix} \\ &\equiv \sum_{k>0} \begin{pmatrix} c_k^\dagger & c_{-k} \end{pmatrix} H(k) \begin{pmatrix} c_k \\ c_{-k}^\dagger \end{pmatrix}. \end{aligned} \tag{D.6}$$

The eigenvalue of $H(k)$ is denoted as $\epsilon_k = \pm E_k = \pm 2\sqrt{(J\cos k - \Gamma)^2 + J^2 \sin^2 k}$. As corresponding eigenvectors, we define

$$H(k) \begin{pmatrix} u_k & -v_k^* \\ v_k & u_k^* \end{pmatrix} = \begin{pmatrix} u_k & -v_k^* \\ v_k & u_k^* \end{pmatrix} \begin{pmatrix} E_k & 0 \\ 0 & -E_k \end{pmatrix}, \qquad U_k = \begin{pmatrix} u_k & -v_k^* \\ v_k & u_k^* \end{pmatrix}. \tag{D.7}$$

Using this unitary matrix, the Hamiltonian is represented as

$$H = \sum_{k>0} E_k(\alpha_{k+}^\dagger \alpha_{k+} + \alpha_{k-}^\dagger \alpha_{k-} - 1), \tag{D.8}$$

where

$$\begin{pmatrix} \alpha_{k+} \\ \alpha_{k-}^\dagger \end{pmatrix} = U_k^\dagger \begin{pmatrix} c_k \\ c_{-k}^\dagger \end{pmatrix}. \tag{D.9}$$

The explicit form of $u_k$ and $v_k$ is given by

$$u_k = \sqrt{\frac{1}{2}\left(1 + \frac{2(J\cos k - \Gamma)}{E_k}\right)}, \quad v_k = -\mathrm{i}\frac{J\sin k}{|J\sin k|}\sqrt{\frac{1}{2}\left(1 - \frac{2(J\cos k - \Gamma)}{E_k}\right)}, \tag{D.10}$$

which is provided in the main text (Eq. (4.43)).

If $N$ is odd, the situation is slightly different. In this case, the Hamiltonian is already diagonalised at $k = \pi$ because the non-diagonal component $\sin k = 0$. Therefore, we should specially treat the momentum $k = \pi$ to avoid double counting as

$$H = -2(J+\Gamma)\left(c_\pi^\dagger c_\pi - \frac{1}{2}\right) + \sum_{k>0} \begin{pmatrix} c_k^\dagger & c_{-k} \end{pmatrix} H(k) \begin{pmatrix} c_k \\ c_{-k}^\dagger \end{pmatrix}. \tag{D.11}$$

A similar behaviour also occurs when we consider the $F = 1$ case. The possible momentum is as follows:

$$k = \begin{cases} -\pi, -\pi + \frac{2\pi}{N}, \ldots, -\frac{2\pi}{N}, 0, \frac{2\pi}{N}, \ldots, \pi - \frac{2\pi}{N}, \pi & N : \text{even} \\ -\pi + \frac{\pi}{N}, -\pi + \frac{3\pi}{N}, \ldots, -\frac{2\pi}{N}, 0, \frac{2\pi}{N}, \ldots, \pi - \frac{3\pi}{N}, \pi - \frac{\pi}{N} & N : \text{odd} \end{cases}. \tag{D.12}$$

Therefore, the Hamiltonian should be written as

$$H = 2(J-\Gamma)\left(c_0^\dagger c_0 - \frac{1}{2}\right) - 2(J+\Gamma)\left(c_\pi^\dagger c_\pi - \frac{1}{2}\right) + \sum_{k>0} \begin{pmatrix} c_k^\dagger & c_{-k} \end{pmatrix} H(k) \begin{pmatrix} c_k \\ c_{-k}^\dagger \end{pmatrix}. \tag{D.13}$$

when $N$ is even and

$$H = 2(J-\Gamma)\left(c_0^\dagger c_0 - \frac{1}{2}\right) + \sum_{k>0}\left(c_k^\dagger \; c_{-k}\right) H(k) \begin{pmatrix} c_k \\ c_{-k}^\dagger \end{pmatrix}. \tag{D.14}$$

when $N$ is odd.

To summarise, when the periodic boundary condition is assumed, we find

- $F = 0$, $N$: even

$$H = \sum_{m=0}^{\frac{N}{2}-1}\left(c_k^\dagger \; c_{-k}\right) H(k) \begin{pmatrix} c_k \\ c_{-k}^\dagger \end{pmatrix}, \qquad k = \frac{2m+1}{N}\pi \tag{D.15}$$

- $F = 0$, $N$: odd

$$H = -2(J+\Gamma)\left(c_\pi^\dagger c_\pi - \frac{1}{2}\right) + \sum_{m=0}^{\frac{N-3}{2}}\left(c_k^\dagger \; c_{-k}\right) H(k) \begin{pmatrix} c_k \\ c_{-k}^\dagger \end{pmatrix}, \qquad k = \frac{2m+1}{N}\pi \tag{D.16}$$

- $F = 1$, $N$: even

$$H = 2(J-\Gamma)\left(c_0^\dagger c_0 - \frac{1}{2}\right) - 2(J+\Gamma)\left(c_\pi^\dagger c_\pi - \frac{1}{2}\right) + \sum_{m=1}^{\frac{N}{2}-1}\left(c_k^\dagger \; c_{-k}\right) H(k) \begin{pmatrix} c_k \\ c_{-k}^\dagger \end{pmatrix}, \qquad k = \frac{2m}{N}\pi \tag{D.17}$$

- $F = 1$, $N$: odd

$$H = 2(J-\Gamma)\left(c_0^\dagger c_0 - \frac{1}{2}\right) + \sum_{m=1}^{\frac{N-1}{2}}\left(c_k^\dagger \; c_{-k}\right) H(k) \begin{pmatrix} c_k \\ c_{-k}^\dagger \end{pmatrix}, \qquad k = \frac{2m}{N}\pi \tag{D.18}$$

Within the thermodynamic limit, $k$ is treated as a continuous variable and we do not have to specially treat the $k = 0, \pi$ modes because they will have a benign role in the physical quantities.

# *Acknowledgements*

First, I would particularly like to thank my supervisor, Prof. Masao Ogata for all his support and fruitful scientific discussions. I would like to thank the referees of this dissertation, Prof. Hidenori Takagi, Prof. Naoki Kawashima, Prof. Zenji Hiroi, Prof. Yusuke Kato, and Prof. Chisa Hotta.

I would respectfully like to express the deepest appreciation to research collaborators Dr. Adarsh S. Patri, Ms. Emily Z. Zhang, Prof. SungBin Lee, and Prof. Yong Baek Kim for fruitful discussions and insightful advice. In particular, I would like to express my great appreciation to Prof. Kim for accepting my visiting research in the University of Toronto. I am also deeply grateful to Dr. Hikaru Takeda and Prof. Masafumi Udagawa for their insightful comments and encouragement to the collaborative research. My deepest appreciation goes to Dr. Hiroyasu Matsuura for fruitful scientific discussions and his supports in many academic aspects. I would like to appreciate all colleagues of Ogata group for everyday conversations, scientific discussions, and supports.

I am also supported through the Program for Leading Graduate Schools (MERIT). I would like to thank the assistant supervisor, Prof. Takasada Shibauchi for discussions and advice in the MERIT program.

Finally, but not least, I thank my family and friends for their great supports and encouragement.

# Bibliography


[1] W. Witczak-Krempa, G. Chen, Y. B. Kim, and L. Balents: Annual Review of Condensed Matter Physics **5**, 57 (2014).

[2] R. Schaffer, E. Kin-Ho Lee, B.-J. Yang, and Y. B. Kim: Rep. Prog. Phys. **79**, 094504 (2016).

[3] L. Balents: Nature **464**, 199 (2010).

[4] M. J. P. Gingras and P. A. McClarty: Rep. Prog. Phys. **77**, 056501 (2014).

[5] L. Savary and L. Balents: Rep. Prog. Phys. **80**, 016502 (2017).

[6] Y. Okamoto, M. Nohara, H. Aruga-Katori, and H. Takagi: Phys. Rev. Lett. **99**, 137207 (2007).

[7] T.-H. Han, J. S. Helton, S. Chu, D. G. Nocera, J. A. Rodriguez-Rivera, C. Broholm, and Y. S. Lee: Nature **492**, 406 (2012).

[8] S. T. Bramwell and M. J. P. Gingras: Science **294**, 1495 (2001).

[9] J. G. Rau and M. J. Gingras: Annu. Rev. Condens. Matter Phys. **10**, 357 (2019).

[10] A. Kitaev: Annals of Physics **321**, 2 (2006).

[11] G. Jackeli and G. Khaliullin: Phys. Rev. Lett. **102**, 017205 (2009).

[12] J. G. Rau, E. K.-H. Lee, and H.-Y. Kee: Annu. Rev. Condens. Matter Phys. **7**, 195 (2016).

[13] H. Takagi, T. Takayama, G. Jackeli, G. Khaliullin, and S. E. Nagler: Nat Rev Phys **1**, 264 (2019).

[14] P. W. Anderson: Materials Research Bulletin **8**, 153 (1973).

[15] P. W. Anderson: Science **235**, 1196 (1987).

[16] G. Baskaran, Z. Zou, and P. W. Anderson: Solid State Communications **63**, 973 (1987).

[17] I. Affleck and J. B. Marston: Phys. Rev. B **37**, 3774 (1988).

[18] N. Read and S. Sachdev: Phys. Rev. Lett. **66**, 1773 (1991).

[19] C. Nayak, S. H. Simon, A. Stern, M. Freedman, and S. Das Sarma: Rev. Mod. Phys. **80**, 1083 (2008).

[20] B. J. Kim, H. Ohsumi, T. Komesu, S. Sakai, T. Morita, H. Takagi, and T. Arima: Science **323**, 1329 (2009).

[21] K. W. Plumb, J. P. Clancy, L. J. Sandilands, V. V. Shankar, Y. F. Hu, K. S. Burch, H.-Y. Kee, and Y.-J. Kim: Phys. Rev. B **90**, 041112 (2014).

[22] A. Banerjee, J. Yan, J. Knolle, C. A. Bridges, M. B. Stone, M. D. Lumsden, D. G. Mandrus, D. A. Tennant, R. Moessner, and S. E. Nagler: Science **356**, 1055 (2017).

[23] A. Shitade, H. Katsura, J. Kuneš, X.-L. Qi, S.-C. Zhang, and N. Nagaosa: Phys. Rev. Lett. **102**, 256403 (2009).

[24] J. Chaloupka, G. Jackeli, and G. Khaliullin: Phys. Rev. Lett. **105**, 027204 (2010).

[25] Y. Singh and P. Gegenwart: Phys. Rev. B **82**, 064412 (2010).

[26] K. Kitagawa, T. Takayama, Y. Matsumoto, A. Kato, R. Takano, Y. Kishimoto, S. Bette, R. Dinnebier, G. Jackeli, and H. Takagi: Nature **554**, 341 (2018).

[27] R. Yadav, R. Ray, M. S. Eldeeb, S. Nishimoto, L. Hozoi, and J. van den Brink: Phys. Rev. Lett. **121**, 197203 (2018).

[28] F. Bahrami, W. Lafargue-Dit-Hauret, O. I. Lebedev, R. Movshovich, H.-Y. Yang, D. Broido, X. Rocquefelte, and F. Tafti: Phys. Rev. Lett. **123**, 237203 (2019).

[29] K. Geirhos, P. Lunkenheimer, M. Blankenhorn, R. Claus, Y. Matsumoto, K. Kitagawa, T. Takayama, H. Takagi, I. Kézsmárki, and A. Loidl: Phys. Rev. B **101**, 184410 (2020).

[30] I. Kimchi, J. G. Analytis, and A. Vishwanath: Phys. Rev. B **90**, 205126 (2014).

[31] K. O'Brien, M. Hermanns, and S. Trebst: Phys. Rev. B **93**, 085101 (2016).

[32] A. Biffin, R. D. Johnson, I. Kimchi, R. Morris, A. Bombardi, J. G. Analytis, A. Vishwanath, and R. Coldea: Phys. Rev. Lett. **113**, 197201 (2014).

[33] A. Biffin, R. D. Johnson, S. Choi, F. Freund, S. Manni, A. Bombardi, P. Manuel, P. Gegenwart, and R. Coldea: Phys. Rev. B **90**, 205116 (2014).

[34] K. A. Modic, T. E. Smidt, I. Kimchi, N. P. Breznay, A. Biffin, S. Choi, R. D. Johnson, R. Coldea, P. Watkins-Curry, G. T. McCandless, J. Y. Chan, F. Gandara, Z. Islam, A. Vishwanath, A. Shekhter, R. D. McDonald, and J. G. Analytis: Nat Commun **5**, 4203 (2014).

[35] T. Takayama, A. Kato, R. Dinnebier, J. Nuss, H. Kono, L. S. I. Veiga, G. Fabbris, D. Haskel, and H. Takagi: Phys. Rev. Lett. **114**, 077202 (2015).

[36] J. G. Rau, E. K.-H. Lee, and H.-Y. Kee: Phys. Rev. Lett. **112**, 077204 (2014).

[37] H.-C. Jiang, Z.-C. Gu, X.-L. Qi, and S. Trebst: Phys. Rev. B **83**, 245104 (2011).

[38] J. Reuther, R. Thomale, and S. Trebst: Phys. Rev. B **84**, 100406 (2011).

[39] F. Trousselet, G. Khaliullin, and P. Horsch: Phys. Rev. B **84**, 054409 (2011).

[40] R. Schaffer, S. Bhattacharjee, and Y. B. Kim: Phys. Rev. B **86**, 224417 (2012).

[41] C. C. Price and N. B. Perkins: Phys. Rev. Lett. **109**, 187201 (2012).

[42] C. Price and N. B. Perkins: Phys. Rev. B **88**, 024410 (2013).

[43] J. Knolle, S. Bhattacharjee, and R. Moessner: Phys. Rev. B **97**, 134432 (2018).

[44] J. S. Gordon, A. Catuneanu, E. S. Sørensen, and H.-Y. Kee: Nat Commun **10**, 2470 (2019).

[45] K. Yang, L. K. Warman, and S. M. Girvin: Phys. Rev. Lett. **70**, 2641 (1993).

[46] Y. Shimizu, K. Miyagawa, K. Kanoda, M. Maesato, and G. Saito: Phys. Rev. Lett. **91**, 107001 (2003).

[47] S. Yamashita, T. Yamamoto, Y. Nakazawa, M. Tamura, and R. Kato: Nat Commun **2**, 275 (2011).

[48] Y. Li, G. Chen, W. Tong, L. Pi, J. Liu, Z. Yang, X. Wang, and Q. Zhang: Phys. Rev. Lett. **115**, 167203 (2015).

[49] Y. Shen, Y.-D. Li, H. Wo, Y. Li, S. Shen, B. Pan, Q. Wang, H. C. Walker, P. Steffens, M. Boehm, Y. Hao, D. L. Quintero-Castro, L. W. Harriger, M. D. Frontzek, L. Hao, S. Meng, Q. Zhang, G. Chen, and J. Zhao: Nature **540**, 559 (2016).

[50] J. A. M. Paddison, M. Daum, Z. Dun, G. Ehlers, Y. Liu, M. B. Stone, H. Zhou, and M. Mourigal: Nature Phys **13**, 117 (2017).

[51] M. Hermele, Y. Ran, P. A. Lee, and X.-G. Wen: Phys. Rev. B **77**, 224413 (2008).

[52] S. Yan, D. A. Huse, and S. R. White: Science **332**, 1173 (2011).

[53] B. Fåk, E. Kermarrec, L. Messio, B. Bernu, C. Lhuillier, F. Bert, P. Mendels, B. Koteswararao, F. Bouquet, J. Ollivier, A. D. Hillier, A. Amato, R. H. Colman, and A. S. Wills: Phys. Rev. Lett. **109**, 037208 (2012).

[54] S. Depenbrock, I. P. McCulloch, and U. Schollwöck: Phys. Rev. Lett. **109**, 067201 (2012).

[55] Y. Iqbal, F. Becca, S. Sorella, and D. Poilblanc: Phys. Rev. B **87**, 060405 (2013).

[56] M. Fu, T. Imai, T.-H. Han, and Y. S. Lee: Science **350**, 655 (2015).

[57] M. J. Harris, S. T. Bramwell, D. F. McMorrow, T. Zeiske, and K. W. Godfrey: Phys. Rev. Lett. **79**, 2554 (1997).

[58] E. H. Lieb: Phys. Rev. Lett. **73**, 2158 (1994).

[59] X. Liu, T. Berlijn, W.-G. Yin, W. Ku, A. Tsvelik, Y.-J. Kim, H. Gretarsson, Y. Singh, P. Gegenwart, and J. P. Hill: Phys. Rev. B **83**, 220403 (2011).

[60] Y. Singh, S. Manni, J. Reuther, T. Berlijn, R. Thomale, W. Ku, S. Trebst, and P. Gegenwart: Phys. Rev. Lett. **108**, 127203 (2012).

[61] J. A. Sears, M. Songvilay, K. W. Plumb, J. P. Clancy, Y. Qiu, Y. Zhao, D. Parshall, and Y.-J. Kim: Phys. Rev. B **91**, 144420 (2015).

[62] R. D. Johnson, S. C. Williams, A. A. Haghighirad, J. Singleton, V. Zapf, P. Manuel, I. I. Mazin, Y. Li, H. O. Jeschke, R. Valentí, and R. Coldea: Phys. Rev. B **92**, 235119 (2015).

[63] J.-Q. Yan, S. Okamoto, Y. Wu, Q. Zheng, H. D. Zhou, H. B. Cao, and M. A. McGuire: Phys. Rev. Materials **3**, 074405 (2019).

[64] J. Xing, E. Feng, Y. Liu, E. Emmanouilidou, C. Hu, J. Liu, D. Graf, A. P. Ramirez, G. Chen, H. Cao, and N. Ni: Phys. Rev. B **102**, 014427 (2020).

[65] S.-H. Do, S.-Y. Park, J. Yoshitake, J. Nasu, Y. Motome, Y. S. Kwon, D. T. Adroja, D. J. Voneshen, K. Kim, T.-H. Jang, J.-H. Park, K.-Y. Choi, and S. Ji: Nature Phys **13**, 1079 (2017).

[66] J. Nasu, M. Udagawa, and Y. Motome: Phys. Rev. B **92**, 115122 (2015).

[67] Y. Kasahara, T. Ohnishi, Y. Mizukami, O. Tanaka, S. Ma, K. Sugii, N. Kurita, H. Tanaka, J. Nasu, Y. Motome, T. Shibauchi, and Y. Matsuda: Nature **559**, 227 (2018).

[68] C. Hickey and S. Trebst: Nat Commun **10**, 530 (2019).

[69] M. Hermele, M. P. A. Fisher, and L. Balents: Phys. Rev. B **69**, 064404 (2004).

[70] S.-S. Lee and P. A. Lee: Phys. Rev. Lett. **95**, 036403 (2005).

[71] S. Florens and A. Georges: Phys. Rev. B **70**, 035114 (2004).

[72] F. J. Burnell and C. Nayak: Phys. Rev. B **84**, 125125 (2011).

[73] H.-H. Lai and O. I. Motrunich: Phys. Rev. B **84**, 085141 (2011).

[74] H. Kusunose: Bussei Kenkyu **97**, 730 (2012).

[75] Y. Yanagi: Bussei Kenkyuu Denshiban **6**, 061202 (2016).

[76] H. Kusunose: J. Phys. Soc. Jpn. **77**, 064710 (2008).

[77] S. Hayami and H. Kusunose: J. Phys. Soc. Jpn. **87**, 033709 (2018).

[78] S. Sugano, Y. Tanabe, and H. Kamimura: *Multiplets of Transition-Metal Ions in Crystals* (Academic Press, New York and London, 1970).

[79] A. S. Patri, M. Hosoi, and Y. B. Kim: Phys. Rev. Research **2**, 023253 (2020).

[80] A. S. Patri, M. Hosoi, S. Lee, and Y. B. Kim: Phys. Rev. Research **2**, 033015 (2020).

[81] H. Kusunose: *Electron Theory of Spin-orbit-coupled Physics* (Kodansha, May 2019).

[82] Y. Yanase: Bussei Kenkyuu Denshiban **7**, 072204 (2018).

[83] H. Watanabe and Y. Yanase: Phys. Rev. B **96**, 064432 (2017).

[84] K. Hattori and H. Tsunetsugu: J. Phys. Soc. Jpn. **83**, 034709 (2014).

[85] K. Matsubayashi, T. Tanaka, A. Sakai, S. Nakatsuji, Y. Kubo, and Y. Uwatoko: Phys. Rev. Lett. **109**, 187004 (2012).

[86] T. Onimaru, K. T. Matsumoto, Y. F. Inoue, K. Umeo, T. Sakakibara, Y. Karaki, M. Kubota, and T. Takabatake: Phys. Rev. Lett. **106**, 177001 (2011).

[87] T. Onimaru, K. T. Matsumoto, Y. F. Inoue, K. Umeo, Y. Saiga, Y. Matsushita, R. Tamura, K. Nishimoto, I. Ishii, T. Suzuki, and T. Takabatake: J. Phys. Soc. Jpn. **79**, 033704 (2010).

[88] I. Ishii, H. Muneshige, Y. Suetomi, T. K. Fujita, T. Onimaru, K. T. Matsumoto, T. Takabatake, K. Araki, M. Akatsu, Y. Nemoto, T. Goto, and T. Suzuki: J. Phys. Soc. Jpn. **80**, 093601 (2011).

[89] I. Ishii, H. Muneshige, S. Kamikawa, T. K. Fujita, T. Onimaru, N. Nagasawa, T. Takabatake, T. Suzuki, G. Ano, M. Akatsu, Y. Nemoto, and T. Goto: Phys. Rev. B **87**, 205106 (2013).

[90] M. Matsushita, J. Sakaguchi, Y. Taga, M. Ohya, S. Yoshiuchi, H. Ota, Y. Hirose, K. Enoki, F. Honda, K. Sugiyama, M. Hagiwara, K. Kindo, T. Tanaka, Y. Kubo, T. Takeuchi, R. Settai, and Y. Ōnuki: J. Phys. Soc. Jpn. **80**, 074605 (2011).

[91] A. Sakai, K. Kuga, and S. Nakatsuji: J. Phys. Soc. Jpn. **81**, 083702 (2012).

[92] M. Tsujimoto, Y. Matsumoto, T. Tomita, A. Sakai, and S. Nakatsuji: Phys. Rev. Lett. **113**, 267001 (2014).

[93] S. Lee, S. Trebst, Y. B. Kim, and A. Paramekanti: Phys. Rev. B **98**, 134447 (2018).

[94] A. S. Patri, A. Sakai, S. Lee, A. Paramekanti, S. Nakatsuji, and Y. B. Kim: Nat Commun **10**, 4092 (2019).

[95] M. Hosoi, E. Z. Zhang, A. S. Patri, and Y. B. Kim: arXiv:2201.00828 [cond-mat] (2022).

[96] S. Onoda and Y. Tanaka: Phys. Rev. B **83**, 094411 (2011).

[97] S. Onoda and Y. Tanaka: Phys. Rev. Lett. **105**, 047201 (2010).

[98] S. Lee, S. Onoda, and L. Balents: Phys. Rev. B **86**, 104412 (2012).

[99] Tang, Nan, Sakai, Akito, Kimura,Kenta, Nakamura, Shota, Matsumoto, Yosuke, Sakakibara, Toshiro, and Nakatsuji, Satoru: Bulletin of the American Physical Society, Vol. Volume 64, Number 2, March 2019.

[100] K. Kimura, S. Nakatsuji, J.-J. Wen, C. Broholm, M. B. Stone, E. Nishibori, and H. Sawa: Nat Commun **4**, 1934 (2013).

[101] Y. Machida, S. Nakatsuji, S. Onoda, T. Tayama, and T. Sakakibara: Nature **463**, 210 (2010).

[102] L. Savary and L. Balents: Phys. Rev. Lett. **108**, 037202 (2012).

[103] A. Yaouanc, P. Dalmas de Réotier, P. Bonville, J. A. Hodges, V. Glazkov, L. Keller, V. Sikolenko, M. Bartkowiak, A. Amato, C. Baines, P. J. C. King, P. C. M. Gubbens, and A. Forget: Phys. Rev. Lett. **110**, 127207 (2013).

[104] J. Robert, E. Lhotel, G. Remenyi, S. Sahling, I. Mirebeau, C. Decorse, B. Canals, and S. Petit: Phys. Rev. B **92**, 064425 (2015).

[105] J. D. Thompson, P. A. McClarty, D. Prabhakaran, I. Cabrera, T. Guidi, and R. Coldea: Phys. Rev. Lett. **119**, 057203 (2017).

[106] A. M. Hallas, J. Gaudet, N. P. Butch, M. Tachibana, R. S. Freitas, G. M. Luke, C. R. Wiebe, and B. D. Gaulin: Phys. Rev. B **93**, 100403 (2016).

[107] Y.-P. Huang, G. Chen, and M. Hermele: Phys. Rev. Lett. **112**, 167203 (2014).

[108] Y.-D. Li and G. Chen: Phys. Rev. B **95**, 041106 (2017).

[109] A. Banerjee, S. V. Isakov, K. Damle, and Y. B. Kim: Phys. Rev. Lett. **100**, 047208 (2008).

[110] O. Benton: Phys. Rev. B **102**, 104408 (2020).

[111] E. M. Smith, O. Benton, D. R. Yahne, B. Placke, J. Gaudet, J. Dudemaine, A. Fitterman, J. Beare, A. R. Wildes, S. Bhattacharya, T. DeLazzer, C. R. C. Buhariwalla, N. P. Butch, R. Movshovich, J. D. Garrett, C. A. Marjerrison, J. P. Clancy, E. Kermarrec, G. M. Luke, A. D. Bianchi, K. A. Ross, and B. D. Gaulin: arXiv:2108.01217 [cond-mat] (2021).

[112] A. Bhardwaj, S. Zhang, H. Yan, R. Moessner, A. H. Nevidomskyy, and H. J. Changlani: arXiv:2108.01096 [cond-mat] (2021).

[113] K. Tomiyasu, K. Matsuhira, K. Iwasa, M. Watahiki, S. Takagi, M. Wakeshima, Y. Hinatsu, M. Yokoyama, K. Ohoyama, and K. Yamada: J. Phys. Soc. Jpn. **81**, 034709 (2012).

[114] H. Guo, K. Matsuhira, I. Kawasaki, M. Wakeshima, Y. Hinatsu, I. Watanabe, and Z.-a. Xu: Phys. Rev. B **88**, 060411 (2013).

[115] A. Bertin, P. Dalmas de Réotier, B. Fåk, C. Marin, A. Yaouanc, A. Forget, D. Sheptyakov, B. Frick, C. Ritter, A. Amato, C. Baines, and P. J. C. King: Phys. Rev. B **92**, 144423 (2015).

[116] V. K. Anand, A. K. Bera, J. Xu, T. Herrmannsdörfer, C. Ritter, and B. Lake: Phys. Rev. B **92**, 184418 (2015).

[117] E. Lhotel, S. Petit, S. Guitteny, O. Florea, M. Ciomaga Hatnean, C. Colin, E. Ressouche, M. R. Lees, and G. Balakrishnan: Phys. Rev. Lett. **115**, 197202 (2015).

[118] J. Xu, V. K. Anand, A. K. Bera, M. Frontzek, D. L. Abernathy, N. Casati, K. Siemensmeyer, and B. Lake: Phys. Rev. B **92**, 224430 (2015).

[119] B. Gao, T. Chen, D. W. Tam, C.-L. Huang, K. Sasmal, D. T. Adroja, F. Ye, H. Cao, G. Sala, M. B. Stone, C. Baines, J. A. T. Verezhak, H. Hu, J.-H. Chung, X. Xu, S.-W. Cheong, M. Nallaiyan, S. Spagna, M. B. Maple, A. H. Nevidomskyy, E. Morosan, G. Chen, and P. Dai: Nat. Phys. **15**, 1052 (2019).

[120] J. Gaudet, E. M. Smith, J. Dudemaine, J. Beare, C. R. C. Buhariwalla, N. P. Butch, M. B. Stone, A. I. Kolesnikov, G. Xu, D. R. Yahne, K. A. Ross, C. A. Marjerrison, J. D. Garrett, G. M. Luke, A. D. Bianchi, and B. D. Gaulin: Phys. Rev. Lett. **122**, 187201 (2019).

[121] R. Sibille, E. Lhotel, V. Pomjakushin, C. Baines, T. Fennell, and M. Kenzelmann: Phys. Rev. Lett. **115**, 097202 (2015).

[122] H. Yan, O. Benton, L. Jaubert, and N. Shannon: Phys. Rev. B **95**, 094422 (2017).

[123] Y. Huang, K. Chen, Y. Deng, N. Prokof'ev, and B. Svistunov: Phys. Rev. Lett. **116**, 177203 (2016).

[124] H.-J. Yang, N. Shannon, and S. Lee: Phys. Rev. B **104**, L100403 (2021).

[125] J. Xu, C. Balz, C. Baines, H. Luetkens, and B. Lake: Phys. Rev. B **94**, 064425 (2016).

[126] J. Xu, O. Benton, A. T. M. N. Islam, T. Guidi, G. Ehlers, and B. Lake: Phys. Rev. Lett. **124**, 097203 (2020).

[127] S. Zhang, H. J. Changlani, K. W. Plumb, O. Tchernyshyov, and R. Moessner: Phys. Rev. Lett. **122**, 167203 (2019).

[128] R. Moessner and J. T. Chalker: Phys. Rev. Lett. **80**, 2929 (1998).

[129] M. Lakshmanan: Philosophical Transactions of the Royal Society A: Mathematical, Physical and Engineering Sciences **369**, 1280 (2011).

[130] E. R. Gagliano and C. A. Balseiro: Phys. Rev. Lett. **59**, 2999 (1987).

[131] E. Dagotto: Rev. Mod. Phys. **66**, 763 (1994).

[132] M. Kawamura, K. Yoshimi, T. Misawa, Y. Yamaji, S. Todo, and N. Kawashima: Computer Physics Communications **217**, 180 (2017).

[133] M. Gohlke, G. Wachtel, Y. Yamaji, F. Pollmann, and Y. B. Kim: Phys. Rev. B **97**, 075126 (2018).

[134] Z. Hiroi, K. Matsuhira, and M. Ogata: J. Phys. Soc. Jpn. **72**, 3045 (2003).

[135] J. Carrasquilla, Z. Hao, and R. G. Melko: Nat Commun **6**, 7421 (2015).

[136] J.-J. Wen, S. M. Koohpayeh, K. A. Ross, B. A. Trump, T. M. McQueen, K. Kimura, S. Nakatsuji, Y. Qiu, D. M. Pajerowski, J. R. D. Copley, and C. L. Broholm: Phys. Rev. Lett. **118**, 107206 (2017).

[137] P. Bonville, S. Guitteny, A. Gukasov, I. Mirebeau, S. Petit, C. Decorse, M. C. Hatnean, and G. Balakrishnan: Phys. Rev. B **94**, 134428 (2016).

[138] Y. Tokiwa, T. Yamashita, D. Terazawa, K. Kimura, Y. Kasahara, T. Onishi, Y. Kato, M. Halim, P. Gegenwart, T. Shibauchi, S. Nakatsuji, E.-G. Moon, and Y. Matsuda: J. Phys. Soc. Jpn. **87**, 064702 (2018).

[139] L. Savary and L. Balents: Phys. Rev. Lett. **118**, 087203 (2017).

[140] A. W. Kinross, M. Fu, T. J. Munsie, H. A. Dabkowska, G. M. Luke, S. Sachdev, and T. Imai: Phys. Rev. X **4**, 031008 (2014).

[141] J. Steinberg, N. P. Armitage, F. H. L. Essler, and S. Sachdev: Phys. Rev. B **99**, 035156 (2019).

[142] J. A. Hodges, P. Bonville, A. Forget, M. Rams, K. Królas, and G. Dhalenne: J. Phys.: Condens. Matter **13**, 9301 (2001).

[143] A. Wörl, T. Onimaru, Y. Tokiwa, Y. Yamane, K. T. Matsumoto, T. Takabatake, and P. Gegenwart: Phys. Rev. B **99**, 081117 (2019).

[144] F. Weickert, P. Gegenwart, C. Geibel, W. Assmus, and F. Steglich: Phys. Rev. B **98**, 085115 (2018).

[145] R. Küchler, C. Stingl, Y. Tokiwa, M. S. Kim, T. Takabatake, and P. Gegenwart: Phys. Rev. B **96**, 241110 (2017).

[146] M. Majumder, R. S. Manna, G. Simutis, J. C. Orain, T. Dey, F. Freund, A. Jesche, R. Khasanov, P. K. Biswas, E. Bykova, N. Dubrovinskaia, L. S. Dubrovinsky, R. Yadav, L. Hozoi, S. Nishimoto, A. A. Tsirlin, and P. Gegenwart: Phys. Rev. Lett. **120**, 237202 (2018).

[147] T. A. Bojesen and S. Onoda: Phys. Rev. Lett. **119**, 227204 (2017).

[148] N. Martin, P. Bonville, E. Lhotel, S. Guitteny, A. Wildes, C. Decorse, M. Ciomaga Hatnean, G. Balakrishnan, I. Mirebeau, and S. Petit: Phys. Rev. X **7**, 041028 (2017).